Synthesis and application of photoactive nanomaterials for antimicrobial and catalytic activity

Connor Bourgonje

Thesis submitted to the University of Ottawa in partial fulfillment of the requirements for the degree of:

Doctorate of Philosophy

In

Chemistry

Department of Chemistry and Biomolecular Sciences

Faculty of Science

University of Ottawa

Supervisor: Juan (Tito) Scaiano

Dedicated to my late mother, Terry, and my dad, Everett - the two greatest role models a kid could ever ask for.

Without mom's brilliance, and dad's strength of character, none of this would be possible.

In everything I do, I strive to be a reflection of them.

Thanks for everything.

Abstract

In this work we sought to investigate the fascinating and powerful interactions between light and metal nanoparticles of silver (AgNPs) and palladium (PdNPs) to enhance their applications in photobiology and catalysis. This work begins with the synthesis of citrate capped silver NPs using in-flow irradiation of various Norrish Type-1 photoinitiators with $AgNO_3$ to generate AgNP "seeds" rapidly, and at relatively large scale. Using these seeds, we can take advantage of their high sensitivity to light to further drive the growth of these small AgNPs into larger, more complex structures such as triangles and decahedra without having to add bulky surfactants or polymers. In this approach, we can control nanoparticle shape using different wavelengths of LED illumination, while adjusting citrate concentration can allow for the fine tuning of AgNP absorbance throughout the visible spectrum, and into the NIR region. Using our light-generated AgNPs, we observe potent light-activated antibacterial effects when irradiating the NPs with light wavelengths corresponding to their plasmonic absorbance. These particles are able to totally wipe out bacterial cultures in batch at high bacterial concentrations at AgNP concentrations as low as 10 ppm. These highly antibacterial NPs can also be fixed to a heterogenous support, glass wool (AgNPs@GW), to act as a heterogenous antibacterial agent, effectively killing bacteria under white light irradiation for effective in-flow treatment of bacteria contaminated water. We show that the antibacterial effects from these particles may be derived from a combined light-activated heating effect, along with light-induced reactive oxygen species (ROS) generation. Applying these same lessons to industrially relevant reactions, in our final chapter we utilize the same versatile support, glass wool, to fix PdNPs, making an effective heterogenous nitro-to-amine photocatalyst. Using a broad range of characterization methods, we demonstrate the effectiveness of high-resolution light microscopy techniques (confocal, TIRF, FLIM) at visualizing the catalytic sites on PdNP coated GW fibres. Under these conditions, we show that Pd on GW is a stable and robust catalyst for the nitro-to-amine reaction, showing little catalyst migration or loss of activity, even after several hours on continuous flow.

This work demonstrates the utilization of visible and NIR irradiation to control nanoparticle synthesis, enhance antibacterial activity, develop in-flow water treatments, and drive flow-photoreactors. Altogether, this thesis aims to demonstrate the enhanced capabilities of materials when they interact with light, effectively enhancing their already fascinating properties.

Acknowledgements

Firstly, I must thank my loving parents who have always encouraged and supported me no matter where my career took me. I owe my love of science to my late mother who herself was passionate about science and healthcare until her final days. She was my driving force at many points of this degree, and my only regret is that she never got to read this thesis.

I also want to thank my dad for his never-ending support of my dreams. Dad taught me to love life in all its forms, and the importance of community. While mom pushed me in school, dad showed me how to be a good friend, and a reliable neighbor, and these skills have served me well in my time at uOttawa.

There are so many people who have helped form me into the scientist that I am today. My undergraduate supervisor Dr. Max Anikovskiy was instrumental in my journey, and without his mentorship I never would have had the courage to do this. Ever since I arrived in Ottawa my supervisor Tito Scaiano has gone above and beyond for me. The Scaiano Lab has felt like my family in Ottawa, and it all starts with Tito. Through what has been at times the hardest years of my life, Tito and has done everything in his power to support me and encourage me to follow my heart, and I will be forever grateful. Tito always says that our education should not be limited to our experiments; we must be students of life, and when we leave school for our careers we should leave as better humans. The culture in this lab is unlike any other, and I am so lucky to have shared the lab with such great people.

I also want to thank the many professors who I have worked with on various initiatives that were very close to my heart in the Faculty of Science, especially Dr.'s Deryn Fogg, Jeffrey Keillor, Adam Shuhendler, Jaclyn Brusso, and Sue McKee. I have learned so much about leadership and advocacy from these professors (and others), and occasionally I even learned a little bit about science too.

Finally, I have so many friends to count between Ottawa and Alberta who have kept me sane over the last 5 years. Through the pandemic, and countless late nights writing reports, grading papers, and running experiments, I have been blessed with a network of people who have never given up on me, even when the weight of life kept me from being my best self. I've leaned a lot on my circles over the last few years, and I hope that you will do me the honor of returning the favor one day. If I could pass on any wisdom to the reader, it's that my life got a lot better when I learned to ask for help, and I owe that to the amazing people I've met during my time in Sundre, Calgary, Ottawa, and now Edmonton.

Table of Contents

List of Figures

List of Schemes and Tables

Chapter 1 - Introduction

1.1: Let There Be Light

Since *Homo erectus* first learned to harness light as a tool (in the form of fire) over ~1.5 million years ago,[1] we humans have been addicted. Few things in life are as ubiquitous in our history as light. Whether it be the sun bearing down on us on a clear summer day, or the streetlights guiding us home after a long night out; light is woven into the tapestry of human history, culture, and society. Even our most ancient and sacred ceremonies are interwoven with light and colour; from Diwali to Hanukkah to the countless sun deities that humanity has venerated over the millennia, light has been a cornerstone of human celebration and fascination for time immemorial.

So important was the worship of the sun in some cultures, that it may have even inadvertently guided humanities' first steps into the world of photochemistry.[2,3] Some of these early examples of light being used to do chemistry began to emerge over 4000 years ago in ancient Egypt – a civilization with numerous major deities directly associated with the sun. The Egyptians found that boiled extracts of the *Ammi majus* plant could be used to treat the rare skin depigmentation disorder, vitiligo.[2] In this practice, patients would consume the extract and lay in roofless temples dedicated to their sun deities, bathing in the healing rays of their chosen solar patron.[4] Unbeknownst to them, just beneath their skin the solar radiation was activating one of the first known photochemical reactions ever performed by humans.[3] In this ancient example, psoralen rich extracts of the *Ammi majus* plant act as a photosensitizer, undergoing UVA induced cross-linking with nucleotides – the building blocks of DNA – while irreversibly fusing into the DNA of cells in regions with low skin pigment, ultimately leading to cell death (Fig.1.1.1).[5,6] This treatment is so effective at reversing the disease that more refined derivatives of *Ammi majus* extracts are still used today in modern photochemotherapy treatments, and now is applied to a wide range of diseases including psoriasis, lymphoma, and eczema, among others.[7]

Four thousand years later the technique that the Egyptians developed lives on, but the world they once knew is unrecognizable. One thing that never changed, however, is our reverence of the sun and light, and our recognition of the seemingly infinite power it contains. While our physical understanding of this power may differ, nevertheless we still endeavor to harness the power of the sun through solar cells, and still bathe in light – either solar or synthetic – for a variety of medical treatments.[8] An unknowing onlooker may even mistake our own modern practices for solar worship.

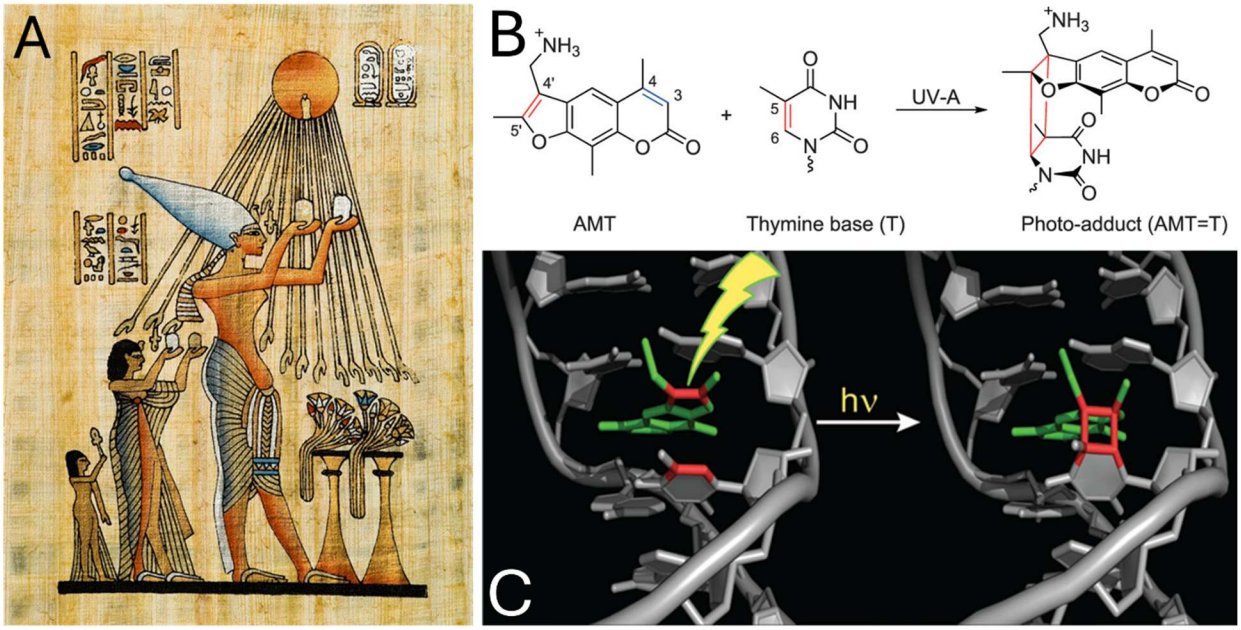

Fig. 1.1.1: A) Reproduction of ancient Egyptian artwork depicting the offerings of gifts to the sun in the presence of urns adorned with medicinal plants.[3] B) Reaction scheme describing the formation of a photo-adduct between psoralen derivative 4'-aminomethyl-4,5',8-trimethylpsoralen (AMT), and a thymine nucleotide.[6] C) Depiction of AMT intercalation and photoaddition into a DNA helix through UVA induced cross-linking.[6] Panel A reproduced with permission of the Royal Society of Chemistry. Panels B&C reproduced with the permission of the American Chemical Society.

Look no further than the millions of people who gathered to observe the total solar eclipse in April of 2024, many of these observers making costly pilgrimages across oceans and continents to witness several minutes of solar glory.

The sun has also been a major driver of many inventions which we encounter on a daily basis. After all, this unrelenting, nearly inescapable barrage of electromagnetic energy surrounds us daily, affecting nearly everything that we encounter. A large portion of human history has been spent trying to fight against the negative effects of light. Many fashion trends, the multibillion-dollar sunglass industry, and the field of sunscreens all owe their success to humanity trying to protect ourselves from sunlight. Even the iconic innovation of using tinted glass used in the beer bottling industry was developed to protect the components of hops, namely iso-humulone, from being photolyzed into more bitter compounds which are known to sully the flavor of the beverage.[9]

1.2: Photochemistry

Despite our long history of battling (and worshipping) the sun, humans in the last 150 years have returned to our ancient roots of using light as a tool to drive chemical processes. Giacomo Ciamician (1857-1922) is often heralded as the father of this revolution.[10] His work around the turn of the 20th century with Paul Silber became some of the first examples of photochemistry in modern science, with their early works demonstrating the photochemical reductions of compounds such as aldehydes, ketones, quinones and nitro compounds, all using light to substitute harsher reagents or reaction conditions.[11] It is important to note that these reactions were performed under solar illumination, as electrical lighting sources during the time of Ciamician were both expensive and inferior to the irradiance of the sun (Fig. 1.2.1).

In more recent years, innovations in light sources have allowed modern man to emulate and even surpass the irradiance of the sun with instruments that can fit in the palm of one's hand. The most advanced lasers can easily cost hundreds of thousands of dollars, requiring intricate optical set-ups and highly trained technicians. Luckily, the growing market for less advanced light emitting diodes (LEDs) and lasers has also made efficient, intense, and user-friendly light sources broadly accessible. To put the pace of these innovations into perspective: I was born in 1996 - 3 years after Shuji Nakamura developed his approach to producing high-brightness blue GaN based LEDs – an invention which earned him a share of the 2014 Nobel Prize in Physics.[12] This invention was critical to the development of white LEDs – which require a blue LED paired with a yellow emitting phosphor to create white light. This revolutionized consumer electronics, leading to a rapid overhaul of personal and commercial lighting. The continued development of LED technology into the 21st century has provided researchers with convenient, powerful, and increasingly affordable light sources spanning the ultraviolet (UV), visible, and near infra-red (NIR) regions of the electromagnetic spectrum.[12,13] With conventional illumination sources becoming so effective and affordable, there has never been a better time to explore the applications of photochemistry to solve real world problems. Photochemical reactors can now be manufactured with relative ease, and an entry level LED illumination system can be constructed for little more less than the cost of a steak dinner.[14] Subsequently, exploration in photochemistry has become incredibly popular in the last decade, finding broad applications in luminescent materials, photocatalysis, polymerization, medicine, microelectronics/fluidics, and water treatment, to only name a few fields that are reaping the rewards of using light to enhance chemistry.[15,16]

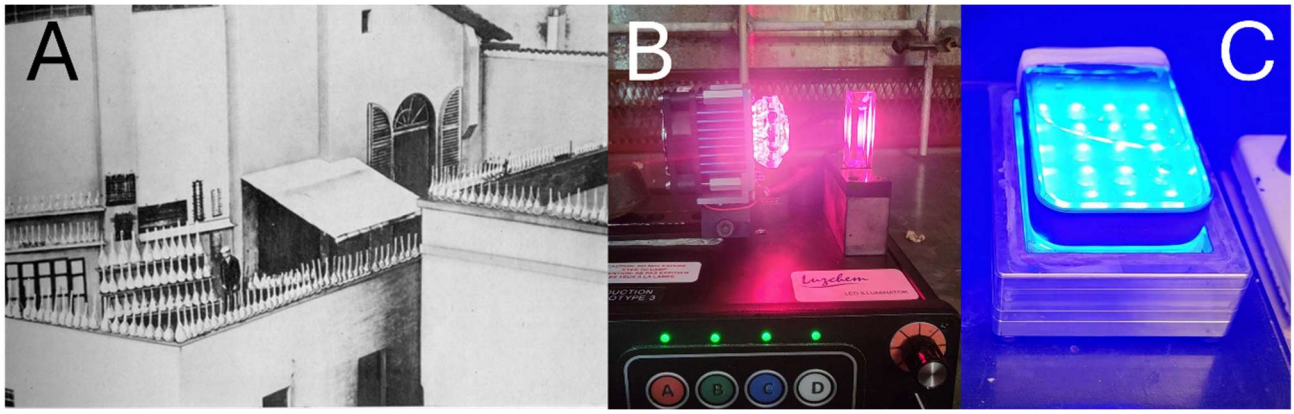

Fig. 1.2.1: Photochemistry then and now. A) Dr. Giacomo Ciamician along with his many photochemical reactions on the roof of the Chemical Institute at the University of Bologna.[10] B&C) Modern LED illuminators used in this thesis. Panel A reproduced with permission of the Royal Society of Chemistry.

Photochemical reactions are defined by two laws: the Grotthus-Draper Law and Stark-Einstein Law, also known as the first and second laws of photochemistry, respectively.[17] The first rule of photochemistry states that in order for a photochemical reaction to occur, a photon must be absorbed by the system of interest. In turn, the second law states that for each of these photons absorbed by system, only one molecule can be excited. During an excitation event, the energy of the incident photon is absorbed by a "ground state" (S_0) electron. Exciting it to a higher energy level, known as an excited state (S_x, where x is a number greater than 0) electron in the target molecule.[18] From this excited state, the electron must then relax back down to the ground state. This can be done through intramolecular transitions to dissipate the absorbed energy. Such transitions include intersystem crossing, internal conversion, or fluorescent/phosphorescent emission.[18] These are often summarized in the popularized format of a Jablonski diagram, which best applies to examples of organic photochemistry (Fig. 1.2.2).

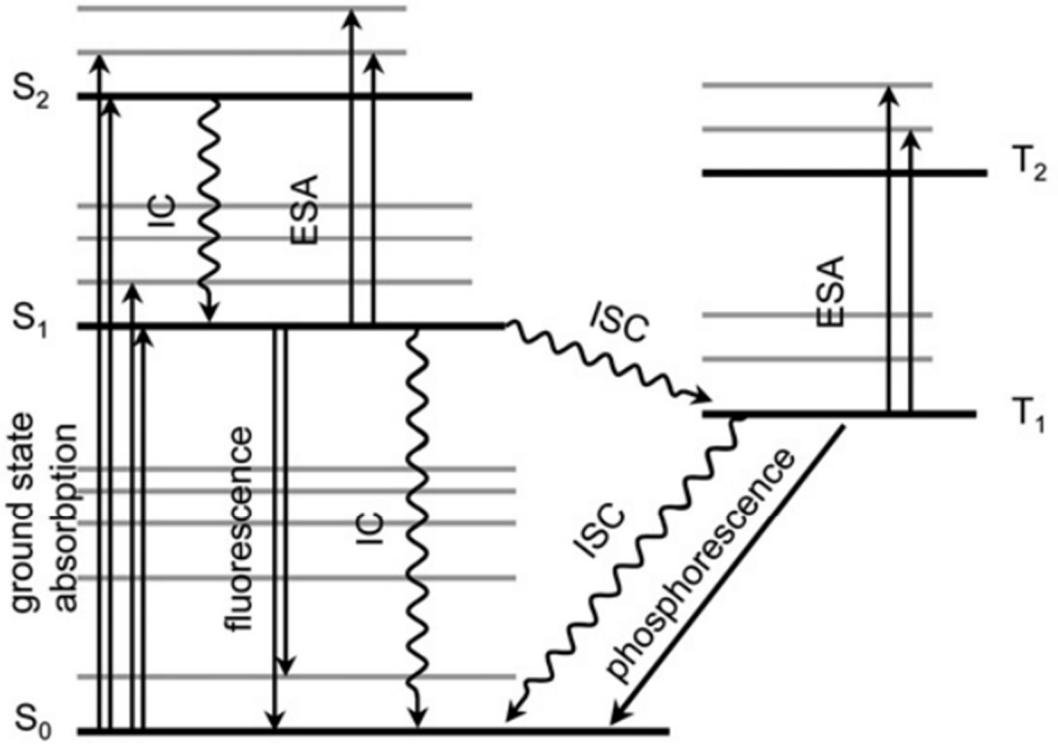

Fig. 1.2.2: A simple Jablonski diagram.[19] Upward arrows depict excitation events. Downward arrows represent mechanisms of excited state decay, where straight arrows are radiative (light producing) decay, and wavy lines represent non-radiative forms of decay. IC: internal conversion, ISC: intersystem crossing, ESA: excited state absorbance, S_n: singlet states, and T_n: triplet states. Reproduced with permission of the Royal Society of Chemistry.

In some cases, a molecule can use the energy of an excited state to do work, such as bond rotation, isomerization, or bond cleavage, potentially generating new photoproducts and photogenerated radicals.[20] Under the right conditions, many useful interactions between different excited and non excited molecules are possible as well, including energy transfer,[21] reactive oxygen species (ROS) generation,[22] cross-linking (i.e, in the *Ammi majus* example),[6] and a range of other processes.[23]

Other examples of light excitation exist for inorganic materials, such as in semi-conductors, quantum dots, and plasmonic materials.[24] While these materials have their own more-or-less analogous mechanisms for carrying out photochemical processes, it is clear that different materials are difficult to describe using just one broad definition. However, each of these examples are connected by their capacity to be transformed through light excitation from materials which may otherwise be stable or unreactive into powerful drivers of chemical change. The development and discovery of these photoactive materials have become incredibly popular and profitable in the 21st century.[17]

The increasing popularity of photochemistry makes sense for a number of practical reasons:

i) Affordability & Accessibility

Light is an incredibly predictable, affordable, and abundant reagent. While the cost of light sources varies with complexity, the electricity to power them is far cheaper than any chemical additive, and typically far easier to work with.[15] While commercial light sources require electricity, sunlight is free. Subsequently, there is considerable potential for developing reactions that can be driven by solar light.[25] This has particular potential in addressing challenges in remote or impoverished areas, especially for water treatment.

ii) Controllability

By controlling reactions with light rather than chemical additives, researchers gain far greater control over their reactions. Want your reaction to proceed slower? Use less light. Want to stop it all together? Simply turn off your light source. In more complicated systems, it is possible to activate different materials at different stages of a reaction using different colors of light, or even to regenerate catalysts after they've been "spent" in crop rotation-like practices.[26] The technique of "critical timing" can be used to stop a reaction at its midpoint, allowing for the generation of valuable intermediates, such as semi hydrogenated compounds.[27]

iii) Localization

Articulating light sources can be easily manipulated to target specific regions of interest. This is especially useful in the medical field of phototherapy, where medical researchers and practitioners can use light-activated drugs to localize drug activity to specific regions of the body.[28] This targeted approach can also reduce the amount of drug that needs to be administered to a patient, while reducing off-site reactions for faster recovery times and reduced side effects in patients.

iv) Greener, safer chemistry

The reduced reliance on additives and ability to drive catalysis makes photochemistry a prime candidate for green development, allowing researchers to perform reactions with materials which are potentially safer to work with, and less toxic to the environment.[29] The development of green photocatalysts is a significant area of study, and has the potential to revolutionize many industries. Photochemical

degradation and removal of toxic waste products has also seen significant progress in recent years, largely due to the potential for photodegradation of contaminants in-flow.

v) Flow compatibility

Flow chemistry is an increasingly popular approach to scaling reactions from the lab bench to industrially relevant throughputs.[30] In this paradigm, a transparent flow vessel can be loaded with insoluble photocatalysts and activated with external or internal light sources. Using heterogeneous photocatalysis, reactions can be scaled without extra additives, working hand-in-hand with the goals of green chemistry, while also bridging the gap between research and industry.[31]

With so many advantages, the allure of photochemistry is understandable. And yet, even I must admit that before arriving at the Scaiano Lab I underestimated just how powerful and convenient light can be when used as a reagent.

Herein, I endeavor to highlight the interactions between light and nanomaterials, and describe the advances we have made in nanomaterial synthesis (Chapter 2), antimicrobial activity (Chapter 3), water treatment (Chapter 4), and flow catalysis (Chapter 5).

1.3: Metal Nanoparticles

Plasmonic Materials

Much like photochemistry, the story of nanomaterials is one with ancient origins, with materials such as carbon nanotubes, metal nanoparticles such as gold, silver, and copper appearing in many ancient works such as pottery and glasswork.[32] Perhaps the most famous example is the Lycurgus cup – a caged glass cup from the late Roman period (~300 CE) which brilliantly changes colour in different lighting due to a mixture of gold and silver nanoparticles trapped within the glass of the piece (Fig.1.3.1).[33]

While the ancient artists and craftsmen almost certainly did not realize exactly what they were working with, they were captivated by the unique optical properties of these miniaturized metal particles. Nanomaterials continued to be used in various artforms long after the Romans faded into history. Whether in ceramics, metallurgy, or stained glass, nanomaterials have been subtly hiding in plain sight for generations. Nanoparticles first began to emerge in literature in the late 1800's, however the assignment of the "nano" title is retroactive.[34,35]

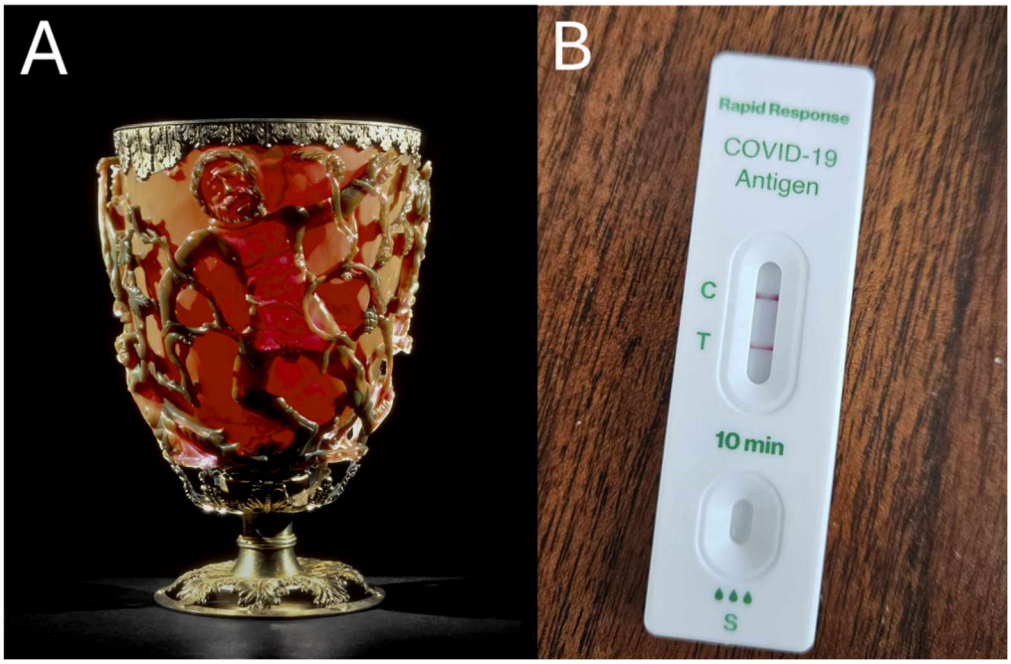

Fig. 1.3.1: Nanoparticles over the years: A) The Lycurgus cup with light transmitting through the nanoparticle embedded glass.[33] © The Trustees of the British Museum. B) A COVID-19 Rapid Response test utilizing colored nanoparticles to create a sensitive colorimetric assay for detecting COVID-19 antigen.

In this era researchers could not visualize nanomaterials, but they began to observe strange light interactions from mixtures of reduced metal salts and metal oxides that could not be explained by conventional understandings at the time.[36] The field of nanomaterials as a cohesive realm of study began to gain momentum in the latter half of the 20th century with the invention of electron microscopy techniques, notably transmission electron microscopy (TEM), which was first developed in the 1930s (albeit at very low magnification initially), and scanning tunneling microscopy (STEM) in 1980, which truly sparked a chain reaction which has catapulted nanomaterial science to the forefront of science and technology.[37] In 1959 Richard Feynman gave his famous “Plenty of room at the bottom” speech, signaling a new era of discovery in the nano-realm.[38] Continued advances in imaging technology have managed to drive rapid innovation within the field, securing nanotechnology a spot as one of the fastest growing areas of research in the 21st century. With a full toolkit of modern characterization techniques, we can now attribute the unique features observed in nanomaterials to their nanometric geometries (generally 1-100 nm), providing them with completely different physical and optical characteristics compared to their bulk counterparts.[37] These materials have proven to be powerful tools in 21st century technology, finding applications in physics, biology, engineering, and chemistry, and making strong strides in industry.[39]

The cornerstone of this body of work was the investigation of silver nanoparticles (Chapters 2-4), as well as the application and investigation of catalytic palladium nanoparticles with advanced light microscopy (Chapter 5). Both of these noble metals exhibits remarkable light-activated characteristics on the nanoscale, and have massive market shares in the industrial use of nanomaterials.[40] The source of the fascinating interactions with light seen in these materials (and many other metals) is the photophysical phenomenon known as localized surface plasmon resonance (LSPR).[41] LSPR is caused by the interactions of surface electrons in certain metal nanoparticles with the changing electromagnetic field produced by incident photons, inducing rapid oscillations in the polarization of electrons, creating an "electron cloud" (Fig.1.3.2).[42] As a result, nanoparticle colloids may be observed to have distinctive rich colours, corresponding to strong visible absorption bands, often referred to as "plasmon bands", or "plasmonic absorbance". The extinction coefficients of plasmonic materials can be several orders of magnitude superior to those of organic dyes, giving them exceptional optical properties in colorimetric applications.[43] These strong absorbances are a critical component of many nanosensors, perhaps most famously making an appearance in many types of COVID-19 rapid antigen detection tests amidst the global pandemic in 2020 (Fig. 1.3.1).[44] In these types of sensors, the remarkable extinction coefficient of gold and silver nanoparticles enable the visualization of trace levels of viral proteins, allowing for quick, sensitive, point-of-care disease diagnosis. The usefulness of plasmonic absorbance is not only limited to visible sensing applications. By activating the LSPR of nanomaterials using complimentary light irradiation, scientists have been able to unlock new facets of chemical reactivity such as plasmonic super heating, hot carrier generation, and a wide range of photocatalytic reactions such as water splitting, hydrogen generation, photoredox catalysis, among others.[45]

By using complementary light excitation to activate the LSPR of AgNPs and PdNPs in this work, we are able to achieve significant photochemical effects. In the case of AgNPs, we explore the immense light activated antibacterial properties that can be achieved under red and blue light irradiation. Notably, we also observe activated Pd to be quite efficient at hydrogen generation, making it excellent in reductive catalysis. This is especially useful in the nitro-to-amine reduction, a reaction which generates billions annually.[46] Using advanced microscopy techniques, we demonstrate the in-flow stability, and near-surface reduction of nitro compounds by PdNPs fixed to glass wool.

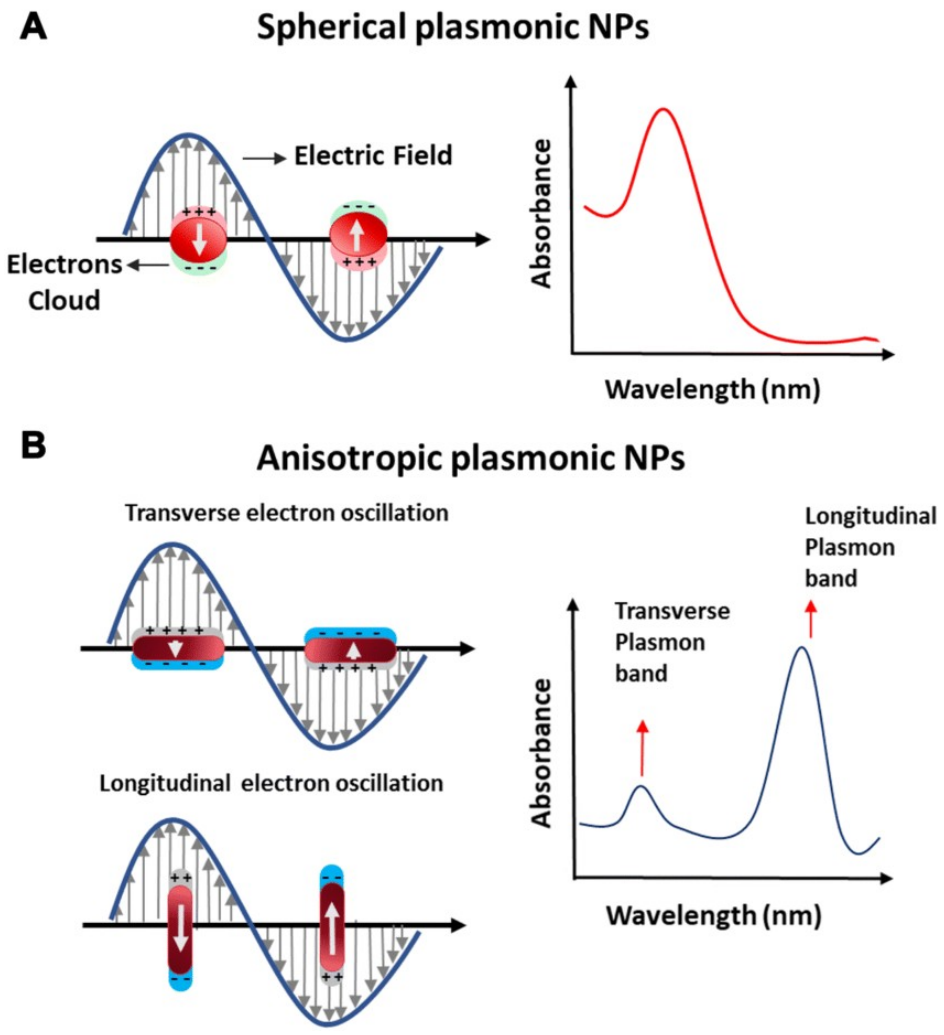

Fig 1.3.2: Graphical representations of localized SPR in nanoparticles in response to incident light, and corresponding visible absorbance spectra for spherical (A) and anisotropic (B) particles.[42] Reproduced with permission of Springer Nature.

Nanomaterial Synthesis

The plasmonic properties of nanomaterials are generally controlled in two ways – controlling particle shape, and controlling particle size.[41,42] As a general rule, particles with more complex morphologies have been reported to have higher plasmonic absorption, and may have more potent light induced properties. This makes the controllable synthesis of complex plasmonic materials such as nanorods, nanotriangles, nanostars, or nanocubes highly sought after.[47]

In most approaches to nanoparticle synthesis there are three key components:

i) A metal precursor source

ii) A reducing agent

iii) A surface stabilizing agent

Using these 3 main components, the synthesis of plasmonic nanoparticles can be described very simply using the homogenous nucleation model, proposed by Le Mer.[48] In a model synthesis, nanoparticle formation is initiated by the reduction of metal ions in solution, yielding atomic metal atoms. Once a critical concentration of metal atoms is reached in solution, they begin to nucleate, forming small colloidal particles. As more metal atoms are produced in solution, they begin to agglomerate on these nuclei, growing them into nanoparticles. While this model is simple and makes many assumptions, it provides a useful basis for understanding the process of particle formation.[48] Under this regime, particle size and shape can be controlled by adding stabilizing agent to a system, resulting in a higher number of nuclei being formed, leading to smaller particles forming. This shift can have a noticeable effect on the plasmonic properties of a batch of materials.[49]

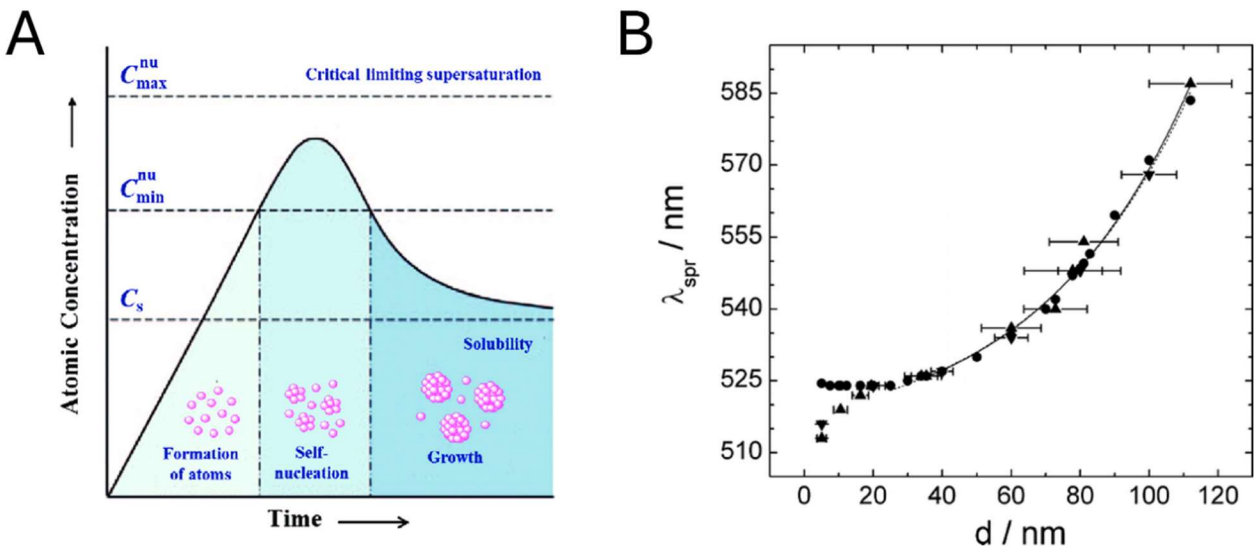

Fig. 1.3.3: A) Graphical depiction of LaMer's principle.[50] B) LSPR wavelength of spherical gold nanoparticles as a function of particle diameter.[49] Panel A reproduced with permission of the Royal Society of Chemistry. Panel B reproduced with permission of the American Chemical Society.

Silver Nanoparticle Synthesis

The controlled synthesis of AgNPs is specifically critical to the work of this thesis, which explores the creation of AgNPs with LSPR bands across the visible and NIR spectrum for photobiological applications.

Silver nanoparticles (AgNPs) have become one of the most recognizable nanomaterials of the 21st century. Like other metal nanomaterials such as gold, these AgNPs feature remarkable properties that cannot be observed in their bulk state, including strong plasmonic absorption[51], ultra-high surface area, antimicrobial activity[52], and catalytically active surfaces[53]. These features have found AgNPs a vast range of everyday applications, with AgNPs being found in anti-odor garments, hospital textiles, self-cleaning surfaces, to name a few real-world examples.[54] In the health sciences, AgNPs have shown great potential in combating antimicrobial resistance due to the innate antimicrobial effects of AgNPs which circumvents bacterial defenses against conventional antibacterial drugs. Other medical applications include accelerating wound healing, enhancing vaccine efficacy, treating ulcers and cancers, and have been used to develop incredibly sensitive colorimetric biosensors thanks to their potent LSPR effects.[55] When it comes to photochemical applications of AgNPs, the field is still relatively young. While photocatalysis using nanomaterials is a promising and well-known field, applications of the materials is often limited to blue-region irradiation due to the tendency for AgNPs to absorb light in the UV/blue region of the light spectrum.

AgNP synthesis has taken on many faces over its existence. The earliest published synthesis was reported in 1889 by M. C. Lea.[35] In this work, the reduction of $AgNO_3$ by trisodium citrate was used for the first time intentionally to yield silver nano-colloids. In this method, at an elevated temperature (~100°C) Ag^+ ions were reduced by citrate, generating what would later be discovered to be small spherical AgNPs stabilized by citrate. Since then, many methods have been used to create similar products, often times using different reducing agents which can perform this synthesis at room temperature, such as sodium borohydride, ascorbic acid, or hydrazine, or the incredibly popular practice of generating AgNPs using bacteria as biofactories.[56] One challenge of AgNP synthesis for many years was the bias for AgNP synthesis methods to produce spherical particles with absorbance in the blue region of the visible spectrum. This limited the control of AgNP optical and physical properties. In recent years, significant efforts have been dedicated to generating AgNPs with more complex structures, and absorbance across a broader range of wavelengths.

Efforts to create new generations of complex AgNPs typically rely on surface modulation of the NPs using bulky surface stabilizers. Through tight surface interactions between the stabilizer and the growing silver particle, the growth of the particle can be directed towards new morphologies.[57] Common stabilizers include surfactants like sodium dodecylsulfate (SDS) or cetyltrimethylammonium bromide (CTAB), or using polymers such as poly(vinyl alcohol) (PVA), and poly(vinyl pyrrolidone) (PVP). By modulating the surface energy of the particles, these stabilizers enable researchers to generate particles such as rods, prisms, triangles, cubes and nanostars.[58] These shapes have absorbance bands which can be shifted all the way from the blue/UV region into the red/NIR region of the light spectrum. The challenge presented by this method, however, is the difficulty in removing these surfactants from the particles post synthesis. Due to the potential for steric hindrance, an ideal nanocatalyst will need to be at least partially cleaned of surfactants in order to maximize effective area on the particle surface.[59]

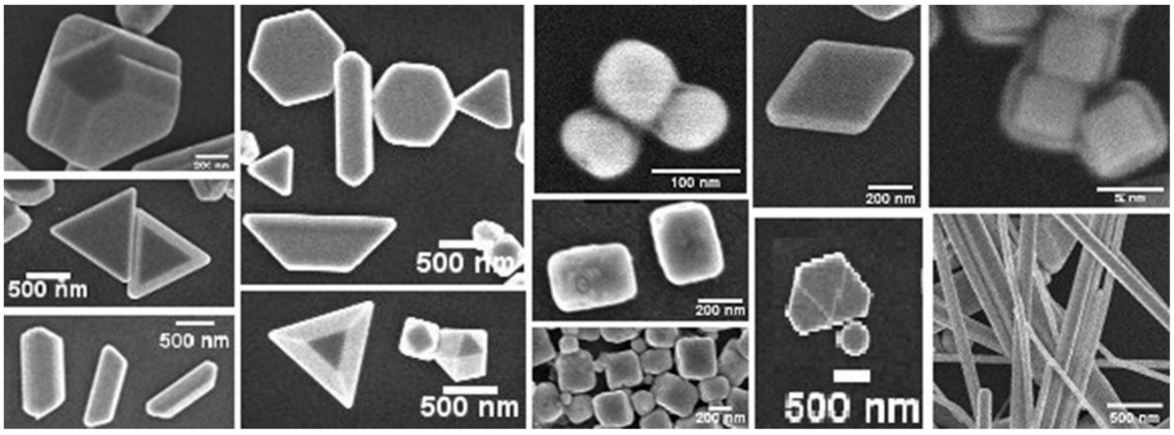

Fig.1.3.4: AgNPs of different shapes prepared using mixtures of PVP and ethylene glycol. Shapes are controlled by changing temperature, and concentrations of PVP and ethylene glycol present.[58] Reproduced with permission of Elsevier.

One way to circumvent this challenge is to employ photochemical growth to control particle properties. Using light to guide the growth of AgNPs is a lesser-known method for controlling NP synthesis. These approaches are a favorite in our research group, largely for the high degree of control that photoinitiators provide. In a typical (dark) reaction, once a reducing agent is added the reaction cannot be halted easily without changing the conditions within the reaction. However, photochemical processes can easily be controlled by the flip of a light switch. In the Scaiano Group, we have adopted several approaches to synthesizing NPs using light irradiation to guide the growth of the particle.[60] In this approach, spherical particles can be generated easily using the photoinitiator Irgacure-2959 (I-2959) under UV irradiation to generate ketyl radicals. These highly reactive products reduce silver salts quickly,

yielding small spherical AgNPs when in the presence of citrate (Chapter 2.1).[61] These particles are referred to throughout this work as “seeds”, a reference to their potential to grow into newer, more complex structures. To grow the seeds, intense LED irradiation is directed into colloidal NP samples for long periods of time, causing them to evolve into newer shapes with no additives (Chapter 2.2).

In general, the goal of this work is to broaden the scope of nanomaterial applications using light as a significant tool in both the synthesis and activation of Ag and Pd nanomaterials. This confluence of ancient traditions honors our timeless fascination with both light and nanomaterials using 21st century advances in illumination technology. This work begins with the synthesis of versatile AgNP seeds in-flow, providing a fast photochemical approach to generating spherical silver nanoparticles with a variety of commercially available photoinitiators (Chapter 2.1).[61] Using these particles, intense coloured LEDs are used to force the evolution of the particles into either decahedra or triangles at batch scale (Chapter 2.2/3).[62] Under irradiation complimentary to their LSPR bands, these particles demonstrate remarkable light activated antibacterial toxicity, reaching total bacterial killing within minutes (Chapter 3). In order to scale up the killing of bacteria for water treatment applications, these particles are then attached to glass wool fibers, effectively creating a heterogenous platform for killing bacteria in large scale through in-flow irradiation (Chapter 4). Finally, in Chapter 5 a similar approach is utilized to produce PdNP coated glass wool fibres for a heterogeneous nitro-to-amine catalyst.[63] Under advanced microscopy, we provide a full-scale characterization of the particles, providing analysis from the bench scale, all the way down to single molecule scale analysis of PdNP performance. If nothing else, I hope that this thesis makes the reader consider the immense power of light, and the ways that is affects not only our research, but our day to day lives in our ever-illuminated world.

References

1. Gowlett, J. A. J. The Discovery of Fire by Humans: A Long and Convoluted Process, *Philos. Trans. R. Soc. Lond. B Biol. Sci.* 2016, 371, 1696.
2. Daniell, M. D.; Hill, J. S. A History of Photodynamic Therapy, *ANZ J. Surg.* 1991, 61 (5), 340–348.
3. M. H. Abdel-kader, *Photodynamic Medicine: From Bench to Clinic*, ed. H. Kostron and T. Hasan, The Royal Society of Chemistry, 2016.
4. Hönigsmann, H. History of Phototherapy in Dermatology, *Photochem. Photobiol. Sci.* 2013, 12 (1), 16–21.
5. Straub, K.; Kanne, D.; Rapoport, H.; Isaacs, S. T.; Straub, K. The Reaction of the Psoralens with Deoxyribonucleic Acid, *Q. Rev. Biophys.* 1984, 17 (1), 1–44.
6. Diekmann, J.; Gontcharov, J.; Fröbel, S.; Torres Ziegenbein, C.; Zinth, W.; Gilch, P. The Photoaddition of a Psoralen to DNA Proceeds via the Triplet State, *J. Am. Chem. Soc.* 2019, 141 (34), 13643–13653.
7. Galiatsatos, P.; Maydan, D. D.; Macalpine, E.; Schleupner, B.; Aitchison, A. H.; Lerner, A. D.; Levy, B.; Halthore, A.; Eward, W. Psoralen: A Narrative Review of Current and Future Therapeutic Uses, *J. Cancer Res. Clin. Oncol.* 2024, 150 (3), 130.
8. Terman, M. Evolving Applications of Light Therapy, *Sleep Med. Rev.* 2007, 11 (6), 497–507.
9. Vogler, A.; Kunkely, H. Photochemistry and Beer, *J. Chem. Educ.* 1982, 59 (1), 25–27.
10. Giacomo Ciamician (1857–1922), *Green Chem.* 2004, 6 (1), G13–G13.
11. Albini, A.; Fagnoni, M. Green Chemistry and Photochemistry Were Born at the Same Time, *Green Chem.* 2004, 6 (1), 1–6.
12. Nakamura, S. Background Story of the Invention of Efficient Blue InGaN Light Emitting Diodes (Nobel Lecture), *Ann. Phys.* 2015, 527 (5–6), 335–349.
13. Cho, J.; Park, J. H.; Kim, J. K.; Schubert, E. F. White Light-Emitting Diodes: History, Progress, and Future, *Laser Photon. Rev.* 2017, 11 (2), 1600147.
14. Wallner, O.; Mamonov, K.; Ortis, F.; Michel, D.; Michel, M. Assembly and Application of a Low Budget Photoreactor, *Chem. Methods* 2021, 1 (5), 240–244.
15. Buglioni, L.; Raymenants, F.; Slattery, A.; Zondag, S. D. A.; Noël, T. Technological Innovations in Photochemistry for Organic Synthesis: Flow Chemistry, High-Throughput Experimentation, Scale-up, and Photoelectrochemistry, *Chem. Rev.* 2022, 122 (2), 2752–2906.
16. Cambié, D.; Bottecchia, C.; Straathof, N. J. W.; Hessel, V.; Noël, T. Applications of Continuous-Flow Photochemistry in Organic Synthesis, Material Science, and Water Treatment, *Chem. Rev.* 2016, 116 (17), 10276–10341.
17. Albini, A. *Photochemistry : Past, Present and Future*. Springer Berlin Heidelberg 2016.
18. Scaiano, J. *Photochemistry Essentials*, American Chemical Society, 2022.
19. Zimmermann, J.; Zeug, A.; Röder, B. A Generalization of the Jablonski Diagram to Account for Polarization and Anisotropy Effects in Time-Resolved Experiments, *Phys. Chem. Chem. Phys.* 2003, 5 (14), 2964–2969.
20. Scaiano, J. C. A Beginners Guide to Understanding the Mechanisms of Photochemical Reactions: Things You Should Know If Light Is One of Your Reagents, *Chem. Soc. Rev.* 2023, 52 (18), 6330–6343.
21. Zhou, Q. Q.; Zou, Y. Q.; Lu, L. Q.; Xiao, W. J. Visible-Light-Induced Organic Photochemical Reactions through Energy-Transfer Pathways, *Angew. Chem. Int. Ed.* 2019, 58 (6), 1586–1604.
22. Pibiri, I.; Buscemi, S.; Palumbo Piccionello, A.; Pace, A. Photochemically Produced Singlet Oxygen: Applications and Perspectives, *ChemPhotoChem* 2018, 2 (7), 535–547.
23. Mohamadpour, F.; Amani, A. M. Photocatalytic Systems: Reactions, Mechanism, and Applications, *RSC Adv.* 2024, 14 (29), 20609–20645.
24. Kamat, P. V. Photophysical, Photochemical and Photocatalytic Aspects of Metal Nanoparticles, *J. Phys. Chem. B* 2002, 106 (32), 7729–7744.

25. Oelgemöller, M. Solar Photochemical Synthesis: From the Beginnings of Organic Photochemistry to the Solar Manufacturing of Commodity Chemicals, *Chem. Rev.* 2016, 116 (17), 9664–9682.
26. Elhage, A.; Lanterna, A. E.; Scaiano, J. C. Catalytic Farming: Reaction Rotation Extends Catalyst Performance, *Chem. Sci.* 2019, 10 (5), 1419–1425.
27. Cely-Pinto, M.; Wang, B.; Scaiano, J. C. Photocatalytic Semi-Hydrogenation of Alkynes: A Game of Kinetics, Selectivity and Critical Timing, *Nanomater.* 2023, 13 (17), 2390.
28. Dai, T.; Huang, Y. Y.; Hamblin, M. R. Photodynamic Therapy for Localized Infections – State of the Art, *Photodiagnosis Photodyn. Ther.* 2009, 6 (3–4), 170.
29. Crisenza, G. E. M.; Melchiorre, P. Chemistry Glows Green with Photoredox Catalysis, *Nat. Commun.* 2020 11:1 2020, 11 (1), 1–4.
30. Ehm, T. R. Flow Photochemistry as a Tool in Organic Synthesis, *Chem. Eur. J.* 2020, 26 (71), 16952–16974.
31. Yang, C.; Li, R.; Zhang, K. A. I.; Lin, W.; Landfester, K.; Wang, X. Heterogeneous Photoredox Flow Chemistry for the Scalable Organosynthesis of Fine Chemicals, *Nat. Commun*. 2020 11:1 2020, 11 (1), 1–8.
32. Schaming, D.; Remita, H. Nanotechnology: From the Ancient Time to Nowadays, *Found. Chem.* 2015, 17 (3), 187–205.
33. Freestone, I.; Meeks, N.; Sax, M.; Higgitt, C. The Lycurgus Cup - A Roman Nanotechnology, *Gold Bull.* 2008, 40 (4), 270–277.
34. Thompson, D. T. Michael Faraday's Recognition of Ruby Gold: The Birth of Modern Nanotechnology, *Gold Bull.* 2008, 40 (4), 267–269.
35. Cahey Lea, by M. Allotropic Forms of Silver, *Am. J. Sci.* 1889, s3-37 (222), 476–491.
36. Nowack, B.; Krug, H. F.; Height, M. 120 Years of Nanosilver History: Implications for Policy Makers, *Environ. Sci. Technol.* 2011, 45 (4), 1177–1183.
37. Bayda, S.; Adeel, M.; Tuccinardi, T.; Cordani, M.; Rizzolio, F. The History of Nanoscience and Nanotechnology: From Chemical–Physical Applications to Nanomedicine, *Mol.* 2020, 25 (1), 112.
38. Toumey, C. Plenty of Room, Plenty of History. *Nat. Nanotechnol*. 2009 4:12 2009, 4 (12), 783–784.
39. Malik, S.; Muhammad, K.; Waheed, Y. Nanotechnology: A Revolution in Modern Industry, *Mol.* 2023, 28 (2), 661.
40. Habibullah, G.; Viktorova, J.; Ruml, T. Current Strategies for Noble Metal Nanoparticle Synthesis, *Nanoscale Res. Lett.* 2021 16:1 2021, 16 (1), 1–12.
41. Lv, S.; Du, Y.; Wu, F.; Cai, Y.; Zhou, T. Review on LSPR Assisted Photocatalysis: Effects of Physical Fields and Opportunities in Multifield Decoupling, *Nanoscale Adv.* 2022, 4 (12), 2608–2631.
42. Alba-Molina, D.; Giner-Casares, J. J.; Cano, M. Bioconjugated Plasmonic Nanoparticles for Enhanced Skin Penetration, *Top. Curr. Chem.* 2020, 378 (1), 1–17.
43. Anker, J. N.; Hall, W. P.; Lyandres, O.; Shah, N. C.; Zhao, J.; Van Duyne, R. P. Biosensing with Plasmonic Nanosensors, *Nat. Mater.* 2008 7:6 2008, 7 (6), 442–453.
44. BTNX | Products. https://www.btnx.com/Product?id=2010 (accessed 2024-09-25).
45. Wang, T.; Wang, H.-J.; Lin, J.-S.; Yang, J.-L.; Zhang, F.-L.; Lin, X.-M.; Zhang, Y.-J.; Jin, S.; Li, J.-F. Plasmonic Photocatalysis: Mechanism, Applications and Perspectives, *Chinese J. Struc. Chem.* 2023, 42 (9), 100066.
46. Yaghmaei, M.; Lanterna, A. E.; Scaiano, J. C. Nitro to Amine Reductions Using Aqueous Flow Catalysis under Ambient Conditions, *iScience* 2021, 24 (12), 103472.
47. Grzelczak, M.; Pérez-Juste, J.; Mulvaney, P.; Liz-Marzán, L. M. Shape Control in Gold Nanoparticle Synthesis, *Chem. Soc. Rev.* 2008, 37 (9), 1783–1791.
48. Whitehead, C. B.; Özkar, S.; Finke, R. G. LaMer's 1950 Model for Particle Formation of Instantaneous Nucleation and Diffusion-Controlled Growth: A Historical Look at the Model's Origins, Assumptions, Equations, and Underlying Sulfur Sol Formation Kinetics Data, *Chem. Mater.* 2019, 31 (18), 7116–7132.
49. Haiss, W.; Thanh, N. T. K.; Aveyard, J.; Fernig, D. G. Determination of Size and Concentration of Gold Nanoparticles from UV-Vis Spectra, *Anal. Chem.* 2007, 79 (11), 4215–4221.

50. Jana, S. Advances in Nanoscale Alloys and Intermetallics: Low Temperature Solution Chemistry Synthesis and Application in Catalysis, *Dalton Trans.* 2015, 44 (43), 18692–18717.
51. Loiseau, A.; Asila, V.; Boitel-Aullen, G.; Lam, M.; Salmain, M.; Boujday, S. Silver-Based Plasmonic Nanoparticles for and Their Use in Biosensing, *Biosens.* 2019, Vol. 9, Page 78 2019, 9 (2), 78.
52. Bruna, T.; Maldonado-Bravo, F.; Jara, P.; Caro, N. Silver Nanoparticles and Their Antibacterial Applications, *Int. J. Mol. Sci.* 2021, 22 (13).
53. Dong, X. Y.; Gao, Z. W.; Yang, K. F.; Zhang, W. Q.; Xu, L. W. Nanosilver as a New Generation of Silver Catalysts in Organic Transformations for Efficient Synthesis of Fine Chemicals, *Catal. Sci. Technol.* 2015, 5 (5), 2554–2574.
54. Deshmukh, S. P.; Patil, S. M.; Mullani, S. B.; Delekar, S. D. Silver Nanoparticles as an Effective Disinfectant: A Review, *Mater. Sci. Eng. C Mater. Biol. Appl.* 2019, 97, 954.
55. Xu, L.; Wang, Y. Y.; Huang, J.; Chen, C. Y.; Wang, Z. X.; Xie, H. Silver Nanoparticles: Synthesis, Medical Applications and Biosafety, *Theranostics* 2020, 10 (20), 8996.
56. Ivanov, I.; Manolov, S.; Phuong, N.; Nguyen, U.; Dang, N. T.; Doan, L.; Thu, T.; Nguyen, H. Synthesis of Silver Nanoparticles: From Conventional to 'Modern' Methods—A Review, *Processes* 2023, Vol. 11, Page 2617 2023, 11 (9), 2617.
57. Chugh, D.; Viswamalya, V. S.; Das, B. Green Synthesis of Silver Nanoparticles with Algae and the Importance of Capping Agents in the Process, *J. Genet. Eng. & Biotechnol*. 2021, 19 (1), 126.
58. Lalegani, Z.; Seyyed Ebrahimi, S. A. Optimization of Synthesis for Shape and Size Controlled Silver Nanoparticles Using Response Surface Methodology, *Colloids Surf. A Physicochem. Eng. Asp.* 2020, 595, 124647.
59. Liu, M.; Kong, Y.; Hu, H.; Kovács, N.; Sun, C.; Zelocualtecatl Montiel, I.; Gálvez Vázquez, M. de J.; Hou, Y.; Mirolo, M.; Martens, I.; Drnec, J.; Vesztergom, S.; Broekmann, P. The Capping Agent Is the Key: Structural Alterations of Ag NPs during CO2 Electrolysis Probed in a Zero-Gap Gas-Flow Configuration, *J. Catal.* 2021, 404, 371–382.
60. Stamplecoskie, K. G.; Scaiano, J. C. Light Emitting Diode Irradiation Can Control the Morphology and Optical Properties of Silver Nanoparticles, *J. Am. Chem. Soc.* 2010, 132 (6), 1825–1827.
61. Yaghmaei, M.; Bourgonje, C. R.; Scaiano, J. C. Facile Scale-Up of the Flow Synthesis of Silver Nanostructures Based on Norrish Type I Photoinitiators, *Mol.* 2023, 28 (11), 4445.
62. Bourgonje, C. R.; da Silva, D. R. C.; McIlroy, E.; Calvert, N. D.; Shuhendler, A. J.; Scaiano, J. C. Silver Nanoparticles with Exceptional Near-Infrared Absorbance for Photoenhanced Antimicrobial Applications, *J. Mater. Chem. B* 2023, 11 (26), 6114–6122.
63. Wang, B.; Bourgonje, C. R.; Scaiano, J. C. Fiber-Glass Supported Catalysis: Real-Time, High-Resolution Visualization of Active Palladium Catalytic Centers during the Reduction of Nitro Compounds, *Catal. Sci. Technol.* 2023, 13 (4), 1021–1031.

Chapter 2 – Controlling the synthesis of silver nanoparticles using light as a driving force

Background

This chapter represents the research that I first began when I came to uOttawa – the synthesis of AgNPs using light as a tool to drive and control the synthesis of AgNPs. In Chapter 2.1 we sought to design a flow photoreactor for synthesizing AgNPs seeds (sAgNPs) using a variety of commercially available photoinitiators. This paper explores a rapid, scalable approach to producing AgNPs with spherical morphologies and diameters <10 nm using a range of commercially available photoinitiatiors. These particles have characteristic absorbance peaks around 400 nm, resulting in characteristically yellow suspensions. On this paper, I share co-first authorship with Mahzad Yaghmaei (first listed), another PhD from the Scaiano Lab. In this work Mahzad brought her experience with flow reactors, while I brought expertise in synthesizing silver nanoparticles, having done this reaction dozens of times in batch scale reactions. My contribution was in optimizing the reaction conditions through batch scale experiments, AgNP characterization, while also performing some of the flow experiments, in particular with photoinitiators I-2959, I-184, and D-1173.

The second part of this Chapter (2.2) showcases the use of light to guide the synthesis of decahedral and triangular AgNPs with more complex structures and tunable plasmonic absorption bands throughout the visible spectrum. Our goal here was to design a method for controlling the size and optical properties of our particles using a light-guided approach, with a key goal of designing particles with red/NI absorbance for biological applications (demonstrated in Chapter 3). The great strength of this method is that by using only LED irradiation, we are able to "guide" the growth of sAgNPs until they are new structures entirely, with the final shape of the particles depending on the wavelength of light used. In this case we used blue light (450 nm) to generate decahedral AgNPs (dAgNPs) and red light (635 nm) to yield triangular nanoparticles (tAgNPs). The particles are remarkably stable, and would go on to be used in Chapter 3 and 4 as potent light-activated antibacterial agents.

The principles outlined in both parts of this Chapter have gone on to spark future projects, with our former undergraduate student and soon-to-be (at the time of writing) MSc student Carly Frank investigating the combination of our flow reactor set-up with various coloured LEDs to generate AgNPs of different size and shape with much more efficiency and narrower size distributions.

2.1: Published work: Facile Scale-Up of the Flow Synthesis of Silver Nanostructures Based on Norrish Type I Photoinitiators

M. Yaghmaei[i], C. R. Bourgonje[i], J. C. Scaiano. *Molecules*, 2023, 28 (11), 4445

[i] These authors contributed equally.

Abstract

Silver nanoparticles have become one of the most commercially and industrially relevant nanomaterials of the 21st century, owing to their potent antibacterial properties, as well as their useful catalytic and optical properties. Although many methods have been explored to produce AgNPs, we favor the photochemical approach using photoinitiators to produce AgNPs, owing to the high degree of control over reaction conditions, and the generation of so-called AgNP 'seeds' that can be used as-is, or as precursors for other silver nanostructures. In this work, we explore the scale-up of AgNP synthesis using flow chemistry and assess the usefulness of a range of industrial Norrish Type 1 photoinitiators in terms of flow compatibility and reaction time, as well as the resulting plasmonic absorption and morphologies. We establish that while all the photoinitiators used were able to generate AgNPs in a mixed aqueous/alcohol system, photoinitiators that generate ketyl radicals showed the greatest promise in terms of reaction times, while also showing greater flow compatibility compared to photoinitiators that generate α-aminoalkyl and α-hydroxybenzyl radicals. These findings help to establish a guideline for adapting photochemical AgNP syntheses to flow systems, helping to improve the scalability of the method in one of the largest industries in nanomaterial chemistry.

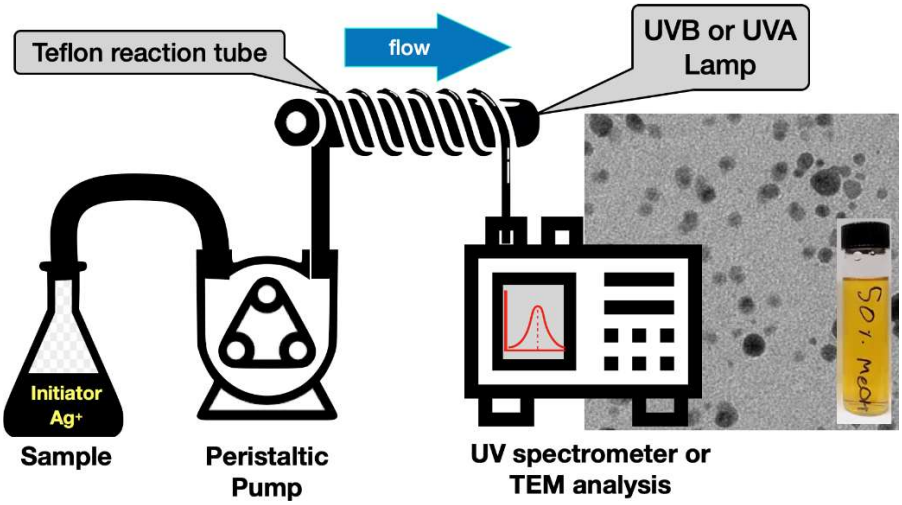

Introduction

Numerous free radical photoinitiators have been designed based on the Norrish Type I reaction involving C-C α-cleavage of carbonyl compounds.[1,2,3,4] In selected cases, one of the radicals generated is a strong electron donor; such systems are of great interest for the production of metal nanoparticles as they produce reducing agents with excellent spatial and temporal control.[1,5,6,7] Further, an additional benefit is kinetic control, as the light source irradiance can be readily adjusted by either controlling the power supplied (dimming), or simply changing the source-sample distance.

Many metal ions are excellent quenchers of excited states and frequently this quenching can limit the efficiency of photoinitiators. For these initiators to be effective, the Norrish Type I cleavage must be extremely fast and since most cleavages occur from the triplet state, this requires very short-lived triplet states.[5] A molecule that we have long recognized as a good nanoparticle precursor is Irgacure-2959 (I-2959), which has been widely employed in our group. I-2959 has a triplet lifetime of ~8 ns [3] and cleaves with a quantum yield of one in acetonitrile[8], Scheme 2.1.1.

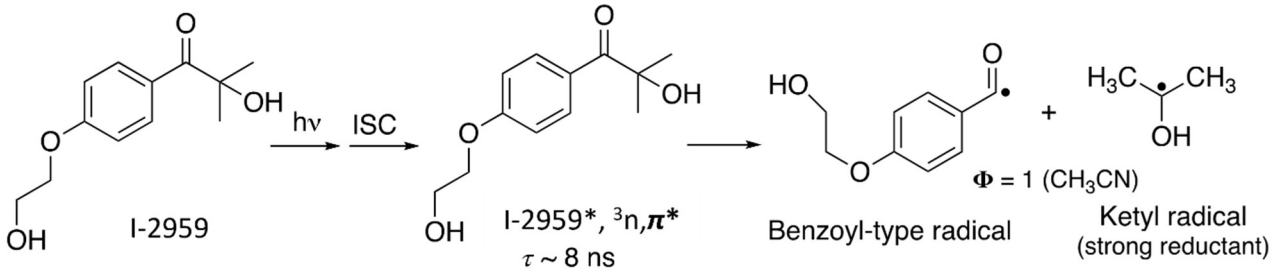

Scheme 2.1.1: Mechanism for the decomposition of Irgacure 2959 (I-2959) showing the formation of the strongly reducing ketyl radical. Under typical reaction conditions the benzoyl radical yields the corresponding carboxylic acid that can behave as a mild nanoparticle stabilizer.

Early work on the use of carbonyl compounds to generate metal nanoparticles frequently required very long exposure times[9], probably the result of the use of molecules with long-lived triplets that were readily quenched by the metal ions, typically Ag(I) or Au(III). Further, the need to generate strongly reducing radicals was not always recognized.

Among reducing radicals, ketyl and α-aminoalkyl radicals are convenient sources, both operating by proton-coupled electron transfer reactions (PCET) and with commercial precursors readily available[1]. Scheme 2.1.2 illustrates the mechanism for silver; although, the same applies (with adjusted stoichiometry) for other ions, such as Au(III). Once the silver atoms have been produced, their next step is to form Ag_2,[10] eventually leading to nanoparticle formation.

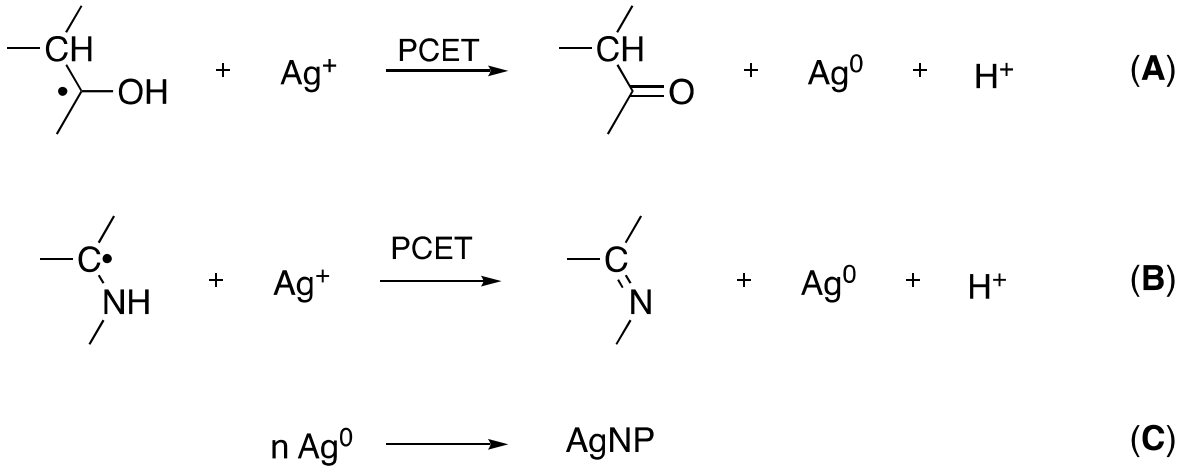

Scheme 2.1.2: Electron transfer from ketyl and α-aminoalkyl radicals to reduce Ag(I) to Ag^0, reactions A and B, respectively, which eventually generates silver nanoparticles (AgNP), reaction C.

In this contribution, we examine several readily available radical photoinitiators frequently used in polymerization applications; although, our applications concentrate on the synthesis of nanostructures, illustrated here with silver seeds, small nanoparticles that we require for the production of other nanostructures with biological applications. We know that the morphology and size dispersity of nanostructures can depend on the precursor, including distinct byproducts, as well as on other additives, such as citrate that is of particular interest for our applications.

While nanoparticle synthesis is usually performed in batch reactions, in the last decade, there has been an interest in converting many reactions to flow systems, where scale-up is frequently easier and safety risks, if applicable, can be reduced.[11,12] In our laboratory, we have recently developed a flow actinometer that allows the quantification of the key reagent in photochemical reactions: light.[8] As we determined experimental irradiances in the UVA and UVB regions, we realized that our experimental geometry was exceptionally efficient in delivering photons to a flow reactor consisting of a narrow Teflon tube. In fact, in our preliminary work, we studied how short the residence time (<60 s) of the sample could be, and we discovered that our pumps were not fast enough to establish a threshold for quantitative Ag^+ to Ag^0 conversion. The answer to this issue is presented in the sections that follow. Scheme 2.1.3 shows the structures we tested.

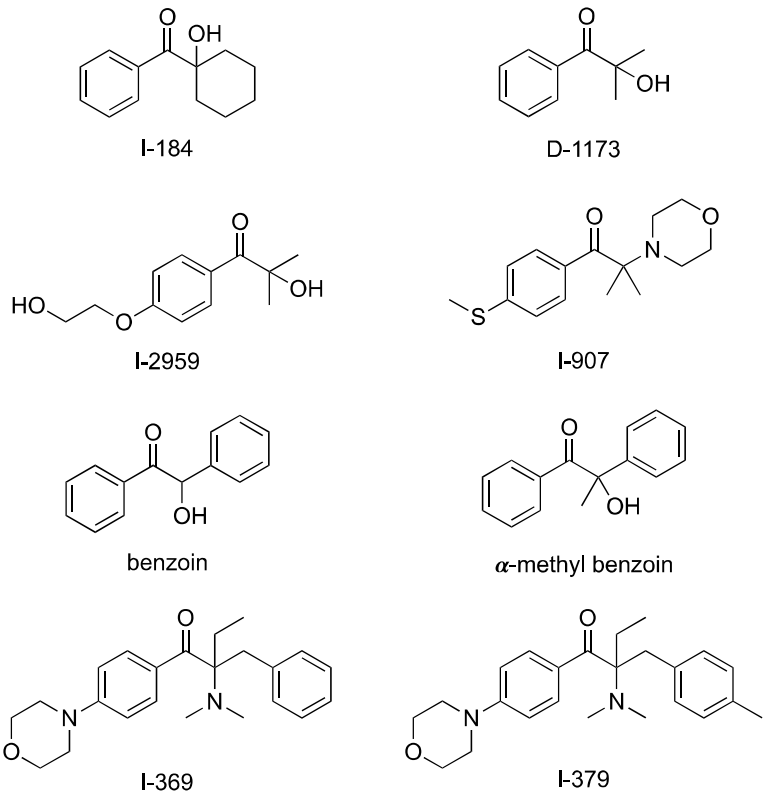

Scheme 2.1.3: Structure of the molecules studies as precursors for AgNP. The letter 'I' is used as an abbreviation for Irgacure, and 'D' is used as an abbreviation for Darocur.

Materials and Methods

Materials

Chemicals and materials were sourced from multiple suppliers for the experimental work. Ciba Specialty Chemicals supplied the initiators I-184, I-907, I-369, I-379, and D-1173, while Sigma Aldrich provided the benzoin. BASF supplied I-2959, and Alfa Aesar provided alpha-hydroxy-alpha-methylbenzyl phenyl ketone. Solvents were purchased from Fisher chemical.

Spectroscopy

UV–Vis spectroscopy was performed using a Cary 7000 UV–Vis spectrometer for bench reactions and for flow when needed; this instrument can measure high absorbances reliably. A Cary 60 UV–Vis spectrometer was normally used for flow reactions. Transmission electron microscopy (TEM) was performed using an FEI Tecnai G2 spirit Twin TEM microscope. Some exemplary TEM images of sAgNPs and corresponding size histograms are shown in the text; images and histograms of sAgNPs made using the remaining photoinitiators can be found in the Appendix (A.2.1.1- A.2.1.8).

Batch Reactions

Batch reactions (without flow) were performed in 20 mL glass vials containing in a typical reaction 0.2 mM $AgNO_3$, 0.2 mM photoinitiator, and 1 mM trisodium citrate dissolved in a 1:1 mixture of MeOH and water. Samples were deoxygenated under gentle argon bubbling for 20 min before being placed in a photoreactor containing 6 UVB lamps for 15 min. Samples were analyzed with UV–Vis spectroscopy and TEM as-prepared without any purification.

Similar preparations were also prepared using acetonitrile and ethanol as co-solvents. Notably, without the addition of co-solvent, most photoinitiators were not easily dissolved.

Flow Reactions

The light sources were 8 W fluorescent lamps from Luzchem installed on an EXPO panel from the same supplier. Teflon tubing (STT-15) was procured from Component Supply Company, Sparta, TN, USA. The pump (minipuls 3) was purchased from Gilson. The Teflon tubing has an outside diameter of 1.80 mm and an inside diameter of 1.50 mm corresponding to a wall thickness of 0.15 mm. We have shown before that this setup leads to an experimental optical path of 0.15 cm.[8] A diagram of the flow reactor is shown in Fig. 2.1.S1.

Results and Discussion

This section is divided according to the methodologies used to synthesize nanoparticles and their characterization. The objective of this contribution is to establish a fast and reliable method to produce silver nanoparticles in a continuous flow. These small particles are sometimes described as 'seeds' and can be used to generate complex silver structures.[13]

Spectroscopy of Initiators and Lamps Used

Our studies were performed with several photoinitiators that generate strongly reducing free radicals of the ketyl or α-aminoalkyl type with the structures shown in Scheme 2.1.3. They usually have strong absorptions in the UVA or UVB region and their spectra are shown in Fig. 2.1.1A. The spectra for the UVA and UVB lamps used (mostly the latter) are shown in Fig. 2.1.1B. The same wavelength scale is used for both to facilitate vertical comparisons.

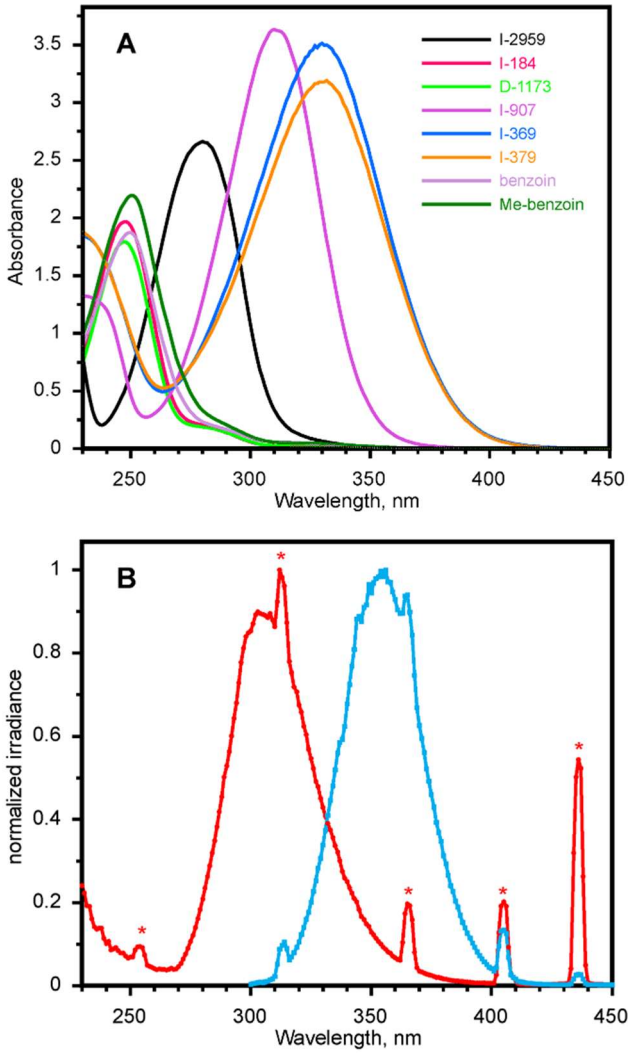

Fig. 2.1.1: (A) Spectra of the initiators used at 0.2 mM in 1:1 aqueous methanol. All spectra in panel A were recorded using a Cary 7000 spectrometer that can handle high absorbances, as the Cary 60 instrument used elsewhere in this paper showed saturation at A > 2.7 in a 1 cm cuvette. The actual optical path under flow conditions is 0.15 cm and there is no saturation under these conditions. (B) Normalized spectra for the UVA (blue) and UVB (red) lamps utilized in this work. The sharp lines are leftovers (marked with '*') from typical mercury emission lines at 254, 313, 365, 405, and 436 nm.

Batch Experiments and Controls

A number of preliminary batch experiments were performed in order to find out the preferred conditions for the flow work on which this contribution centers. In spite of the low concentrations required (frequently sub-millimolar) some of the initiators showed limited aqueous solubility, the exception being I-2959, where its glycol-like moiety facilitates solubility while also causing a red shift in the absorbance. Three co-solvents were tested: acetonitrile, ethanol, and methanol. The results with

acetonitrile were disappointing as it seemed to slow down or inhibit nanoparticle formation, even at amounts as low as 25%, while the alcohols performed well as long as the solvent mixture did not exceed 50% alcohol (Fig. 2.1.S2-2.1.S4). In the end, we settled on 50:50 methanol/water (*v*/*v*) as the preferred solvent (but not the only one) as it seemed compatible with all the initiators, with $AgNO_3$ and with citrate used as a particle stabilizer. An example of solvent studies is presented in Fig. 2.1.2 for I-2959 irradiated with UVB light for 15 min under an argon atmosphere; here, the Ag plasmon band seems best for 25% methanol; however, 50% still shows a well-resolved band and is a better choice when taking solubilities into consideration. Furthermore, when >50% MeOH was used, the absorption of the AgNP suspensions begin to drop considerably. For this reason, the reaction condition chosen for flow reactions going forward was 1:1 MeOH:H_2O.

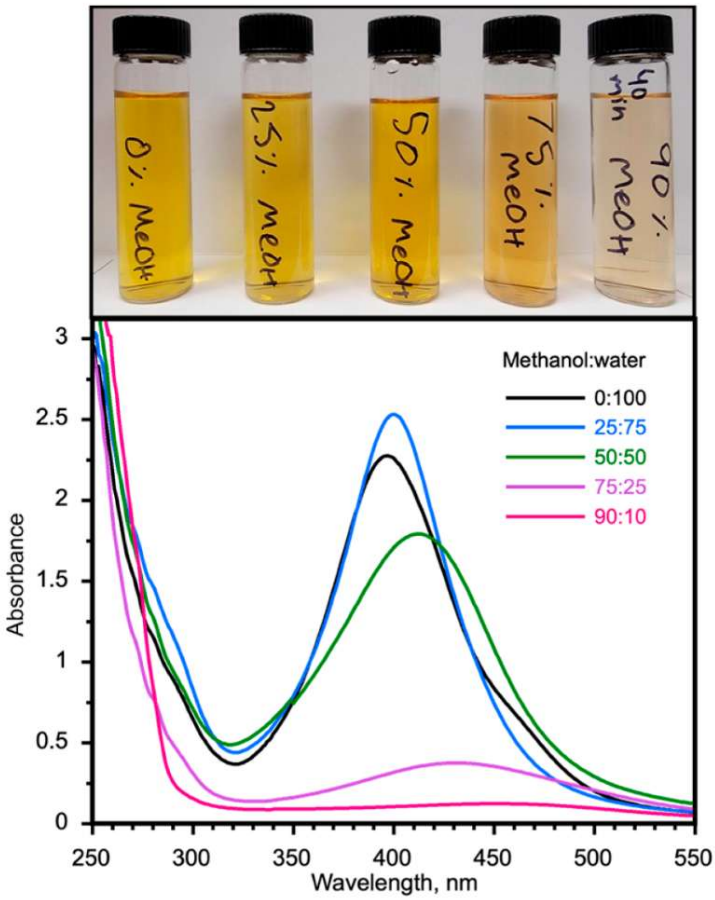

Fig. 2.1.2: AgNPs synthesized in solutions containing different fractions of CH_3OH ranging from 0% to 90%. Each reaction initially contains 1 mM citrate, 0.2 mM $AgNO_3$, and 0.2 mM of I-2959. All samples were irradiated for 15 min in a photoreactor with 6 UVB lamps, except for the 90% CH_3OH sample, which required 40 min to yield any noticeable color.

A very interesting observation from the batch experiments is that the initiator-to-Ag^+ stoichiometric ratio required is less than one. If in Scheme 2.1.1 one assumes that only the ketyl radical leads to Ag^+ reduction, then the minimum stoichiometric requirement would be 1.0. This is illustrated in Fig. 2.1.3, where, for example, an 82% yield is obtained with 0.1 mM I-2959 and 0.2 mM Ag^+, when the maximum anticipated yield would be 50% if only the ketyl radical is reactive. Clearly, the other materials in the reaction, citrate or methanol, may contribute to the reduction process. Citrate is known to be a modest reducing agent towards silver[14] and an established one in the case of gold.[15] In the case of methanol, the $\dot{C}H_2OH$ radical is a good reducing agent, but its formation would require H-abstraction by the benzoyl radical of Scheme 2.1.1, a process that is expected to be slow, given the C-H bond dissociation energy of methanol,[16] yet some contribution may be expected given that methanol is 12.4 M in the system. It is noted that in Fig. 2.1.3 there is a small drop in absorbance from the batch made with 0.4 mM of initiator – this is attributed to batch-to-batch fluctuations in particle absorbance.

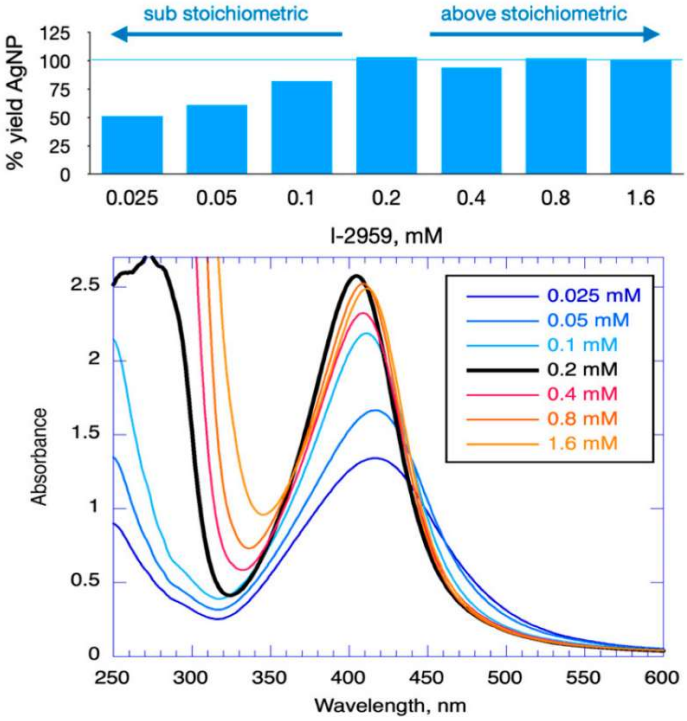

Fig. 2.1.3: Effects of varying photoinitiator concentration in batch reaction. Top: Relative max absorption yield for AgNP suspensions in comparison to the stoichiometric ratio of I-2959 to $AgNO_3$ for solutions with I-2959 concentrations ranging from 0.025 to 1.6 mM. Each reaction uses 0.2 mM of $AgNO_3$, 1 mM of citrate, and 1:1 CH_3OH:H_2O. Solutions were irradiated for 15 min in a photoreactor with six 8W UVB bulbs. Bottom: Corresponding UV–Vis absorption spectra of AgNP plasmon bands with varying concentrations of I-2959. The black heavier line corresponds to the stoichiometric concentration of I-2959. Note that 0.1 mM initiator (light blue) generates 82% of the signal obtained with the stoichiometric concentration.

Among the initiators in Fig. 2.1.1, I-369 and I-379 are interesting because of their excellent absorbance match with the mission of the UVA lamp, something that may be advantageous in the presence of organic molecules (e.g., produced in catalytic processes) that are more likely to photodegrade with UVB than with UVA. However, this initiator presents consistency problems mentioned in the Supplementary Materials and addressed also in the flow experiments section.

Based on the results of bench experiments, it was decided to proceed using 0.2 mM of initiator, 0.2 mM of $AgNO_3$, and 1 mM of trisodium citrate dissolved in 1:1 MeOH:H_2O in order to best dissolve all of the initiators, while still producing AgNPs with strong, consistent plasmon bands.

Several other experiments were performed in batch and are described in the Supplementary Materials. In general, they show that the first three entries in Table 2.1.1 yield AgNP in a clean fast process with plasmon bands consistent with predominantly spherical particles, something confirmed in the TEM images (see Appendix). Our best and most consistent results were obtained with initiators that yield ketyl radicals. The next section illustrates the excellent performance of ketyl radical generators under flow conditions.

Nanoparticle Synthesis Using Flow Strategies

The synthesis of AgNPs in flow was performed using the same experimental strategy as in a recent paper where we developed an actinometer for flow photoreactions.[8] Briefly, we utilize as light source 8 W fluorescent tubes from Luzchem, which are 30 cm long and with a diameter of 16 mm. The lamp is tightly wrapped with Teflon tubing with an outside diameter of 1.80 mm and an inside diameter of 1.50 mm corresponding to a wall thickness of 0.15 mm. The flow cavity in the tube is about 6.3 m long with a liquid capacity of 10 mL. The experimentally determined optical path is 0.15 cm.[8] The sample is supplied by a peristaltic pump with adjustable flow rate feeding from a container where the sample can be deaerated, normally with argon. At the exit, samples can be collected in vials or cuvettes, or be directly fed to a flow cell in a Cary-60 absorbance spectrometer. Particles undergo ripening over the next few hours in a process that can also depend on the presence or not of oxygen; however, the spectra shown throughout this chapter correspond to nascent particles under argon and the time lapse between the flow system and the spectrometer is usually less than one minute. We note at the onset that the most reliable initiators were those yielding ketyl radicals. This is illustrated in Fig. 2.1.4, for a very short residence time, where all three initiators yield approximately the same plasmon band with comparable intensity.

Table 2.1.1: Summary of flow photochemistry results of silver nanoparticle production with different initiators, using 0.2 mM of $AgNO_3$, 0.2 mM of initiator, and 1 mM of citrate in deaerated solvent with UVB lamp (see Scheme 2.1.3).

Initiator	Solvent	λ max FWHM (nm)	Residence Time (min)	Notes
I-184	Water	400 50	0.8	Clean no deposits in the flow tube
	1:1 CH_3OH:Water	420 100	4	
D-1173	Water	400 60	0.8	Clean no deposits in the flow tube
	1:1 CH_3OH:Water	415 95	0.8	
I-2959	Water	400 50	0.7	Clean no deposits in the flow tube
	1:1 CH_3OH:Water	415 80	0.8	
I-907	1:9 CH_3OH:Water	445 160	4	Heavy black deposits in the flow tube
	1:1 CH_3OH:Water	445 150	8	
Benzoin	Water	400 85	30	Very weak signals
	1:1 CH_3OH:Water	410 80	0.8	Yellow deposits in the flow tube
α-Me Benzoin	Water	400 70	0.8	Yellow deposits in the flow tube
	1:1 CH_3OH:Water	405 80	0.8	Faint yellow deposits in flow tube
I-369 [a]	1:1 CH_3OH:Water	410 90	4	Heavy black deposits in the flow tube
I-379	1:1 CH_3OH:Water	410 90	6	Heavy black deposits in the flow tube
	2:3 CH_3OH:Water	410 80	10	

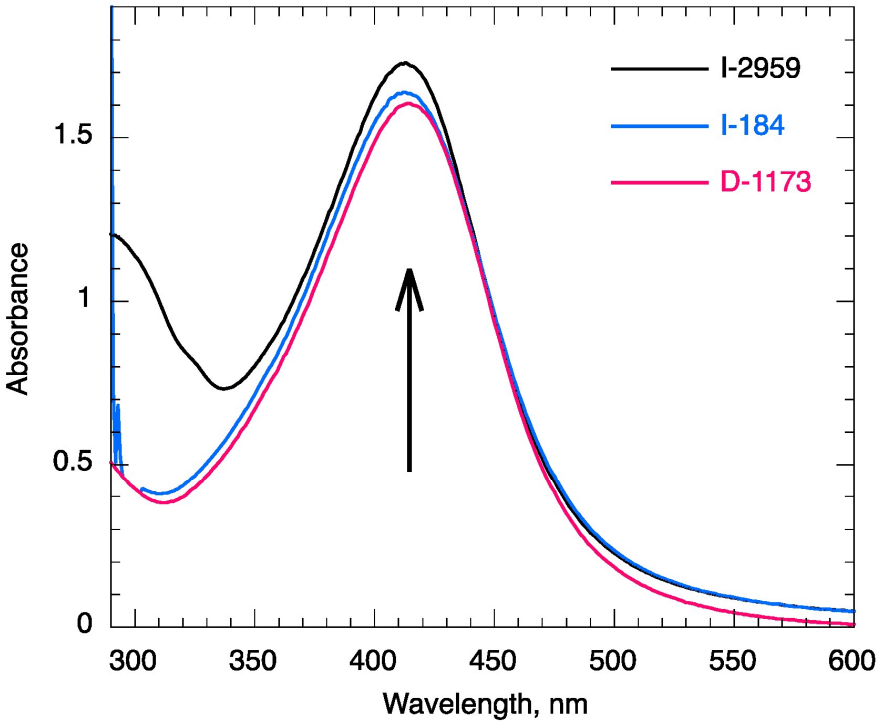

Fig. 2.1.4: Comparison of initiators yielding ketyl radicals with high efficiency, produced under flow conditions with 0.2 mM of each photoinitiator, 0.2 mM of $AgNO_3$, 1 mM of citrate, and 1:1 CH_3OH:H_2O and a residence time of 0.8 min. The arrow indicates growth during irradiation. The spike at 290 nm in the I-184 graph is due to bubbles in the flow.

Fig. 2.1.5A shows the spectra recorded for AgNP with different residence times; the remarkable observation is that a residence time of 40 s is enough to achieve the 100% conversion of a 0.2 mM Ag^+ solution, this short residence time corresponds to the maximum flow speed for our pump and is equivalent to nearly one liter per hour. The reality is that we do not know how fast we could go and still have 100% conversion; however, it is interesting to note that the residence time of 0.8 min is much shorter than the required irradiation time of 15 min seen in the batch reaction, which yields only 6 mL of product.

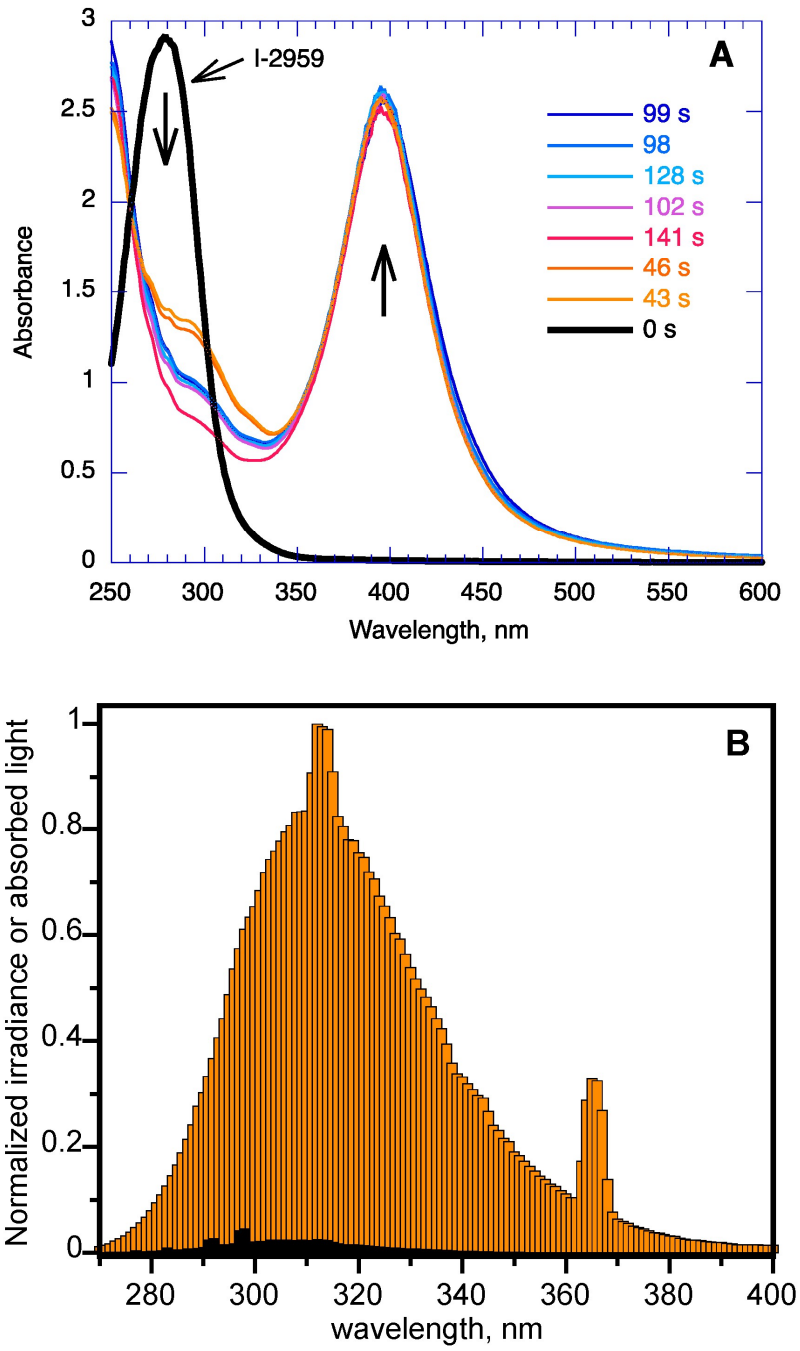

Fig. 2.1.5: (A) Different residence times irradiated with UVB light and using I-2959 as initiator. Note that the residence times are not in increasing order, but rather are randomized; this is done to make sure any effects observed are not the result of a systematic change in the conditions. Silver nitrate (0.2 mM), sodium citrate (1 mM), I-2959 (0.2 mM) in water) purged with Argon and irradiated with a UVB lamp with different residence times (seconds) in 6.3 m Teflon tubing with a total irradiated volume of 10 mL. The arrow indicates growth during irradiation; (B) spectral distribution of the UVB lamp (normalized, orange) and the fraction of light absorbed by the I-2959 solution. (black), with the spectrum corrected for 0.15 cm optical path.

The high yield contrasts with the fact that only 2.17% is being absorbed by I-2959 at a 0.2 mM concentration for the 1.5 mm optical path of the Teflon tubing. Intrigued by this result we used the actinometric determination method that we developed,[8] to compare the chemical conversion of 0.2 mM with the light absorbed by the initiator (see our recent contribution on actinometry for detailed calculations).[8] In the shortest (40 s) residence time, the dose absorbed was 0.00012 Einstein L^{-1}. This leads to a quantum yield for the $Ag^+ \rightarrow Ag^0$ conversion of 1.67 ± 0.17. Clearly more than one Ag^+ conversion per photon, but probably not high enough to suspect a chain reaction. We suspect that this is an autocatalytic process, just as it is in silver photography, where silver clusters lead to the reduction of neighboring Ag^+ or salts in the presence of a reducing agent – in this case citrate may act as the reducing agent, enabled by autocatalytic AgNP surfaces.[17] Possibly the UVB illumination contributes to this growth. The reducing agent can be methanol or citrate, more likely the latter. This is consistent with the results of batch experiments and illustrated in Fig. 2.1.3. In general, I-2959, I-184, and D-1173 showed very similar behavior and the results obtained, along with those for other initiators are summarized in Table 2.1.1, with further details available in the Supplementary Materials. The photochemistry of some of these initiators has been examined in a classic publication from Turro's group.[3]

Another example with more complex photochemistry is shown in Fig. 2.1.6 for I-379, where the initiator (λ_{max}~325 nm) has a good overlap with the UVB lamp (see Fig. 2.1.1) and is rapidly consumed, with essentially none left after 3.1 min. However, the AgNP plasmon band continues to grow and peaks at ~29 min. Once again, this suggests that the growth of the plasmon band reflects an autocatalytic process similar to that in silver photography,[17] but stimulated by light. Notice also that the Teflon tubing (see top inset) develops black deposits after the flow tube has been used for 3 h. These deposits are believed to be silver or Ag_2O formed during the prolonged exposure. We note that no deposits were observed when I-2959, I-184, or D-1173 were used as initiators. The deposits can be readily removed by flowing nitric acid and the Teflon tube can be reused.

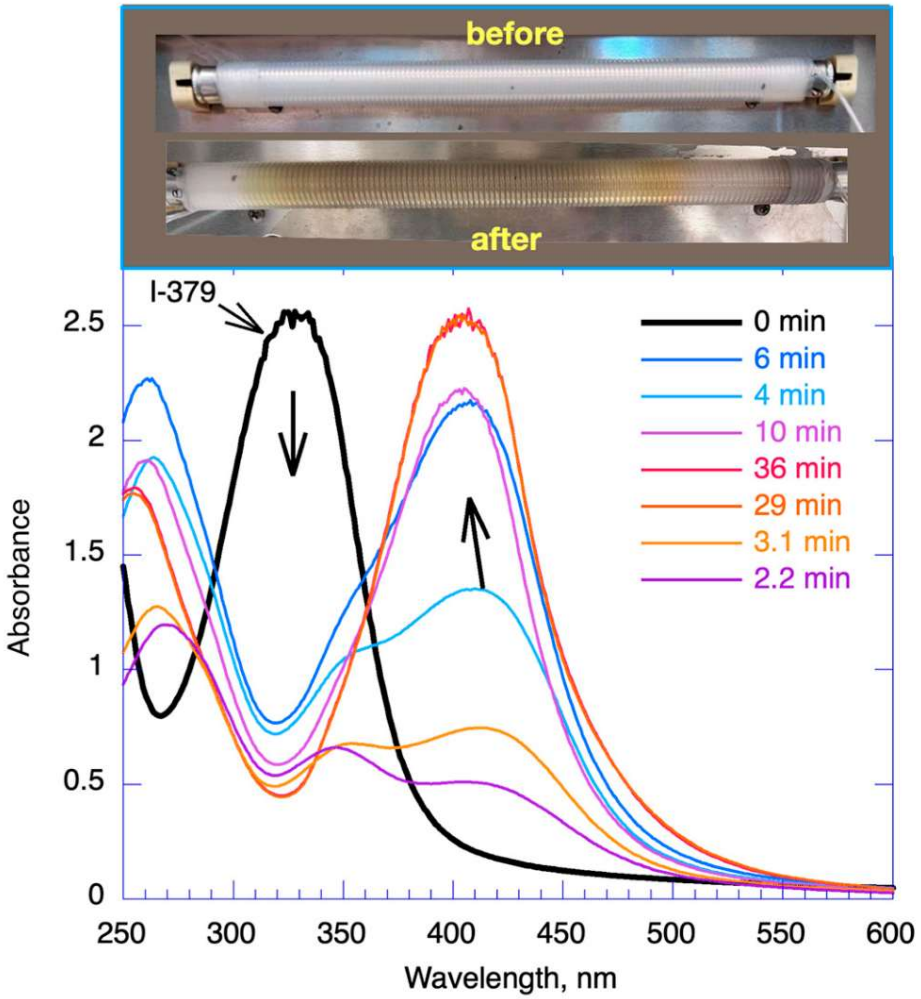

Fig. 2.1.6: Different residence times irradiated with UVB light and using I-379 as initiator. Silver nitrate (0.2 mM), sodium citrate (1 mM), I-379 (0.2 mM) in 2:3 CH_3OH:water purged Argon and irradiated with a UVB lamp with different residence times. Notice that the initiator (black with λ_{max}~323 nm is consumed in the first 2 min and has a slight blue shift at long irradiation times. The inset at the top shows the Teflon-wrapped lamp before and after experiment by using I-379 as an initiator. Notice the black deposits on the latter.

The initiator I-369 showed behavior very similar to I-379, as expected, given the similarity of the two structures (see Table 2.1.1).

Initiator I-907 shows the best overlap with the UVB lamp (see Fig. 2.1.1), producing strongly reducing α-aminoalkyl radicals, and the sulfur center should help stabilize nanoparticles. Its performance is good, but it produces nanostructures with a shifted plasmon band (~440 nm compared with the typical 395 nm), and the band is quite broad, Fig. 2.1.7. The plasmon band stops growing after 8–10 min.

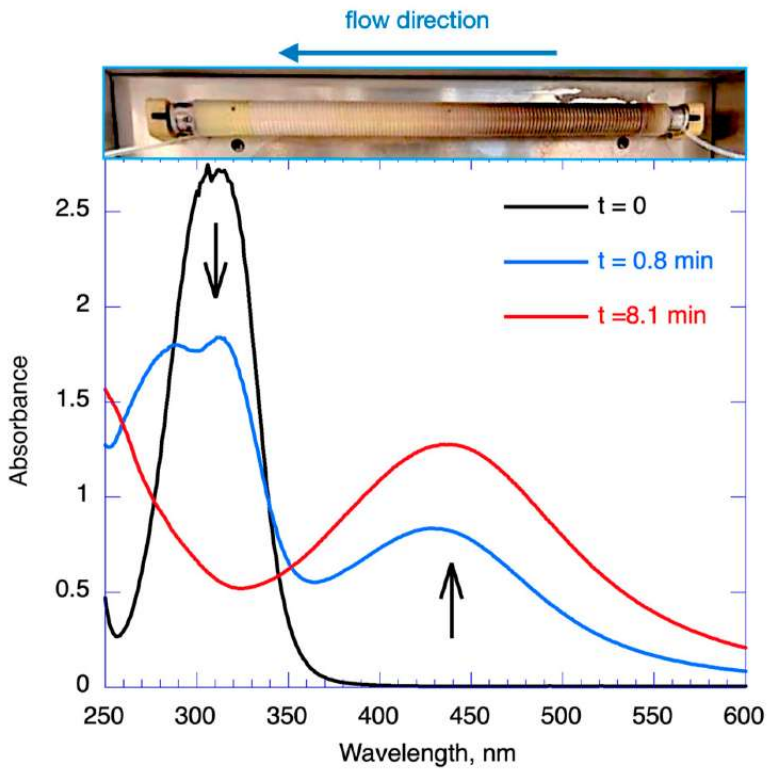

Fig. 2.1.7: Different residence times irradiated with UVB light and using I-907 as initiator. Sample: Silver nitrate (0.2 mM), I-907 (0.2 mM), trisodium citrate (1 mM), and 1:1 CH_3OH:water purged with argon. The inset at the top shows the Teflon-wrapped lamp after using I-907 as an initiator. Notice the black deposits, and in particular the dark areas are predominantly on the right side from which the reagents are fed to the system.

The photochemistry of I-907 generates reducing α-aminoalkyl radicals (Scheme 2.1.4). The benzoyl radical is expected to form the corresponding aldehyde or carboxylic acid, and both can stabilize AgNP, given the presence of a thioether.

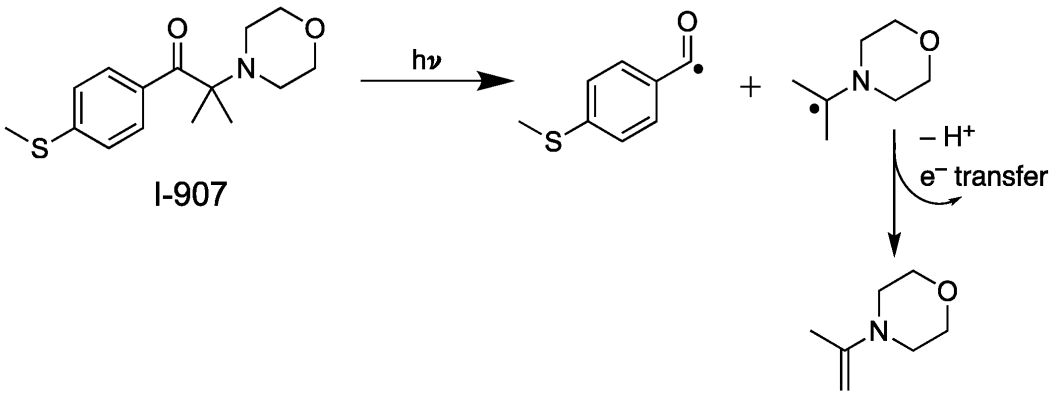

Scheme 2.1.4: Anticipated Norrish Type I reaction of I-907 and chemistry of the α-aminoalkyl radical.

Overall, I-907 is a reasonable initiator but produces particles with a red-shifted plasmon band and requires periodic nitric acid treatment of the Teflon tubing to clean up the silver deposits.

Finally, we come to the examples of benzoin and α-methylbenzoin. Benzoin is known to have a very short triplet state with a lifetime of around 1 ns.[2,18] Reports normally use non-aqueous solvents; although, measurements in methanol have been reported.[2] Benzoin has a rather low extinction coefficient, which becomes a disadvantage, for example, in polymer chemistry applications.[4] Frequently, the absorbance is enhanced by the addition of thioether substitution,[3,4] something that is also evident when comparing the spectra of benzoin and I-907 in Fig. 2.1.1. To the best of our knowledge, benzoin has not been studied in water.

Unfortunately, benzoin proved to be a very inefficient initiator in water, but it was reasonably efficient in 50% aqueous methanol, see Fig. 2.1.8. In contrast, α-methyl benzoin was very efficient, even in water (Fig. 2.1.8A), while the absorption spectra of the two ketones are very similar, with λmax~250 nm. Even in 50% aqueous methanol, the performance is good. Notice that after 1.3 min, the main effect of irradiation is a red shift of the plasmon band and a gradual decrease in absorbance at the maximum. Overall, while benzoin seems a challenging initiator, α-methylbenzoin seems straightforward and quite efficient, even in water (Fig. 2.1.1A). We speculated that benzoin in water may undergo some enolization, but the very limited aqueous solubility led to the failure of the NMR work aimed at detecting any enol formation. In the context of this work, which is aimed at practical recommendations for initiators for nanoparticle fabrication, benzoin is not recommended, while α-methylbenzoin is.

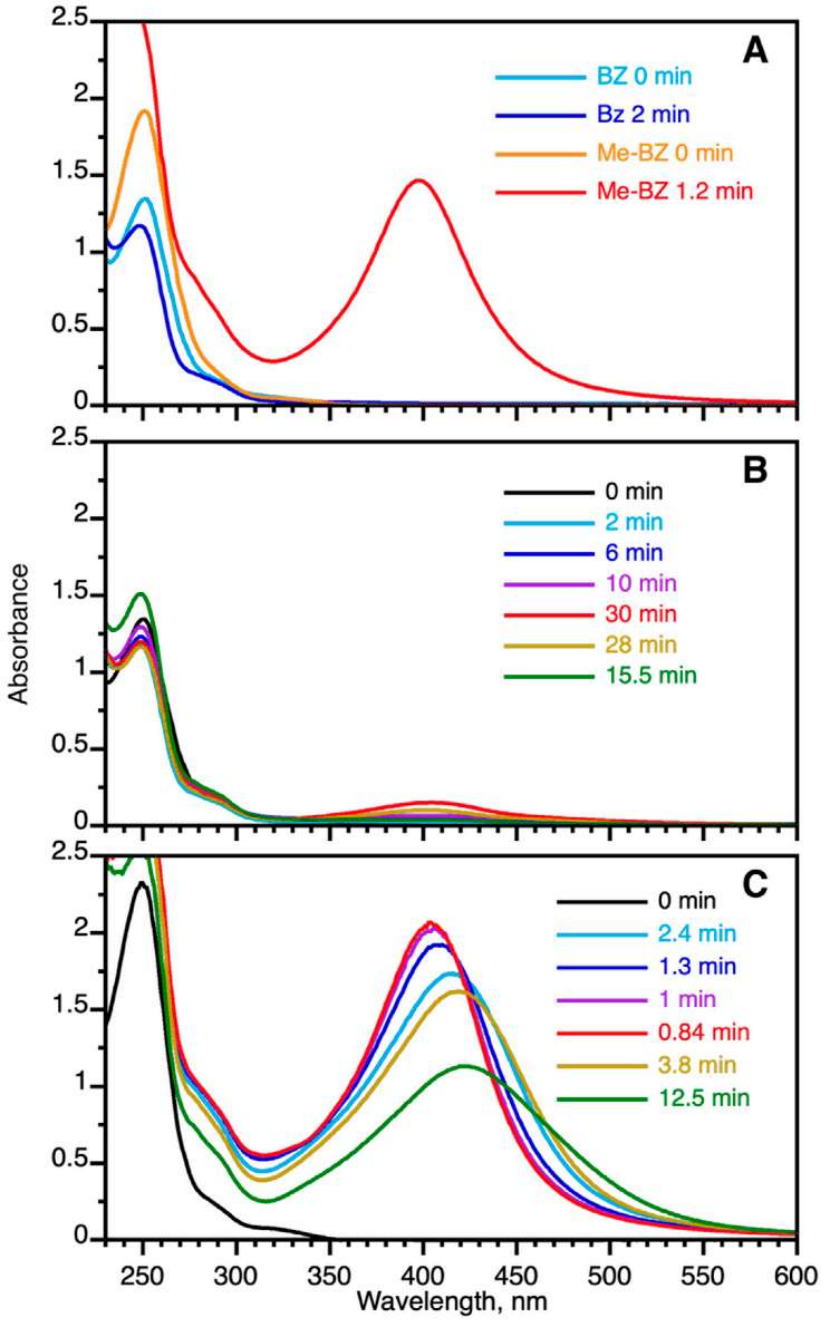

Fig. 2.1.8: Benzoin as an initiator for spectra corresponding to different residence times in min. Silver nitrate (0.2 mM), benzoin (0.2 mM), and trisodium citrate (1 mM) were deaerated with argon and irradiated with UVB lamp in a flow system with 6.3 m Teflon tubing. The order shown in each panel for residence times corresponds to the sequence of acquisition, ensuring that no systematic order is used (A) in water comparing benzoin (totally inefficient) with α-methylbenzoin, the latter showing intermediate efficiency; (B) benzoin in water showing that at long residence times, there is a slow growth of the plasmon band; (C) spectra in 1:1 CH_3OH:water. Notice that the top absorbance is nearly 30 times larger in panel (C), and further, the highest absorbance is achieved in ~1 min.

Concentration Tolerance and Stability during Long Fabrication Times

We were also interested in establishing to what extent the continuous generation of particles in the flow system would offer consistent results. We were also interested in establishing if AgNP could be produced at higher concentrations, and then diluted just before use. For this work, we chose I-184, one of the highly reliable initiators. The results in Fig. 2.1.9A confirm that a higher concentration of reagents can be readily utilized and dilution to the spectrometer absorbance range shows an excellent well-resolved plasmon band. In the context of continuous production of nanoparticle solutions Fig. 2.1.9B, the 400 nm absorbance shows variations of ±2% over a 6 h period, illustrating the high reliability of the method.

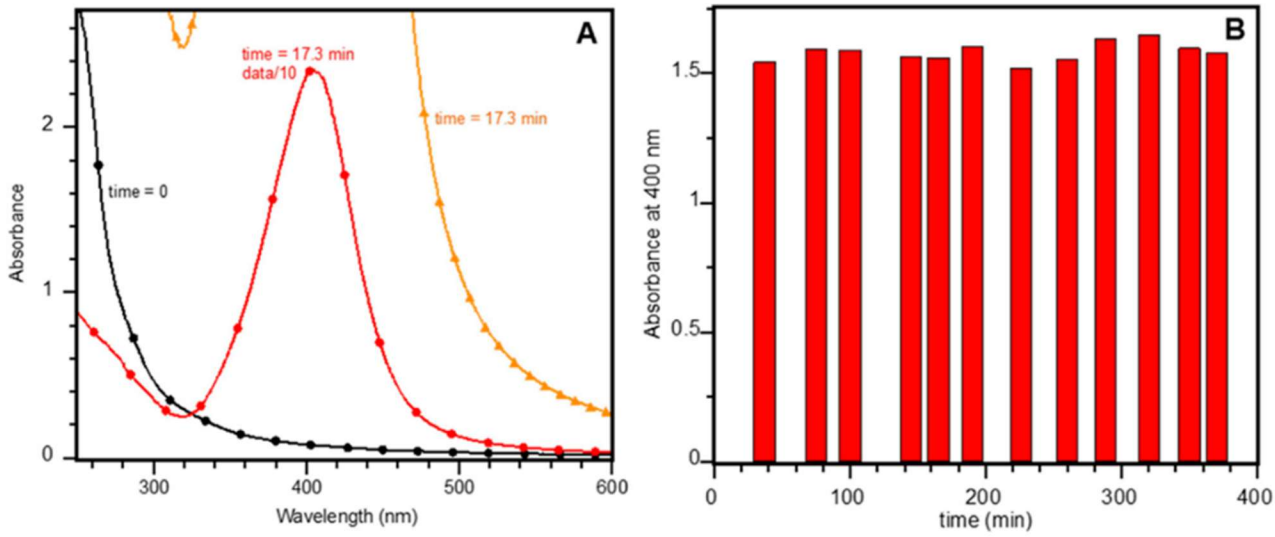

Fig. 2.1.9: (A) For our concentration study, we used silver nitrate (2 mM), I-184 (2 mM), and trisodium citrate (10 mM), in MeOH 10%, in water deaerated with Ar, under UVB irradiation with a residence time of 17.3 min. The absorbance axis has been limited to the 2.7 specification for the Cary 60 spectrometer and the graph includes a sample diluted 10 times. (B) Monitored at 400 nm for over 6 h, with silver nitrate (0.2 mM) and all other parameters identical to panel (A).

Characterization of the Nanostructures Prepared

AgNP morphologies for all the initiators were approximately spherical, with D-1173, I-2959, and I-907 producing seeds with the smallest size and narrowest size distributions (Table 2.1.2). Conversely, I-379 and I-369 yielded the largest seeds with broader size distributions. TEM images (Fig. 2.1.10) and histograms for NPs made with each initiator are available in the Appendix (Fig. A.2.1.1 – A.2.1.8), with

corresponding UV–Vis spectra for each sample used for the TEM imaging shown in Fig. 2.1.S7. It should be noted that gaussian fits are included in each size distribution as a visual aid. However, it can be seen in some cases (such as I-2959, Fig. A.2.1.1) that the gaussian fit does not perfectly match the size distribution in the histogram – this is due to the limit of detection of the instrument making it difficult to measure the size of particles below 1 nm. Meanwhile, large particles can be easily measured, leading to a sampling bias.

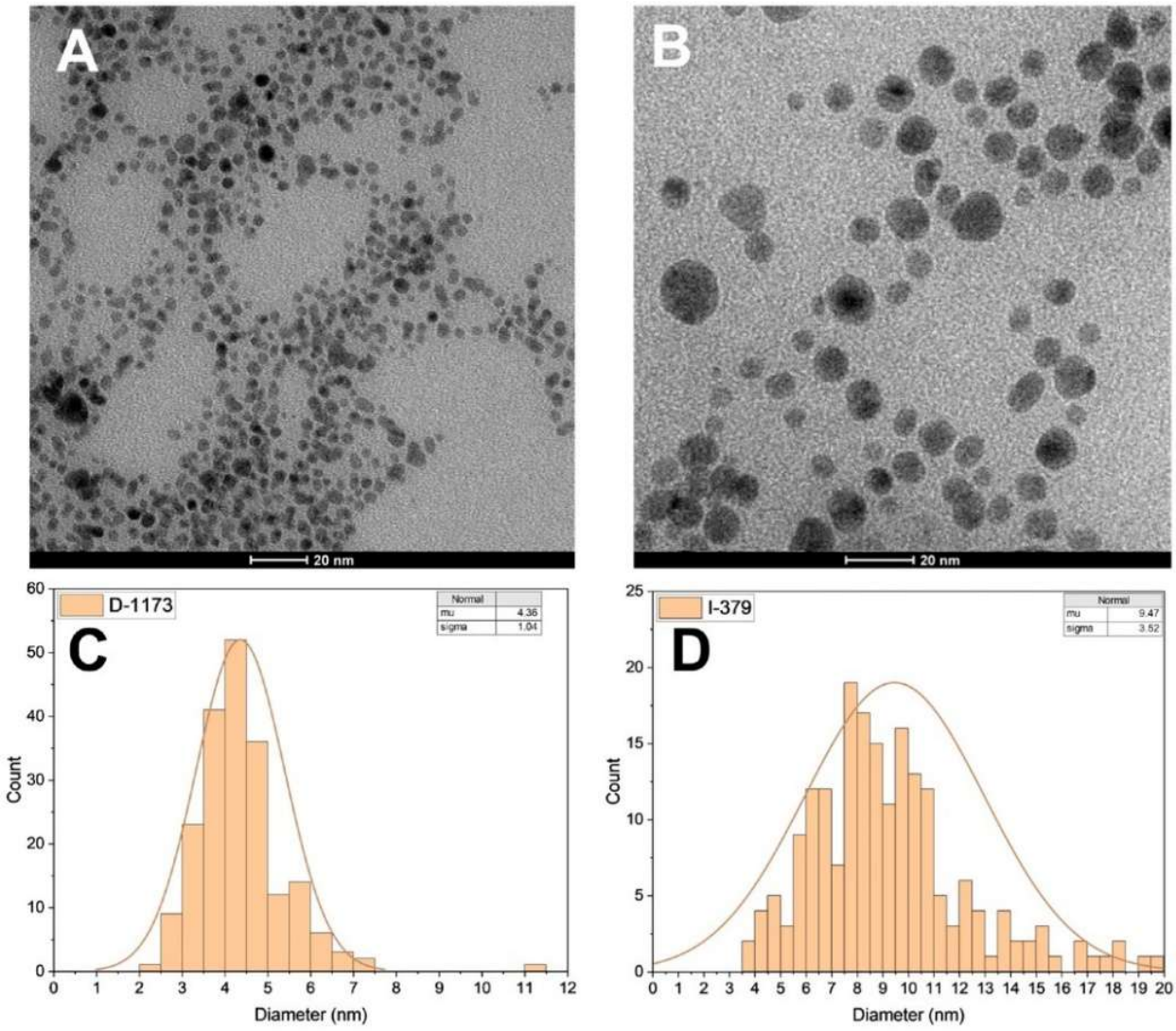

Fig. 2.1.10: TEM image of AgNPs generated with D-1173 (A) and I-379 (B) synthesized in-flow using 50% MeOH and their corresponding particle size histograms ((C,D), respectively). Histograms were made from the counting of 200 particles. XRD for similarly stabilized particles is available in the literature.[19]

Table 2.1.2: Average diameters and standard deviation of AgNPs synthesized using each photoinitiator with optimized flow conditions. All values are based on the counting of 200 nanoparticles.

Initiator Used	Average Diameter (nm)	Standard Deviation (nm)
I-2959	4.6	1.8
D-1173	4.4	1.0
I-184	7.6	2.6
I-907	5.3	1.5
I-369	8.6	4.2
I-379	9.5	3.5
benzoin	6.1	2.2
α-methylbenzoin	8.3	2.7

Conclusions

The photochemical synthesis of silver nanoparticles under flow conditions has proven extremely efficient and reproducible, yielding suitable AgNP seeds under UVB irradiation with exposure times of less than one minute for the best initiators. The recommended initiators are those yielding ketyl radicals efficiently following Norrish Type I cleavage. Among the eight structures shown in Scheme 2.1.3, four of them are highly recommended, I-184, D-1173, α-methylbenzoin, and I-2959. The last of which showing the best absorption properties, adequate aqueous solubility, and is readily available. We anticipate that the seeds produced here will enable the synthesis of other morphologies with interesting biological applications.[13,20]

Supplemental Information

Figures In Appendix:

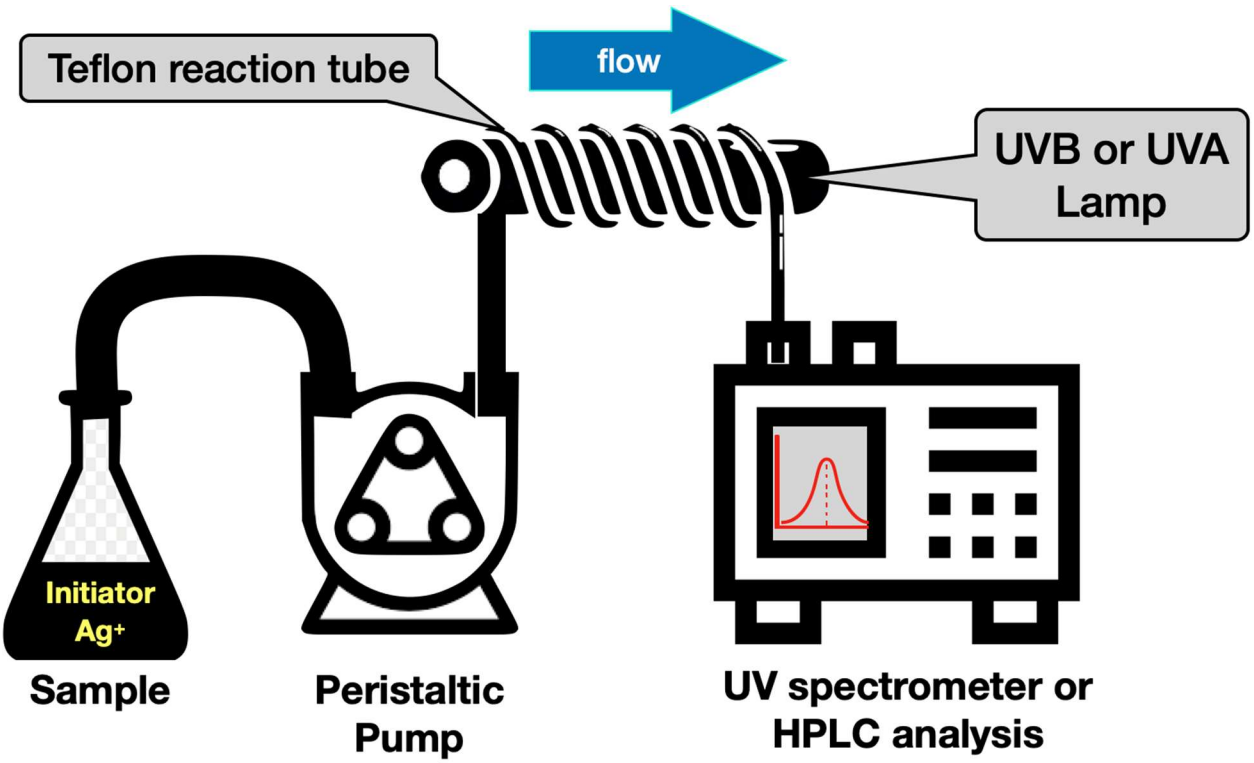

Fig. 2.1.S1: Schematic representation of the experimental flow system.

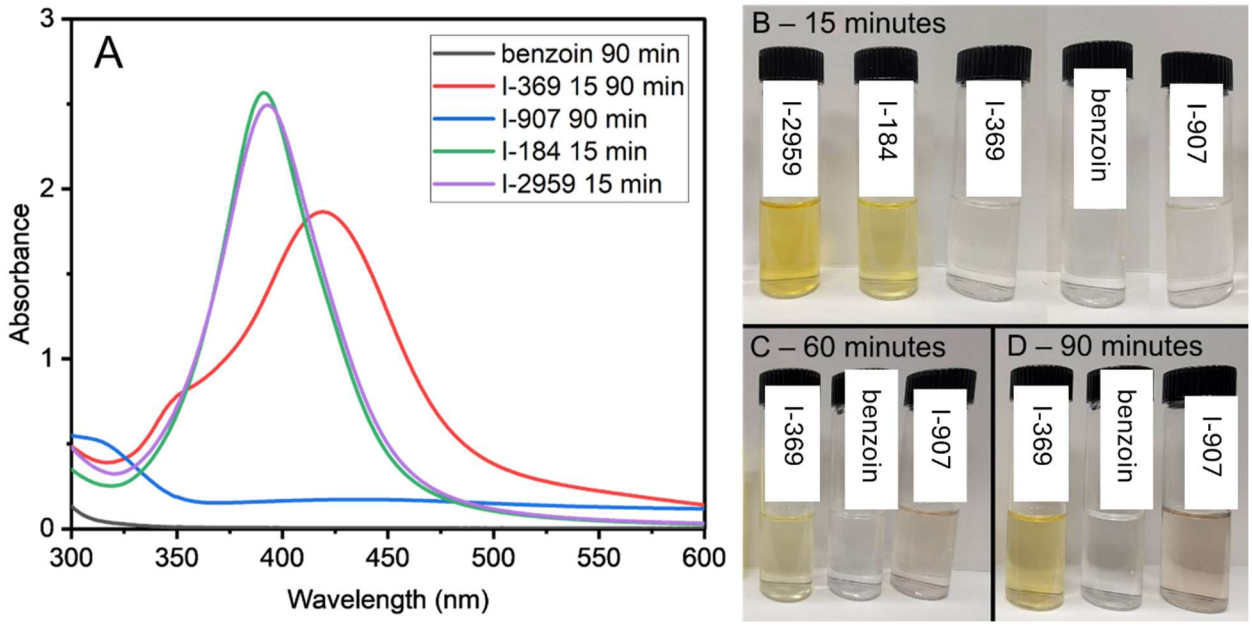

Fig. 2.1.S2: A) UV-Vis spectra of AgNP solutions produced using 0.2 mM I-2959, I-184, I-369, benzoin, or I-907 as photoinitiators in water. I-2959 and I-184 completed the reaction in 15 min, while I-369 required 90 min to generate similar levels of AgNP absorbance. Benzoin and I-907 did not yield any notable plasmonic absorbance peaks within 90 min of reaction. Corresponding appearance of the nanoparticle suspensions at 15 min (B), 60 min (C), and 90 min (D) are shown in the right panel. It should be noted that I-2959 dissolved easily.

Fig. 2.1.S3: Appearance of solutions containing 0.2 mM $AgNO_3$, 1 mM citrate, and 0.2 mM of either I-2959 (labelled "A") and I-184 (labelled "E") as initiators, in mixtures of MeCN and water (0%, 25%, 50%, 75% and 100% MeCN) following 15 min of irradiation with in a photoreactor with 6 8W UVA lamps (for the 0% MeCN samples). The samples containing MeCN showed no change after 15 min. The MeCN containing samples were subsequently irradiated for a total of 90 min, but still did not yield any AgNPs.

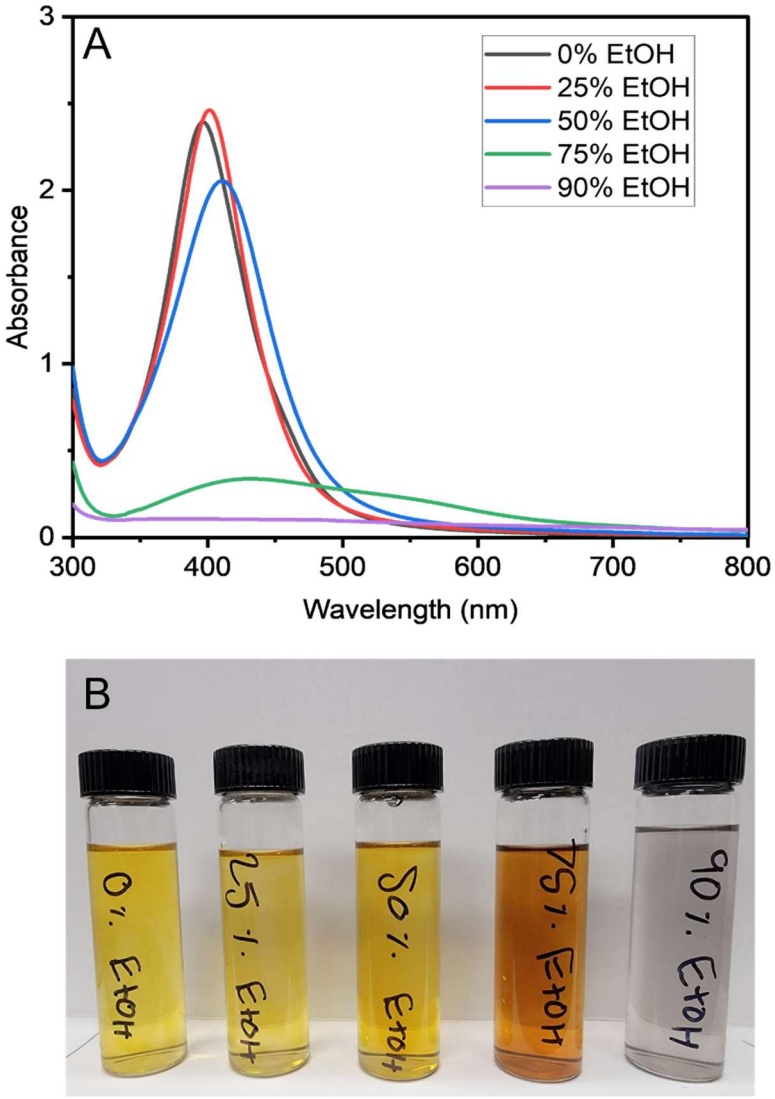

Fig. 2.1.S4: A) UV-Vis spectra of AgNPs synthesized in batch scale, using 0.2 mM I-2959 as an initiator. Solutions were prepared in mixtures of EtOH/H_2O in ratios ranging from 0 to 90% EtOH, and irradiated for 15 min in a photoreactor with 6 8W UVB lamps. The 90% EtOH sample was irradiated for an additional 25 mins, as little color could be seen after 15 min of irradiation. B) Corresponding appearance of AgNPs produced in solutions containing different fractions of EtOH following reacting under UVB.

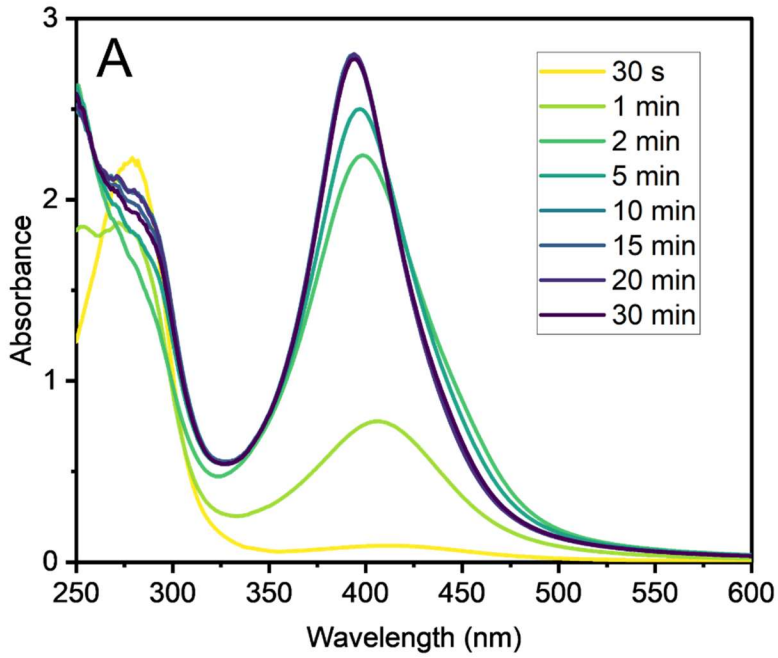

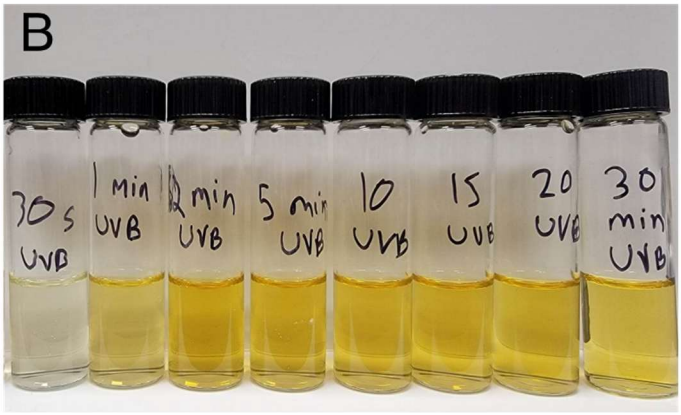

Fig. 2.1.S5: A) UV-Vis spectra of AgNPs synthesized in single batches, using 0.2 mM I-2959 in H_2O. Samples were irradiated in a photoreactor with 6 UVB lamps for 30 sec to 30 min to determine the endpoint of the reaction. B) The appearance of the corresponding nanoparticle suspensions.

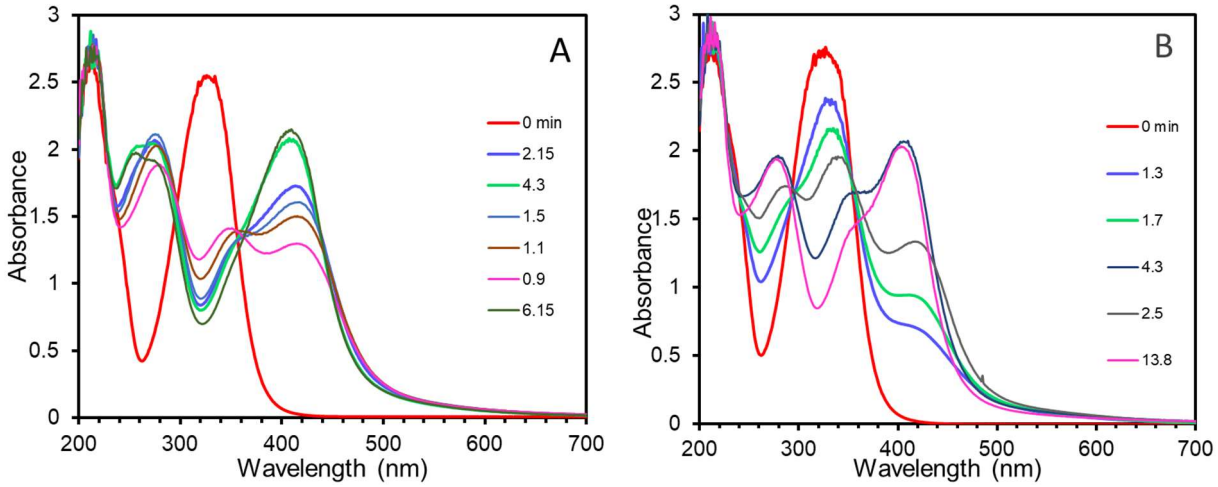

Fig. 2.1.S6: I-369 as an initiator for spectra corresponding to different residence times in min. Silver nitrate (0.2 mM), benzoin (0.2 mM), and trisodium citrate (1 mM) in 1:1 CH3OH: water deaerated with argon and irradiated in a flow system with 6.3 m Teflon tubing with (A) UVB lamp and (B) UVA lamp.

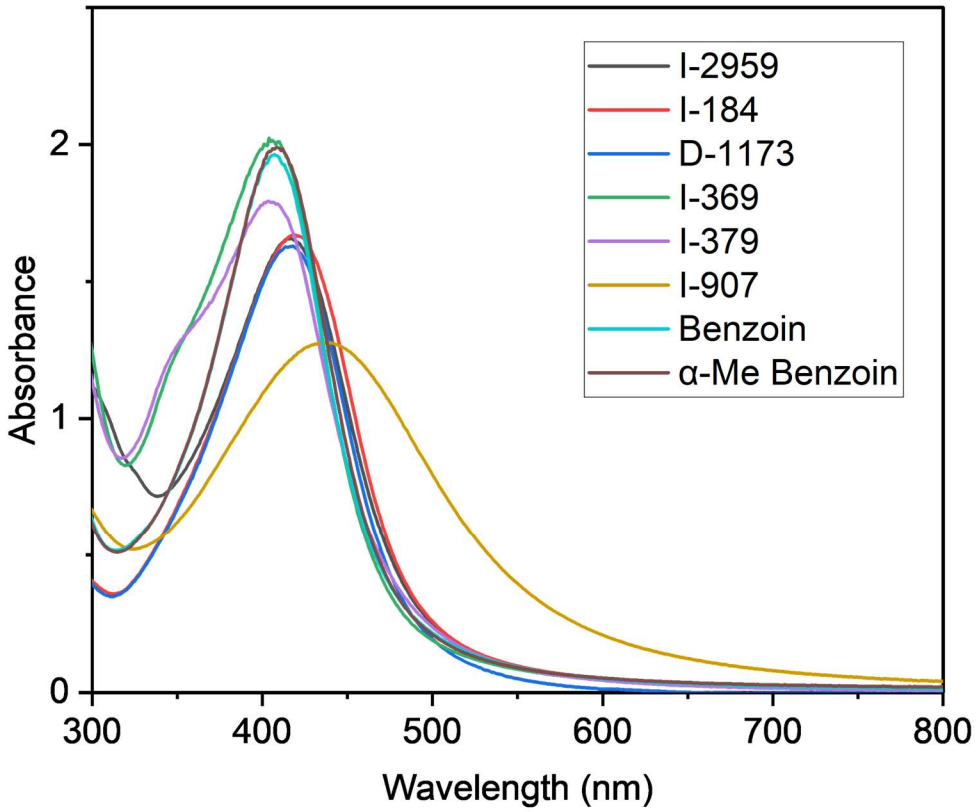

Fig. 2.1.S7: UV-Vis spectra of AgNPs made in-flow using 50% MeOH, 1 mM citrate, 0.2 mM AgNO3, 0.2 mM of photoinitiator under UVB irradiation. Flow rates for each are shown in Table 2.1.1. Corresponding TEM and histograms are shown in the Appendix (A.2.1.1-A.2.1.8).

2.2: LED-driven, surfactant-free, photochemical synthesis of silver nanostructures with tunable plasmon absorptions across the visible and NIR regions

Introduction

This part of Chapter 2 outlines a room temperature aqueous one-pot synthesis of AgNPs of higher order structures using AgNP seeds (sAgNPs) - similar to those seen earlier in this chapter - as a precursor. Using LED illumination as the driving force, we are able to produce citrate stabilized AgNPs with tunable shapes and sizes, with plasmonic absorption bands spanning the entire UV-Vis and even some of the NIR spectrum, as will become essential for Chapters 3 and 4.[20] In this synthesis method, sAgNPs are irradiated with light, causing the particles to morph and grow, differentiating into different shapes depending on the wavelength of light they are exposed.[13] We experimented separately with two different wavelengths of LEDs in this work - with 450 nm (blue) illumination yielding decahedral AgNPs (dAgNPs) and 635 nm (red) illumination yielding triangular particles (tAgNPs). In the case of tAgNPs, the final wavelengths of the particles can be tuned from 600 nm to 1400 nm, beyond which our aqueous samples cannot be measured easily due to the water absorption cut-off. Decahedral particles however undergo a much less drastic shift in absorption, with plasmon bands ranging from 490 - 510 nm, albeit with much narrower size distributions. Using this light-driven approach has several strengths. Firstly, it does not require bulky stabilizers such as surfactants or polymers to generate exceptionally stable particles with complex morphologies, which was attractive to us for catalytic and biological applications. The properties of our products in this method are highly tunable, able to generate AgNPs with absorbances across the visible and NIR spectrum. This is especially true for tAgNPs in particular, making these particles very useful for plasmon enhanced applications.[20]

The synthetic approach involves two distinct steps – first is the synthesis of sAgNPs, small (~5 nm) particles which act as the precursor for the larger AgNPs.[13] In this step, different amounts of citrate were added to control the final size of the resulting AgNPs, though the citrate concentration has minimal effects on sAgNP characteristics. As discussed in Chapter 2.1, the seeds are produced by generating ketyl radicals from the Norrish Type I cleavage of I-2959 under UVA light, generating Ag^0 which coalesces into AgNP seeds under citrate stabilization (Scheme 2.1.1).[1]

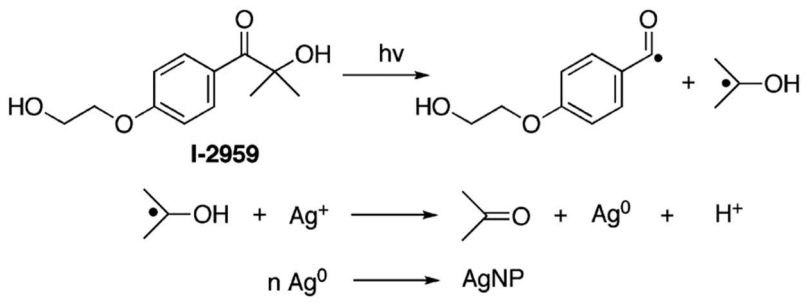

Scheme 2.2.1: Norrish type I cleavage of I-2959 by UVA light.[1,13]

The second phase of the reaction is the growth of the sAgNPs into larger, more stable decahedral or triangular AgNPs with controllable plasmonic absorbances. In this step the light source used selects for the final shape of the NPs, with blue LED illumination yielding decahedral dAgNPs, and red illumination yielding triangular tAgNPs.

Materials and Methods

Materials

Silver nitrate (ACS reagent, 99.9+%) was purchased from Alfa Aesar. Trisodium citrate dihydrate (99%) was purchased from Fisher Scientific. Irgacure-2959 (I-2959) was a gift from BASF Chemicals. All water used is ultra pure, prepared by purification of deionized water using a Thermo Scientific™ Barnstead™ GenPure™ water purification system (a conductivity of 18 MΩ cm^{-1}). The reaction flasks used were Rabbit Leak-Free Discreet Flask (Black) - R4-06138 3.25" x 1.2" x 6" bottles ordered from Amazon.

Seed Synthesis

The seeds for this project were made in batch, rather than in flow (as seen earlier in this chapter), using I-2959 as the photoinitiator to enable aqueous conditions. To generate sAgNPs, in a flat, transparent plastic vessel, an aqueous solution of 0.2 mM $AgNO_3$, 0.2 mM I-2959, and between 1-15 mM trisodium citrate is degassed for 30 min in the dark under a steady flow of argon. The transparent solution is then illuminated in a Luzchem UV photoreactor under 8 UVA bulbs for 15 min, yielding a deep yellow suspension of AgNP seeds with prominent absorbance centered around 400 nm (see Fig. 2.1.S4).

AgNP Growth

In the same container, the seed suspensions are exposed to air for 30 min in the dark to reoxygenate the solution and ensure that the sAgNPs are fully formed. After this, the seed suspension is laid flat on either a blue (450 nm) or red (635 nm) 24-LED well-plate illuminator (WPI, by Luzchem Research Inc), and shaken gently on an orbital shaker, ensuring that solution is consistently disturbed for the duration of the synthesis. The samples are then irradiated on the illuminators for 24 h for the blue WPI, or 48 h for the red WPI (Fig. 2.2.1). Once complete, the particle suspensions are washed via centrifugation at 6,000 RPM for 60 mins and resuspended in ultrapure water. This process is performed three times total before storing the particles in the dark in glass containers. The resulting suspensions are stable for months, even if left on the benchtop – however they were stored in the dark as a precaution. The dAgNP suspensions have a distinctive bright orange color, while the tAgNPs range from deep blue to purple depending on the citrate concentration used.

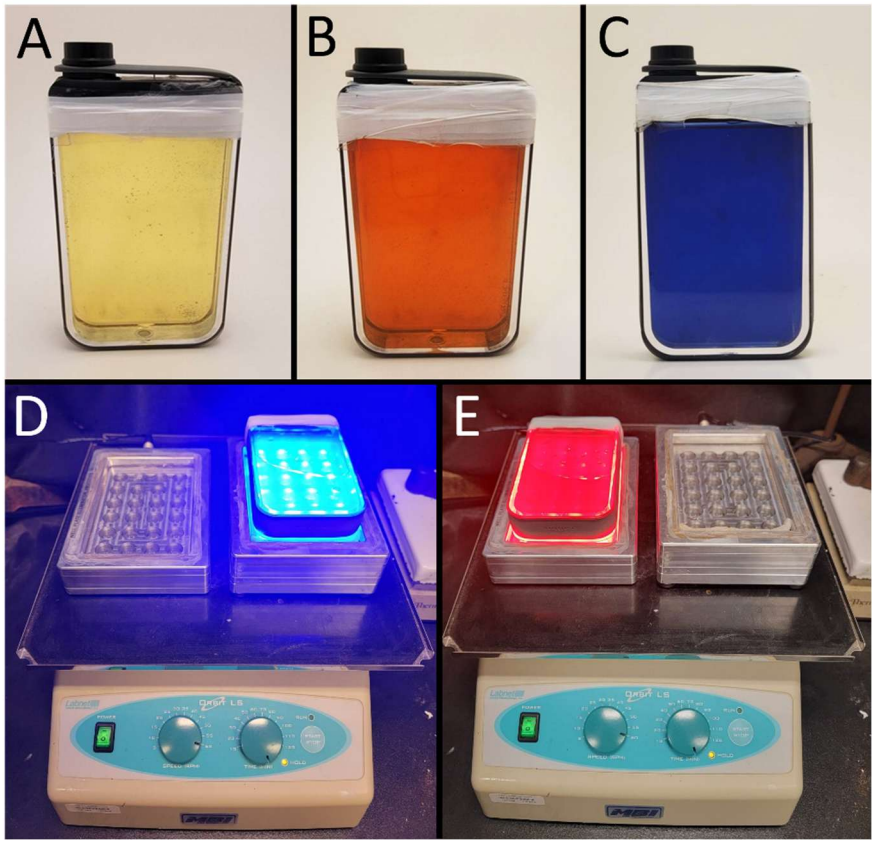

Fig. 2.2.1: Appearance of sAgNPs (A), dAgNPs (B) and tAgNPs (C) made using 10 mM of citrate. D&E show the blue (450 nm) and red (635 nm) well plate illuminators in operation, atop an orbital shaker.[20]

Characterization

UV-Vis-NIR absorbance measurements were taken using a Cary 7000 Universal Measurement Spectrophotometer. TEM images were collected using a FEI Tecnai G2 spirit Twin TEM, and average particle sizes were estimated from the measurements of ~200 individual particles per sample. For dAgNPs and tAgNPs, particle size is determined by the base-tip distance, i.e. the distance from a vertex to the midpoint of the opposite edge of the particle. When measuring particles, only particles with decahedral or triangular character were measured; large agglomerates and leftover AgNP seeds were not measured. All size measurements were taken manually using ImageJ.

Real time absorbance acquisition

Real time spectral acquisition was performed using two different approaches. For the dAgNPs, a 3 mL cuvette was placed in a Cary 60 equipped with a "qpod 2e cuvette holder" by Pacific Northwest, with an open window through which light can be directed into the AgNP seed suspension using a 450 nm LEDi by Luzchem. Measurements were taken every 20 min for 24 h, with the reaction reaching completion around the 20 hour mark.

For the tAgNPs, a different approach needed, as a Cary 7000 spectrometer was needed to measure NIR absorbance. A 200 mL batch of AgNPs was connected to a flow cuvette using Teflon tubing attached to a peristaltic pump to regularly flow fresh solutions from the batch into the cuvette, and then back into the batch container. Measurements were taken every 30 min for 48 h, with the reaction being stopped at 48 h.

It should be noted that due to the observation methods and lack of purification employed at each time point, there is some variability in how the collected spectra appear compared to the AgNPs used in the manuscript.

Results and Discussion

In this work the synthesis of AgNPs with a variety of morphologies has been achieved without the use of bulku surfactants or strongly bound stabilizers through the light-directed growth of sAgNP precursors into more complex morphologies. This work is a continuation of a previous study in the group where it was established that the use of LED irradiation can guide the growth of sAgNPs to generate different shapes of AgNPs.[7,13] This work builds on these findings by establishing an approach to controlling the

plasmonic absorbance of the products throughout the visible and NIR regions (up to 1400 nm). One of the key components of this work was the use of Well Plate Illuminators (WPI) by Luzchem (Fig. 2.2.1). These illuminators consist of 24 individual LEDs, arranged specifically to align with the wells in a 24-well plate. Rather than using well plates, however, we opted to use plastic flasks with similar lateral dimensions to standard 24 well plates, allowing us to scale our reaction up from 3 mL to 200 mL. Scaling the reaction up was essential not only for generating volumes that are useful for other applications, such as antibacterial testing [20] as will be seen in Chapter 3, but also the wide, flat vessels combined with orbital shaking provides more uniform light and temperature throughout the reaction, an improvement from previous iterations where polydispersity was a challenge (note that while we improve on this, our tAgNPs are still not truly monodisperse).[13] Additionally, when our LED driven method was first developed [13], we did not have the ability to monitor plasmonic absorbance beyond 900 nm, making it impossible to truly explore the tuning of tAgNP plasmonic absorbance.

In the aforementioned works,[7,13] it is established that by irradiating sAgNPs with LEDs of various colours, we can can grow those particles into more defined structures, hence the moniker “seeds”. In this work, these sAgNPs are used as the building blocks for larger silver nano decahedra and triangles when irradiated with either blue (450 nm) or red (635 nm) LEDs, respectively. This phenomenon is further controlled by manipulating citrate concentrations in the reaction, allowing for the accurate tuning of the AgNPs size and plasmonic absorption properties. As shown in Fig. 2.2.2, AgNP absorbance maxima could be controlled to a great extent for tAgNPs (Fig. 2.2.2A), with plasmon bands spanning much of the visible-NIR spectrum when citrate is increased from 1mM to 10 mM. This effect is much more pronounced in the case of tAgNPs, with plasmon bands ranging from 600 nm to 1400 nm, compared to the dAgNPs where the range is 490 nm to 510 nm (Fig. 2.2.2B). The size dependent shift in AgNP extinction is consistent with trends where larger plasmonic particles feature red-shifted LSPR bands, similar to the principle of quantum confinement.[21,22] However, in particles larger than a few nanometers, their optical properties also depend heavily on Mie scattering, local surface interactions, and heterogenous electromagnetic field effects within the particles.[22,23] In angular shapes such as nanotriangles, plasmonic excitation induces highly localized electromagnetic fields localized to AgNP vertices.[24] As particle size increases, these fields become further apart, leading to wider, lower energy LSPR wavelengths, while allowing for greater optical tuning, as seen in Fig. 2.2.2.

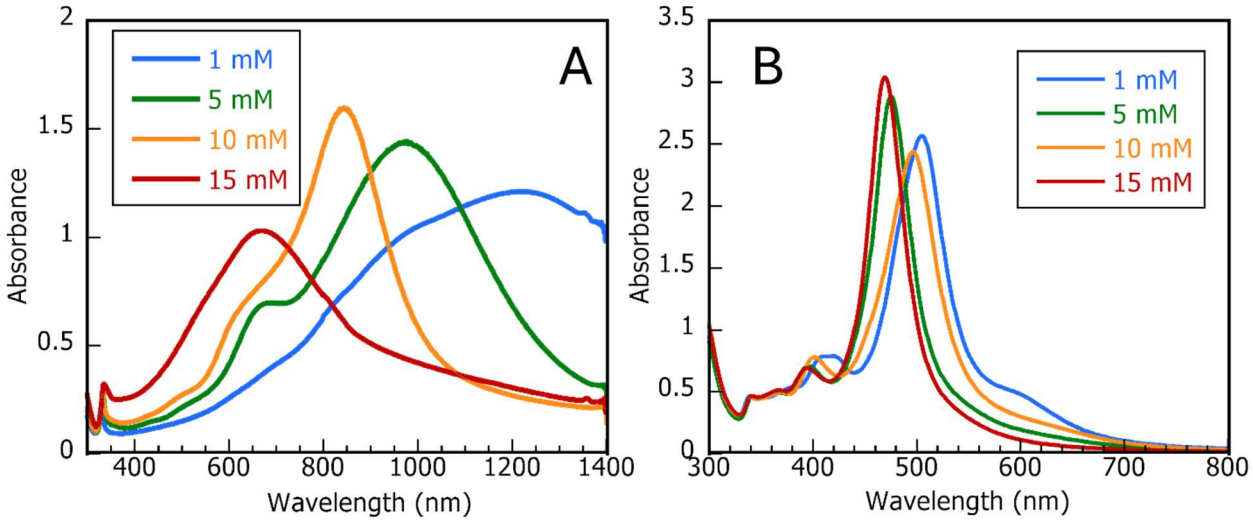

Fig. 2.2.2: Absorbance spectra of batch-scale AgNPs made using 1-15 mM of citrate. Legends indicate the [citrate] used to synthesize each batch of AgNPs. A) UV-Vis-NIR absorbance spectra of tAgNPs following 48 h of 635 nm irradiation using a red WPI. B) UV-Vis absorbance spectra of dAgNPs following 24 h of 450 nm irradiation using a blue WPI.[25]

Interestingly, the absorbance wavelength of the final particles do not match the wavelength of the incident light. This effect, which we refer to as "plasmon pushing" is shown in Fig. 2.2.3, where the growth of the particles was monitored in real-time to observe any intermediate particles. As shown in Fig. 2.2.3, over the first few hours of the respective reactions, there is a sharp decrease in the sAgNP absorbance band at 400 nm, accompanied by the emergence of a peak near ~460 nm for the dAgNPs, and ~700 nm for the tAgNPs. These peaks continue to shift as the particles grow, demonstrating that the plasmon pushing phenomenon likely originates from a two-step process where 1) a particle with absorption near the incident photons is formed from sAgNP precursors, followed by 2) the growth of these particles to their larger final structures, ultimately shifting their absorption bands away from the wavelength of the incident photons. Our belief is that the initial intermediate particles (i.e., those emerging at 460 and 700 nm in Fig. 2.2.3) are the products of sAgNPs stochastically agglomerating in solution. These agglomerates would normally dissociate quickly under dark conditions. However, as Ag nanostructures are photocatalytic, they may be fused together and grown if light is absorbed, possibly by catalyzing the reduction of Ag^+ by citrate along the surface of the particles. We speculate that these early shifts in absorbance reflect the presence of proto-particles that eventually grow into the final AgNPs.

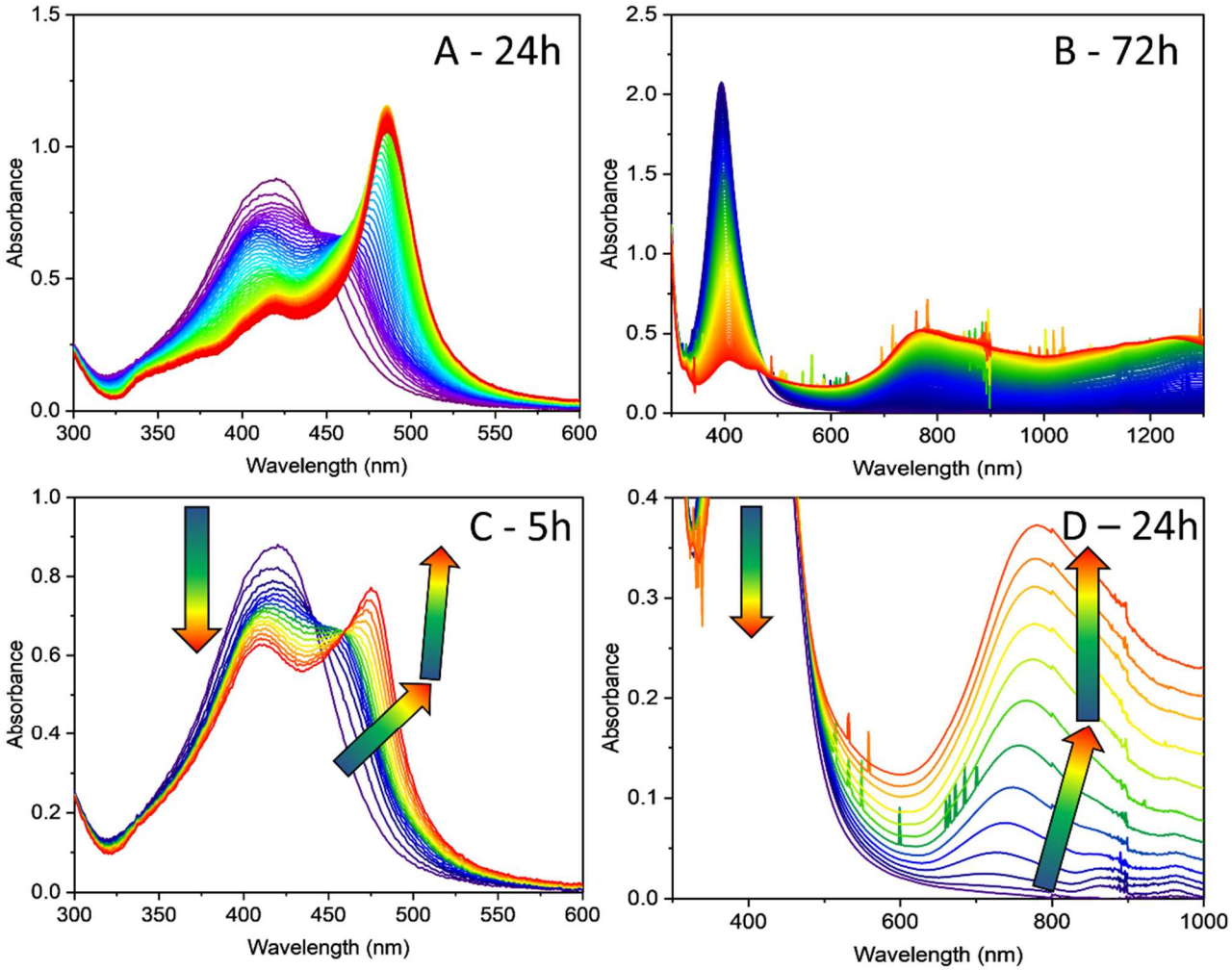

Fig. 2.2.3: UV-Vis-NIR absorbance measurements taken throughout the growth of dAgNPs (A&B) and tAgNPs (C&D), monitored in real time during AgNP growth. The colour scheme of the traces and corresponding arrows reflects the passage of time from early blue traces, towards the end of the AgNP growth process, represented by red traces. Arrows indicate the general directionality of absorbance changes over time. Spectra present in C and D are shown to highlight the early shift in absorbance which originates near the wavelength of the incident light before shifting to longer wavelengths. A) The total change in absorbance over 20 h for Ag seeds irradiated with a 450 nm LED illuminator. UV-Vis spectra were measured every 20 min for A and C. C) Early shift in absorbance over the first 5 h of 450 nm LED illumination. B) The total change in absorbance over 72 h for AgNP seeds irradiated on a 635 nm LED well plate illuminator. UV-Vis-NIR spectra for B and D were taken every 30 min. D) Early absorption shift over the first 24 h of irradiation with 635 nm illumination.[20]

This concept of an unstable pseudo-particle that evolves into the final form under irradiation is supported in a recent work from our lab by Frank et al.,[25] which shows that the light-guided synthesis helps evolve particles into different thermodynamically stable states, enabling more complex particle morphologies. A key observation from the study, as well as this work, is that the tAgNPs and dAgNPs are photo stable, and can be exposed to ambient light without the particles losing their physical or optical characteristics. However, the study demonstrates that under prolonged intense blue light illumination partially formed tAgNPs can be converted into decahedra, while the same is not true in the reverse direction. This suggests that illumination of increasing intensity enables alternative pathways of growth towards highly thermodynamically stable states which manifest as different AgNP shapes corresponding to the energy of incident light used.[25] A crucial component of these transitions is the presence of citrate. It has been proposed that citrate is a crucial agent in growing tAgNPs due to its adhesion to the (111) facet of tAgNP, directing NP growth.[26] This selective force favors the planar growth of tAgNPs, or even dAgNPs under higher energy irradiation.[20] The same observation has been made for other carboxyl containing capping ligands, particularly those containing two or more carboxyl groups separated by a two carbon backbone such as succinate, citramalate, and cis-aconatate.[26] Meanwhile, the same study shows that similar molecules with carboxyl moieties spaced apart by zero, one or three carbon atoms such as oxalate, malonate, and glutarate, respectively, are reported to not be as effective at generating planar AgNPs, making citrate an essential component of this synthesis.[26]

The ability to shift the absorbance of our AgNP seeds is especially powerful for the tAgNPs, allowing the plasmonic absorbance of the particles to be “pushed” throughout the deep red and NIR region, an area with special significance in biomedical applications due to the importance of the “biological window” (see Chapter 3 for elaboration). The drastic difference in plasmon pushing effectiveness between dAgNPs and tAgNPs can be correlated to the relative changes in particle size, and the geometry of the structures.

As shown in Fig. 2.2.4, the base-tip length range of tAgNPs ranges from 175 nm to 108 nm, as citrate is increased. This difference in size is reflected in the corresponding plasmon band maxima, with the 1 and 10 mM [citrate] batches having a sizeable 600 nm gap between their plasmon bands, conveniently allowing for the easy tuning of plasmon bands within this range. Comparatively, dAgNPs undergo a much smaller shift, with sizes ranging from 63 nm to 43 nm, as [citrate] is increased, accompanied by an equally small plasmonic shift from 460 nm to 520 nm.

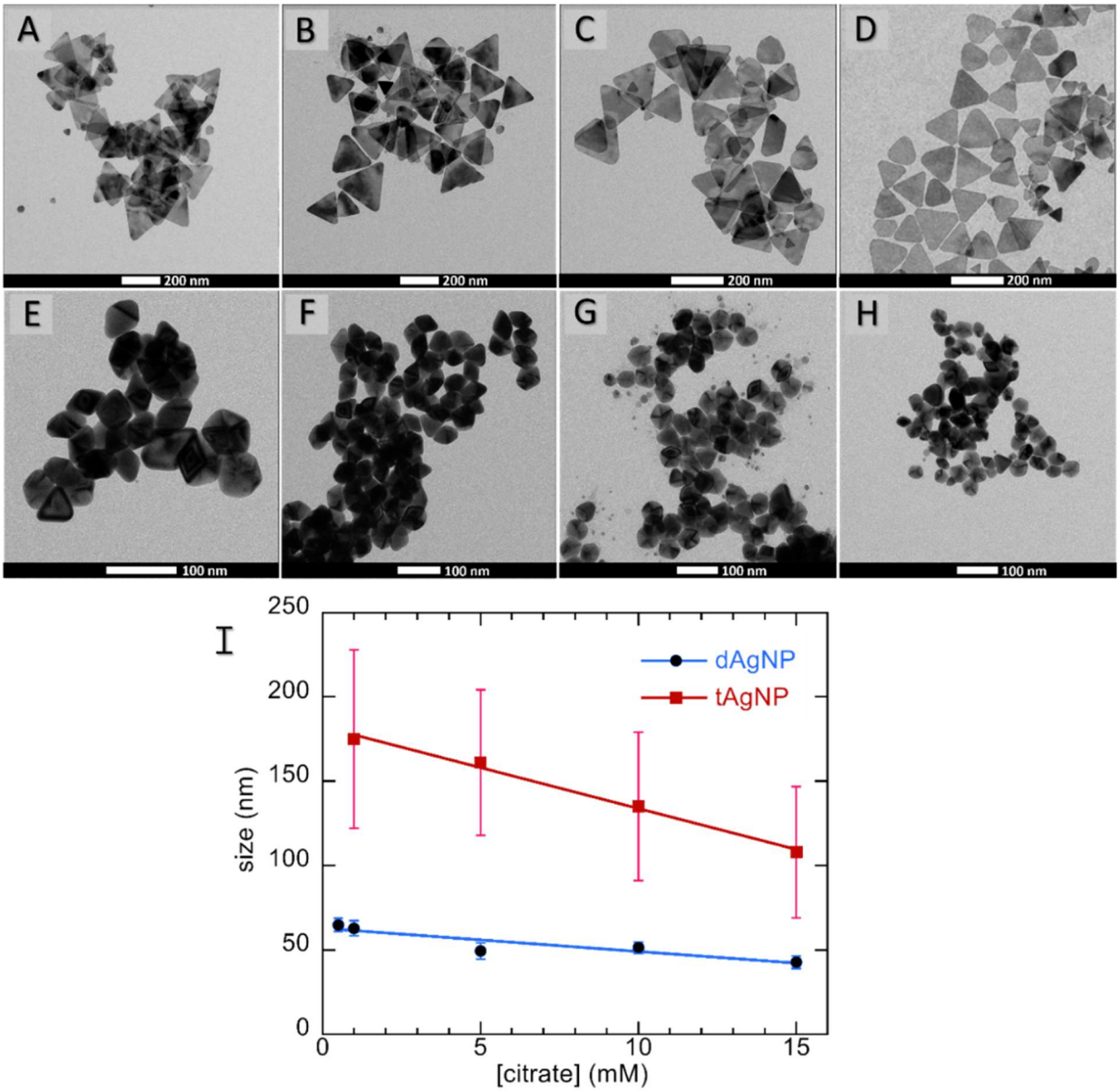

Fig. 2.2.4: TEM images of tAgNPs after 48 of illumination (A-D), and dAgNPs after 24 h of illumination (E-H), and corresponding size distributions for different [citrate] (I). Bars in the size plot represent standard deviation. Images correspond to the syntheses of AgNPs using 1 mM (A,E), 5 mM (B,F), 10 mM (C,G), and 15 mM (D, H) of citrate. White scale bars represent 200 nm for A-D, and 100 nm for E-H.[25]

Conclusion

In this work we highlight the tunable plasmonic properties of our AgNPs generated using a photochemical approach. This approach provides an aqueous, room temperature, and surfactant-free alternative for producing AgNPs with decahedral and triangular morphologies. By tuning [citrate], particle growth can be controlled, allowing for the tuning of plasmonic properties across the visible and NIR spectrum. While both dAgNPs and tAgNPs showed sensitivity to light and [citrate], tAgNPs proved to be especially responsive, allowing for the tuning of their physical and optical properties with a high degree of predictability through “plasmon pushing” and citrate dependent size control. The tunability of the absorption properties is a critical development, allowing us to effectively match the absorbance of our AgNPs to the emission of our NIR LEDs for light enhanced antibacterial experiments, as will be explored further in Chapters 3 & 4.

References

1. J. C. Scaiano, K. G. Stamplecoskie, and G. L. Hallett-Tapley , Photochemical Norrish type I reaction as a tool for metal nanoparticle synthesis: Importance of proton coupled electron transfer, *Chem. Commun.* 2012, *48*, 4798–4808
2. M. Lipson, and N. J. Turro , Picosecond investigation of the effect of solvent on the photochemistry of benzoin, *J. Photochem. Photobiol. A Chem.* 1996, *99*, 93–96
3. S. Jockusch, M. S. Landis, B. Freiermuth, and N. J. Turro , Photochemistry and Photophysics of a-Hydroxy Ketones, *Macromolecules* 2001, *34*, 1619–1626
4. D. S. Esen, N. Arsu, J. P. Da Silva, S. Jockusch, and N. J. Turro , Benzoin type photoinitiator for free radical polymerization, *J. Polym. Sci. Part A Polym. Chem.* 2013, *51*, 1865–1871
5. K. L. McGilvray, M. R. Decan, D. Wang, and J. C. Scaiano , Facile Photochemical Synthesis of Unprotected Aqueous Gold Nanoparticles, *J. Am. Chem. Soc.* 2006, *128*, 15980–15981
6. M. L. Marin, K. L. McGilvray, and J. C. Scaiano , Photochemical Strategies for the Synthesis of Gold Nanoparticles from Au(III) and Au(I) Using Photoinduced Free Radical Generation, *J. Am. Chem. Soc.* 2008, *130*, 16572–16584
7. J.C. Scaiano, P. Billone, C.M. Gonzalez, L. Maretti, M.L. Marin, K. L. McGilvray, and N. Yuan , Photochemical routes to silver and gold nanoparticles, *Pure Appl. Chem.* 2009, *81*, 635–647
8. M. Yaghmaei, and J.C. Scaiano , A simple Norrish Type II actinometer for flow photoreactions, *Photochem. Photobiol. Sci.* 2023, *22,* 1865–1874
9. O. R. Miranda, and T. S. Ahmadi , Effects of Intensity and Energy of CW UV Light on the Growth of Gold Nanorods, *J. Phys. Chem. B* 2005, *109*, 15724–15734
10. K. G. Stamplecoskie, and J. C. Scaiano , Kinetics of the Formation of Silver Dimers: Early Stages in the Formation of Silver Nanoparticles, *J. Am. Chem. Soc.* 2011, *133*, 3913–3920
11. D. Cambié, C. Bottecchia, N. J. W. Straathof, V. Hessel, and T. Noël , Applications of Continuous-Flow Photochemistry in Organic Synthesis, Material Science, and Water Treatment, *Chem. Rev.* 2016, *116*, 10276–10341
12. T. H. Rehm , Flow Photochemistry as a Tool in Organic Synthesis, *Chem. Eur. J.* 2020, *26*, 16952–16974
13. K. G. Stamplecoskie, and J. C. Scaiano , Light Emitting Diode Irradiation Can Control the Morphology and Optical Properties of Silver Nanoparticles, *J. Am. Chem. Soc.* 2010, *132*, 1825–1827
14. X. C. Jiang, C. Y. Chen, W. M. Chen, and A. B. Yu , Role of Citric Acid in the Formation of Silver Nanoplates through a Synergistic Reduction Approach, *Langmuir* 2010, *26*, 4400–4408
15. J. Turkevich, P. C. Stevenson, and J. Hillier , A Study in the Nucleation and Growth Processes in the Synthesis of Colloidal Gold, *Discuss. Faraday Soc.* 1951, *11*, 55–75

16. F. R. Cruickshank, and S. W. Benson, Carbon-hydrogen bond dissociation energy in methanol, *J. Phys. Chem.* 1969, *73*, 733–737

17. J. Belloni , The role of silver clusters in photography, *Comptes Rendus Physique* 2002, *3*, 381–390

18. F. D. Lewis, R. J. Lauterback, H. G. Heine, W. Hartmann, and H. Rudolph , Photochemical a-cleavage of Benzoin Derivatives. Polar Transition States for Free Radical Formation, *J. Am. Chem. Soc.* 1975, *97*, 1519–1525

19. J. G. Mahy, M. Kiendrebeogo, A. Farcy, and P. Drogui , Enhanced Decomposition of H_2O_2 Using Metallic Silver Nanoparticles under UV/Visible Light for the Removal of p-Nitrophenol from Water, *Catalysts* 2023, *13*, 842

20. C. R. Bourgonje, D. R. C. da Silva, E. McIlroy, N. D. Calvert, A. J. Shuhendler, and J. C. Scaiano , Silver Nanoparticles with exceptional near-infrared absorbance for photo-enhanced antimicrobial applications, *J. Mat. Chem. B* 2023, *11,* 6114-6122

21. X. Wang, and Y. Cao , Characterizations of absorption, scattering, and transmission of typical nanoparticles and their suspensions, *J. Ind. Eng. Chem.* 2020, *82*, 324-332

22. J. Lermé, Size evolution of the surface plasmon resonance damping in silver nanoparticles: Confinement and dielectric effects, *J. Phys. Chem. C* 2011, *115*(29), 14098-14110

23. F. Y. Alzoubi, A. A. Ahmad, I. A. Aljarrah, A. B. Migdadi, and Q. M. Al-Bataineh , Localize surface plasmon resonance of silver nanoparticles using Mie theory, *J. Mater. Sci.*: *Mater. Electron.* 2023 *34*, 2128

24. J. Otsuki, K. Sugawa, and S. Jin , Plasmonic triangular nanoprism sensors, *Mater. Adv.* 2021, *2*(1), 32-46

25. C. Frank, C. R. Bourgonje, M. Yaghmaei, and J. C. Scaiano , A color-coordinated approach to the flow synthesis of silver nanoparticles with custom morphologies, *Nanoscale Adv.* 2025, *7*(4), 1163-1172

26. Q. Zhang, N. Li, J. Goebl, Z. Lu, and Y. Yin , A Systematic Study of the Synthesis of Silver Nanoplates: Is Citrate a “Magic” Reagent?, *J. Am. Chem. Soc.* 2011, *133*(46), 18931-18939

Chapter 3 – Light Activated Antimicrobial Silver Nanoparticles

Background

Following our exploration of light-controlled AgNP synthesis, we sought to take advantage of the tunable plasmonic properties of our triangular and decahedral AgNPs. Given their important role as antimicrobial agents, the obvious first step was to investigate how the activation of the particles with complimentary LED illumination could affect their antimicrobial properties. We found that by irradiating our AgNPs with LEDs closely matching their plasmonic absorbance, we could effectively irradicate *E. Coli* and *S. Aureus* cultures within min. This remarkable interaction between AgNPs and light is crucial to maximizing the potential of the particles. Although we did not explore their use in health applications, the comparably low toxicity of our AgNPs towards human cell lines gives us hope that light activation may be the key to unlocking the "silver bullet" potential of AgNPs as therapeutic agents with high toxicity towards infectious agents, and low toxicity towards mammals. In this published work we attribute the increased antibacterial activity to the release of reactive oxygen and nitrogen species (ROS & RNS, respectively), as well as the conversion of light energy into heat by the particles.

While I am 1st author on this paper, this paper benefited greatly from my collaborating authors. Daliane Regis Correa da Silva, a fellow PhD student in the Scaiano Lab played a major role in much of the bacterial work, along with our undergraduate student Ella McIlroy. Nick Calvert from the lab of Dr. Adam Shuhendler performed the human cell line work, including the flow cytometry and nanoparticle uptake experiments.

3.1: Published work: Silver nanoparticles with exceptional near-infrared absorbance for photoenhanced antimicrobial applications

C. R. Bourgonje, D. R. C. da Silva, E. McIlroy, N. D. Calvert, A. J. Shuhendler, J. C. Scaiano. *Journal of Materials Chemistry B*, 2023, 11 (26), 6114-6122

Abstract

In this work, we outline a simple method for synthesizing decahedral and triangular silver nanoparticles using light to tune particle shape and spectral characteristics. Notably, we were able to generate triangular silver nanoparticles with exceptional absorbance in the near-infrared (NIR) region, with high spectral overlap with the biological window, making them particularly promising for biological applications. We further demonstrate that under complementary LED illumination, these excitable plasmonic particles display exceptional antibacterial properties, several orders of magnitude more potent than similar particles under dark conditions or under illumination that does not match particle absorbance. This work demonstrates the powerful effects that LED lights can have on the antibacterial activity of AgNPs, providing an inexpensive and easily implemented route to unlocking the full potential of AgNPs in photobiological applications.

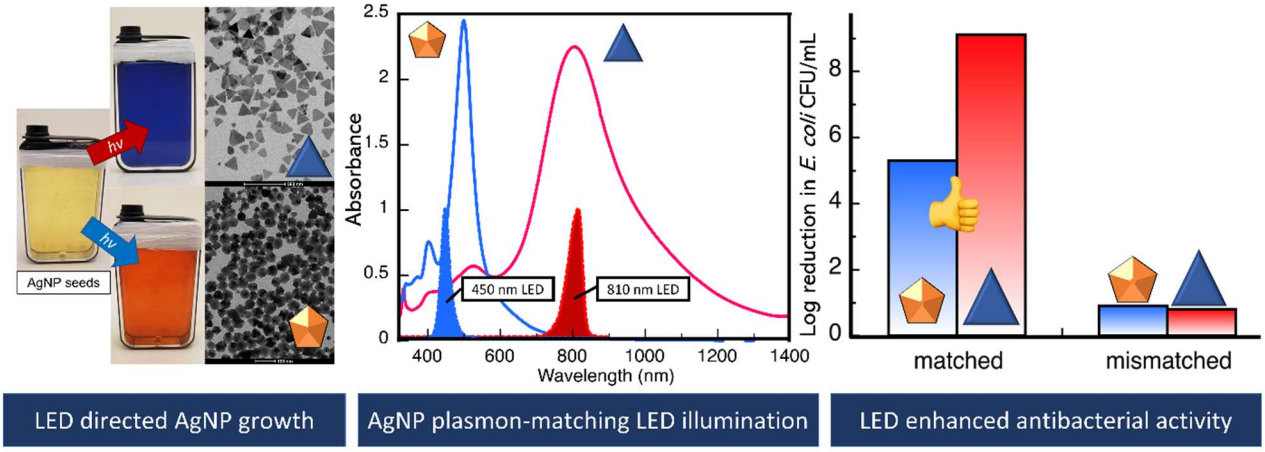

Introduction

Since their mainstream inception in the 20th century, silver nanoparticles (AgNPs) have been a hot topic across science, engineering, and commerce.[1] Today, AgNPs represent the largest use of nanomaterials in consumer goods, in part due to their use as antibacterial agents.[2,3] The broad-spectrum antibiotic properties of AgNPs, which are even effective against antibiotic-resistant bacteria, continue to be an important area of development for biomedical materials.[3,4]

AgNPs display very interesting optical properties due to the phenomenon of localized surface plasmon resonance (LSPR).[3,5,6] This remarkable feature has been widely explored for a variety of metal nanoparticles, giving these plasmonic materials exceptionally strong visible absorbance in regions known as plasmon bands.[5] When excited, plasmonic nanoparticles can experience a variety of effects such as hot electron generation, reactive oxygen species (ROS) generation, and plasmonic super heating, among others.[7,8] It is surprising that within the vast number of studies on the antibacterial effects of silver nanoparticles, very few have investigated the use of AgNPs as phototherapeutic agents (PTAs) or for photodisinfection.

PTAs are a class of materials that can interact with light to perform biological functions in the field of photodynamic therapy (PDT). These materials have many advantages over standard drugs due to their light-activated functionalities. For example, light-dependent treatments can be easily targeted to afflicted areas by directing the light source and controlling the exposure time, reducing undesired off-target reactions compared to nontargeted approaches,[7,9] thus providing spatial and temporal control.[10]

One of the challenges when using light-responsive materials in biological and medical applications is finding materials that are able to absorb light and be chemically active within the biological window.[11] This region of the visible and near-infrared (NIR) spectra between 650 and 1350 nm is key to designing materials for biological applications as it represents the wavelengths which can best penetrate tissues.[12] This is because within this spectral region the scattering of tissues is greatly reduced compared to at lower wavelengths, while the competitive absorbance of biological features such as hemoglobin, melanin, fat, and water are relatively low.[8,9,11] While many materials and organic compounds can be activated by high-energy visible and UV light, the high light attenuation of these wavelengths in biological settings limits their efficacy as PTAs in medical and biological settings.[13] It is therefore crucial to design photoactive materials for biomedical purposes with strong absorbance and inducible chemical

activity in the NIR region, an application for which AgNPs are promising candidates, as demonstrated in this work.

The first step in realizing the potential of AgNPs as PTAs is generating AgNPs with morphologies that display strong NIR plasmon bands. This in itself is somewhat of a challenge unless the use of surfactants (such as CTAB)[14] or polymer coatings[15] is employed; however, these can hinder the biocompatibility of the particles. To get around this obstacle, our group[16] and others[17] have demonstrated the use of light to grow nanoparticles with specific light-dependent structures and properties, without the need for bulky surfactants.

In a recent contribution, Zhou[12] tested triangular and spherical silver structures irradiated with 808 nm laser excitation as antibacterials for *E. coli* and *S. aureus*. The results showed a far better antibacterial performance for triangular plates, illustrating the advantages of using the NIR biological window for AgNP excitation. We wondered to what extent the effect was entirely due to the use of triangular plates or the matching of particle absorbance and irradiation wavelength and if the same results could be achieved using LED irradiation. In addition to being more affordable and accessible, LEDs can cover larger areas of effect than lasers and are less damaging to skin, leading to reduced negative effects when used in PDT.[18]

In this work, using a modified version of our previous LED-guided AgNP synthesis, we generate citrate-capped triangular AgNPs with high NIR absorbance, along with blue absorbing decahedral dAgNPs to assess their potential as LED-activated PTAs.[16] Our studies with NIR- and blue-light-absorbing particles and complementary LED irradiation at 810 nm and 450 nm show that antibacterial performance can be dramatically increased by matching absorbance and irradiation wavelength.

By using LEDs with high spectral overlap with the plasmonic absorbance of our AgNPs, we can trigger remarkable photoinduced toxic effects on bacterial cultures, even with Ag concentrations that are nontoxic under dark conditions. These findings showcase the exceptional, yet often-overlooked, photoinduced biological activity of AgNPs under LED irradiation, making a strong case for the use of AgNPs as photodisinfectants and potentially PTAs.

Experimental section

The AgNP synthesis consists of two light-mediated steps we reported previously (see Chapter 2).[16] The first step of the synthesis is the reduction of Ag^+ ions by photogenerated ketyl radicals. The resulting Ag^0 agglomerates[19] generate small spherical particles which act as the AgNP seeds and possess strong absorbance around 400 nm (Fig. 3.1.S1).[16]

The second stage of the synthesis is the light-guided growth of the AgNPs around the seeds. This process is carried out using either a blue (450 nm) or red (635 nm) Luzchem well plate illuminator (WPI), consisting of 24 individual LEDs (Fig. 3.1.S2).

Using WPIs to irradiate the seed solutions, batches of AgNPs from 2 mL to 200 mL could be synthesized, depending on the reaction vessels used. For the sake of this work, all particles for antibacterial work were made in 200 mL batches.

Materials

Silver nitrate (ACS reagent, 99.9+%) was purchased from Alfa Aesar. Trisodium citrate dihydrate (99%) was purchased from Fisher Scientific. Irgacure-2959 (I-2959) was a gift from BASF Chemicals. Luria–Bertani (LB) broth was purchased from Sigma Aldrich, and Mueller Hinton (MH) agar was purchased from BD Life Sciences. Dulbecco's modified Eagle's medium (DMEM), dextrose, fetal bovine serum (FBS), penicillin–streptomycin, tripsin–EDTA, and the LIVE/DEAD™ viability/cytotoxicity kit for mammalian cells were acquired from ThermoFisher Scientific. All water used was ultrapure, obtained by purification of deionized water using a Thermo Scientific™ Barnstead™ GenPure™ water purification system (a conductivity of 18 MΩ cm^{-1}).

Seed synthesis

In a typical synthesis, an aqueous solution of 0.2 mM $AgNO_3$, 0.2 mM I-2959, and 10 mM trisodium citrate is deaerated for 30 min under a steady flow of argon under dark conditions. The solution is then irradiated in a UV photoreactor under 8 UVA bulbs for 15 min, yielding a yellow suspension of AgNP seeds (Fig. 3.1.S1, and Fig. 3.1.S2a).

AgNP growth

To grow the seeds into triangular or decahedral AgNPs, the seed suspensions are first exposed to air and left in the dark for 30 min to reoxygenate the solution. After this, the suspensions are irradiated using either a blue (450 nm, for dAgNPs) or red (635 nm, for tAgNPs) WPI under gentle shaking for 24 and 48 h, respectively. The resulting suspensions are bright orange for the dAgNPs and deep blue for the tAgNPs (Fig. 3.1.S2). The particles are then washed *via* centrifugation at 10 000 rpm for 60 min and resuspension in ultrapure water, repeated 3 times before storage in the dark.

Antibacterial assays

Prior to antibacterial work, Ag levels in acid-digested aliquots from AgNP stocks were determined using ICP-OES; then batches were diluted to 40 ppm.

Bacterial strains and storage conditions

The experiments were performed using *Escherichia coli* CF073 and *Staphylococcus aureus* ATCC25923. Stock cultures were maintained in Tryptone soy broth (TSB) and stored at −80 °C in 10% glycerol.

Minimum inhibitory concentration

The minimum inhibitory concentration (MIC) was determined by the broth microdilution method. The initial bacterial inoculum was prepared at a concentration of 1.6×10^8 colony forming units (CFU) per mL (OD_{600} = 0.2) in 5% LB broth. Using a 96-well plate, 100 µL of the bacterial suspension and 100 µL of AgNP solutions at different concentrations were mixed. All measurements were run in triplicate. The plates were incubated in the dark for up to 16 h at 37 °C. After incubation, the drop plate method was used to count viable cells. In brief, aliquots of each sample were properly diluted in phosphate-buffered saline (PBS) and seeded in MH agar plates. Colony forming units (CFU) were counted from the agar plates after 14 h of incubation at 37 °C.

Antibacterial activity

The antibacterial activity of AgNPs was tested against *E. coli* and *S. aureus*. Using a glass vial, 500 µL of the bacterial suspension at 1.6×10^8 CFU per mL (OD_{600} = 0.2) in 5% LB was mixed with 500 µL of AgNP solutions. The solutions were irradiated for up to 15 min using an LED illuminator (LEDi, Luzchem Research Inc.) at 810 nm (0.99 W cm^{-2}) or 450 nm (0.93 W cm^{-2}).

Control experiments were run under the same conditions in the dark. After treatment, cells were immediately diluted in sterile PBS and plated using the drop plate method. Viable cells were counted using the drop plate method. Antibacterial activity was expressed as log reduction using the following equation:

$$\log \text{reduction} = \log_{10}\left(\frac{\text{viable cells before treatment(CFU per mL)}}{\text{viable cells after treatment(CFU per mL)}}\right)$$

Antibacterial activity under an anaerobic atmosphere

The experiments under an anaerobic atmosphere were done similar to the antibacterial tests previously described. First, 500 µL of *E. coli* suspensions at 1.6×10^8 CFU per mL (OD_{600} = 0.2) in 5% LB and AgNP solutions at 20 ppm in water were purged with N_2 for 10 min prior to the experiments. After purging, the bacterial and nanoparticle solutions were mixed and irradiated for 1 and 3 min using the complementary lights: 810 nm for tAgNPs and 450 nm for dAgNPs. During the irradiation, vials had nitrogen-filled balloons attached to maintain the anaerobic atmosphere. After irradiation, samples were immediately diluted and plated using the drop plate method, and the results were expressed as log reduction.

Sample preparation for SEM images of E. coli

After treatment with NPs, the *E. coli* solutions were centrifuged at 3500 rpm for 5 min and resuspended with PBS, the washing process was done 2 more times, and solutions were finally collected with PBS. *E. coli* suspensions were added dropwise to the a clean and dry silicon wafer and dried under air. Samples were then incubated in 3% glutaraldehyde for 16 h at 4 °C. After incubation, they were washed in water and dehydrated in a graded series of aqueous ethanol solutions (30–100%). Following dehydration, samples were critical point-dried using liquid CO_2 and coated with 7 nm of gold.

Reactive oxygen/nitrogen species quantification

To detect ROS/RNS production by tAgNPs, a modified 2′,7′-dichlorofluorescein (DCF) assay was adapted from the popular biological assay used to detect ROS in cells.[20] In this modified approach, 2′,7′-dichlorodihydrofluorescein diacetate (H_2DCF-DA) was chemically deacetylated, yielding a nonfluorescent probe, H_2DCF, which reacts with reactive oxygen and nitrogen species (ROS, RNS) to produce a fluorescent probe, DCF.

In a standard assay, a 2 mL solution of H_2DCF and 10 ppm tAgNPs is prepared in a four-sided quartz cuvette and stirred for 20 min under the dark to allow the dye to adsorb on the AgNPs. The sample was then irradiated using a 740 nm LEDi photoreactor by Luzchem, with fluorescence measurements being taken every 5–10 min. This was repeated under dark conditions to compare ROS/RNS generation under light and dark conditions. The DCF assay was repeated in solutions without tAgNPs as a control. It should be noted that there is a baseline level of fluorescent product at the beginning of the reaction – we attribute this to DCF which is inadvertently formed during the preparation of H_2DCF.Cytotoxicity evaluation

tAgNP cytotoxicity was evaluated in human epithelial fibrosarcoma cells (HT-1080). The HT-1080 cells were thawed from frozen and grown to 80% confluency in DMEM supplemented with 10% FBS and 1% penicillin/streptomycin (P/S). Cells were passaged 3 times before being grown to 70% confluency in 6-well plates. At confluency, plated cells were incubated with a 5% dextrose in water (D5W) solution with or without 10 ppm of AgNPs under cell culture conditions (37 °C, 5% CO_2, humidified) for 15 min with or without constant irradiation at 810 nm (0.99 W cm^{-2}). Following incubation, cells were washed with PBS, lifted from the plate with trypsin–EDTA, centrifuged at 400 × *g* (5 min, 4 °C), aspirated, and then resuspended in a 1 mL PBS solution containing 0.2 µM calcein-acetoxymethyl ester (fluorescently staining live cells green) and 16 µM ethidium homodimer-1 (fluorescently staining dead cells red). Live and dead cell populations were counted through flow cytometry using a 488 nm excitation with a 525 nm/40 nm bandpass filter for calcein-acetoxymethyl ester (live cells, green) and a 620 nm/20 nm bandpass filter for ethidium homodimer-1 (dead cells, red). After performing, the viable cell population for each condition was determined by comparing the total number of singly stained, calcein-AM-positive cell counts to the combined total of cells that were singly stained as positive for live or dead using Kaluza analysis software (Beckman–Coulter). Following flow cytometry, cells were replated in supplemented DMEM to evaluate continual proliferation.

Statistical analysis

Statistical analysis was done with R studio (version 1.4.1717). The comparison of multiple groups was done by one-way analysis of variance (ANOVA with Tukey's *Post Hoc* test); *p*-values less than 0.05 were considered statistically significant.

Instrumentation

UV-Vis-NIR absorbance measurements were taken using a Cary 7000 Universal Measurement Spectrophotometer. ICP-OES measurements were taken using an Agilent 5110 VDV ICP-OES Spectrometer. X-ray diffraction (XRD) was done using a Bruker D8 advanced instrument, equipped with a Cu Kα sealed-tube source (λ = 1.54184 Å) powered at 40 kV and 25 mA (1 kW). For the XRD measurements, drops of aqueous solutions of the nanoparticles were added on glass cover slips and let dry at room temperature. Fluorescence measurements were taken using a Photon Technology PTI LS-100 steady-state fluorometer. TEM images were collected using a FEI Tecnai G2 spirit Twin TEM, and average particle sizes were estimated from the measurements of 200 individual particles per sample. SEM images were acquired using a JSM-7500F field emission scanning electron microscope from JEOL Ltd. Bacterial initial concentrations were measured using a SpectraMax M5 microplate reader (Molecular Devices™). Flow cytometry was performed using a Beckman–Coulter Gallios Flow Cytometer. Confocal microscopy was performed using a Nikon A1 confocal microscope fit with a flow cell, adapted from a previous work to monitor AgNPs on a glass slide using H_2DCF as a probe.[21]

Results and discussion

Light-generated AgNP properties

(See Chapter 2 for more detail on AgNP synthesis)

In this work, we used light to synthesize AgNPs with desired shapes and optical properties based on a method previously published by our group.[16] Using a modified version of this procedure, we were able to generate AgNPs with strong absorbance bands in the visible/NIR regions, as shown in Fig. 3.1.1. This change in absorbance is directly related to the size and shape of the nanoparticles generated, with blue light yielding decahedral nanoparticles with absorbance around 500 nm and red/NIR light yielding triangles with absorbance around 800 nm (Fig. 3.1.1). As shown in Fig. 3.1.1, the growth of the AgNPs is substantially affected by the use of light, a phenomenon that can be utilized to tailor the structural and optical properties of AgNPs for target applications.

This light-induced growth has been observed before,[22,23] though the mechanism is rarely debated. Analysis of the UV-Vis-NIR absorption of the AgNPs as they grow under illumination (Fig. 2.2.3) reveals that particles begin their growth at a wavelength near to the wavelength of the incident light, but as time passes and the particles grow, they begin to shift in wavelength.

Our working theory for this plasmonic shift is that the formation of short-lived Ag clusters creates photocatalytically active nanostructures which can absorb these wavelengths of light. When excited, these clusters reduce silver ions, growing the cluster until it becomes a full-sized particle.[23] As the particle grows, the absorbance changes further, yielding a particle with absorbance red-shifted from the incident light (Fig. 2.2.3).

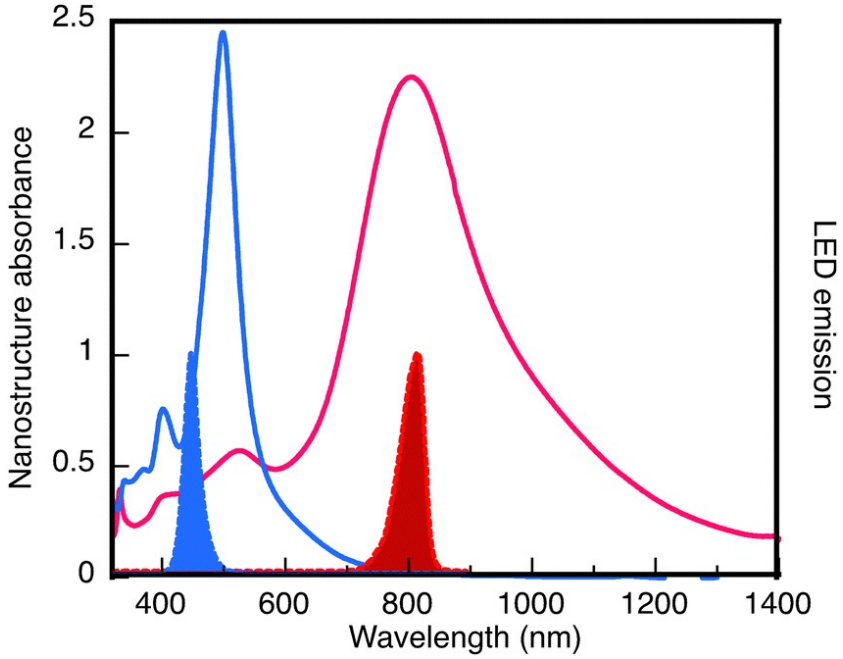

Fig. 3.1.1: Left axis: UV-Vis absorption spectrum of aqueous 20 ppm suspensions of dAgNPs (blue line) and tAgNPs (red line) synthesized using 10 mM citrate growth solutions following purification. Right axis: Normalized emission spectra of the 450 nm and 810 nm LEDs (blue-shaded and red-shaded spectra, respectively) used to irradiate the AgNPs for antibacterial trials.

It is worth noting that in particular for NIR-absorbing triangles (tAgNP), reported spectra frequently stop at $\lambda \leq 900$ nm, a common limitation with many commercial spectrometers. As Fig. 3.1.1 shows, there is important spectral information beyond 900 nm that is often missed.[24] Our spectra are limited to 1400 nm simply because the strong NIR absorption of water prevents measurements in the region.

As seen in Fig. 3.1.2, when grown under blue light, the AgNP seeds grow into decahedra averaging 53 ± 5 nm in width, while red light yields triangles averaging 122 ± 39 nm in base-tip length. These particles have distinct spectral properties, with the dAgNPs featuring sharp absorbance bands around 500 nm, while the tAgNPs display broad NIR absorbance bands around 800 nm (Fig. 3.1.1).

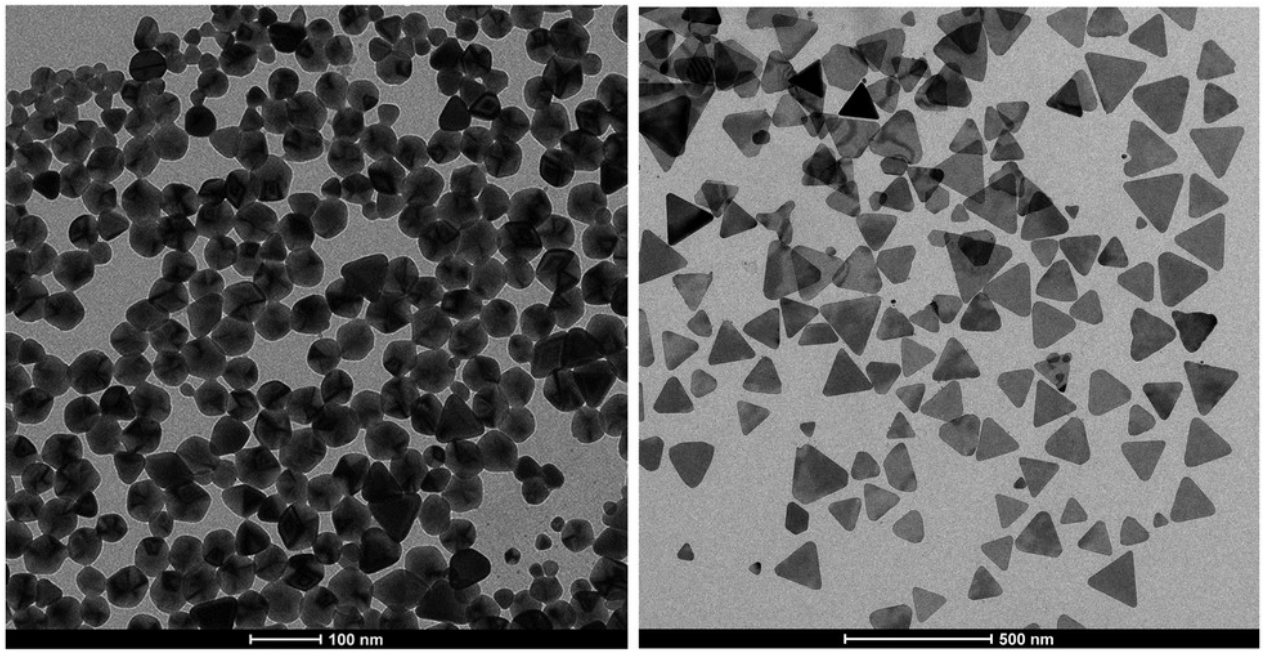

Fig. 3.1.2: TEM micrographs of dAgNPs (left) and tAgNPs (right) used for antibacterial assays.

Crystalline structures of the AgNPs were investigated using XRD; the diffraction peaks at 2θ values of 38.2, 44.2, 64.5, and 77.4° correspond to Bragg's reflection planes (111), (200), (220), and (311) of faced-centred cubic (fcc) metallic silver (JCPDS file no. 04-07883) (Fig. 3.1.S3). The intense peak for the (111) reflection is characteristic of face-centered cubic silver structures,[25] and it is clearly observed in both AgNP structures. In fact, in the tAgNPs, there is complete dominance of the (111) facet, with only one peak visible at 38.2°. Such a pattern is common in triangular and nanoplates structures[25,26] since these forms are a result of a highly selective lateral growth, which occurs due to the higher thermodynamic stability of the (111) facet.[27,28] Both structures have *d*-spacings of 2.36 Å, which corresponds to the (111) planes in fcc lattice, indicating no changes in the crystalline arrangement to hpc lattice, as previously reported for similar structures.[28] We also calculated the crystal sizes using the Scherrer equation; both nanostructures have similar crystalline sizes, 20.8 and 20.9 nm for dAgNPs and tAgNPs, respectively, concluding that the structures are not single crystals.

In many papers producing AgNPs with red-shifted absorbance, surfactants and polymers such as CTAB,[29] PVP,[30] or PEG[31] are typically employed; however, in our method, triangles are generated using trisodium citrate as the only surface stabilization agent.

Remarkably, by using a citrate concentration of 10 mM for the synthesis, we were able to nearly perfectly match our AgNP plasmonic absorbances to our blue (450 nm) and NIR (810 nm) LEDs (Fig. 3.1.1).

Antibacterial activity

To compare the antibacterial activity of the particles and demonstrate their potent photoinduced antibacterial effects, both the triangular and decahedral AgNPs were mixed with *E. coli* or *S. aureus* cultures at concentrations ranging from 5 to 20 ppm and irradiated with either a blue or NIR LED light for up to 15 min. Within 15 min of irradiation, the tAgNPs displayed exceptional antibacterial activity, with antibacterial activity reaching 9 log units – effectively preventing any bacteria from growing at all on our agar plates at Ag concentrations above 10 ppm (Fig. 3.1.S4 & 3.1.S5). Remarkably, even at the less toxic (under dark conditions) concentration of 5 ppm, both types of particles displayed 4 log units of killing within 15 min when irradiated (Fig. 3.1.3). Higher concentrations of tAgNPs at 10 and 20 ppm achieved 9 log units of killing within 10 and 1 min of irradiation, respectively. To ensure that the toxicity was not from the LED irradiation alone, bacteria were also irradiated in the absence of AgNPs (Fig. 3.1.6). Irradiation of the bacterial cultures with LEDs induced far less antibacterial activity ($p < 0.001$), showing one log unit reduction in bacterial viability within the first 10 min, increasing to 3 log units by 15 min of irradiation. Meanwhile, the bacteria incubated under dark conditions with 20 ppm tAgNPs experienced a 1.5 log reduction in population within 15 min, while the 5 ppm tAgNP mixture induced no noticeable toxicity at all. These results indicate a remarkably potent synergistic antibacterial effect when combining the AgNPs with matching LED irradiation, far more potent than the standard approach of using AgNPs under ambient or dark conditions.

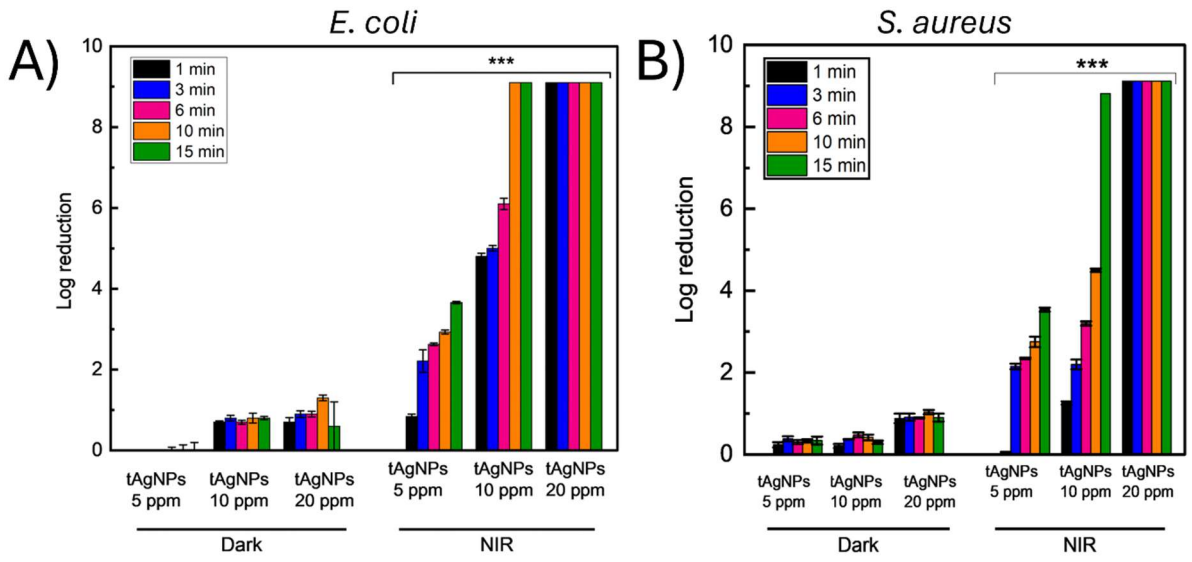

Fig. 3.1.3: Antibacterial activity of tAgNPs against *E. coli* and *S. aureus* under the dark and NIR irradiation. *E. coli* and *S. aureus* cultures were treated from 1 to 15 min, with tAgNPs with concentrations of 5, 10, and 20 ppm. Bacterial growth was determined using the plate counting method. Error bars represent standard deviations of the log reduction (***$p < 0.001$).

Under relatively short irradiation periods of 1 min, Fig. 3.1.4 shows that tAgNPs under 810 nm irradiation had the highest antibacterial effect ($p < 0.001$), achieving 9 log unit reductions, while the dAgNPs under 450 nm irradiation achieved 5 log unit reductions using 20 ppm AgNPs. Under irradiation with noncomplementary light sources (450 nm for tAgNPs and 810 nm for dAgNPs), only 1 log reduction is achieved, performing similarly to AgNPs under dark conditions ($p > 0.05$). These results clearly show that achieving highly potent toxicity depends on the absorption of photons by the AgNP plasmon bands, inducing a process which can increase AgNP antibacterial activity by several log units, representing an extraordinary enhancement.

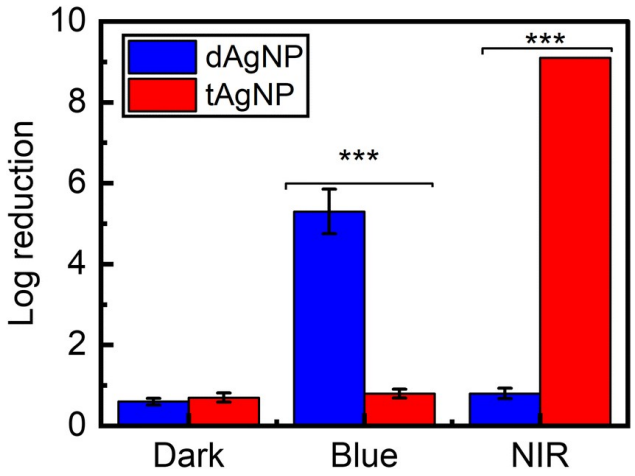

Fig. 3.1.4: Log reductions of *E. coli* CFU following 1 min of treatment with 20 ppm decahedral (blue) or triangular AgNPs (red) under dark conditions, blue irradiation, or NIR irradiation. Error bars represent standard deviations of the log reduction (*$p < 0.05$, **$p < 0.01$, ***$p < 0.001$).

SEM images of the treated bacteria illustrate the effect of the interaction between the AgNPs and the microbial cells. Treated cells present *E. coli* characteristic rod-like shape and smooth surfaces (Fig. 3.1.5a). In comparison, AgNP-treated cells exhibited shrinkage and an irregular shape (Fig. 3.1.5b and c). It is also possible to see an extracellular net-like matrix around the cells, which indicates extrusion of intracellular material and consequently cell death.

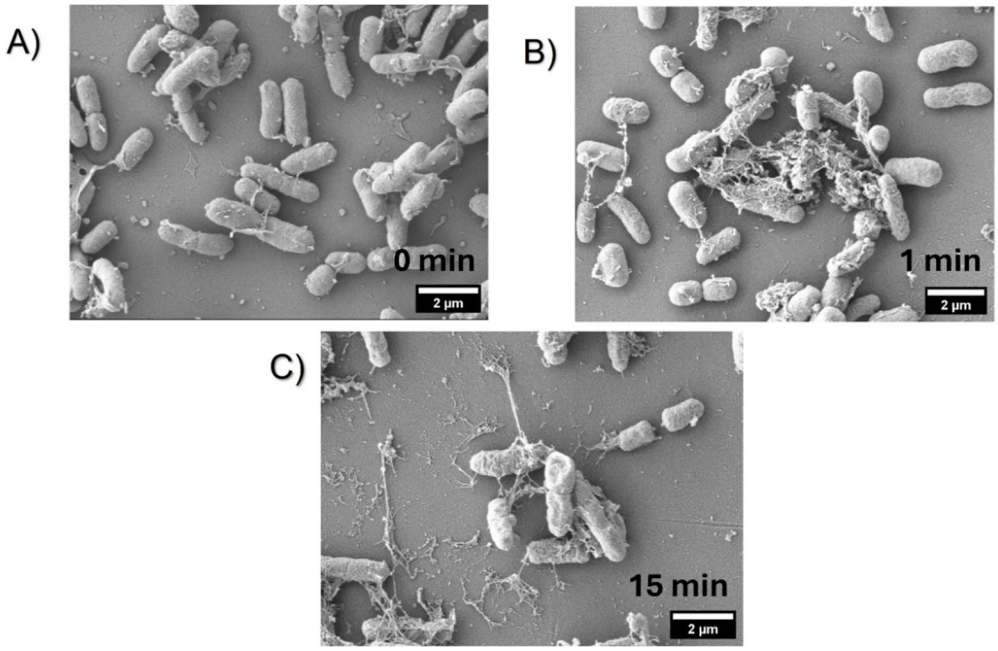

Fig. 3.1.5: SEM images of E. coli (10^8 CFU/mL) deposited from LB broth cultures before AgNP treatment(A), and treated with 20 ppm of tAgNPs and NIR irradiation (810 nm) for 1 min (B) and for 15 min (C).

Mechanism

The toxicity of the AgNPs under irradiation can be attributed to several different factors working together to create a synergistic antibacterial effect. We believe that the antibacterial activity could be attributed to either ROS generation or plasmonic heating.[8] To visualize the generation of ROS, a fluorescent probe, H_2DCF, was chosen.[32] This dye is first received in its acetylated form, initially nonfluorescent. Upon cleavage of these groups, the dye can efficiently react with ROS as well as reactive nitrogen species (RNS) non-specifically, resulting in the formation of an emissive oxidized form of the dye.[20,32] Thus, if ROS/RNS generation is contributing to the toxicity of the NPs under irradiation, it is expected that an increase in emission would be seen from the probe.

When exposed to AgNPs alone, our probe generates no additional emission, suggesting that little to no ROS/RNS are being generated under dark conditions (Fig. 3.1.6 and Fig. 3.1.S8). Under irradiation however, a clear increase in emission is observed, supporting the notion that ROS/RNS generation contributes to the enhanced antibacterial activity of the AgNPs. Control experiments using only H_2DCF without tAgNPs show that under irradiation, there was no increase in emission, suggesting that the tAgNPs are responsible for the increase in emission (Fig. 3.1.S8).

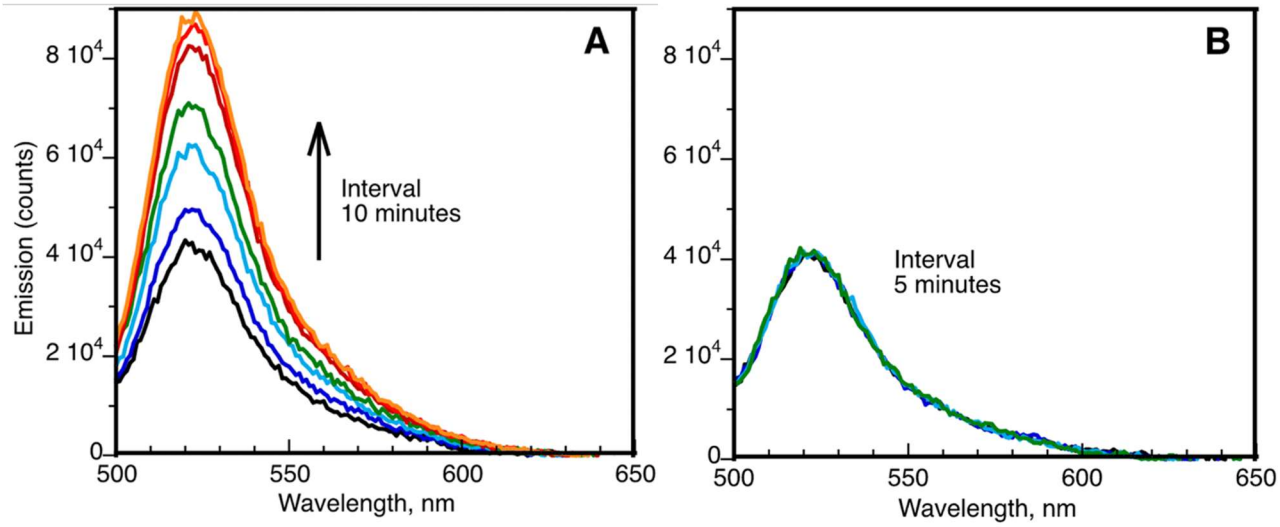

Fig. 3.1.6: Fluorescence intensity of H_2DCF under 480 nm excitation, when mixed with 10 ppm tAgNPs under 740 nm LED illumination (A) and under dark conditions (B). Measurements were taken every 10 min for 1 h. Black trace represents t=0.

To confirm this assertion, confocal microscopy was used to image the localization of ROS generation (Fig. 3.1.S9). In this experiment, AgNPs were fixed to a glass microscope slide and monitored under three different conditions in the presence of H_2DCF. First, the AgNP-treated region of the slide [appearing as a dark streak in Fig. 3.1.S9(a)] was monitored under 488 nm excitation – which we expect to excite the dye if any DCF is produced, providing insight into where ROS are being generated. Next, the sample was excited with a 640 nm laser. This laser is more red-shifted and thus expected to excite the AgNPs but not the dye, yielding no observable emission. Finally, the sample was excited with both lasers, resulting in particle activation and dye excitation, resulting in much higher levels of emission as DCF is produced. Under the dual-laser excitation, not only is there more emission but also the emission is largely collocated with the dark patch of AgNPs, suggesting that it is the NPs directly producing the ROS, rather than mobile Ag clusters or Ag^+. This is supported by previous work by Alarcon *et al.* who demonstrated that AgNP toxicity surpasses that of Ag^+ ions at equivalent levels, suggesting that the mechanism of killing is not simply due to Ag^+ leeching from particles.[33] To further investigate the role of Ag^+ in the amplified antibacterial effects, 10 ppm samples were left under complimentary LEDi irradiation for 6 h to monitor the leeching of Ag from the particles. Interestingly, while tAgNPs yield a slightly higher amount of Ag in their supernatant following the experiment, an opposite effect was seen for dAgNPs, with Ag ppm decreasing from 0.21 ppm to 0.16 ppm, while tAgNPs went from 0.14 to 0.21, suggesting that some low levels of Ag leeching may occur; however, at such low concentrations, it is unlikely to play a major role in the light-induced effects on toxicity (Table 3.1.S1).[34]

In order to differentiate between the antibacterial effects of ROS/RNS and heat generation in this system, it was necessary to repeat the antibacterial experiments in the absence of oxygen to prevent ROS generation (Fig. 3.1.7). When treated in the absence of dissolved and atmospheric O_2 the antibacterial effect of the Ag nanostructures greatly decreased, dropping from 5 log units of killing within 3 min of complementary irradiation to under 2 log units for both dAgNPs and tAgNPs (Fig. 3.1.7). Furthermore, the AgNPs exhibited higher toxicity in the dark in the presence of oxygen than they did under irradiation in an oxygen-free environment, strongly suggesting that oxygen is a key component to their killing mechanism. The decrease in antibacterial activity indicates the importance of O_2 accepting the photogenerated electron and generating of O_2-centered radicals.[35] Despite the large drop in toxicity however, Fig. 3.1.7 also clearly indicates that in the absence of oxygen, there is still a light-induced effect on the bacteria, demonstrating that there are other pathways involved on the bactericidal performance, such as the oxidative potential of photogenerated h^+ and the photothermal effect. [36]

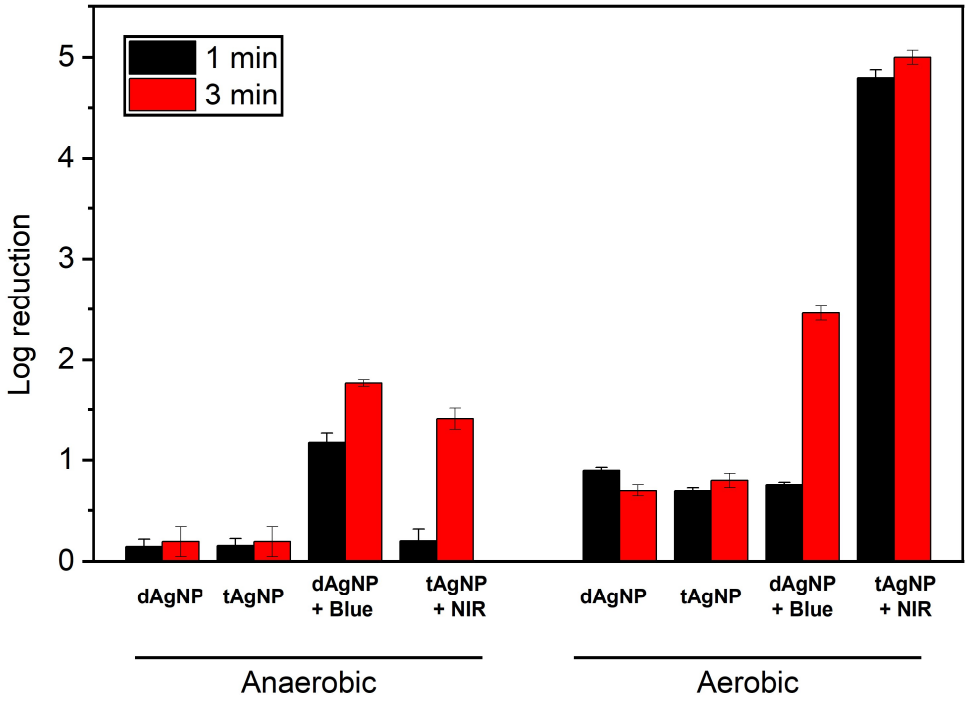

Fig. 3.1.7: Effect of Oxygen on the antibacterial performance of Ag nanostructures. Log reduction of *E. coli* treated with dAgNps in the presence and absence of blue irradiation (450 nm); or with tAgNp in the presence and absence of NIR irradiation (810 nm), under air (aerobic) or N_2 atmosphere (anaerobic). The power density was 0.93W/cm^2 for blue light and 0.99 W/cm^2 and the bacteria were treated with 10 ppm of the Ag nanostructures for 1 and 3 min. Error bars represent standard deviations of the log reduction.

Apart from ROS and Ag^+, it is also possible that localized plasmonic heating has a significant toxic effect on bacteria. While we could not measure this temperature on the nanoscale, macroscopic temperature measurements indicate a notable increase in temperature for suspensions containing tAgNPs, compared to just water (Fig. 3.1.8). The level of investigation in this work cannot specifically attribute this to plasmonic heating, however it is important to acknowledge that these elevated temperatures are high enough to impact bacterial growth. Other works involving antibacterial AgNPs have made similar observations and established silver nanomaterials to have reasonable photoconversion efficiency yields as high 48%, making them useful for photothermal therapy.[34]

Based on those experiments, it is likely that there is a synergic effect between the increase in temperature, which has been shown to impact the integrity and viability of the bacterial cells, and the increase in the oxidative damage caused by the generated ROS/RNS.[37] However, given the dramatic drop in antimicrobial activity when oxygen is absent, it appears that ROS are the main contributor to the toxicity in this system.

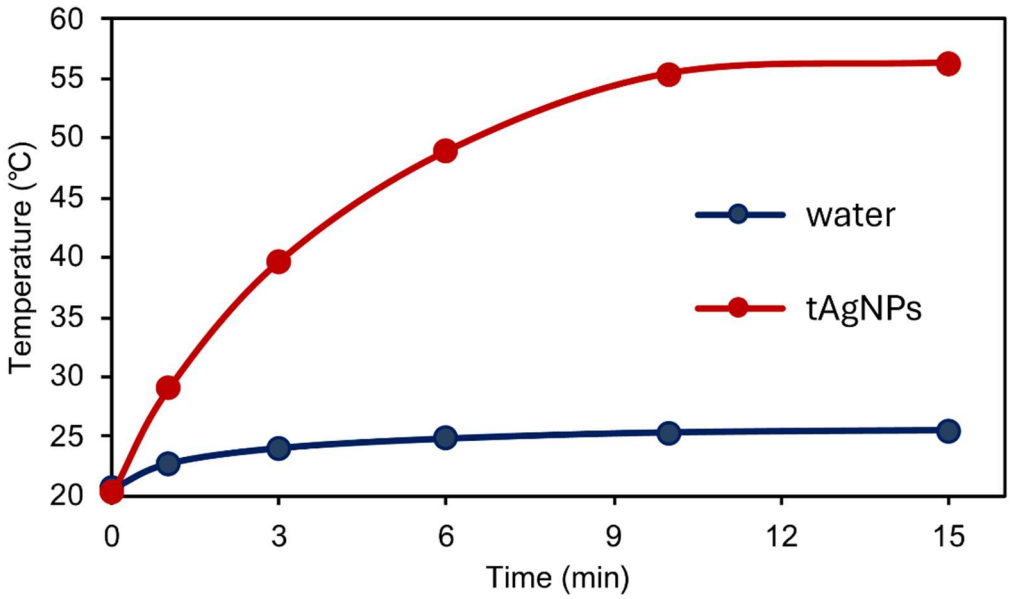

Fig. 3.1.8: Temperature of 5 mL aliquots of MilliQ water (blue) and a 10 ppm tAgNP suspension (red) over several min under NIR irradiation. Both samples were contained in 20 mL scintillation vials with vented lids, held 3 cm above a NIR (810 nm) LEDi head.

Cell cytotoxicity assay

In view of the results from the antibacterial assays, we further evaluated the cellular toxicity of tAgNPs. Preliminary tests were run *in vitro* on the human fibrosarcoma cell line HT-1080. Viability was assessed after cells were incubated with 10 ppm AgNPs for 15 min, which are previously found to have exceptional antibacterial activity (9 log units reduction). Since AgNPs were not stable in standard culture media, experiments were performed in D5W as a medium, which lead to a baseline level of cellular stress (Fig. 3.1.9, first bar). Treatment of cells with AgNPs under dark or light illumination conditions did not result in reduced viability compared to cells incubated in the buffer or cells irradiated with light but free from AgNPs (Fig. 3.1.9). Note that after the exposure to AgNPs and light treatments, cells were replated in adequate media (DMEM) and grew to full confluency. We believe that these preliminary tests support that our AgNPs are more toxic toward prokaryotic cells than to eukaryotic cells, specially under light treatments.

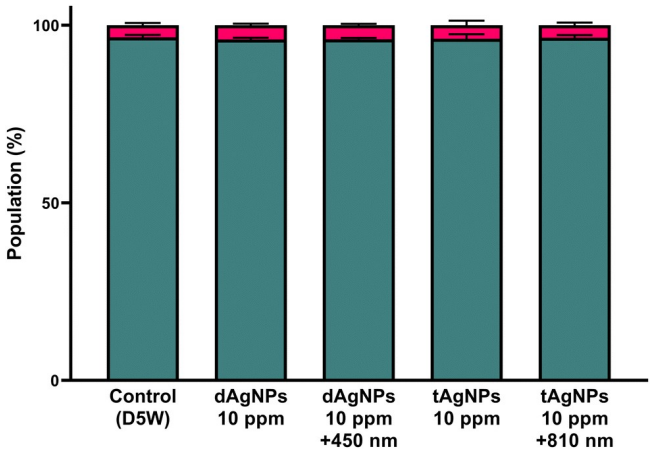

Fig. 3.1.9: Human fibrosarcoma (HT10-80) viability after 15 min treatment with 10 ppm tAgNPs and dAgNPs with and without complementary irradiation (810 nm).

Cell uptake experiments revealed that Ag accumulated in greater amounts (2.5×10^{-6} vs 0.5×10^{-6} ppm/cell) within HT-1080 cells when exposed to tAgNPs compared to dAgNPs (Fig. 3.1.S10). However, this did not translate into higher toxicity toward the cells in the case of both tAgNPs and dAgNPs.

Conclusions

In summary, this work demonstrates the effective use of plasmon excitation with LEDs to increase the antibacterial activity of AgNPs by several orders of magnitude. Using a light-mediated synthesis, we are able to generate silver triangles and decahedra with plasmonic absorbances in the visible and NIR regions. These particles display exceptionally high light-triggered antibacterial activity, requiring only a few min to reach 9 logs of bacterial reduction under LED illumination. Our mechanistic investigation establishes that it is likely due to a combination of ROS generation and increasing thermal stress, with ROS generation performing the bulk of the killing, rather than heat or Ag^+ release. Not only does this highlight the potential of AgNPs as photoactivated therapeutics and disinfectants but also it shows that when working with AgNPs, it is crucial to very carefully control light exposure when assessing particle properties, an often overlooked parameter in many nanomaterial studies. Finally, our light-activated AgNPs combine several crucial factors when applying these materials to human health: subtoxic levels of therapeutic agents for human cell lines, high antimicrobial activity, short treatment times, and *complete* colony eradication. All of this is performed using LEDs as the principal source of light, making it much more accessible to systems which require lasers. Together, these make our LED-activated AgNPs a promising candidate for a variety of applications in disinfection and may open the door to future applications in health.

Supplemental Information

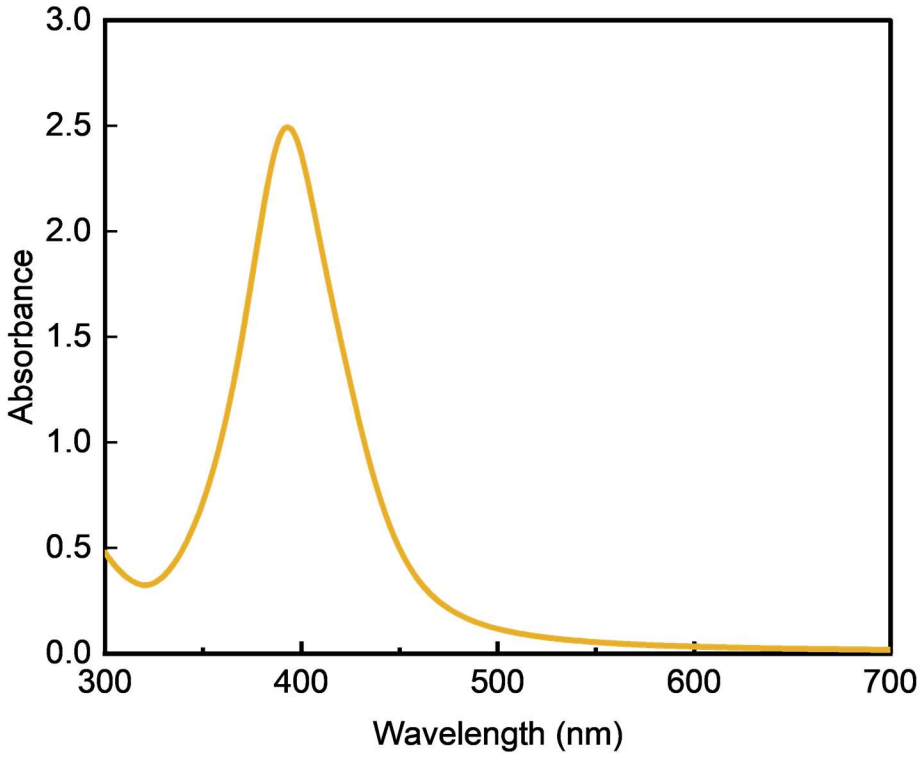

Fig. 3.1.S1: UV-Vis absorption spectrum of aqueous AgNP seeds following UV photoreduction of $AgNO_3$.

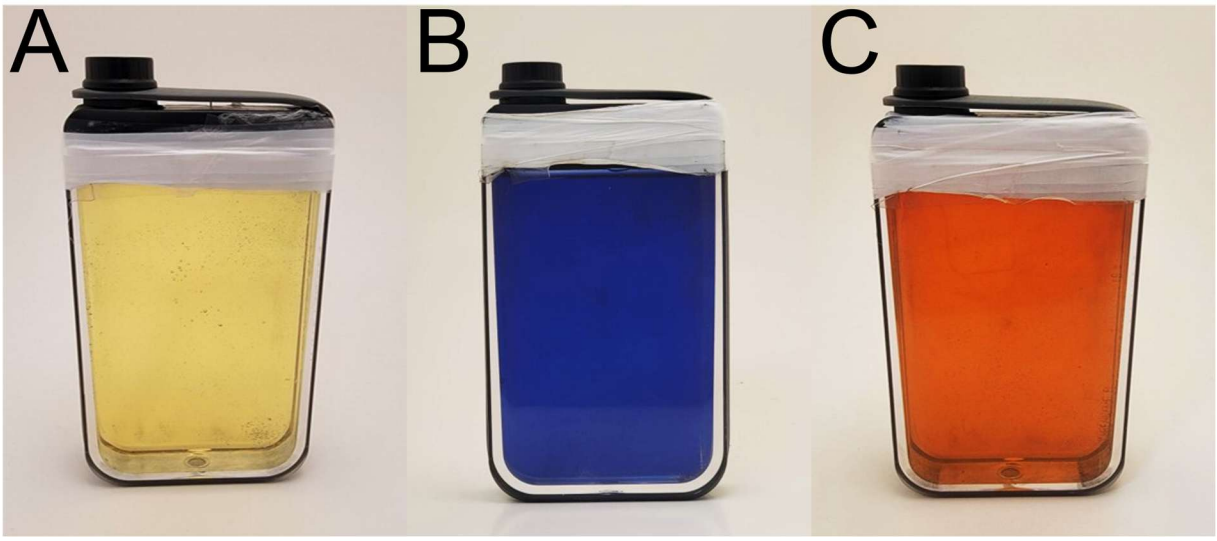

Fig. 3.1.S2: 200 mL batches of AgNP seeds (A), tAgNPs (B), and dAgNPs (C) following synthesis.

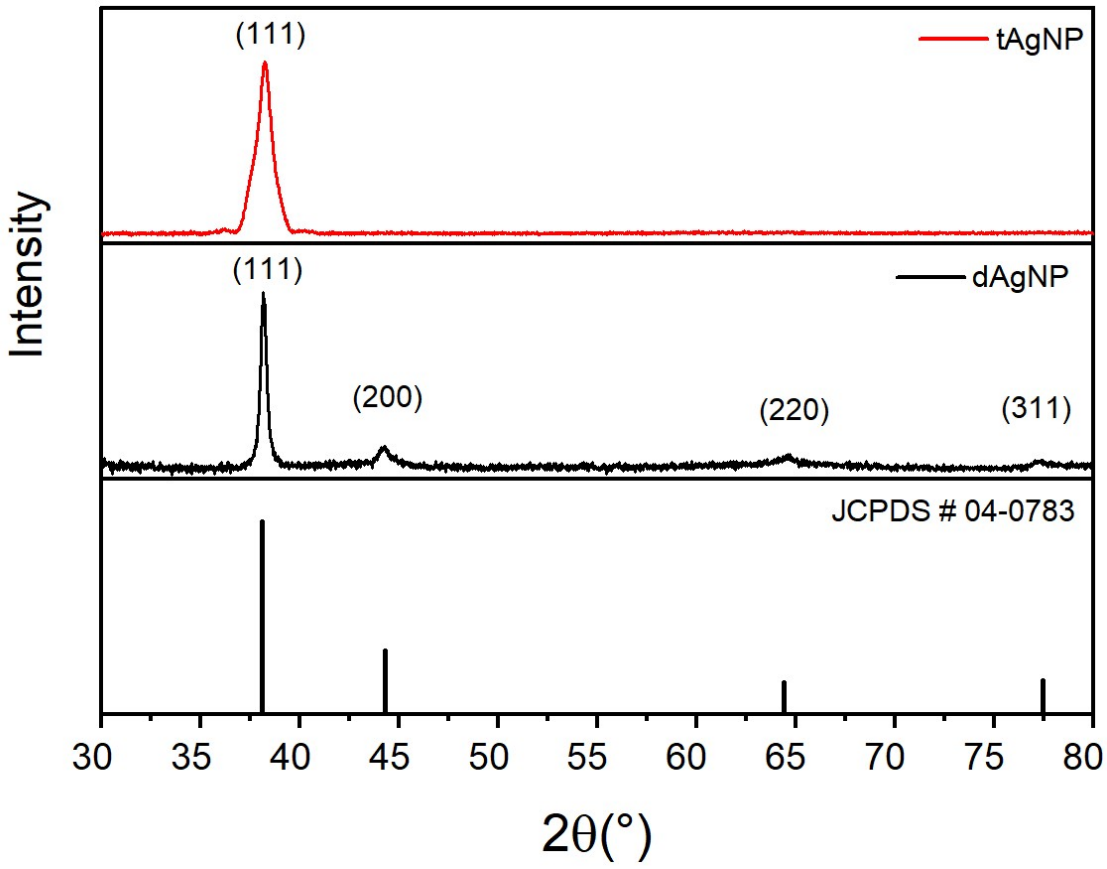

Fig. 3.1.S3: X-ray diffractograms of the Ag nanostructures: tAgNP (red) and dAgNP (black). In the bottom, the diffractogram pattern for metallic silver according to the JCPDS card no: 04-0783.

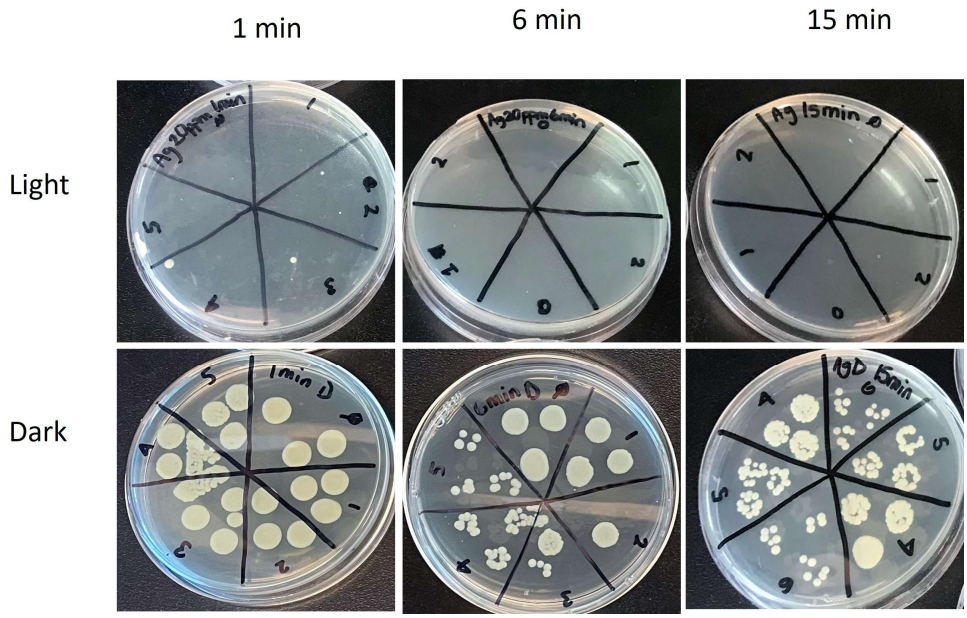

Fig. 3.1.S4: Antibacterial effect of tAgNPs on *E. coli*: Photographs of agar plates on which *E. coli* cells were incubated after treatment with tAgNP in the dark or under NIR irradiation (810 nm, 0.99 W/cm^2) for 1 to 15 min. Each quadrant represents a 10^x dilution (x = corresponding number written on plate).

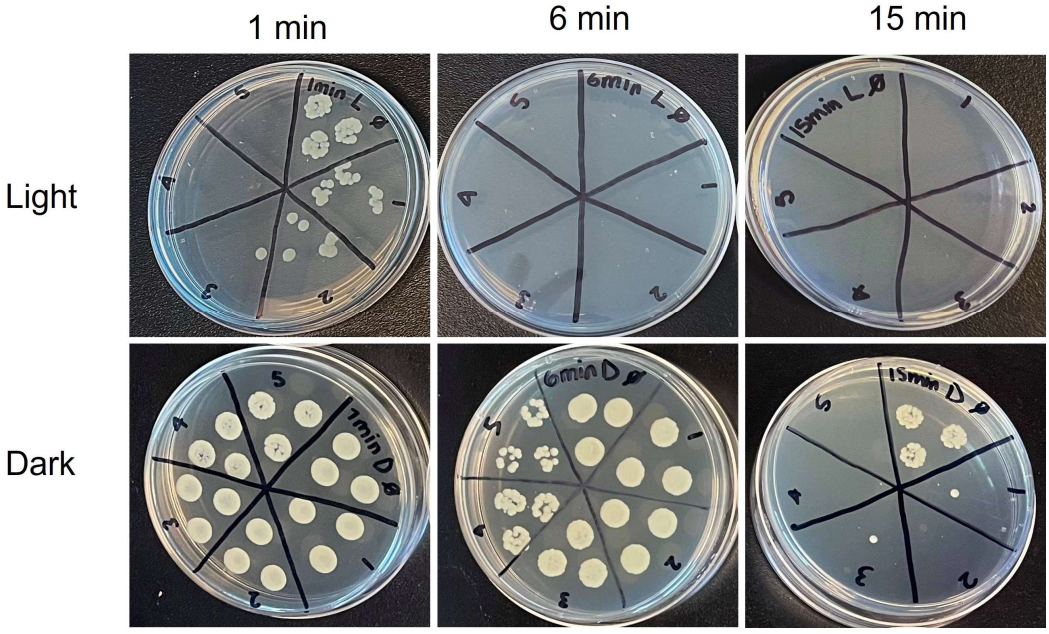

Fig. 3.1.S5: Antibacterial effect of dAgNPs on *E. coli*: Photographs of agar plates on which *E. coli* cells were incubated after treatment with dAgNPs in the dark or under blue irradiation (450 nm, 0.95 W/cm^2) for 1 to 15 min. Each quadrant represents a 10^x dilution (x = corresponding number written on plate).

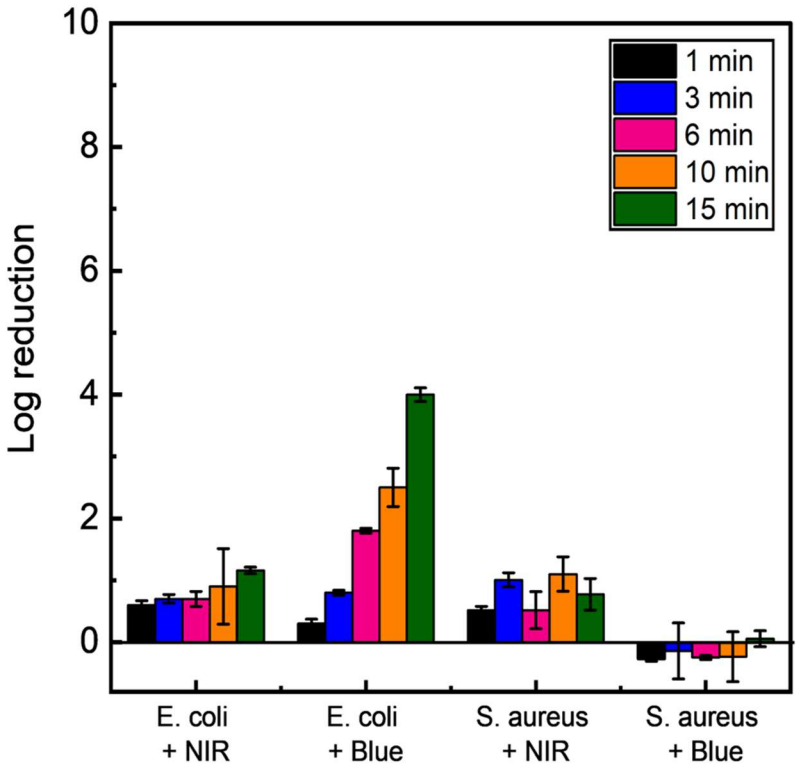

Fig. 3.1.S6: Bacterial survival after irradiation with NIR LED (810 nm) or blue LED (450 nm) for up to 15 min in the absence of AgNPs. Bacterial growth was determined by the plate counting method. Error bars represent the standard deviations of the log reduction (*** $p<0.001$).

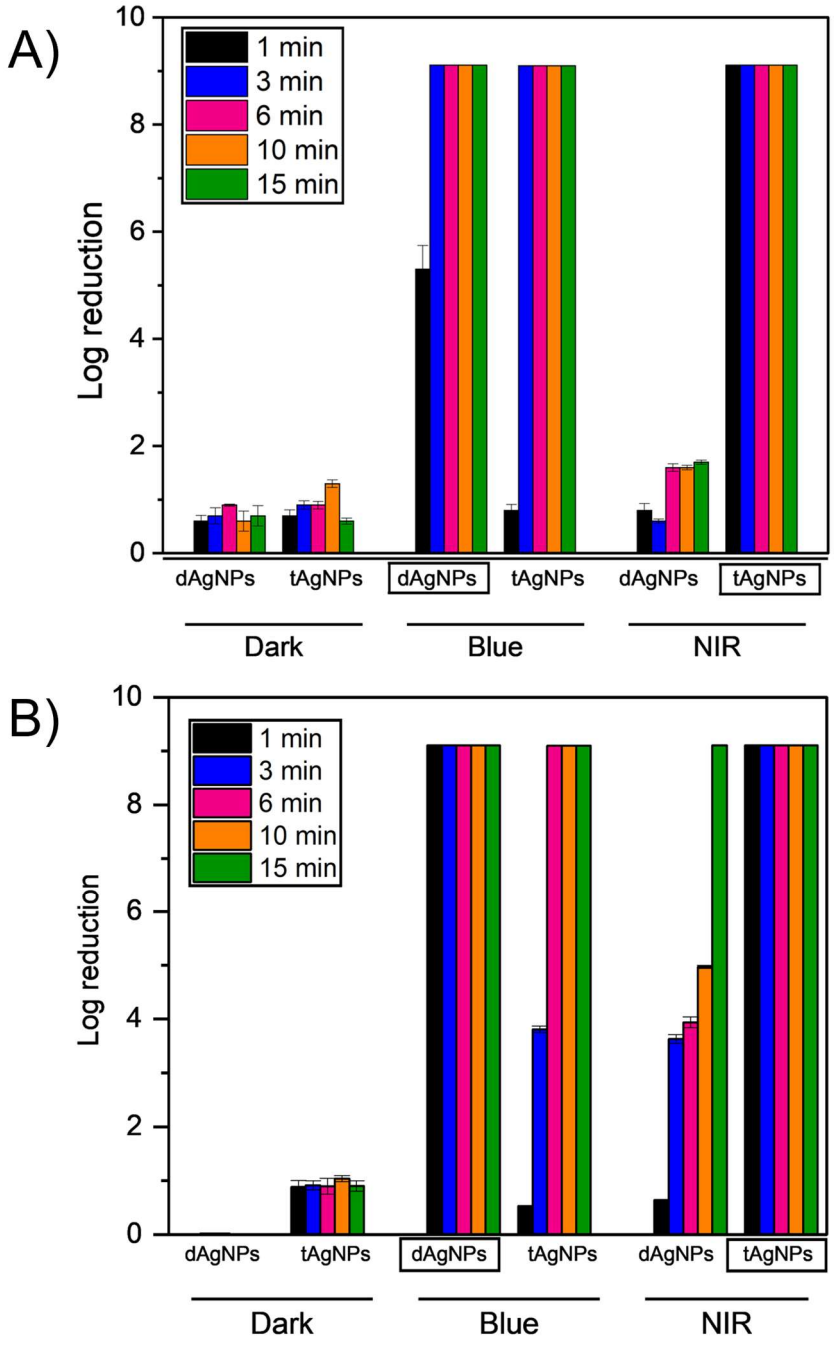

Fig. 3.1.S7: Antibacterial effect of tAgNPs and dAgNPs: log reduction of *E. coli* (A) and *S. aureus* (B) treated with blue light (450 nm) or with NIR (810 nm). The power density was 0.93W/cm^2 for blue light and 0.99 W/cm^2 for NIR light. Bacteria were treated with 20 ppm suspensions of the Ag nanostructures. Complementary AgNP and light are flagged with a black box. Error bars represent standard deviations of the log reduction.

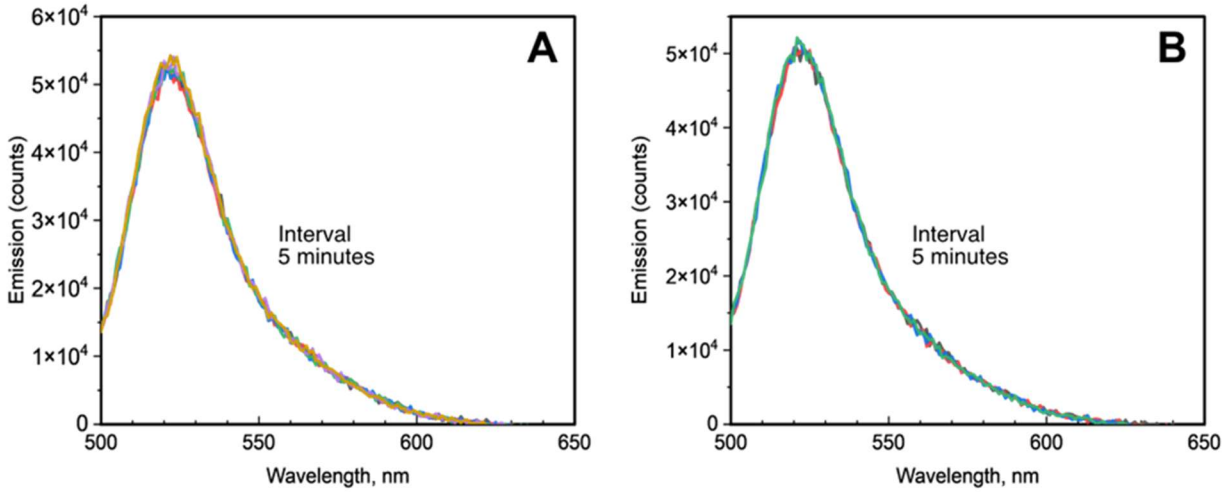

Fig. 3.1.S8: Emission intensity of DCF assay in the absence of AgNPs under NIR irradiation (A) and under dark conditions (B) for 15 min.

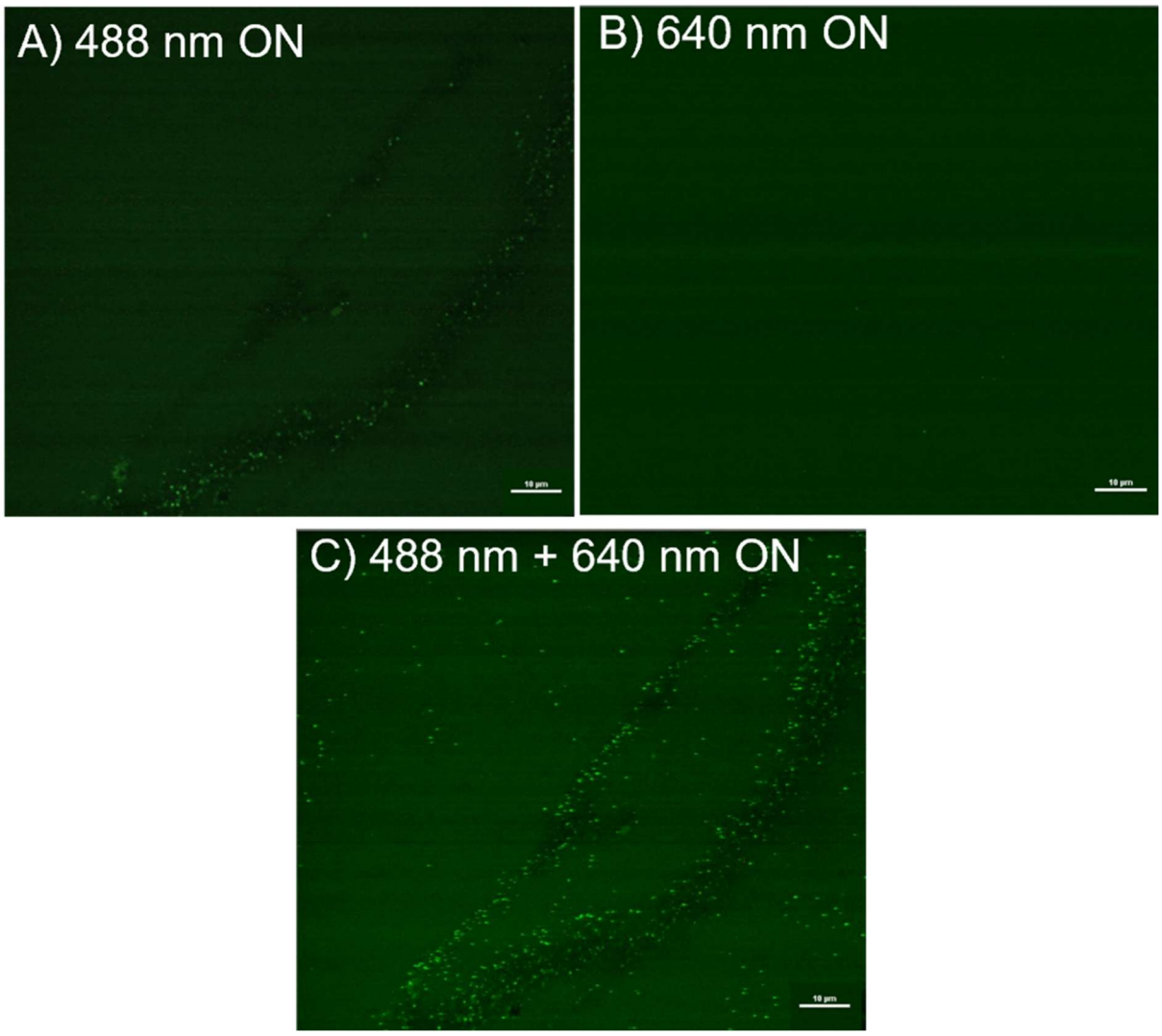

Fig. 3.1.S9: Confocal microscopy images of tAgNPs on a glass slide (seen as dark regions in the images) under gentle flow of fresh H_2DCF using a flow reaction system described elsewhere[21]. In this system, light green bursts represent localized H_2DCF reacting with ROS/RNS to yield the emissive DCF. A) The system with only 488 nm excitation, where only background levels of DCF are expected to be seen. B) The system under 640 nm excitation, a wavelength at which the NPs can absorb, but H_2DCF does not. C) The system excited by both lasers, simultaneously exciting the tAgNPs and the dye simultaneously to yield an increase in overall emission.

Table 3.1.S1: Ag ppm in supernatant of AgNP suspensions following 6 h of complimentary LEDi irradiation, as determined using ICP-OES. Note that the detection limit of the instrument is 0.1 ppm.

	tAgNPs	**dAgNPs**
Initial Ag ppm	0.14	0.21
Ag ppm after 6 h of irradiation	0.21	0.15

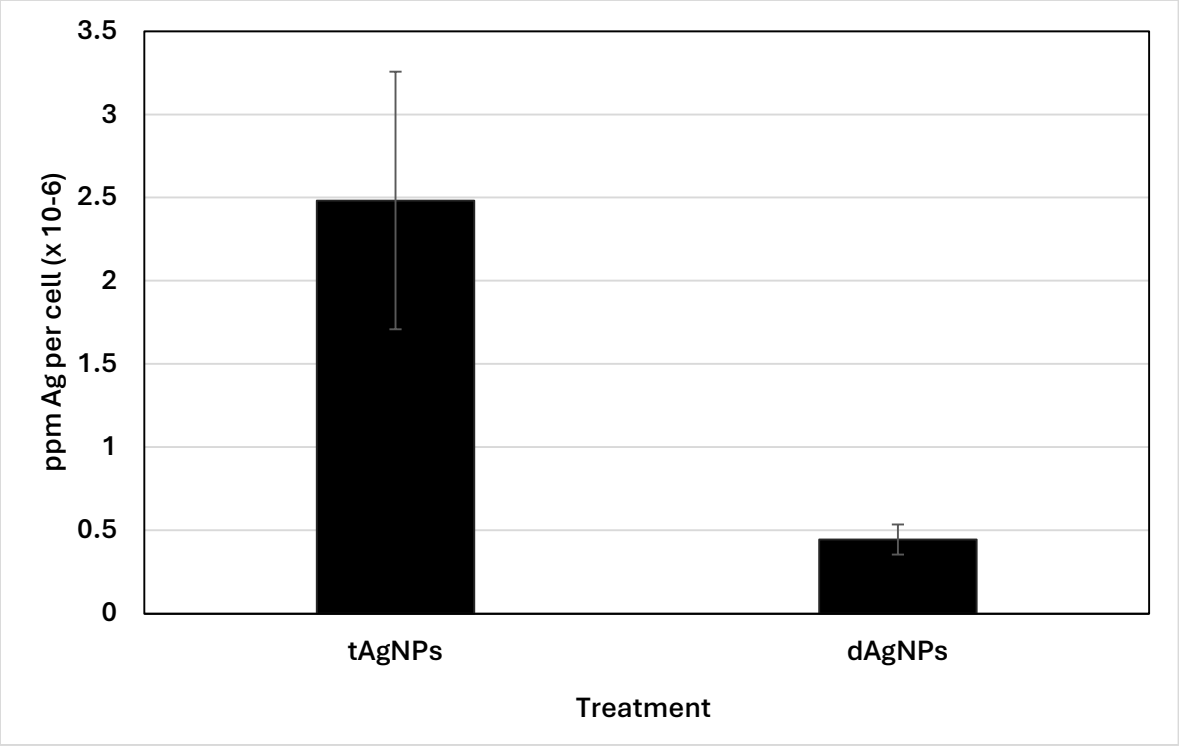

Fig. 3.1.S10: Ag uptake in HT-1080 cells following treatment with AgNPs, as determined by ICP-OES. Results are the average of triplicates, bars represent standard deviation.

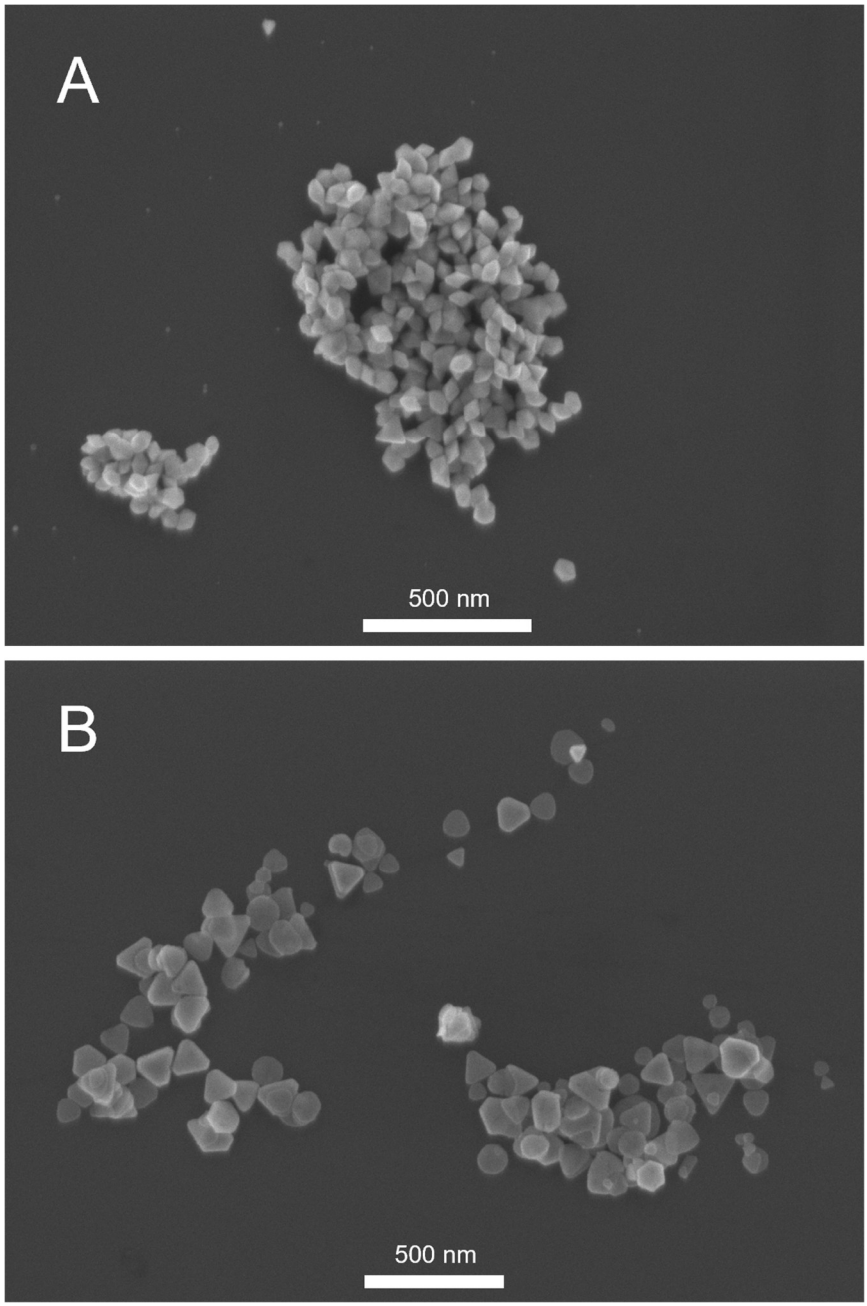

Fig. 3.1.S11: SEM images of (A) dAgNPs, and (B) tAgNPs. Size bars are 500 nm. Note that diamond shaped particles, as seen in A, may represent decahedral particles which are turned on their side.

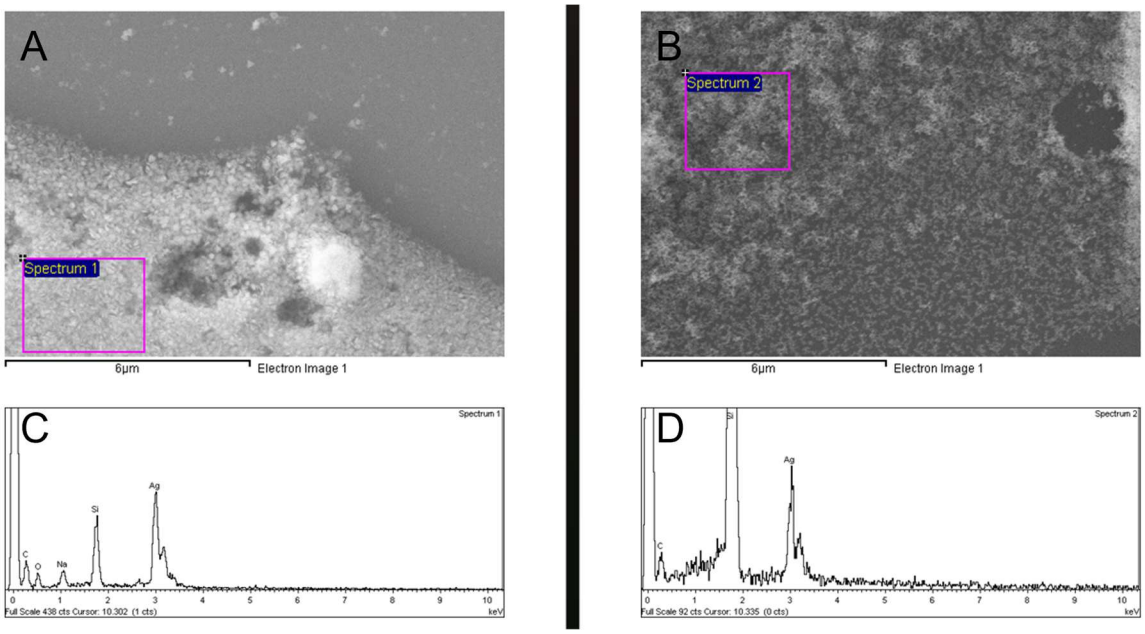

Fig. 3.1.S12: SEM images of densely packed regions of tAgNPs (A) and dAgNPs (B), and corresponding EDS spectra collected from these regions (C & D, respectively).

References

1. B. Calderón-Jiménez , M. E. Johnson , A. R. Montoro Bustos , K. E. Murphy , M. R. Winchester and J. R. Vega Baudrit , Silver Nanoparticles: Technological Advances, Societal Impacts, and Metrological Challenges, *Front. Chem.*, 2017, 5 , 6
2. O. Gherasim , R. A. Puiu , A. C. Bîrcă , A.-C. Burduşel and A. M. Grumezescu , An Updated Review on Silver Nanoparticles in Biomedicine, *Nanomaterials*, 2020, 10 , 2318
3. K. G. Stamplecoskie and J. C. Scaiano , Silver as an Example of the Applications of Photochemistry to the Synthesis and Uses of Nanomaterials, *Photochem. Photobiol.*, 2012, 88 , 762
4. M. K. Rai , S. D. Deshmukh , A. P. Ingle and A. K. Gade , Silver nanoparticles: the powerful nanoweapon against multidrug-resistant bacteria, *J. Appl. Microbiol.*, 2012, 112 , 841
5. S. He , J. Song , J. Qu and Z. Cheng , Crucial breakthrough of second near-infrared biological window fluorophores: design and synthesis toward multimodal imaging and theranostics, *Chem. Soc. Rev.*, 2018, 47 , 4258
6. S. C. Boca , M. Potara , A.-M. Gabudean , A. Juhem , P. L. Baldeck and S. Astilean , Chitosan-coated triangular silver nanoparticles as a novel class of biocompatible, highly effective photothermal transducers for in vitro cancer cell therapy, *Cancer Lett.*, 2011, 311 , 131
7. A. Salleh , R. Naomi , N. D. Utami , A. W. Mohammad , E. Mahmoudi , N. Mustafa and M. B. Fauzi , The Potential of Silver Nanoparticles for Antiviral and Antibacterial Applications: A Mechanism of Action, *Nanomaterials*, 2020, 10 , 1566
8. X. Huang , I. H. El-Sayed , W. Qian and M. A. El-Sayed , Cancer Cell Imaging and Photothermal Therapy in the Near-Infrared Region by Using Gold Nanorods, *J. Am. Chem. Soc.*, 2006, 128 , 2115
9. G. Gunaydin , M. E. Gedik and S. Ayan , Photodynamic Therapy for the Treatment and Diagnosis of Cancer–A Review of the Current Clinical Status, *Front. Chem.*, 2021, 9 , 608
10. I. M. A. Ribeiro , W. Eßbauer , R. Kutlesa and A. Borst , Spatial and temporal control of expression with light-gated LOV-LexA, *G3*, 2022, 12 , jkac178
11. G. Gunaydin , M. E. Gedik and S. Ayan , Photodynamic Therapy—Current Limitations and Novel Approaches, *Front. Chem.*, 2021, 9 , 400
12. Y. Qiao , F. Ma , C. Liu , B. Zhou , Q. Wei , W. Li , D. Zhong , Y. Li and M. Zhou , Near-Infrared Laser-Excited Nanoparticles To Eradicate Multidrug-Resistant Bacteria and Promote Wound Healing, *ACS Appl. Mater. Interfaces*, 2018, 10 , 193
13. B. M. Vickerman , E. M. Zywot , T. K. Tarrant and D. S. Lawrence , Taking phototherapeutics from concept to clinical launch, *Nat. Rev. Chem.*, 2021, 5 , 816
14. M. N. Khan , O. Bashir , T. A. Khan , S. A. Al-Thabaiti and Z. Khan , CTAB capped synthesis of bio-conjugated silver nanoparticles and their enhanced catalytic activities, *J. Mol. Liq.*, 2018, 258 , 133
15. S. Agnihotri , S. Mukherji and S. Mukherji , Size-controlled silver nanoparticles synthesized over the range 5–100 nm using the same protocol and their antibacterial efficacy, *RSC Adv.*, 2014, 4 , 3974
16. K. G. Stamplecoskie and J. C. Scaiano , Light Emitting Diode Irradiation Can Control the Morphology and Optical Properties of Silver Nanoparticles, *J. Am. Chem. Soc.*, 2010, 132 , 1825
17. A. Polywka , C. Tückmantel and P. Görrn , Light controlled assembly of silver nanoparticles, *Sci. Rep.*, 2017, 7 , 45144
    R. Jin , Y. Charles Cao , E. Hao , G. S. Métraux , G. C. Schatz and C. A. Mirkin , Controlling anisotropic nanoparticle growth through plasmon excitation, *Nature*, 2003, 425 , 487

18. E. Sorbellini , M. Rucco and F. Rinaldi , Photodynamic and photobiological effects of light-emitting diode (LED) therapy in dermatological disease: an update, *Lasers Med. Sci.*, 2018, 33 , 1431
19. K. G. Stamplecoskie and J. C. Scaiano , Kinetics of the Formation of Silver Dimers: Early Stages in the Formation of Silver Nanoparticles, *J. Am. Chem. Soc.*, 2011, 133 , 3913
20. J. L. Brubacher and N. C. Bols , Chemically de-acetylated 2′,7′-dichlorodihydrofluorescein diacetate as a probe of respiratory burst activity in mononuclear phagocytes, *J. Immunol. Methods*, 2001, 251 , 81
21. B. Wang , C. R. Bourgonje and J. C. Scaiano , Fiber-glass supported catalysis: real-time, high-resolution visualization of active palladium catalytic centers during the reduction of nitro compounds, *Catal. Sci. Technol.*, 2023, 13 , 1021
22. Z. Bao and C. Q. Lan , Mechanism of light-dependent biosynthesis of silver nanoparticles mediated by cell extract of Neochloris oleoabundans, *Colloids Surf., B*, 2018, 170 , 251
Q. Zhang , C. Chen , G. Wan , M. Lei , M. Chi , S. Wang and D. Min , Solar light induced synthesis of silver nanoparticles by using lignin as a reductant, and their application to ultrasensitive spectrophotometric determination of mercury(II), *Microchim. Acta*, 2019, 186 , 727
23. Y. Zhang , Q. Zhang , X. Ouyang , D. Y. Lei , A. P. Zhang and H.-Y. Tam , Ultrafast Light-Controlled Growth of Silver Nanoparticles for Direct Plasmonic Color Printing, *ACS Nano*, 2018, 12 , 9913
24. H. Jia , W. Xu , J. An , D. Li and B. Zhao , A simple method to synthesize triangular silver nanoparticles by light irradiation, *Spectrochim. Acta, Part A*, 2006, 64 , 956
25. J. Ahmad , X. Wen , F. Li and B. Wang , Novel triangular silver nanoparticle modified membranes for enhanced antifouling performance, *RSC Adv.*, 2019, 9 , 6733
26. S. Chen and D. L. Carroll , Synthesis and Characterization of Truncated Triangular Silver Nanoplates, *Nano Lett.*, 2002, 2 , 1003
27. X. Jiang , Q. Zeng and A. Yu , Thiol-frozen shape evolution of triangular silver nanoplates, *Langmuir*, 2007, 23 , 2218
28. D. Aherne , D. M. Ledwith , M. Gara and J. M. Kelly , Optical properties and growth aspects of silver nanoprisms produced by a highly reproducible and rapid synthesis at room temperature, *Adv. Funct. Mater.*, 2008, 18 , 2005
29. W. Jin , G. Liang , Y. Zhong , Y. Yuan , Z. Jian , Z. Wu and W. Zhang , The Influence of CTAB-Capped Seeds and Their Aging Time on the Morphologies of Silver Nanoparticles, *Nanoscale Res. Lett.*, 2019, 14 , 81
30. Y. Yang , S. Matsubara , L. Xiong , T. Hayakawa and M. Nogami , Solvothermal Synthesis of Multiple Shapes of Silver Nanoparticles and Their SERS Properties, *J. Phys. Chem. C*, 2007, 111 , 9095
31. A. Shkilnyy , M. Soucé , P. Dubois , F. Warmont , M.-L. Saboungi and I. Chourpa , Poly(ethylene glycol)-stabilized silver nanoparticles for bioanalytical applications of SERS spectroscopy, *Analyst*, 2009, 134 , 1868
32. X. Chen , Z. Zhong , Z. Xu , L. Chen and Y. Wang , 2′,7′-Dichlorodihydrofluorescein as a fluorescent probe for reactive oxygen species measurement: Forty years of application and controversy, *Free Radical Res.*, 2010, 44 , 587
33. E. Alarcon, K. Udekwu, M. Skog, N. Pacioni, K. Stamplecoskie, M. González-Béjar, N. Polisetti, A. Wickham, A. Richter-Dahlfors, M. Griffith, J.C. Scaiano, The biocompatibility and antibacterial properties of collagen-stabilized, photochemically prepared silver nanoparticles, *Biomater.* 2012, 33(19), 4947-4956

34. Y. Liu , F. Li , Z. Guo , Y. Xiao , Y. Zhang , X. Sun , T. Zhe , Y. Cao , L. Wang , Q. Lu and J. Wang , Silver nanoparticle-embedded hydrogel as a photothermal platform for combating bacterial infections, *Chem. Eng. J.*, 2020, 382 , 122990
35. H. Xu , F. Qu , H. Xu , W. Lai , Y. Andrew Wang , Z. P. Aguilar and H. Wei , Role of reactive oxygen species in the antibacterial mechanism of silver nanoparticles on Escherichia coli O157: H7, *Biometals*, 2012, 25 , 45
T. W. Ng , L. Zhang , J. Liu , G. Huang , W. Wang and P. K. Wong , Visible-light-driven photocatalytic inactivation of Escherichia coli by magnetic Fe_2O_3–AgBr, *Water Res.*, 2016, 90 , 111
36. S. Rtimi , M. Pascu , R. Sanjines , C. Pulgarin , M. Ben-Simon , A. Houas , J. C. Lavanchy and J. Kiwi , ZrNO–Ag co-sputtered surfaces leading to E. coli inactivation under actinic light: Evidence for the oligodynamic effect, *Appl. Catal., B*, 2013, 138–139 , 113
37. S. Chen , Z. Chu , L. Cao , L. Xu , Q. Jin , N. Liu , B. Chen , M. Fang , W. Wang , H. Qian and M. Shao , Antibacterial mechanism and transcriptomic analysis of a near-infrared triggered upconversion nanoparticles@$AgBiS_2$ for synergetic bacteria-infected therapy, *Nano Res.*, 2022, 15 , 9298

Chapter 4 – Heterogenous AgNPs on glass wool for in-flow light activated bacterial disinfection

Background

While the focus of the Scaiano Group is generally photocatalysis, water treatment is a recent area of study in our group, as we try to apply our expertise to tackle real world problems. Unfortunately, water security is still a pressing need globally in 2024. However, we need not look far from our own borders to find evidence of this; even in one of the most developed countries in the world there are thousands of Canadians, disproportionately from rural Indigenous populations, who are confronted with the harsh reality of drinking water contamination.[1] In the 94 Calls to Action of the Truth and Reconciliation Commission, the Commission clearly highlights the importance of water security to the development of Indigenous communities.[2] Yet, even a decade later these challenges persist. As an academic of Métis heritage working in a university built on the traditional lands of the displaced Algonquin people, I strongly feel that academics need to take a hands on role in addressing the Calls to Action which are within our expertise. By taking on these challenges we can address the inequities within our own borders, while also tackling challenges faced by millions of people abroad. According to the United Nations Global Water Security 2023 Assessment, 610 million people (8% of the global population) are critically water-insecure and 5.52 billion (72% of the world population) are water-insecure.[3] Predictably, these challenges are concentrated in highly industrialized regions where water treatment solutions are either inaccessible, or unaffordable for the local population. In this chapter our goal was to take the knowledge gained in Chapter 3 and combine it with our groups expertise in flow photocatalysis to develop a light activated water purification system based on AgNPs anchored to glass wool.[4]

This work was initially performed in collaboration with fellow Scaiano Lab PhD student, Daliane Regis. Daliane was generous enough to share with me her expertise in building flow reactors for heterogenous catalysis. Dr. M. Jazmin Silvero has also played a major role in this project, largely in assessment of antibacterial properties and performing the in-flow experiments. My contribution to this project was in the synthesis and characterization of AgNPs and the tAgNP@GW catalysts, and project design. It is important to note that this set of experiments is a preliminary exploration of the potential of AgNPs as heterogenous catalysts, and is meant to guide future projects in the realm of AgNP flow reactors for water treatment.

4.1: Flow treatment of contaminated water using AgNPs fixed to APTES treated glass wool

Introduction

Continuing the trend of applying photocatalytic AgNPs to biological applications, we set out to apply the remarkable light-activated antibacterial abilities of our AgNPs to water treatment. However, the AgNP formulations used in our initial publication, highlighted earlier in Chapter 3, have a few drawbacks when trying to use them in water purification:

i) AgNPs in suspension are difficult to recover or remove from a system in their colloidal form

ii) While not toxic at low concentrations, long term consumption of Ag and AgNPs may have negative health effects, and can have adverse environmental impacts

iii) Treating water in batch with AgNP suspensions, as we did in the previous AgNP paper, is not a sustainable or scalable water treatment strategy

Being a group that has been heavily involved in studying flow chemistry in recent years, we thought that an interesting challenge to address by designing heterogenous AgNP catalysts for use in flow reactors. By anchoring our AgNPs to a heterogenous substrate, we can limit the amount of Ag that ends up in the purified sample, while making a reusable material which need not be replaced after every use. One promising substrate for such a catalyst is (3-Aminopropyl) triethoxysilane (APTES) treated glass wool (GW).[5] GW has been investigated heavily in recent years in our group as a reasonably inert support for heterogenous catalysts that retains the catalytic properties of the catalyst used. For example, in Chapter 5 of this thesis we show that GW can act as a stable support for PdNP catalysts, with minimal metal leaching occurring after several hours of flow catalysis.[5] With these features in mind, we sought to create GW anchored AgNPs for the purposes of light-activated bacteria killing under flow conditions.

Experimental

Materials

Silver nitrate (ACS reagent, 99.9+%) was purchased from Alfa Aesar. Trisodium citrate dihydrate (99%) was purchased from Fisher Scientific. Irgacure-2959 (I-2959) was a gift from BASF Chemicals. Luria–Bertani (LB) broth was purchased from Sigma Aldrich, and Mueller Hinton (MH) agar was purchased from

BD Life Sciences. Glass wool (non-treated) was purchased from Sigma Aldrich. 3-Aminopropyl triethoxysilane (APTES, >98%), and 3-mercaptopropyl triethoxysilane (MPTES, >96%) were ordered from TCI chemicals. 2',7'-Dichlorodihydrofluorescein diacetate (DCFDA, >97%) was ordered from Sigma Aldrich.

Surface functionalization of GW

We use an adaptation of the method utilized later in Chapter 5, reported and optimized by former Scaiano PhD student, Aida Elhage.[5,6] Briefly, GW is soaked in a 1% solution of either APTES or MPTES toluene solution under reflux overnight. The resulting GW is reported to be coated with amine or thiol groups, respectively, chemically modifying the surface to have a high affinity for metal nanoparticles. The glass wool is washed 5x with acetone, 5x with ethanol, dried well, then washed 5x with deionized water before use.

Anchoring of AgNPs to treated GW

To coat APTES/MPTES functionalized GW and untreated GW with AgNPs, a suspension of tAgNPs containing 5 ppm Ag (measured with ICP-OES) was first prepared using the methods outlined earlier in Chapter 2.2. Two grams of activated GW was added to a 3 mL aqueous solution containing one of the following formulations: a) 10 ppm tAgNPs, b) 5 ppm tAgNPs + 0.5 mM $AgNO_3$, or c) 1 mM $AgNO_3$.

The mixtures were left soaking overnight under either dark conditions or 635 nm irradiation. The next day, the GW was removed using tweezers and washed by immersion and vigorous agitation for several seconds in EtOH and water, 3x each. The resulting tAgNPs@GW samples showed distinct blue or grey color, while the suspension they were soaked in overnight were markedly clearer and less colorful.

In-flow antibacterial assay

To test the ability of our flow system to eliminate bacteria, we loaded 2 g of tAgNPs@GW into a 30 cm quartz tube with Teflon tubes fixed to either end to facilitate flow. This tube was placed diagonally between two white LED "parking lot" lamps purchased from Amazon, arranged in a tent formation. Using a syringe pump, an *E. coli* suspension containing ~10^6 CFU/mL (first measured by OD_{600}, later counted by plate counting) was pumped into the loaded tube and individual batches of *E. coli* were irradiated under the lamps for periods of 2, 10, and 30 min. After these times, samples were removed from the tube and diluted on MH agar plates, followed by 16 h of incubation at 37°C. Resulting bacterial colonies grown were manually counted on the plates to assess the degree of antibacterial activity.

Confocal microscopy imaging

Confocal microscopy was performed using a Nikon A1 confocal microscope fit with a flow cell, adapted from another project which will be discussed in detail in Chapter 5.[21] Using this approach, tAgNPs@GW fibres are imaged using H_2DCF as a ROS/RNS reporter probe, as described in the previous section (*"Reactive oxygen/nitrogen species quantification"*). This method enables the localization of reactive sites, giving insight into where and when reactions are happening in real time.

Characterization

Imaging of the tAgNPs@GW fibres was performed using a JEOL JSM-7500F field emission SEM. To image the fibres, the fibres were cut down to ~1 cm in length and a thin layer of fibres was gently planted onto carbon tape. Once the optimal synthesis for tAgNPs@GW was determined, diffuse reflectance was measurements were performed using a Cary 7000 Universal Spectrometer using untreated glass wool as a reference material.

Results & Discussion

The first experiment conducted compared the level of AgNP adhesion to APTES treated GW when different formulations of AgNPs and $AgNO_3$ were implemented. Visually, it was notable that the combination of 5 ppm tAgNPs and 0.5 mM $AgNO_3$ appeared to have the most rich blue colour, while the tAgNPs alone showed less intense blue colour, and the $AgNO_3$ alone appeared grey after treatment. The presence of blue colour was believed to be proportional to the success of the procedure at loading AgNPs onto the GW. To test this hypothesis, SEM was performed to compare the surfaces of the 3 treatments (Fig. 4.1.1). These images corroborated visual observations, with the tAgNP + $AgNO_3$ treated glass wool showing a remarkably higher level of surface coverage than the other two treatments. I theorize that the presence of $AgNO_3$ allowed the AgNPs to reduce Ag^+ under illumination, acting as a sort of adhesive, improving the stability of AgNPs attached to the GW surface, while also enabling new particles to be formed on the GW. The combined generation of new particles and growth of existing particles on the GW surface lead to a more polydisperse tAgNP population than is seen in colloidal AgNP mixtures. Anecdotally, when no illumination was used for the synthesis, it took 72 h of soaking to achieve similar levels of colour change on the GW (based on visual observations), so the LED illumination approach was favored going forward to enable quicker nanoparticle anchoring.

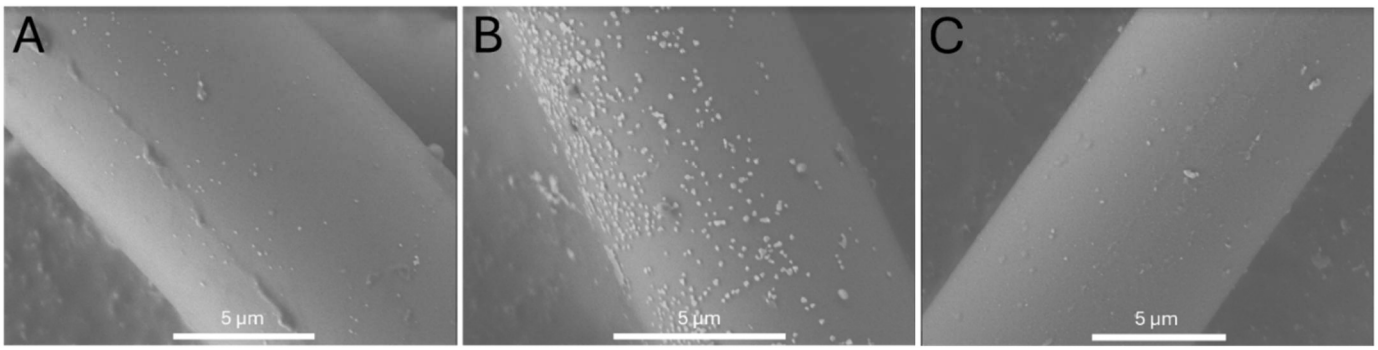

Fig. 4.1.1: SEM images of APTES treated GW after 24 h of 635 nm LED illumination while soaking in a solution containing: A) 10 ppm tAgNPs B) 5 ppm tAgNPs + 0.5 mM $AgNO_3$ and C) 1 mM $AgNO_3$.

The next test was to assess how different surface functionalizations of GW affected the anchoring of AgNPs. To compare with the previous experiment, MPTES treated and untreated GW were exposed to the tAgNP/$AgNO_3$ formulation under the same conditions. After 24 h, the MPTES treated tAgNPs@GW appear grey with slight blue colour persisting, while the untreated GW had very little colour at all. SEM imaging of each sample shows that the MPTES treated fibres have high loading of AgNPs, however the particles appear much smaller than seen in colloidal and APTES anchored tAgNPs, meanwhile the untreated fibre shows little tAgNP anchoring at all (Fig. 4.1.2). Additionally, it also appears that MPTES treated GW affected the morphology of the particles, with the attached NPs appearing smaller and more amorphous than those on the APTES treated GW. This may contribute to the loss of colourful plasmonic absorbance observed, as the plasmonic properties in metal NPs are highly structurally dependent.[7]

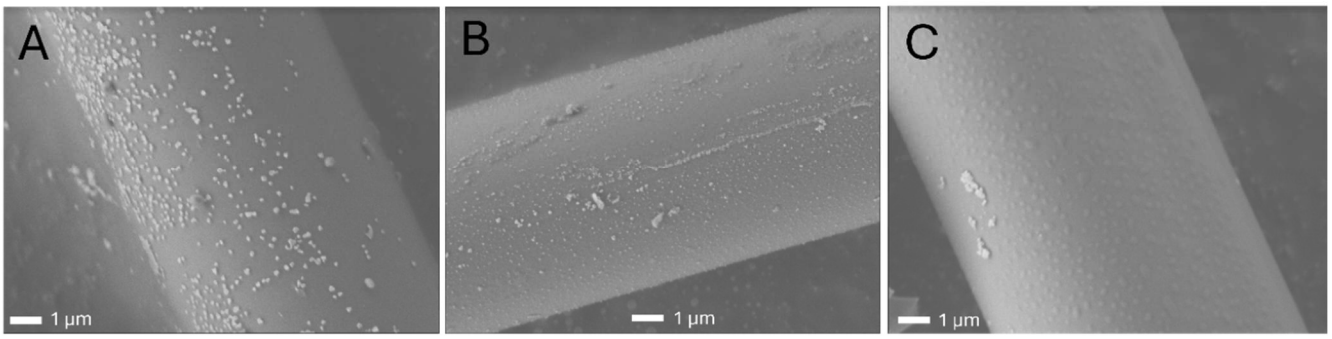

Fig. 4.1.2: SEM images of tAgNPs@GW produced using GW functionalized with A) APTES, B) MPTES, and C) untreated. Samples were immersed in a mixture of tAgNPs and $AgNO_3$ and irradiated with 635 nm LED irradiation on a Luzchem well plate illuminator.

From these experiments, it was decided that the preferred approach to synthesizing tAgNPs@GW was to use APTES treated GW illuminated with 635 nm irradiation while immersed in a combined solution of

tAgNPs and $AgNO_3$. These fibres were chosen for all subsequent experiments, including the antibacterial assays. To better understand the material, diffuse reflectance (DR) measurements were used to characterize the optical properties of the fibres. Interestingly, compared the original particles used in Chapter 3 (Fig. 3.1.1), the APTES anchored tAgNPs have slightly blue shifted absorbance, with their plasmonic peak centered around 750 nm rather than the initial 800 nm, and have increased absorbance across the visible spectrum, which we attribute to the increased polydispersity (Fig. 4.1.3). By inspecting the fibres shown in Fig. 4.1.3, it is clear that there are some regions where the tAgNPs@GW are much darker compared to the rest of the fibre, giving the fibres higher absorbance in the blue region of the visible region, around. DR measurements show that these regions are high in particles which absorb strongly around 425 nm. This suggests that during the irradiation phase, new AgNPs are being formed by the reduction of $AgNO_3$ by photoactivated tAgNPs.

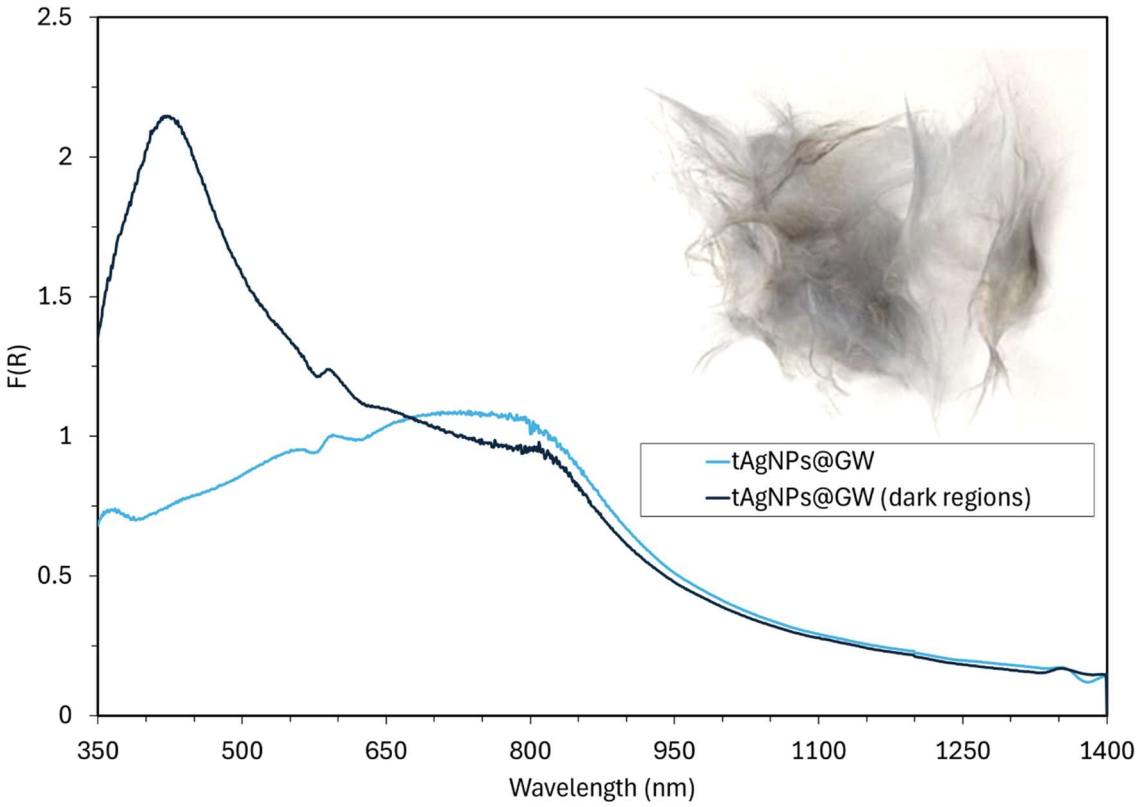

Fig. 4.1.3: DR spectrum of APTES treated tAgNPs@GW produced using the combined tAgNPs/$AgNO_3$ mixture. Inset in image shows appearance of the tAgNPs@GW. The blue trace represents the overall DR of the sample. The black trace represents DR taken from only the dark regions of the fibres.

With the synthesis method for tAgNPs@GW developed, the next objective was to determine if the particles retain their powerful light-activated antibacterial properties in their heterogenous form. To test the performance of tAgNPs@GW, a fairly simple photoreactor was constructed consisting of two commercially available LED floodlights (purchased off Amazon) arranged in a tent-like structure above a quartz flow tube loaded internally with 2 g of tAgNPs@GW (Fig. 4.1.4).

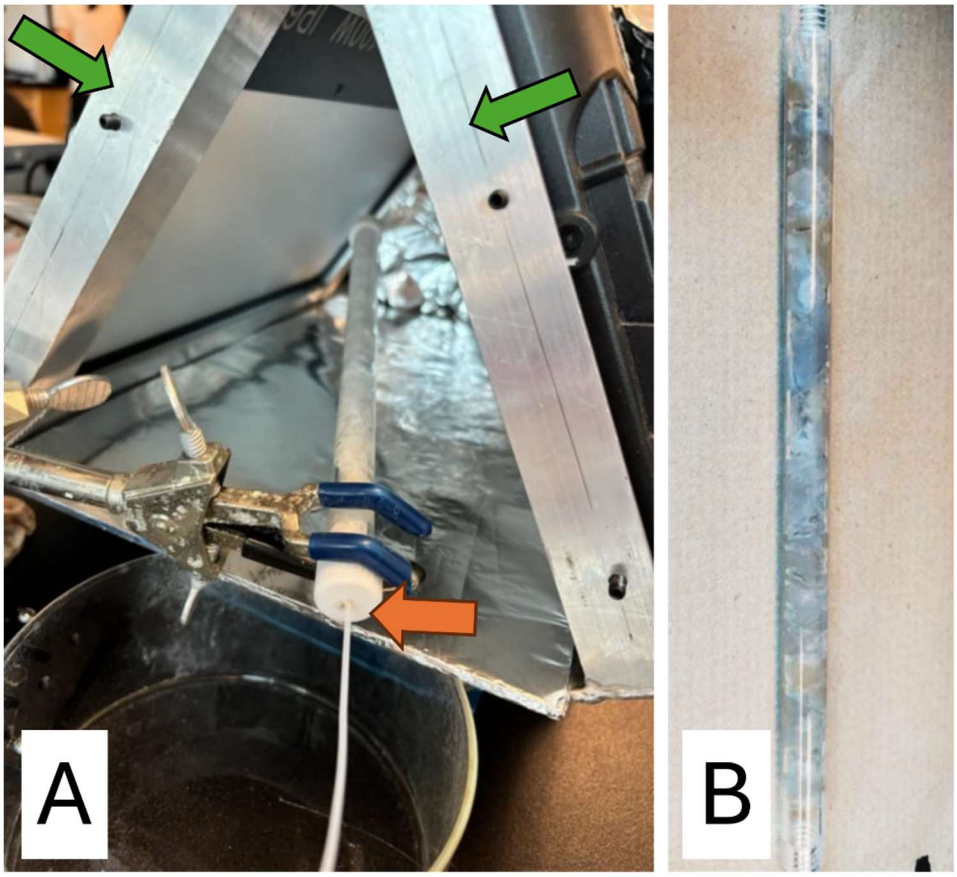

Fig. 4.1.4: A) Antibacterial flow-illumination system. LED floodlights are indicated by green arrows, and the outflow port of the reactor tube is indicated by the orange arrow. Note that the tube is loaded with untreated GW. B) The flow-tube loaded with 2 g of tAgNPs@GW after running antibacterial experiments.

To test the antibacterial activity of the system under light and dark conditions, *E coli* suspensions in PBS were pumped through the vessel, and into collection tubes after residence times of 2, 10, and 30 min. Growth plate counting showed promising results, with total bacterial killing occurring within 2 min for the light activated trials, while the dark condition showed no killing at all (Table 4.1.1). After 10 and 30 min of flow however, both the light and dark trials yielded no viable bacteria. Control experiments performed with untreated GW under light and dark conditions showed no significant killing for cultures irradiated for 2, 10, or 30 min.

Table 4.1.1: Bacterial concentrations in CFU/mL for *E coli* suspensions following passage through the flow reactor, as measured by plate counting. Each reported value is the average of triplicates.

Residence Time	tAgNPs/GW (CFU/mL)		GW (CFU/mL)	
	Dark	Light	Dark	Light
Initial Conc	$10^{5.6}$	$10^{5.6}$	$10^{6.5}$	$10^{6.4}$
2 min	$10^{5.6}$	**0**	$10^{6.5}$	$10^{6.4}$
10 min	**0**	**0**	$10^{6.5}$	$10^{6.4}$
30 min	**0**	**0**	$10^{6.5}$	$10^{6.5}$

The results show no significant light-induced toxicity for GW without tAgNP attachment. Based on the antibacterial mechanisms explored in Chapter 3, we postulate that the bacterial inactivation is achieved through a combination of localized heating within the flow tube, and ROS generation killing bacteria which comes within close contact of the catalyst.

To investigate this, confocal microscopy was used to image the reactivity of the fibres in real time under flow conditions using a similar approach as will be explored in greater detail in Chapter 5, and briefly earlier in Chapter 3 (Fig. 3.1.S9). In this system we are able to localize ROS generation to the tAgNP treated fibres by imaging the conversion of non-fluorescent H_2DCF to DCF which is emissive under 488 nm excitation. Using our 640 nm confocal laser, we were able to simultaneously excite our AgNP@GW fibres, while also exciting any produced DCF using our 488 nm laser (Fig. 4.1.5).

The confocal flow-catalysis experiment showed that the anchored particles were still capable of generating ROS, a process further increased by 640 nm excitation. However, the vast majority (but not all) of DCF emission was limited to the area immediately surrounding the fibres (Fig. 4.1.5). This is significant, as it supports our hypothesis that silver nanoparticles toxicity is not requisite on the leeching of ions to generate antibacterial activity.

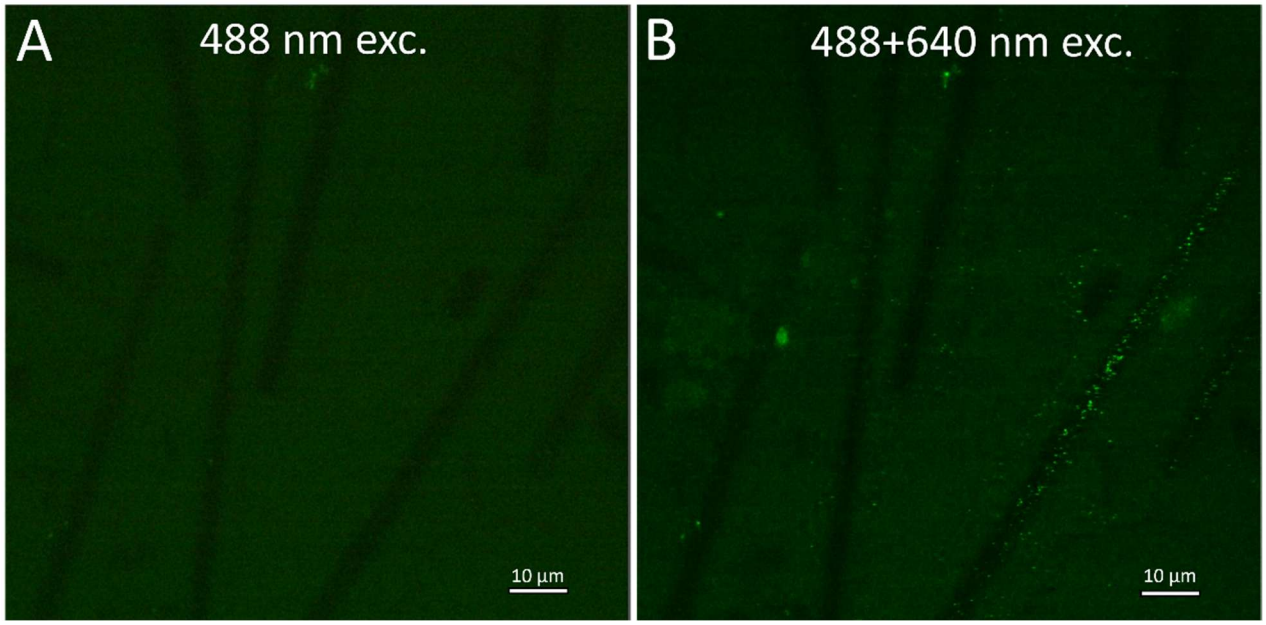

Fig. 4.1.5: Confocal microscopy images of AgNP@GW under flow of H_2DCF solution. A) Confocal imaging using 488 nm excitation, corresponding to the excitation of DCF. B) The same sample under simultaneous excitation with both 488 nm and 640 nm irradiation.

Conclusion

This preliminary exploration into light activated tAgNPs@GW for treating bacteria contaminated water proved to be a preliminary success with great potential for future experiments. This section focused largely on developing a strategy for anchoring tAgNPs onto GW using APTES and MPTES treated fibres, while also demonstrating their ability to maintain high antibacterial activity even in a heterogenous form. Of the surface treatments attempted, the amination of GW surfaces with APTES proved to be the most promising, enabling the uniform anchoring of AgNPs without significantly disrupting their optical properties. Proof-of-concept experiments showed that even in a fairly rudimentary flow system, complete bacterial inactivation could be achieved following just 2 min of residency time when white light illumination was used to irradiate the photoactive tAgNPs which were deposited on APTES treated GW fibres. This is an excellent early result, especially for a system which has significant room for optimization, as will be discussed in more depth in the future directions section of Chapter 6.

References

1. Black, K.; McBean, E. Indigenous Water, Indigenous Voice – a National Water Strategy for Canada's Indigenous Communities, *Can. Water. Resour. J.* 2017, *42* (3), 248–257
2. Truth and Reconciliation Commission of Canada, "Truth and Reconciliation Commission of Canada: Calls to Action," Accessed June 8, 2024

   https://nctr.ca/records/reports/
3. (2023). *Global Water Security 2023 Assessment*. United Nations University Institute United Nations, University Institute for Water, Environment and Health.
4. Berruti, I.; Nahim-Granados, S.; Abeledo-Lameiro, M. J.; Oller, I.; Polo-López, M. I. Recent Advances in Solar Photochemical Processes for Water and Wastewater Disinfection, *Chem. Eng. J. Adv.* 2022, *10*, 100248
5. B. Wang , C. R. Bourgonje and J. C. Scaiano , Fiber-glass supported catalysis: real-time, high-resolution visualization of active palladium catalytic centers during the reduction of nitro compounds, *Catal. Sci. Technol.*, 2023, 13 , 1021
6. A. Elhage , B. Wang , N. Marina , M. L. Marin , M. Cruz , A. E. Lanterna and J. C. Scaiano , Glass wool: a novel support for heterogeneous catalysis, *Chem. Sci.*, 2018, 9 , 6844
7. Henry, A. I.; Bingham, J. M.; Ringe, E.; Marks, L. D.; Schatz, G. C.; Van Duyne, R. P. Correlated Structure and Optical Property Studies of Plasmonic Nanoparticles, *Phys. Chem. C* 2011, *115* (19), 9291–9305

Chapter 5 – Real-time imaging of the Pd catalyzed nitro-to-amine reaction using advanced optical microscopy

Background

This project was launched with the goal of elucidating the nature of Pd catalysts on a single-molecule level during the nitro-to-amine reaction using Pd nanoparticles anchored to glass wool (Pd@GW). To achieve this, we wanted to take advantage of the advanced confocal/FLIM/TIRFM capabilities of our super resolution Nikon Ti2 Eclipse microscope system, combined with conventional methods such as TEM for catalyst characterization, and bench chemistry for reaction monitoring – ultimately providing a comprehensive catalyst characterization from the macro to molecular scale. This was made possible by using a fluorescent on-off probe based on a nitronapthalamide dye. This dye undergoes a large shift in absorbance upon reduction, allowing us to observe the reduction of our probe in real-time with little to no background interference from the oxidized precursor. Using this fluorescent probe, paired with the functionalities of our microscope, we were able to visualize our Pd@GW catalysts in action, under flow conditions. Our results from single-molecule microscopy enabled us to investigate the mechanism for our reaction, including residence time of our probe on our Pd, while also demonstrating that our catalyst is stable over 4 h of consistent flow reaction. This work demonstrates the value of single molecule microscopy in catalyst characterization, while also providing strong evidence that in the catalysis of nitro-to-amine reactions, the mode of catalysis is distinctly heterogeneous, with little to no catalyst migration involved in the mechanism – a point of debate in the literature. Throughout the project I worked closely with Dr. Bowen Wang. In this project I was involved in project design, synthesis of our on-off nitronaphthalimide probe, bench & scale up reactions, and was involved in the confocal and FLIM microscopy experiments alongside Dr. Wang. I also contributed to the writing of the paper, albeit not to the extent of my co-authors.

5.1: Published work: Fiber-glass supported catalysis: real-time, high-resolution visualization of active palladium catalytic centers during the reduction of nitro compounds

B. Wang, C. R. Bourgonje, J. C. Scaiano. *Catalysis Science and Technology*. 2023, 13, 1021

Abstract

The development of new flow-compatible high-performance catalysts requires the understanding of the activity of the material in the nanometric scale. Here we use a combination of fluorescence and electron microscopy, in-flow single molecule fluorescence, and bench chemistry, combined with a fluorogenic system, allowing an intimate understanding of the properties and performance of palladium on glass wool (Pd@GW) in the nitro-to-amine catalytic reduction. The process is monitored starting from the nitro-compounds' reversible association with catalytic centers, to the behavior, interaction, and departure of reduced amine products. The catalyst used, Pd@GW, is ideal for flow heterogeneous catalysis applications requiring a fixed bed catalyst. Using advanced microscopy techniques, we are able to fully characterize our catalyst *in situ*, providing deep insight into the catalytic abilities of the material. We also explore under flow conditions if Pd clusters could migrate and redeposit elsewhere on the surface of the heterogenous support. Overall Pd migration seems to be minimal over several hours, with the catalyst stability assisted by APTES anchoring. Further, some active Pd sites seem to have enhanced catalytic activity after reaction, as evidenced by *in situ* imaging of the catalyst. This deep understanding of the real activity of heterogeneous catalysts will help researchers to improve present catalysts and explore new catalysis systems.

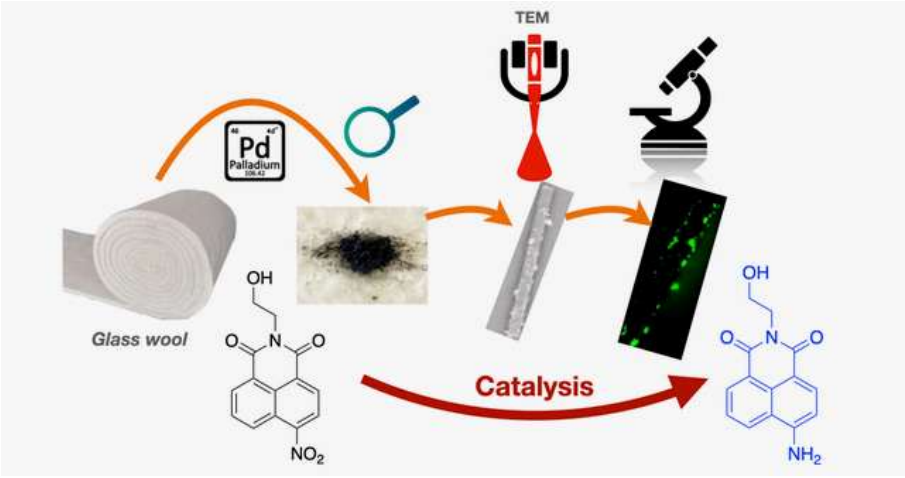

Introduction

Palladium nanostructures are among the most interesting heterogeneous catalysts because they feature high activities in wide applications, such as water splitting,[1] coupling reactions,[2] CO oxidation, and nitro reduction.[3] However, there is still debate about the detailed mechanism of heterogeneous Pd catalytic processes.[4,5] In the simplest cases, as shown in Scheme 5.1.1, the reaction may proceed through a 'truly' heterogeneous process on the catalyst surface where solid Pd^0 remains largely unchanged following the reaction. The catalytic reaction may also be performed through a mechanism resembling homogenous catalysis wherein reactive Pd ions are leached into solution; or a 'semi-heterogeneous' mechanism by the leaching small Pd particles in solution; these pathways are associated with Pd transport.[5,6]

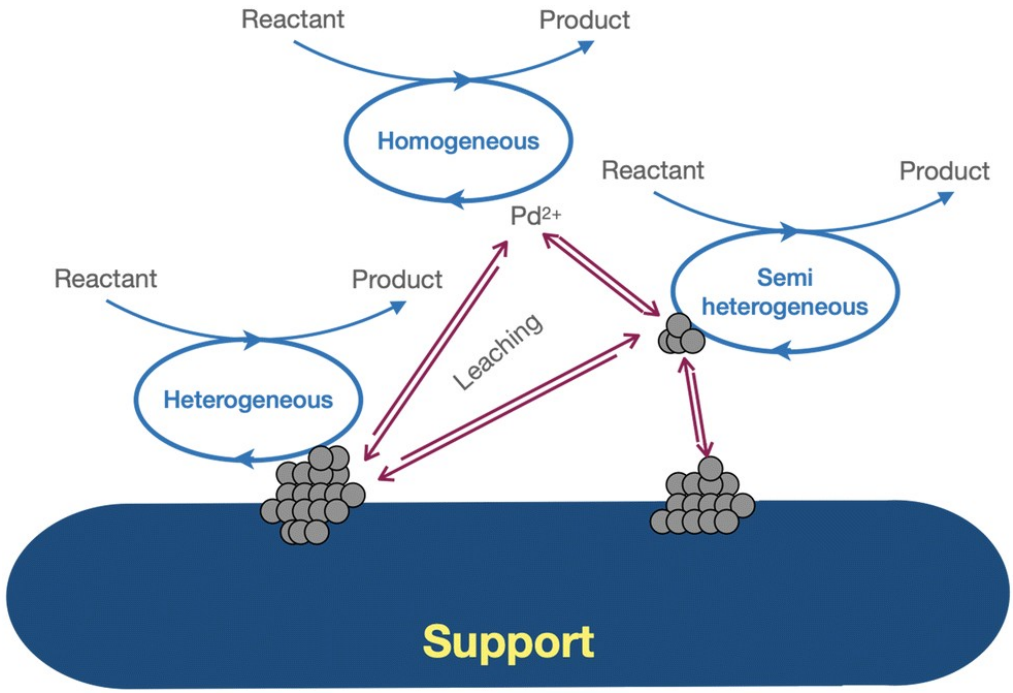

Scheme 5.1.1 Interconversion of different catalyst types in solution. Heterogeneous process: reactant attached and formed product on the Pd catalyst surface. Homogeneous process: reactions catalysed by leaching of Pd ions in solution. Semi-heterogeneous process: reactions catalysed by leaching of Pd clusters.

In C–C coupling, many researchers propose a dynamic process of transformation of Pd species from the surface to dissolved palladium of Suzuki reactions[7] and Heck reactions.[8] In the proposed mechanism, the solid Pd will be released into active Pd(II) complexes and some Pd(II) will re-adsorb onto the support, agglomerating into different sized Pd particles.[9]

The study of palladium leaching, agglomeration, and migration under reaction conditions is still a challenge. To monitor palladium leaching the traditional approach is to use ICP-OES/MS and poisoning tests to gauge the total leaching or heterogeneous performance at a particular reaction time. However, while testing leaching does provide information on the stability of heterogenous catalysts, it does not shed light on micro-scale catalyst particle migration, which can be a major factor in some Pd reactions. For Pd agglomeration and migration analysis, surface morphology techniques such as electron microscopy are extremely useful in heterogeneous catalysis research, but can only characterize the structure before and after the reaction period. In addition, electron microscopy largely provides information under non-reactive conditions. That is, electron microscopy can yield detailed structural information, but generally under high vacuum conditions where no liquid phase reaction takes place. Thus, researchers can only infer the reactivity of heterogenous catalysts from their surface structures. Usually, these predictions also rely on other techniques such as XPS, EDS, and XRD.[10] However, these methods are also not directly reflective of the heterogeneous catalytic reactivities under reaction conditions.

Compared to the 'end-point' leaching or structural change results, it is more important to understand the dynamic reactivity changes during the reaction under *in situ* conditions, something that is often overlooked in catalysis research. To acquire this level of detail, single molecule spectroscopy (SMS) has been widely used in catalysis research. Over the past decade, this approach has enabled the understanding of some reaction mechanisms at the single-molecule level with single catalytic site resolution.[11–14]

Recently, our group published a single molecule investigation on Pd@TiO_2 catalyzed Suzuki reactions.[15] The results proved that palladium can migrate by millimetres during the coupling reaction under *in situ* flow conditions. However, this may only be true for TiO_2 supported Suzuki reactions, and the need for further investigation of Pd catalyst behaviour remains.

As the field moves forward, we are interested in three questions:

(i) Is Pd agglomeration/migration happening in other reactions?

(ii) Does the surface affect Pd stability?

(iii) Is there observable Pd agglomeration/migration occurring during the reaction under *in situ* conditions?

In this paper, we focus on the Pd catalysed nitro reduction reaction. Reduction of nitro compounds to the corresponding amines is a significant reaction with great importance in both academia and industry.

As we move forward developing flow-compatible materials, we emphasize the development of catalytic materials based on glass wool (GW), a largely unexplored support decorated with metal or metal oxide nanoparticles.[16–18] Glass wool is reasonably inert, easy to modify and decorate, inexpensive, and readily available. These GW-based materials have proven efficient in several catalytic processes.[16, 17, 19] Additionally, GW anchored catalysts can easily be removed from their environment (*e.g.*, with tweezers) within seconds, making their use much simpler compared to centrifugation or filtration which may be needed with powder catalysts.

However, when working with fixed-bed flow catalysts it is necessary to understand the behaviour of catalytic sites *in situ*. Such information can enhance our understanding of catalyst performance, and help design effective and robust flow catalysts. In order to gain this understanding, we selected palladium nanostructures deposited on GW (Pd@GW) a material that has shown excellent catalytic properties in earlier work for the nitro reduction reaction.[13,16]

There are several reports about deactivation of Pd catalysts by Pd leaching. In the Pd catalysed phenol hydrogenation reaction, the Pd loading decreased from 5.0% to 3.9% for commercial Pd/C after the 3rd run. For the amino-functionalized nanoporous polydivinylbenzene supported Pd catalyst, the loading decreased from 4.8% to 4.6% after the phenol hydrogenation reaction.[20] Nájera *et al.* reported the use of Pd loaded on carbon quantum dots for nitro reduction, where leaching of Pd from the catalyst after ten runs was found to be 16%. The TEM images of the reused catalyst after ten runs showed that the structure was largely preserved.[21]

There are also reports where Pd leaching is below the detection limit in the nitro reduction reaction.[22–25] Most Pd in hydrogenation reactions can be reused for as many as five runs without any palladium leaching in the reduction reaction.[22] Kobayashi *et al.*[23] reported polysilane-supported palladium in the continuous-flow hydrogenation of aromatic nitro compounds. It was noted that leaching of palladium was not observed in any of the reactions (detection limit: 0.03 ppm). Pd on Pd/ZrP and FP@Si@Pd/C showed no Pd leaching after nitro reduction by the hot filtration test.[24,26] Colacot[27] developed fibre catalysts Pd-FibreCat/Pd-SMOPEX and applied them in coupling reactions. The leaching of Pd is also minimal under their drastic conditions.

The glass fibres used in this study have a diameter of ~10 μm, making them suitable for many imaging techniques, such as electron microscopy, conventional optical microscopy, confocal microscopy and fluorescence lifetime imaging microscopy (FLIM). Combined, these techniques enable the capture of uniquely intimate details of the catalytic process, from the association of reactants at the catalytic site,

to their conversion to products, their release dynamics and the interaction during the brief period in which nascent products remain near the catalytic site. Thus, while SEM or TEM could characterize the nanostructures, they provide little detail on reactivity. Meanwhile, diffraction limited techniques, even with super-resolution strategies, can miss information on surface morphology and behaviour during catalysis. In fact, simultaneous analysis of molecular kinetics and visualization of morphology in real-time under reaction conditions is rarely reported.

The work in this contribution aims at achieving a detailed understanding of catalysts based on glass wool which holds great promise for heterogeneous flow catalysis, including photocatalysis. The simplicity and availability of GW make the understanding of its role important if this material is to gain acceptance as a standard tool in organic catalysis. Here we try to understand how the active material, palladium in our case, deposits on GW and how this affects the material performance beyond simple catalyst immobilization. With this goal in mind, we combine single molecule techniques and confocal/FLIM microscopy to visualize reactions on the heterogeneous catalyst. We were also able to monitor the same fibres by optical, fluorescence and electron microscopy, all for the same material that shows excellent performance at the bench. The reaction of choice to characterize our system is the reduction of an organic molecule with a nitro moiety to the corresponding amine, Fig. 5.1.1(a), where NN3 is a molecule also utilized in earlier work.[28]

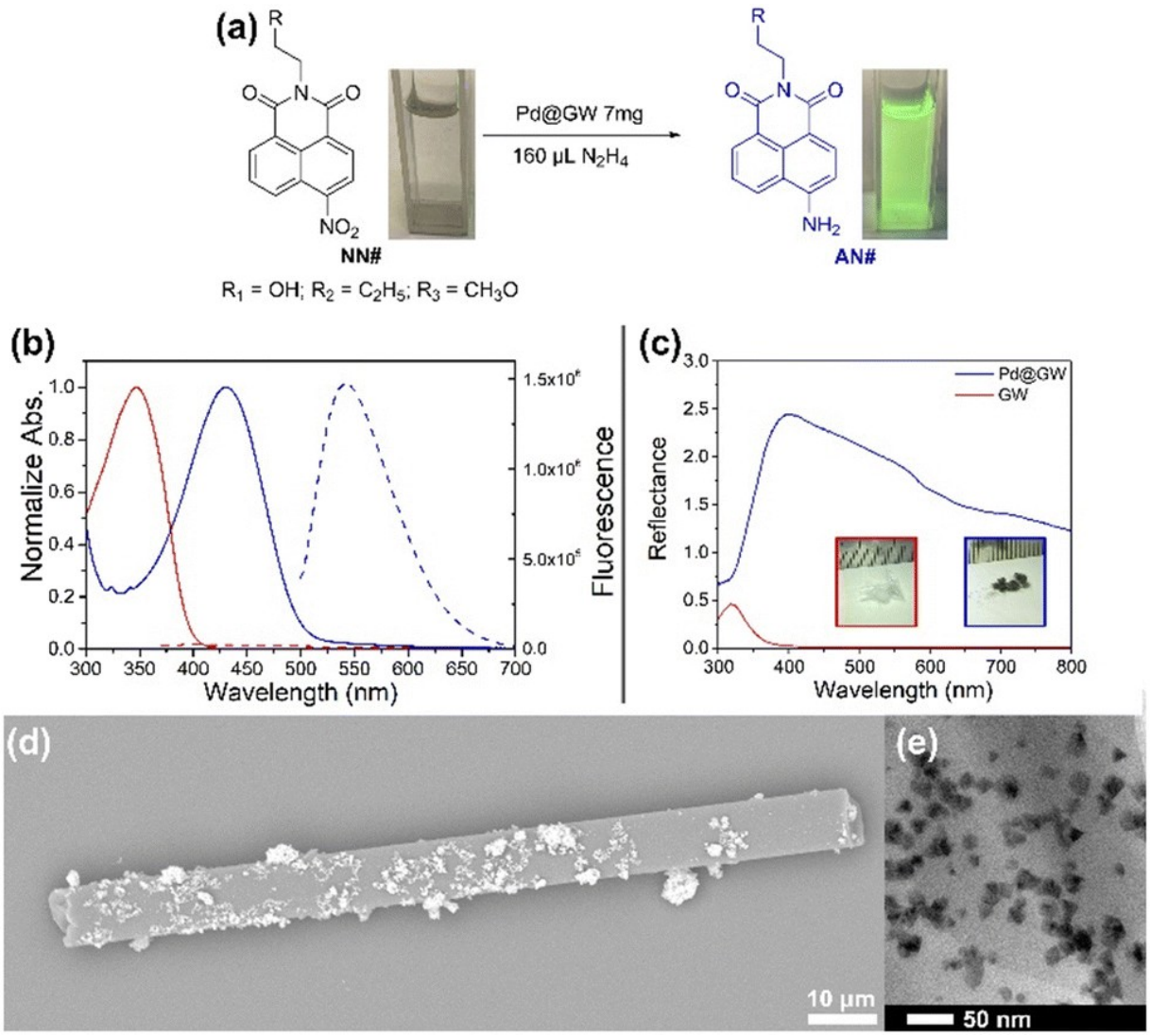

Fig. 5.1.1: (a) Reduction of the fluorogenic probes NN# (#: 1–3) R1: –OH, R2: $–C_2H_5$, R3: $–OCH_3$. Cuvette images show solutions of 0.1 mM NN2 under UVA light (365 nm, 4 W) for NN2 and AN2 in the presence of acetic acid (100 µL 3.3 M acetic acid). (b): Normalized absorption (solid line) and fluorescence (dashed line) spectra of NN1 (100 µM in water, red) and AN1 (100 µM in water, blue). Excitation wavelengths used were 350 nm for NN1, and 488 nm for AN1. Note that fluorescence is not normalized and the difference in amplitude reflects the contrast of the dye (AN1 *vs.* NN1). The UV–vis and fluorescence of AN2 are shown in Fig. 5.1.S1. (c) Diffuse reflectance spectrum of GW and Pd@GW. The inset are photos of GW (left) and Pd@GW (right) (the ruler small division is 1 mm). (d) SEM (COMPO-mode) of a Pd@GW fiber on a coverslip after fluorescence microscopy experiments; (e) shows a close-up TEM image of the of Pd@GW surface. The Pd@GW loaded coverslip was removed from the flow cell after the microscopy experiment and analyzed by SEM. The EDS analysis (Fig. 5.1.S10) confirmed that PdNPs were successfully decorated onto the GW by the I-2959 photoreduction process.

Experimental

Materials

4-Nitro-1,8-naphthalic anhydride (95%), Butylamine (99.5%), Ethanolamine (98%), Glass Wool (Non-Treated, pkg of 50 g), Methanol (spectrophotometric grade > 99.8%), Hydrazine solution 35 wt.% in H_2O, Palladium (II) acetylacetonate (99%) were purchased from Sigma-Aldrich. Irgacure-2959 was a gift from BASF and I-907 from Ciba Specialty Chemicals. All solvents (HPLC grade) were dried using molecular sieves. The MilliQ water was obtained by purification of deionized water using a Thermo Scientific™ Barnstead™ GenPure™ water purification system (conductivity 18 MΩ cm-1).

Catalyst synthesis

Palladium on glass wool (Pd@GW) was prepared by a procedure reported earlier by our group, using GW that had been pre-treated with APTES.[16] This method successfully attaches APTES to the surface of GW, as shown by XPS and NMR in our previous work.[16,29] Briefly, GW was washed with NaOH solution to remove the organic debris and washed with piranha solution before treatment with APTES as described previously [the 10 µm wide fibers used are very long (a few centimeters), too long for microscopy, where the preference is to have the fibers rest flat on the surface of the cover slip used]. In order to obtain microscope-compatible fibers, we ground APTES-treated fibers to obtain pieces in the 40–100 µm length range. Palladium decoration was performed following this initial grinding. We anticipate Pd decoration on the walls of the fibers, but unlikely on the ends that do not have APTES derivatization. We note that for bench experiments the preparation of Pd@GW was the same except the grinding step was not performed.

In order to decorate the APTES treated GW with Pd, Pd^{2+} must be reduced to form PdNPs. Pd^{2+} can be reduced using common reducing agents such as $NaBH_4$ or H_2,[30] or through photochemical reduction.[31] In this work a photochemical approach was favored as it allows for easy temporal control over the reaction, and generates PdNPs with the desired morphologies.[13]

Under UVA irradiation, photoinitiator Irgacure-2959 (I-2959) can generate highly reductive ketyl radicals through Norrish I cleavage,[32] and reduce the Pd^{2+} ion to Pd^0. Palladium atoms aggregate spontaneously to form nanostructures on glass wool. In order to remove all organic debris, a calcination process at 500 °C was applied before microscopy experiments. The Pd@GW synthesis scheme is shown in Scheme 5.1.2, along with a representative TEM image and a histogram showing the size distribution (Fig. 5.1.5).

The particles were largely heterogenous with many spherical particles with a few triangular plates[33] and their size was 13.5 ± 0.4 nm. Fig. 5.1.1 shows several images of the catalytic fibers, from their macroscopic appearance to fragments of individual fibers and the details of PdNPs on the GW surface. A size histogram and corresponding region of measurement is available in Fig. 5.1.5.

Glass wool pre-treatments

Firstly, 500 mg of as-purchased glass wool was washed with 1 M NaOH solution under sonication (15 min × 3) and rinsed with MilliQ water. After drying under argon, the glass wool was treated with piranha solution (3:1 concentrated sulfuric acid and 30% hydrogen peroxide solution) for 3 h. Then the pre-treated glass wool was rinsed with MilliQ water and dried under argon.

Activation using (3-Aminopropyl) triethoxysilane (APTES)

The pre-treated glass wool was immersed in 1% APTES solution in toluene (99.5%) and refluxed overnight. After cooling down to room temperature, the APTES-treated glass wool was washed with toluene (5×), methanol (5×), and MilliQ water (5×) before drying under argon. The APTES-treated glass wool was then ground to small pieces and kept under argon.

Palladium decoration

The palladium was deposited on glass wool by a photo-doping method using I-2959 (**1**) as photoinitiator[16]. The ketyl radicals (**3**) were generated under UVA irradiation by Norrish Type I cleavage. The active radicals generated then reduce Pd^{2+} into Pd^0. The Pd^0 aggregate to Pd cluster or Pd nanoparticles and attached on the surface of APTES-modified glass wool. Briefly, 500 mg of APTES modified glass wool were immersed in 150 mL MeOH solution of 75 mg $Pd(acac)_2$ and 113 mg of I-2959. The system was purged with argon for 15 min and left under UVA irradiation for 4 h. The palladium modified glass wool (Pd-GW) was then washed with MeOH (3×) and MilliQ (3×) to remove unattached Pd particles and organic residue. The clean Pd@GW was dried and stored under argon for future use. The Pd loading Pd@GW was 2.0± 0.3% by ICP-OES.

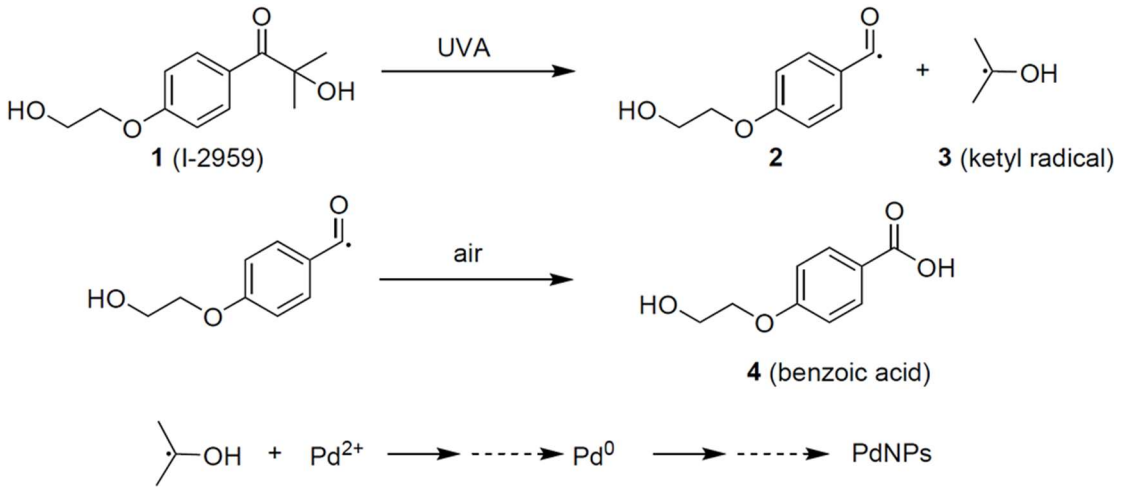

Scheme 5.1.2: Photolysis of I-2959 and its radical products in the synthesis of Pd nanoparticles. The benzoyl radical (2) form corresponding benzoic acid (3). In earlier reports, the benzoic has been shown to stabilize metal nanoparticles.[39]

Fluorescent on-off probe synthesis

In order to test for catalytic activity we needed fluorogenic molecules with good fluorescence contrast. Based on earlier work[28] we decided to use nitronaphthalimides (see Fig. 5.1.1(a)). In this work two different nitronaphthalimide probes were synthesized, each with a functionalized chain containing an alcohol (NN1) or alkyl (NN2) functional group (Fig. 5.1.1(a)). The goal was to produce probes suitable for monitoring the bench reaction in aqueous and organic conditions. However, for microscopy experiments NN1 was exclusively used, as it features superior solubility in aqueous conditions. The synthesis of NN2 is available in the SI.

Synthesis of NN1

4-nitro-1,8-naphthalic anhydride (195 mg, 0.8 mmol) and a slight excess of ethanolamine (52 µL, 0.87 mmol) were dissolved in 30 mL of ethanol and refluxed for 3 h (Scheme 5.1.3). After cooling down to room temperature, the solvent was removed under reduced pressure. The product, NN1, was purified by recrystallization, yielding light yellow needle-like crystals. The absorption and fluorescence spectra are shown in SI section 2, the NMR and ESI spectra are in SI section 4.

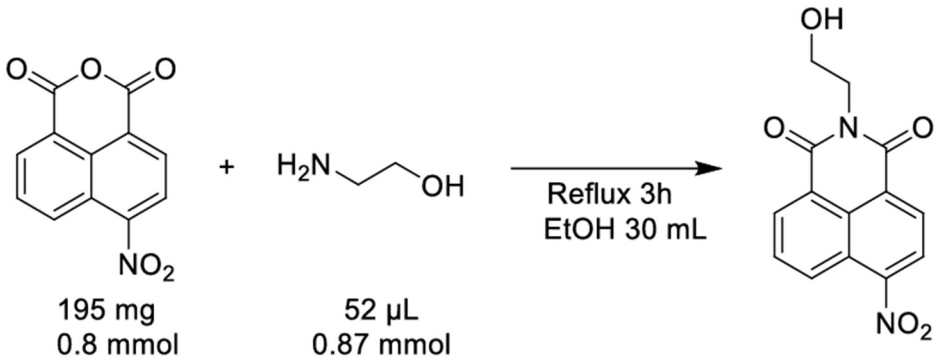

Scheme 5.1.3: Synthesis of NN1.

The details of the synthesis for NN2 are given in the SI (Scheme 5.1.S1). The reductive chemistry that leads to a major fluorescence enhancement is shown in Fig. 5.1.1(b). In the oxidized form of the dye, the molecule features no absorption at the excitation wavelength of 488 nm and subsequently no fluorescence under our confocal excitation regime. Reduction of the nitro group of NN# leads to the highly fluorescent amine form, AN#. This effectively creates an "off–on" switch to detect the reduction of the probe, allowing the visualization of reactive Pd sites on our catalyst. To test our "off–on" emission, the bench scale NN# reduction reactions are shown in the SI (Fig. 5.1.S1–5.1.S7).

Imaging techniques

All microscopy experiments were carried out in a Nikon Eclipse Ti2 inverted microscope equipped with a Ti2 platform and confocal work with a Nikon A1 system. A Becker and Hickl FLIM module was incorporated in the same Nikon system. Briefly, a solution of NN1 and N_2H_4 was pumped through a Pd@GW loaded flow cell; a typical 100 µm long GW fiber has a weight of about 0.02 µg and contains about 0.4 ng of Pd. The NN1 reduction was catalyzed by Pd@GW and formed AN1 on the catalyst surface. The *in-situ* product AN1 was excited by a CW 488 nm laser for TIRFM and confocal work, while a pulsed 488 nm laser was used for FLIM. The samples were analyzed by confocal, FLIM, and single molecule techniques through 488 long pass filters. The microscopy experiment setup is shown in Fig. 5.1.2.

Studies were performed on the same fibers used in other optical experiments, including transmission electron microscopy and FLIM. In our 3D confocal and FLIM studies the vertical step of each '*z*' stack is 100 nm, and the pixel size is 70 nm. When we examined the selected fiber under reactive NN1 flow conditions we collected 41 images, equivalent to 4.1 µm in the *z* axis. The complete set of 41 images is included in the Fig. 5.1.S17 and 5.1.S18, while four selected ones are shown in Fig. 5.1.3.

Catalyst loaded coverslip preparation

The Pd@GW catalysts were deposited on a glass coverslip and placed in an oven for annealing process at 500 ℃ to burn off any organic residue before microscope experiments. The loaded coverslip was cooled down to room temperature and placed in a flow cell (Live Cell Instruments, Chamlide model CF-S25-B-C) for the experiment.

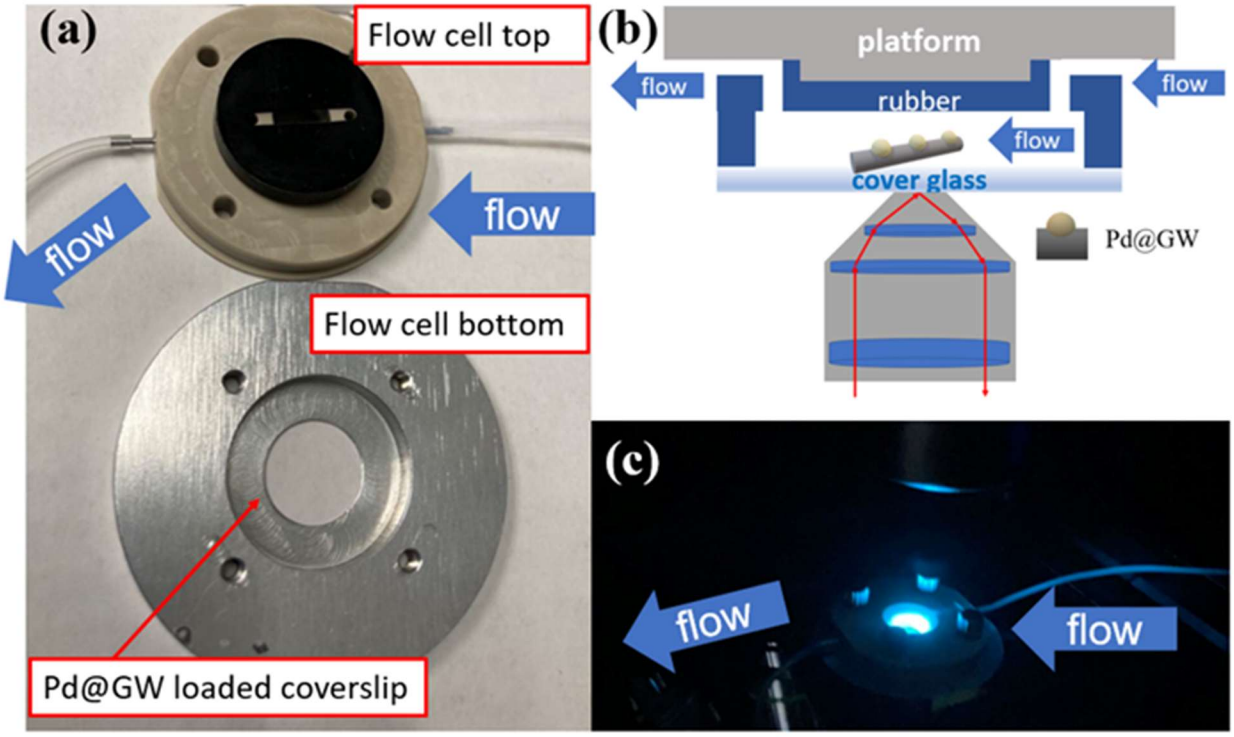

Fig. 5.1.2: (a) Picture of flow cell, a Pd@GW loaded coverslip was placed in the flow cell bottom. (b) Scheme of flow cell mounted on the top of objective and laser light path. (c) Mounted flow cell in the microscope, the blue light in the middle of flow cell from the 488 nm laser.

Single molecule experiments

1 mL of 1μM NN1 water solution, 160 μL of N_2H_4 solution (35%, ×100 dilution in water) and 100 μL of acetic acid (0.033M in water) were premixed and injected into the flow cell immediately. The reaction solution was introduced into the flow cell using a syringe pump with 0.5mL/h speed. Fluorescence signals were collected by an ANDOR iXon Ultra EM-CCD camera. Imaging was performed using the NIKON NIS Elements confocal imaging software.

Confocal experiments

Following the single molecule experiment, 1 mL of 0.1mM NN1 water solution, 160 µL of N_2H_4 solution (35%, in water) and 100 µL of acetic acid (3.3M in water) were premixed and injected into the flow cell immediately. The reaction solution was introduced into the flow cell using a syringe pump with 0.5mL/h speed. Fluorescence signals were collected by an ANDOR iXon Ultra EM-CCD camera. Imaging was performed using the NIKON NIS Elements confocal imaging software.

Confocal experiments with different concentrations

Different concentrations of NN1 water solution, 160 µL of N_2H_4 solution (35%, in water) and 100 µL of acetic acid (3.3 M in water) were premixed and injected into the flow cell immediately. The reaction solution was introduced into the flow cell using a syringe pump with 0.5 mL/h speed. The flow cell was pre-rinsed with 0.3 mL of the respective solution before recording each trial. A 50 s 'Time measurement' was applied during the flow reaction.

FLIM experiments

Without moving the sample, the reaction of NN1 to AN1 was examined by B&H FLIM control module in the NIKON system. The instrument was equipped with B&H BDS-SM picosecond diode lasers delivering picosecond light pulses (480.511 nm, 50MHz, BDS-488-SM-FBC). The fluorescence signal is collected by an ID-100-50 SPAD detector and processed using the Becker & Hickl SPC-150N TCSPC/FLIM module.

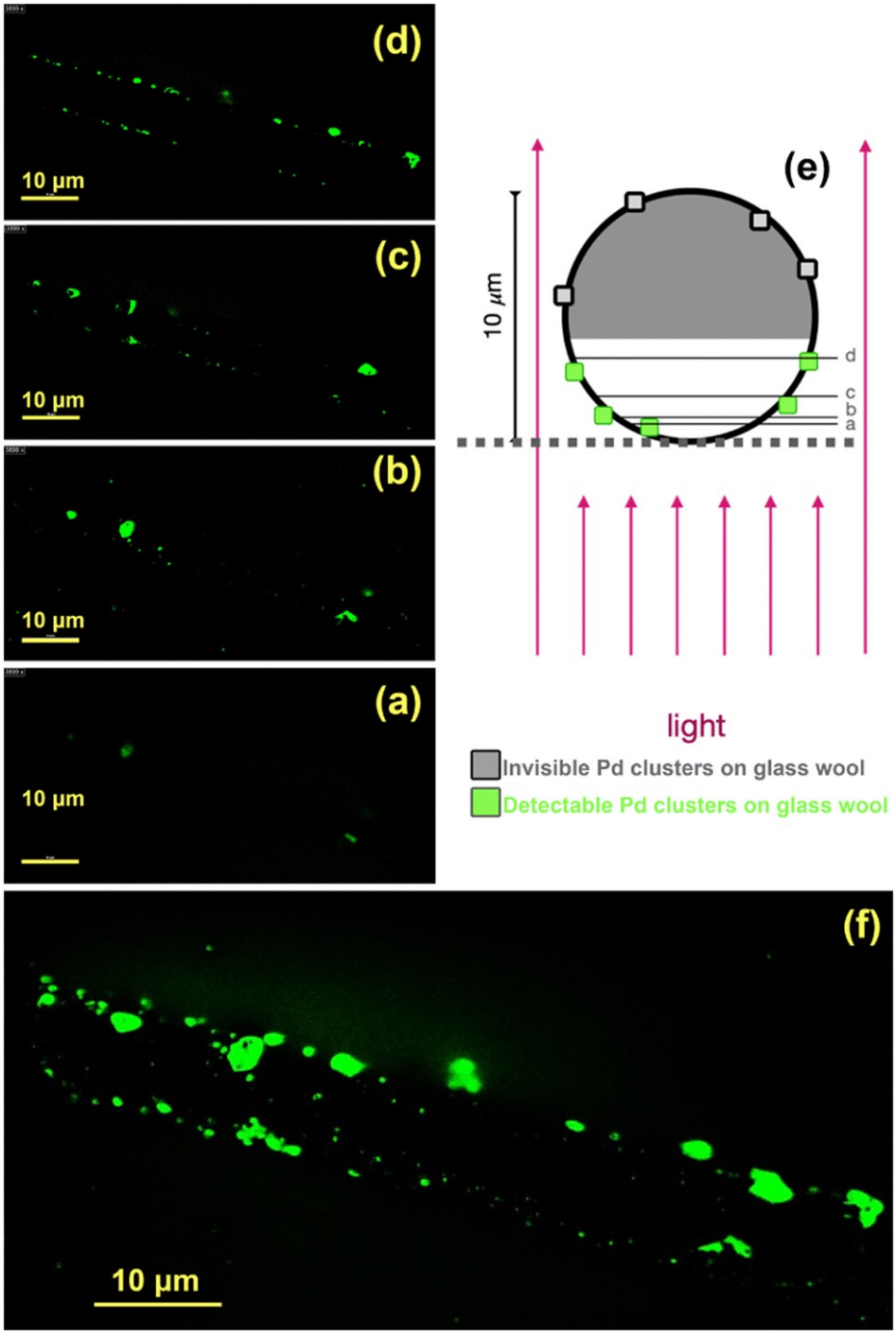

Fig. 5.1.3: (a–d) Representative confocal images at selected distances from the bottom of the fiber (in contact with the cover slip). The green regions show reactive areas, where the fluorescence from nascent AN1 products is captured. (e) The green squares represent detectable fluorescent spots, while grey squares are invisible in these experiments, regardless of their possible fluorescence. The thin horizontal lines in the scheme are labelled to show the positions of the images on the left (a–d). (f) Confocal 2D fluorescence image (sum of 41 *z*-planes as illustrated in Fig. 5.1.S17 and 5.1.S18).

In the confocal experiment of Fig. 5.1.3, the sample is illuminated by a 488 nm CW laser and the fluorescence detected from the bottom, as the fiber sits on a cover slip. While the fiber is made of glass, for practical purposes, the upper half is not detectable, as direct illumination is only received by particles on the surface of the lower half of the fiber, see the diagram in Fig. 5.1.3. In effect, the fiber is an imperfect cylindrical lens, randomly placed on the cover slip. Distances in Fig. 5.1.3 correspond to the separation between the confocal *x*–*y* plane and the cover slip surface. Notice that as we move up, the width of the sample (fluorescent spots in the *x*–*y* plane) increases, but is always below 10 μm. For additional imaging details, including FLIM, TIRFM, and electron microscopy, see the SI.

Results and discussion

Once a fibre, such as the one shown in Fig. 5.1.1(d), undergoes reaction, the evidence for catalytic events can be detected by the emission of fluorescence at or near palladium sites. Using confocal fluorescence microscopy one can see the emission in images on the *x*–*y* plane and for a given depth in the vertical or *z*-plane (see Fig. 5.1.3). We will now discuss a 2D image, the sum of 41 *z*-planes which illustrates the emission observed when a 0.1 mM aqueous solution of NN1 and hydrazine flows over the catalyst, Fig. 5.1.3(f). See Fig. 5.1.2 for details of the flow set up.

The SI includes fluorescence maps of the same fibre at different *z*-axis levels across the thickness of the fibre placed in the *x*–*y* plane. The 2D sum image of Fig. 5.1.3(f) is the result of combining a stack of 41 confocal images on different *z*-focus planes. Each *z* step is 100 nm, in total covering about half the fibre diameter (4.1 μm), nearest to the cover slip. Confocal experiment details are provided in the SI.

There is a fundamental difference between the information in Fig. 5.1.1(d) and in fluorescence microscopy acquisitions, Fig. 5.1.3(f). The SEM image in the former (combined with EDS spectra, see the SI) shows the presence of Pd structures, but does not show if they have catalytic activity, or how much. In contrast, emission centers in fluorescence microscopy are unequivocal evidence for the formation of highly fluorescent AN1. The fact that the emission can be quantitatively extinguished by flowing solvent shows that AN1 is not irreversibly attached to Pd centers. Even where the fluorescence shows the occurrence of the reduction chemistry displayed in Fig. 5.1.1, the cluster of Pd nanostructures does not necessarily have the same catalytic activity everywhere. Using confocal microscopy it is possible to map this real activity on the Pd@GW surface. This is illustrated in Fig. 5.1.4 for one specific Pd feature selected from the top region in the figure and is about 2.1 μm wide.

Analysis across different sets of cross-sections and various Pd features of different sizes shows significant intensity variations. This real reactivity difference cannot be characterized by electron microscopy. However, individual nanoparticle activity cannot be directly resolved. This is not surprising, as the pixel size (70 nm for confocal microscopy) is about five times larger than the average PdNP, measured at 13.5 ± 0.4 nm (Fig. 5.1.5).

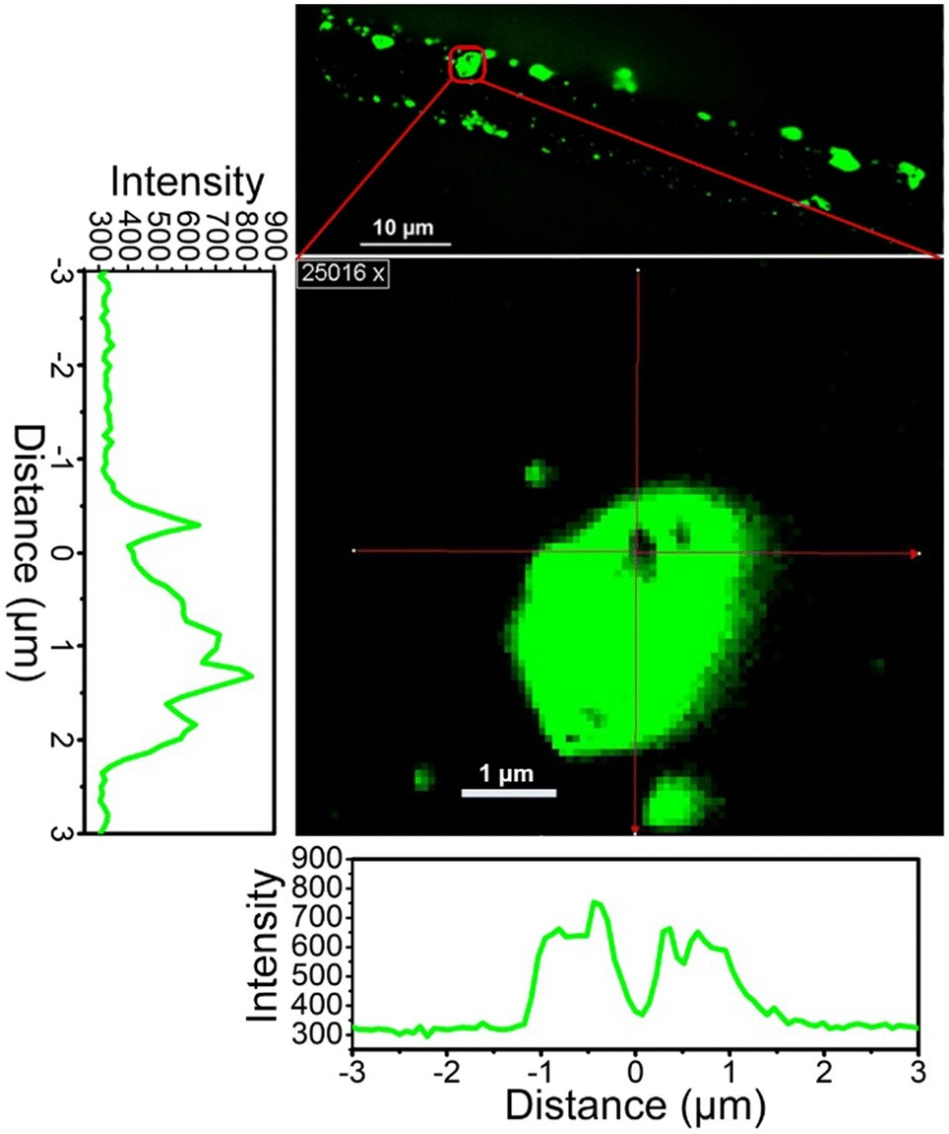

Fig. 5.1.4: Emission intensity profile across a selected PdNP cluster (region of interest outlined in red). The crosshair shows the regions represented in the horizontal and vertical intensity profiles, centered around a dark spot (inactive area) in the catalytic site. Images of other Pd features and for this image near the brightest region are included in the SI. Note that beyond the valley where only weak emission is detected, the intensity is not constant (see Fig. 5.1.6). Pixel size is about 70 nm.

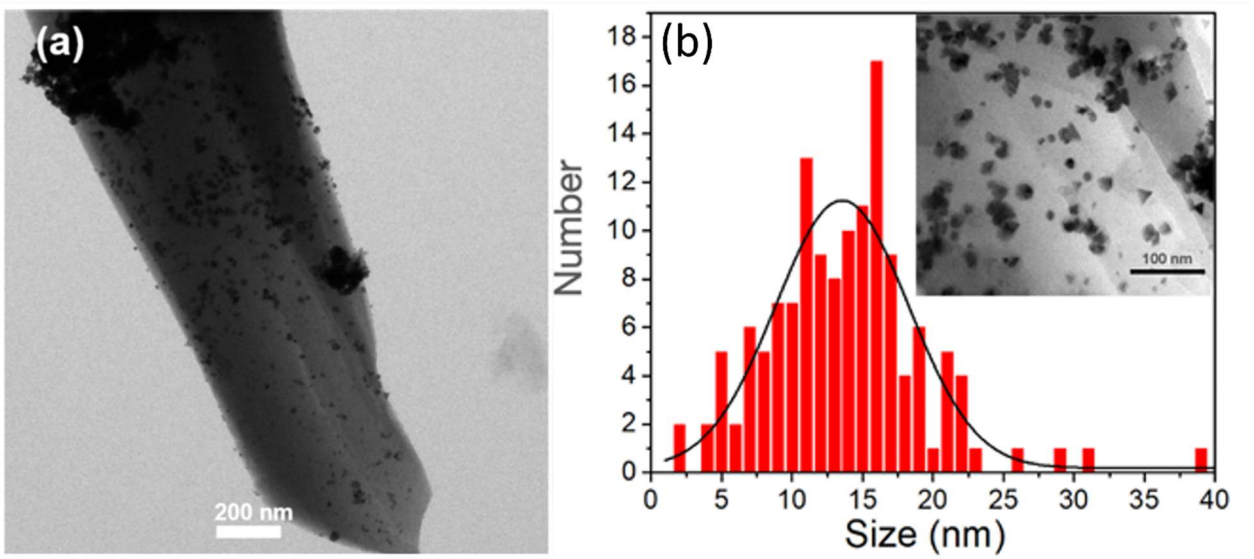

Fig. 5.1.5: (a) TEM image of representative fragment of Pd@GW. (b) Particle size distribution for PdNP in Pd@GW. Inset: Representative TEM image of PdNPs on Pd@GW fragment. Note that only stand-alone particles were included for counting, so large clusters do not count towards the size histogram.

It is possible to identify from the confocal images a few areas of interest, principally where catalytic sites are located, and thus induced emission is taking place. This is illustrated for 0.1 mM NN1 solution in the top panel in Fig. 5.1.6(a), while the (b) panel shows the emission levels monitored over a 50 s (500 images) period for a fixed reagent concentration. The areas selected in Fig. 5.1.6 do not represent single catalytic particles (Fig. 5.1.1(e)), but rather clusters of PdNPs with many catalytic sites. We have tested for a linear dependence between the steady state concentration of the fluorescent product [$AN1_{ss}$] and the solution concentration of the nitro reagent, [NN1]. This is illustrated in Fig. 5.1.6(c and d) for several of the areas in Fig. 5.1.6(a), further details are available in the SI, Fig. 5.1.S20–5.1.S26. We note that sites #3, #4 and #5 are control sites with no detectable catalytic activity, with sites #3 and #4 monitoring an inert region of the fiber and site #5 being away from the fiber altogether.

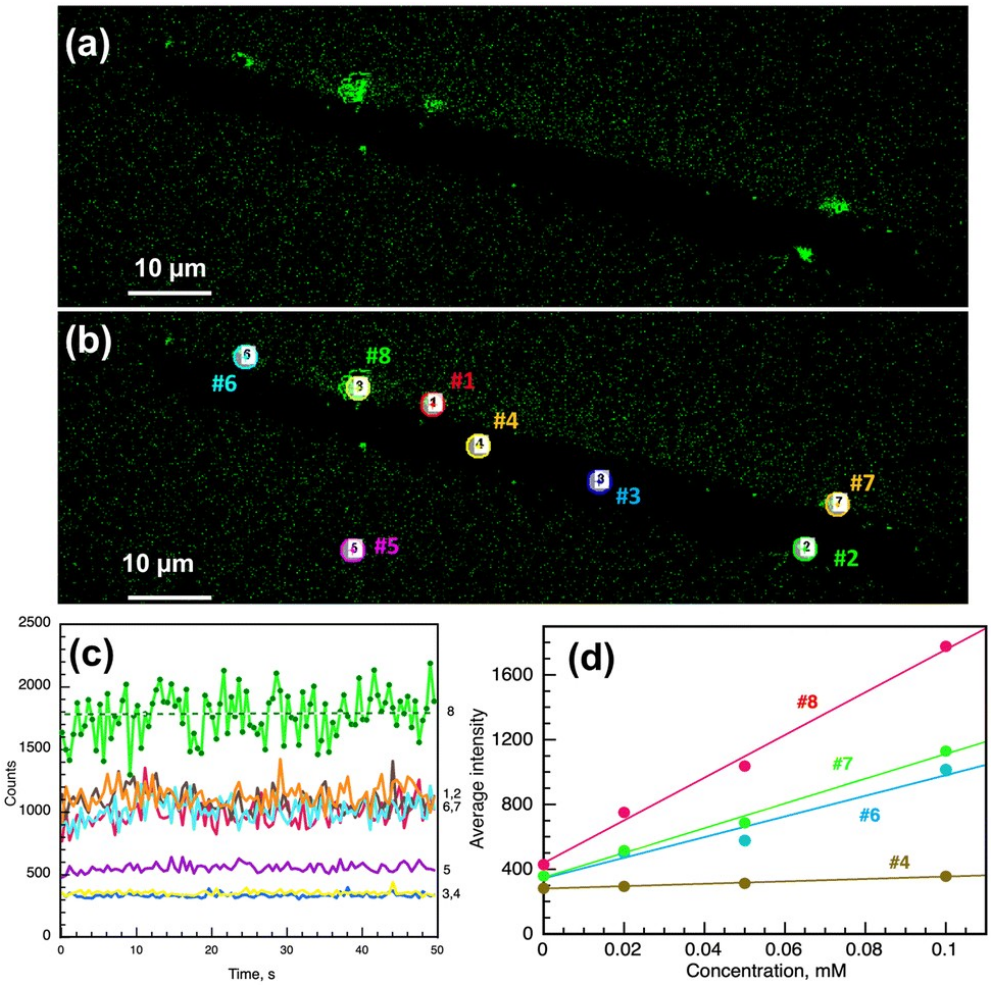

Fig. 5.1.6: (a) A selected layer of the confocal image of the fiber of Fig. 5.1.3(f) (700 nm from the bottom); (b) selected areas of interest, and (c) emission counts recorded in selected regions (region numbers shown on the right). Fluctuations usually amount to ±10% and reflect true emission changes at these locations (*i.e.*, they exceed random noise). For location #8 (the same location as Fig. 5.1.4) the actual points have been included to emphasize emission variations; the horizontal green dash line shows the average emission (1776 counts at location 8) compared with background (#5) and inert surface on the Pd@GW catalyst (#3 and #4). Sites #1, #2, #6, #7 and #8 are representative Pd sites on GW. Confocal fluorescence intensity traces under different concentrations are included in the Fig. 5.1.S20–5.1.S26. (d) Average fluorescence intensity as a function of NN1 concentration for positions #4, #6, #7 and #8. Fluorescence of other locations is shown in the SI.

While the plots of Fig. 5.1.6(d) show the expected linear dependence, the slopes are different. This reflects that at each location the number and density of catalytic sites is different. In the context of the proposed mechanism (*vide infra)* this can be rationalized as variations of [Pd@GW] for each selected region. The variations with NN1 concentrations can be achieved by changing the concentration in real time on the same fiber sample, including cancelling the fluorescence by flowing water. This supports that the initial association step with the catalytic site is an equilibrium. Further, the majority of active

sites in clusters of Pd@GW must be vacant most of the time. If this was not the case, increasing the concentration of the reagent could not have a linear effect on [AN1$_S$]. In fact, under saturation conditions increasing [NN1] would have no effect on the observable emission intensity.

In order to learn about $k_{release}$, we performed single molecule experiments using Total Internal Reflection Fluorescence Microscopy (TIRFM), where the frequency and duration of emission events can provide information on the dynamics of the catalytic process. Fig. 5.1.7 illustrates such measurements for one specific location on the fiber where catalytic events show repeated emission bursts from the same region. We note that the region (3 × 3 pixels) is large enough to incorporate multiple catalytic sites. Note that the bursts are of approximately equal amplitude, a common observation for events involving the generation of just one molecule per emission burst.

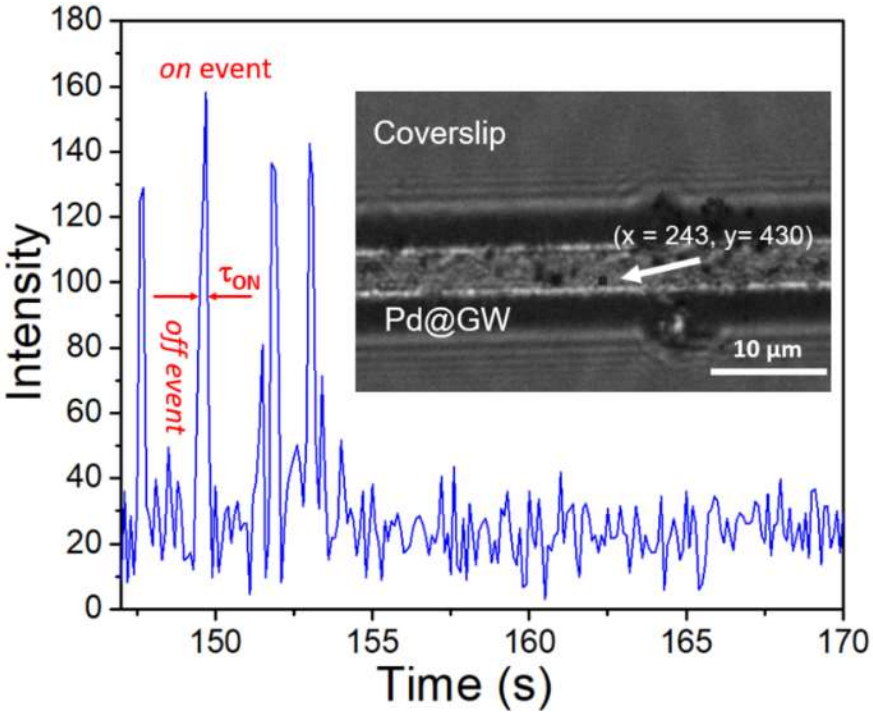

Fig. 5.1.7: Segment of a typical TIRFM emission trajectory over time of one catalytic area on Pd@GW. Data points captured every 100 ms. Inset: white light images of the selected area for 1µM NN1 reacting with 160µL of 0.035% N_2H_4 in the presence of 100 µL of 33 mM acetic acid. A top view of 3D confocal image of same fiber was shown in Fig. 5.1.S27.

Examination of Fig. 5.1.7 and similar trajectories elsewhere on the fibre reveal τ_{ON} values that are typically around 0.3 s, corresponding to $k_{release}$ values of about 3.3 s^{-1}. This corresponds to rapid reaction product release and thus a contributing factor in the very high efficiency of Pd@GW reductive catalytic processes.

From discussions above, the fluorescence signal could reveal the *in situ* formed AN1 products on the Pd surface. In order to investigate the Pd catalytic NN to AN property and its corresponding Pd surface structure, a representative Pd@GW catalyst fiber was characterized by confocal microscopy and SEM, as shown in Fig. 5.1.8. The exact same fiber was carefully marked and characterised by SEM after use in the microscopy experiment. The colocalization analysis helps us understand the relationship between structure and real catalytic ability. It is worth noting that SEM observes the surface morphology from above the catalyst loaded coverslip (Fig. 5.1.8(g)). However, the fluorescence signals were collected from the bottom half of the fiber (Fig. 5.1.8(h)). In order to colocalize the fluorescence images with electron micrographs, the Pd@GW catalyst was inverted using conductive tape (Fig. 5.1.S32). The bottom half of the catalyst was then characterized by SEM (Fig. 5.1.8(e)). The inversion process and original SEM images are shown in Fig. 5.1.S32. The green areas in Fig. 5.1.8(d) indicate the active Pd particles on the inert GW support (background). Similar shape Pd structures are observed in Fig. 5.1.8(e) by SEM. From the superimposed image, Fig. 5.1.8(f), we could find that most confocal signals match with the Pd clusters from SEM. The superposition of confocal and SEM images is shown in Fig. 5.1.S33. A representative EDS analysis of the catalytic area (green area in Fig. 5.1.8(d)) is shown in Fig. 5.1.S34.

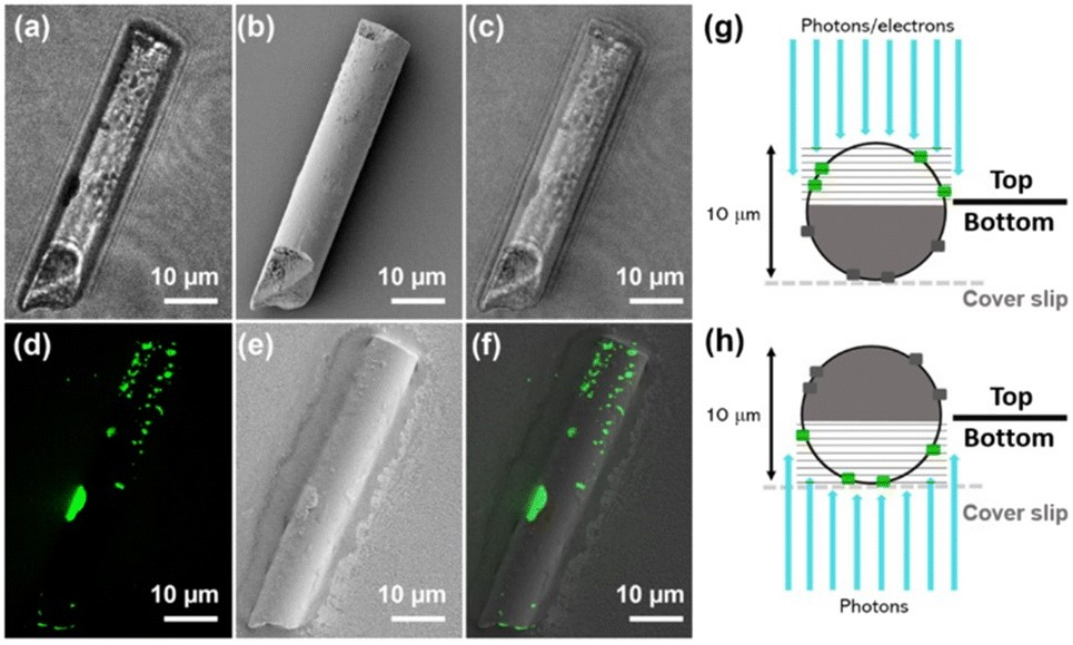

Fig. 5.1.8: (a) White light transmission image and (b) SEM image of the same Pd@GW fiber from the top view; (c) overlap of (a) and (b); top view scheme is shown in (g). (d) Confocal stack image, (e) SEM image of the same Pd@GW fiber from the bottom view; (f) overlap of (d) and (e); bottom view scheme is shown in (h). The EDS of the top and bottom side of Pd@GW is shown in the SI.

We felt that it would be important to establish if nascent $AN1_S$, once formed and before release were involved in interaction with PdNPs or simply with the GW surface. This cannot be visualized with optical methods such as the ones employed above, as it would require localization in the <10 nm scale. For this purpose, we carried out Fluorescence Lifetime Imaging (FLIM) measurements, anticipating that the fluorescence lifetime may contain location information for AN1. These measurements need to be performed with a different excitation laser (pulsed *vs.* CW) and in a different concentration regime. However, we were able to measure fluorescence lifetimes of 1.7 ns at the surface reaction regions, compared with 3.0 ns for molecules in the area away from the fiber. These measurements establish a shorter lifetime in the catalytic reaction region. The FLIM images and the representative locations are shown in Fig. 5.1.9. Since metallic surfaces are generally strong excited state quenchers,[34] the evidence supports that the nascent fluorophore ($AN1_S$) remains at or near the Pd surface until its irreversible departure (in about 0.3 s) takes place.

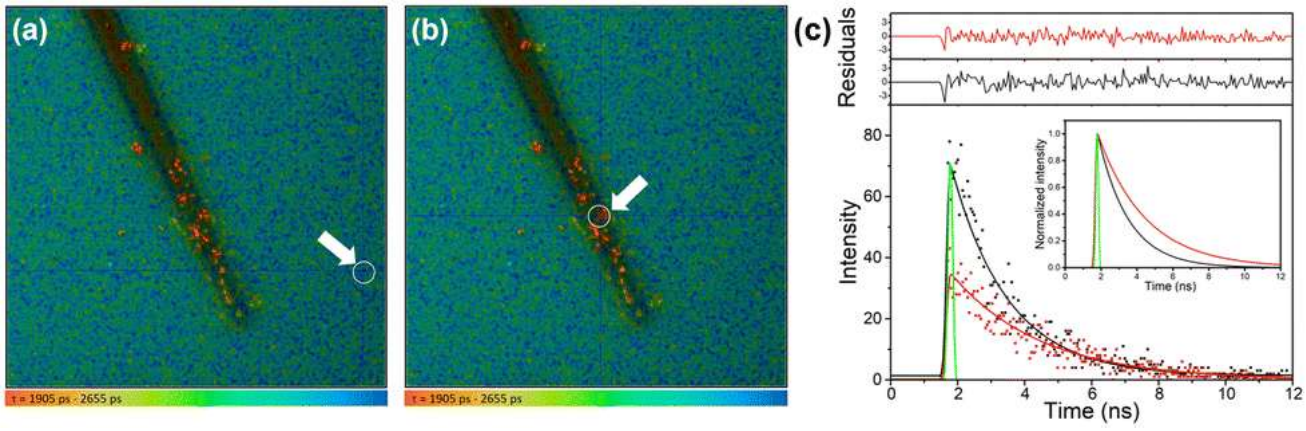

Fig. 5.1.9: FLIM images in random blank areas (a) and Pd cluster (b). The red areas are catalytic regions. Fluorescence decay traces (c) monitored by FLIM in catalytic regions (black) and in random areas (red) away from the glass fiber. Residuals are shown at the top of the figure. The inset shows the same decay fit traces as in the main figure, but normalized to facilitate viewing the lifetime difference between catalytic and random regions. The FLIM image with time scale is shown in (a) and (b).

To further investigate the catalytic behavior of Pd@GW, a comparison of confocal and FLIM images at different *z*-steps of the same catalytic fibers was recorded. Images for different *z*-steps obtained by confocal microscopy and FLIM are shown in Fig. 5.1.10. The depth of each selected level was calculated as shown in Fig. 5.1.10(k). Compared with confocal images, the FLIM technology offers an enhanced image of the active Pd particles. A comparison of a white light transmission image with FLIM has been included in Fig. 5.1.S35, which also incorporates an analysis of profiles of FLIM intensity and lifetimes.

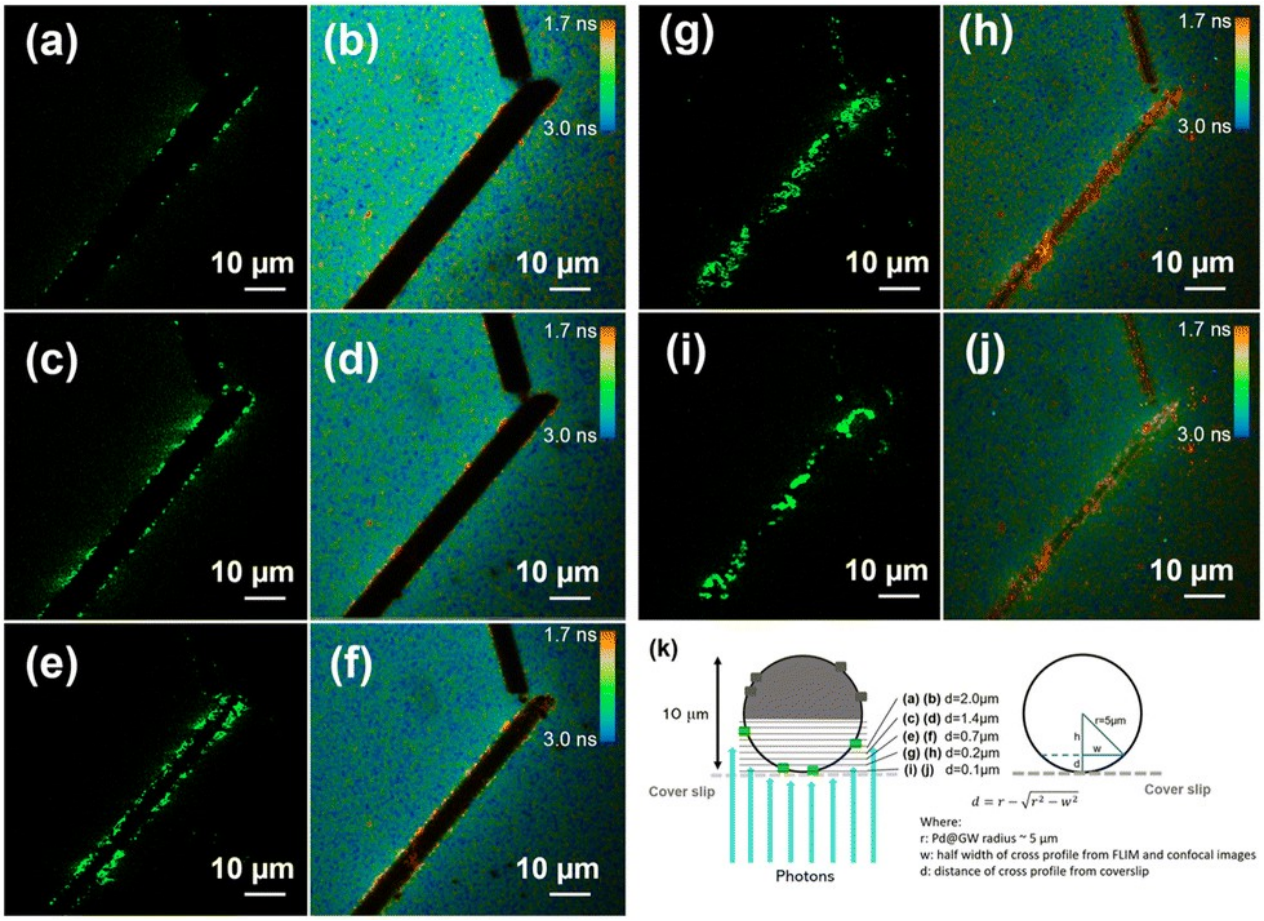

Fig. 5.1.10: Comparison of confocal and FLIM images at different *z* positions, (a) and (b) 2.0 µm from the cover slip, (c) and (d) 1.4 µm from the cover slip, (e) and (f) 0.7 µm from the cover slip, (g) and (h) 0.2 µm from the cover slip, (i) and (j) 0.1 µm from the cover slip. (k) Different depth of each selected level and depth calculation by catalyst width. The right section shows the *z* position of each image, as calculated from catalyst widths in each frame. The comparison of white light, confocal microscopy and FLIM images is shown in Fig. 5.1.S35.

As we earlier published,[13] the Pd@GW catalysts could successfully be applied in a large-scale flow system for the reduction of nitrobenzene. In those experiments, the catalyst could be reused many times, even under prolonged flow conditions. If the catalysis was occurring predominantly in solution, as suggested by some prior studies,[35] it would be unlikely for the Pd to retain catalytic ability for several consecutive cycles, as the catalyst would be washed away under flow conditions. Therefore, it is important to further investigate the behavior of Pd particles during the reaction.

In order to investigate the durability of Pd@GW and extend its application in the flow system we designed a microscopy experiment to explore the possibility of Pd catalytic site loss or migration during the nitro-to-amine catalytic reaction. First, we imaged the active Pd sites by confocal microscopy, and another set of confocal images was recorded after 4 h of NN1 to AN1 reaction on the same fiber area under constant flow.

The comparison of site changes in that ROI is shown in Fig. 5.1.11. The white light image of that fiber is shown in Fig. 5.1.S37. We could identify two kinds of Pd sites in the ROI in Fig. 5.1.11. The first kind of Pd site is anchored to the GW support, and the second kind were particles on the coverslip but outside the Pd@GW area (those particles were formed during the sample preparation).

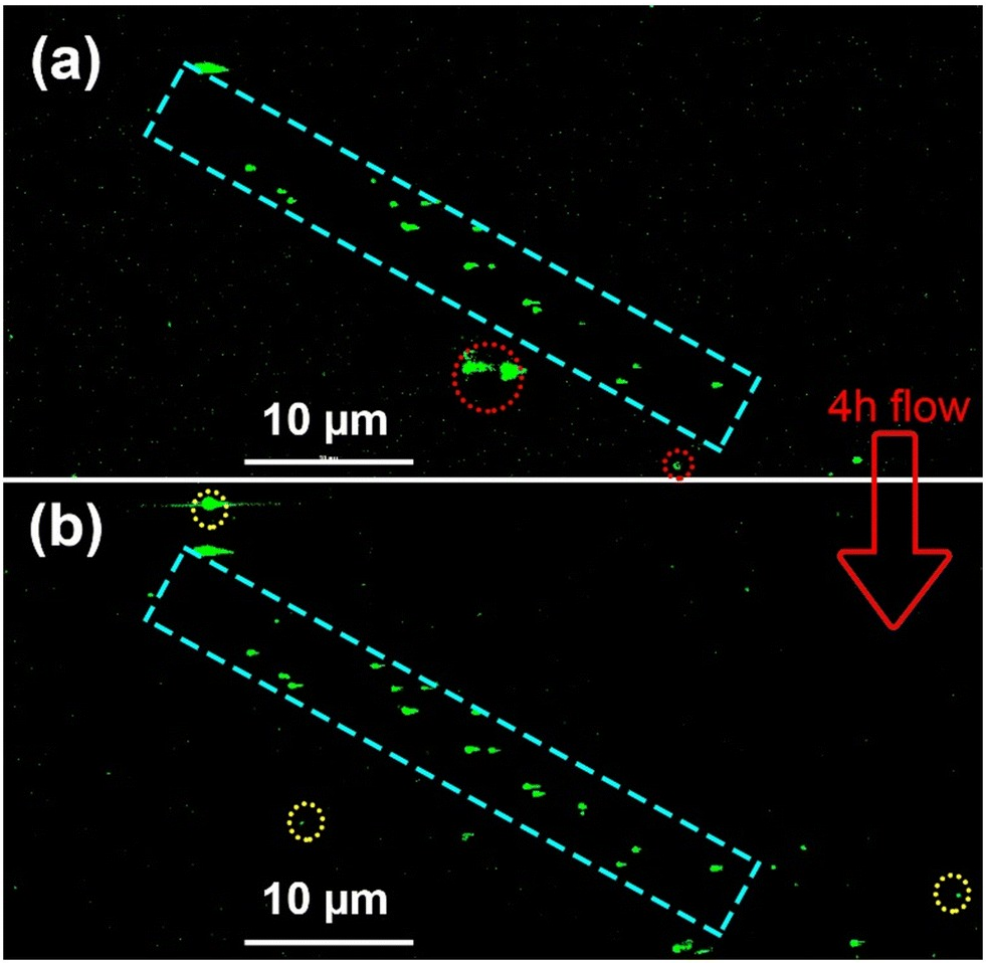

Fig. 5.1.11: Comparison of confocal images before (a) and (b) after 4h of NN1 to AN1 flow reaction. The 2D image is the 2D sum of 20 *z*-planes with 100 nm *z*-step. The Pd@GW area is shown by light blue rectangle. The Pd sites outside of the rectangle are loaded on the coverslip. Pd sites marked with red circles were washed away by flow; Pd clusters marked with yellow circles show where Pd particles migrate after a 4 h reaction.

From Fig. 5.1.11(a), we could find that some isolated particles already exist on the microscope slide at the beginning of the experiment, serving as a control. Comparing Fig. 5.1.11(a) and (b), we can determine that the active Pd sites attached to the glass fiber do not migrate over the duration of the 4 h reaction; in contrast, most non-fixed particles on the coverslip were flushed away by the flow (marked with red). There are new Pd sites (marked with yellow) formed which may come from migration during the 4 h flow reaction.

This difference in behaviours between the Pd particles on Pd@GW and Pd debris on the coverslip can be explained by the APTES modification that was applied to the GW before the Pd decoration. APTES surface modification results in PdNPs and clusters being firmly anchored to the GW through the strong interaction between the Pd and the amine functionalized GW. Other research also shows that silica and titania nanosphere surfaces modified with –SH or $–NH_2$ could remarkably block the aggregation and leaching of Pd metal nanoparticles.[36]

Emphasizing the importance of surface treatment, in our work the Pd clusters (especially for large Pd clusters) on the coverslip are not anchored, and were therefore easily washed away by the flowing solution.

The total number of Pd sites on the coverslip before and after the reaction is shown in Fig. 5.1.12 (black column). Of the Pd on the untreated glass slide, several are washed away under flow reaction. Meanwhile, some new Pd structures are washed into the frame (Fig. 5.1.12, grey bar). On the other hand, the Pd sites on the APTES treated GW remain the same after 4 h of flow reaction (Fig. 5.1.12, red bar). The total nitro reaction activity was compared by site areas and average intensity. From Fig. 5.1.12, we can conclude that the unanchored Pd sites will agglomerate and migrate, leading to a change of catalytic activity. In contrast, the APTES treated GW proves to be an effective support, preventing Pd migration, even under flow conditions.

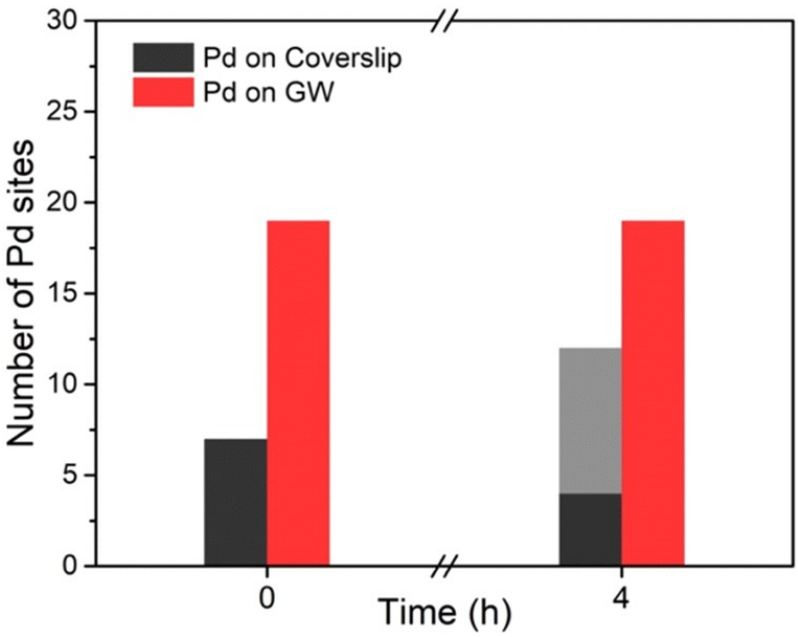

Fig. 5.1.12: Comparison of Pd sites and their activities on the glass coverslip (black), glass fiber (red) and new formed Pd sites (grey) after 4 h flow reaction. No equivalent increase was observed in the case of Pd@GW. The number of Pd sites is shown as column graph.

Fig. 5.1.11 demonstrates that the Pd@GW possesses remarkable temporal, structural and catalytic stability. To understand in detail how the surface sites potentially change in activity or location, we selected nine representative Pd sites on Pd@GW from Fig. 5.1.13(a) and (b); we can extract the time evolution of their intensity profile at the same locations. The results, shown in Fig. 5.1.13(d), show a nearly identical intensity profile line of the catalyst surface before (a) and after (b) 4 hour reaction on the same catalyst surface. An overlapped image is shown in (c). From (c), we could find that most of the active Pd sites remain at the same location after 4 h of reaction (and active flow). To compare the activities of each Pd cluster on the surface, the *in situ* AN1 product fluorescence intensity profiles were extracted and are shown in (d). The intensity peak widths are almost unchanged. In addition, the intensity (and thus, activity) is largely stable after reaction; in fact, the integral of activity increases by 10% over the 4 h period, which we regard as within acceptable fluctuations. Remarkably, sites #6 and #7 reveal some increased activity beyond expected fluctuations after 4 h. The intensity difference of those catalytic sites may result from the on–off behavior of Pd nanoparticles in heterogeneous catalysis processes.[37]

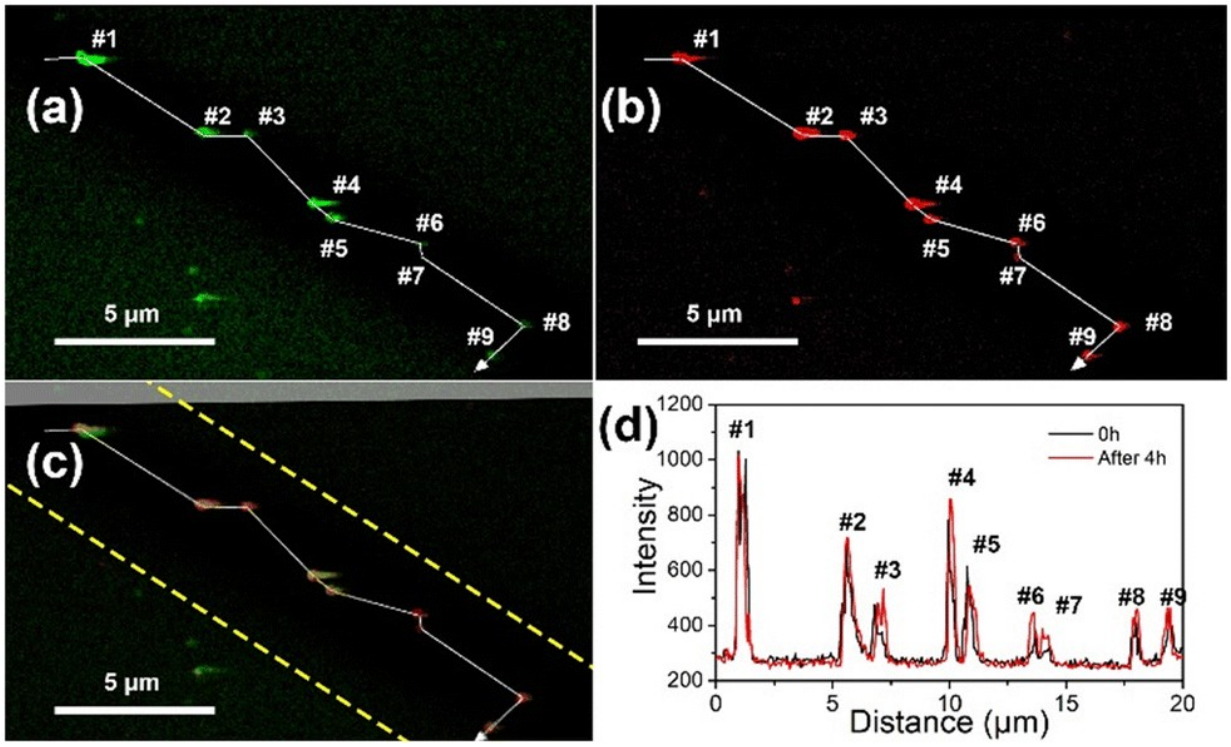

Fig. 5.1.13: Intensity profile of selected Pd sites (#1–#9, as shown in (a) and (b)) on the catalyst surface before (a) and after (b) 4h of reaction, while (c) shows an overlap of the (a) and (b) signals. The solid lines are RE used in (d) as the horizontal axis; (d): the *in-situ* fluorescence intensity profile of the reaction product, AN1 for (a), (green) and (b) (red).

In order to facilitate the interpretation of results from different techniques, we offer a description of the proposed mechanism (Scheme 5.1.4) that is supported by the various techniques employed in this contribution and reported above.

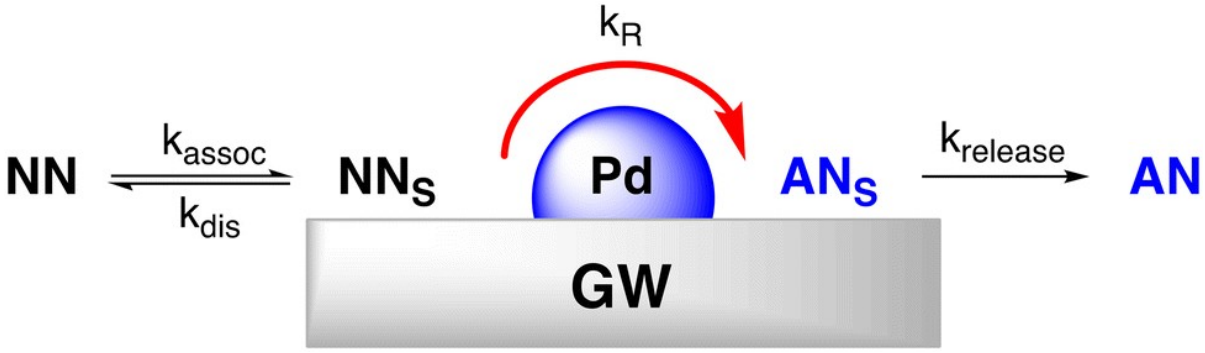

Scheme 5.1.4: Proposed reaction mechanism showing an association equilibrium between solution NN and NN_S, (NN on surface). Following catalytic on-surface conversion to AN_S, then AN is irreversibly released to the solution.

The kinetic and equilibrium expressions for the mechanism of Fig. 5.1.1 are given in equations (1)–(5), where the subscript 'ss' corresponds to steady state conditions under NN1 slow flow (0.5 mL h^{-1}) at a constant concentration and with $[N_2H_4]$ also constant.

$$K_{eq.} = \frac{k_{assoc}}{k_{dis}} = \frac{[NN_S]}{[NN] \times [Pd@GW]} \quad (1)$$

$$[NN_S] = K_{eq.}[NN] \times [Pd@GW] \quad (2)$$

$$AN_S \text{ formation: } \frac{\delta[AN_S]}{\delta t} = k_R [NN_S] \quad (3)$$

$$\text{steady state: } [AN]_{ss} = \frac{k_R [NN_S]}{k_{release}} \quad (4)$$

$$[AN]_{ss} = \frac{k_R K_{eq.} [NN] \times [Pd@GW]}{k_{release}} \quad (5)$$

$$\underset{\text{intensity}}{\text{Fluorescence}} \propto [AN]_{ss} \propto f\left([NN] \times \underset{\text{sites}}{\text{catalytic}}\right) \quad (6)$$

Several features of the mechanism proposed can be identified in the mechanism of Scheme 5.1.4. For example, the linearity with concentration observed in Fig. 5.1.6 requires a small value of $K_{eq.}$; that is, most catalytic sites must be unoccupied at any given time. Further, our TIRFM studies suggest a prompt release of the product once the reaction is complete, with a residence time in the order of 300 ms; the observation is consistent with the ease with which AN1 is eliminated when clean solvent is flown over the sample. The short fluorescence lifetime determined by FLIM suggests that most of this residence time is spent near the Pd centers, as metals are known to be good quenchers of excited states.[38]
The spatial stability of the catalytic sites over several hours (Fig. 5.1.11–5.1.13) shows that Pd migration does not play an important role and suggests that APTES is an excellent choice for Pd anchoring. In contrast, in a recent report relating to C–C coupling, we showed that in the case of $Pd@TiO_2$ Pd atoms or clusters could migrate by millimeters over several hours when no APTES was used to anchor the Pd.[15] Not only in this case are the material and reaction different, but also in the case of $Pd@TiO_2$ migration analysis which was based on Pd landing on pristine TiO_2 and thus against a bare

substrate making arrival easier to detect than that in the case of Pd@GW, where we can conclusively state that large (but sub-micron) catalytic areas are not mobile in the hour-time scale in spite of the possible transport of minor amounts of material. Our data serves to highlight the importance of stability against migration that APTES can confer to catalytic materials. Given that catalytic sites involve many Pd atoms or clusters, it is possible that some Pd leaches, but the amount is sufficiently small to not affect the overall catalytic activity of each site.[13] If such leaching occurs, we see no evidence that they land or are retained in the vicinity of the fibre, as this would generate new catalytic (and thus emissive) spots. If such deposits occur, they must be beyond the monitored region of about 120 µm.

The remarkable stability of the emission locations and to a large extent their intensities, observed in the fluorescence profile over several hours, provides strong evidence that the Pd@GW structures experiences little if any migration of catalytic sites, which would result in lost activity. This is a testament to the strong catalyst adherence on the APTES-treated GW surface, making this catalyst robust, stable and environmentally safe for flow catalysis applications. We note that the pixel size for confocal microscopy is 70 nm, and thus many PdNPs can be located within these dimensions.

Conclusion

In this work the catalyst Pd@GW, where APTES acts as an anchor, has been shown to have high reactivity in the nitro to amine reduction. Advanced optical microscopy methods, combined with electron microscopy, show that the catalytic sites on the glass fiber are stable for extended periods of time, even under flow conditions. The reduction occurs at the Pd sites and the amine product has a residence time of ∼300 ms before its departure. This time seems to be spent in the proximity of the Pd catalytic site, judging from the reduced fluorescence lifetime. The combination of fluorescence and electron microscopy, in-flow single molecule fluorescence, and bench chemistry provide an intimate understanding of the catalytic process.

Supplemental Information

Table of Contents

1 - Materials and Methods

Instruments

The palladium (Pd) was grafted on the support by photo-doping using Irgacure 2959 (I-2959) as the photoinitiator under UVA irradiation (Luzchem LZC-4V photoreactor equipped with 8 UVA lamps). NMR spectra were recorded at room temperature in a Bruker Avance 400 spectrometer. The palladium loading was analyzed by inductively coupled plasma atomic emission spectrometry (ICP-OES, Agilent 5110 VDV ICP-OES Spectrometer). The MS spectra were analyzed by electrospray ionization tandem mass spectrometry (ESI) (Agilent 6125B single quadrupole LC/MSD system). The optical characterization of the molecular probes in methanol was performed with a UV–visible spectrometer (Cary 100 or Cary 60, Agilent Technologies) and a fluorescence spectrometer (Photon Technology International). The Total Internal Reflection Fluorescence Microscopy (TIRFM) experiments were carried out in a Nikon Eclipse Ti2 inverted microscope equipped with a Ti2 platform with motorized XYZ, motorized TIRF illumination, a Perfect System Focus to maintain focus through time, and an ANDOR iXon Ultra EM-CCD camera controlled by NIS-Elements software (Nikon, New York, NY, USA). The images were captured using an oil-immersion objective (SR HP Apo TIRF 100×H NA=1.49 WD=120µm) and irradiated with a 488 nm continuous wave (CW) laser light filtered through the excitation filter (483-494 nm). The light emitted was collected by the same objective and filtered with an emission filter (525-549 nm). An exposure time of 100 ms per frame was used. The data was analyzed by ImageJ and a home written Python program[11]. The confocal images were obtained using the Nikon A1 confocal microscope with 488 nm excitation continuous wave (CW) lasers. The high resolution 3-dimensional confocal image was generated from a stack of 2D images with a vertical spacing of 0.1 µm per image. All the images were processed by NISElements software. FLIM image was acquired using the Becker and Hickl (B&H) FLIM module from Nikon. A 488 nm pulsed laser was employed in FLIM experiments. The lifetime of AN in FLIM images were analyzed by B&H SPCImage software. The B&H FLIM was equipped with B&H BDS-SM picosecond diode lasers that deliver picosecond light pulses (480.511 nm, 50MHz, BDS-488-SM-FBC). The fluorescence signal from NN to AN reaction were recorded by an SPC-150N TCSPC/FLIM module. All microscope experiment reaction solutions were pumped into the flow cell using an NE-300 Just Infusion™ Syringe Pump.

Synthesis of Nitronaphthalimide Dyes

Synthesis of NN2

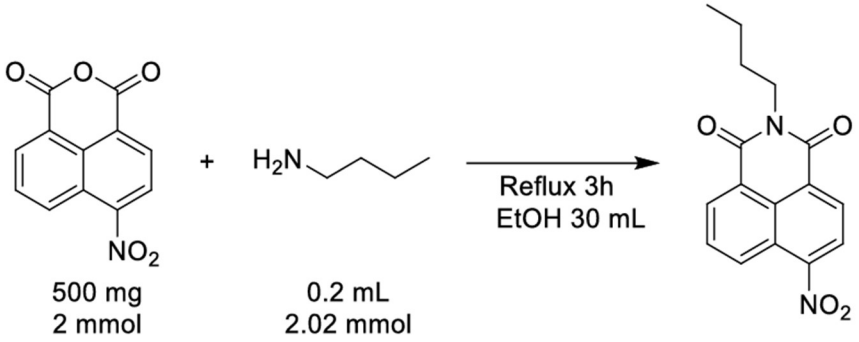

Scheme 5.1.S1: Synthesis NN2

4-nitro-1,8-naphthalic anhydride (500 mg, 2 mmol) and butylamine (200 µL 2.02 mmol) were dissolved in 30 mL ethanol and under refluxed for 2 h. After cooling down to room temperature, the solvent was removed under reduced pressure. The product was purified by a flash column. The absorption and fluorescence spectra are shown in SI section 2, and the NMR and ESI spectra are in SI section 4.

Synthesis of NN2-NHOH

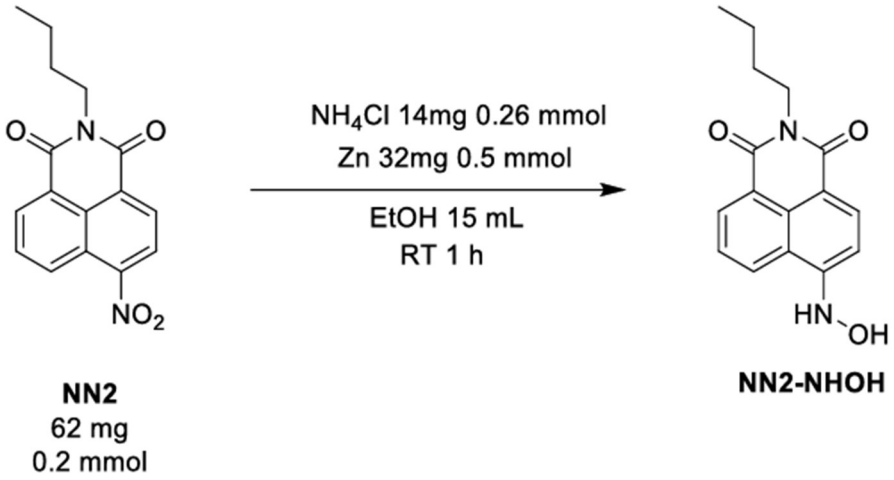

Scheme 5.1.S2: Synthesis NN2-NHOH

NN2 (62 mg, 0.2 mmol) and ammonium chloride (14mg, 0.26mmol) was dissolved in 15 mL ethanol. After adding 32 mg of zinc particles, the system was stirred at room temperature for 1 hour. The zinc particles were removed by centrifuge and concentrated under reduced pressure. The product was analyzed by HPLC-MS.

2 - Nitronaphthalimide reduction: bench scale reactions

In order to investigate the nitronaphthalimides reduction reaction mechanism, we first examined NN1 and NN2 reduction on bench scale reaction under different conditions. The two dyes were produced to investigate the behavior of the dye in aqueous (NN1) and organic (NN2) environments.

NN2 reduction reaction using H_2 as reducing agent

NN2 was first reduced by hydrogen gas in present of Pd@GW. 3mL of 0.1 mM NN2 was dissolved in MeOH and 7 mg Pd@GW, Scheme 5.1.S3. A continues stream of hydrogen was purged through the system. The reaction was monitored by UV-vis.

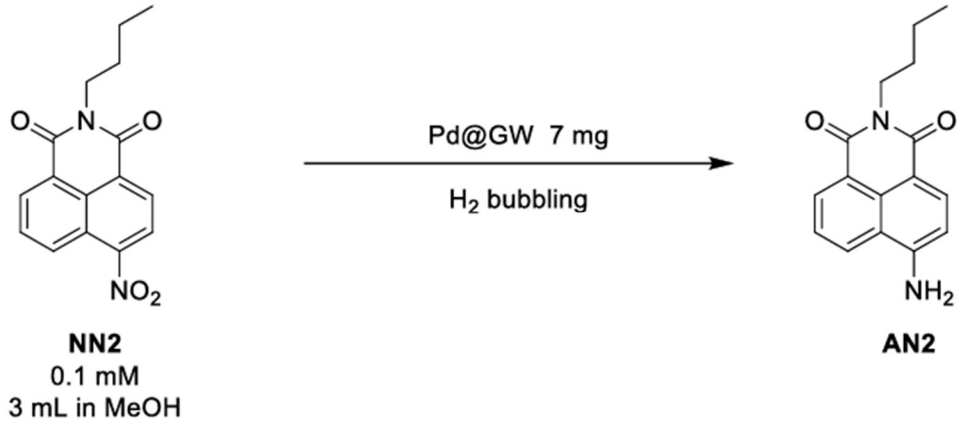

Scheme 5.1.S3: Reduction of the fluorogenic probe NN2 by Pd@GW using H_2.

The UV absorption of system was shown in Fig. 5.1.S1. From the Fig. 5.1.S1 (b), the NN2 peak (black line) decreased and showed a new peak around 440 nm in 5 min. The result shows that the NN2 was reduced to AN2 in 5 min in the presence of hydrogen bubbling and Pd@GW. During the reaction, Pd@GW could be removed easily by tweezers (insert image) before the UV-Vis characterization. Compared with a long-time centrifuge post-process when using P25 based catalyst, the Pd@GW could provide an easy and fast separation process after reaction.

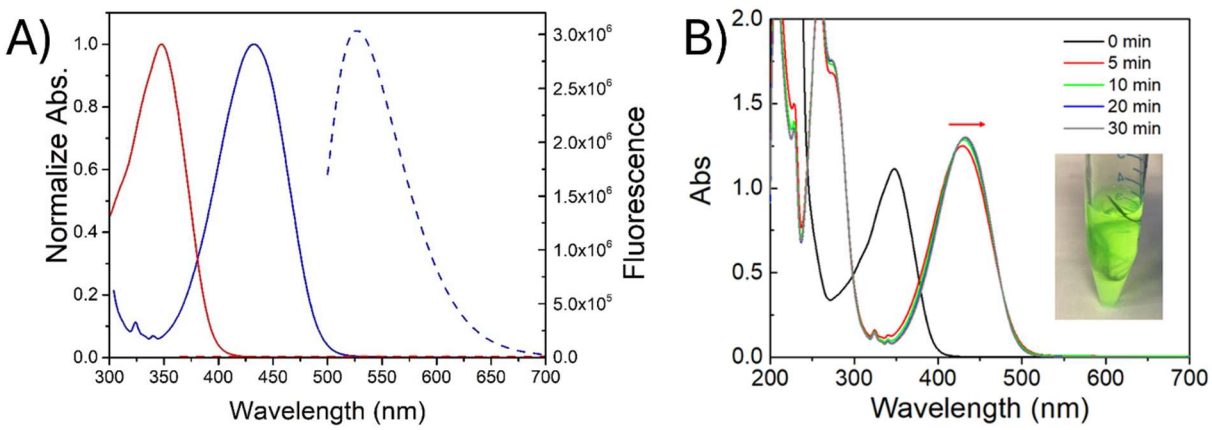

Fig. 5.1.S1: (a) Normalized absorption (solid line) and fluorescence (dash line) spectra of NN2 (100 µM in water, red) and AN2 (100 µM in MeOH, blue). Excitation laser: λ_{ex}=350 nm for NN2, and λ_{ex}=488 nm for AN2. Note that fluorescence is not normalized and the difference in amplitude reflects the contrast of the dye emission intensity at equal concentration. (b) Reduction of the fluorogenic probe NN2 by Pd@GW. Reaction conditions: 3 mL of 0.1 mM NN2 MeOH solution was added 7 mg Pd@GW, the system was gently bubbled with H_2 flow. Inset image: Pd@GW catalyst in the reaction media after reduction.

From Fig. 5.1.S1, we could find a small red shift of product absorption in the first 5 min. Based on direct reduction route of aromatic nitro compound [40] we believe a hydroxylamine (NN2-NHOH) intermediate was formed during the reaction using H_2. In order to prove our idea, NN2-NHOH was synthesized. The UV-vis of NN2-NH-OH were shown in Fig. 5.1.S2 (ESI shown in Fig. 5.1.S16). From the UV-vis of NN2-NHOH, the absorption is matched with the intermedia in the NN2 reduction reaction using H_2.

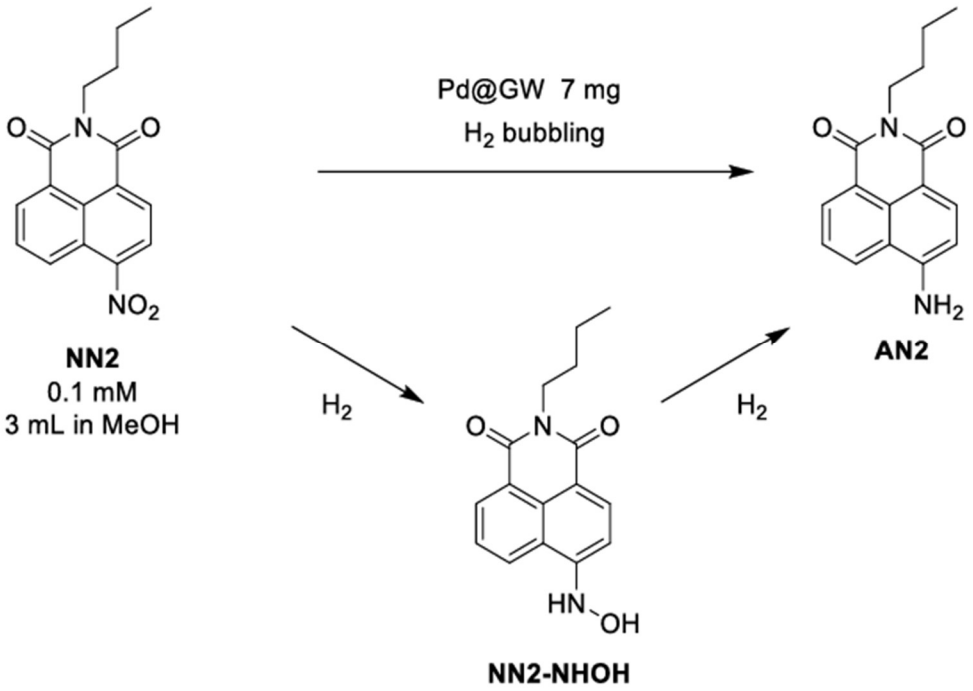

Scheme 5.1.S4: Proposed reaction pathways for NN2 reduction reaction under H_2 bubbling.

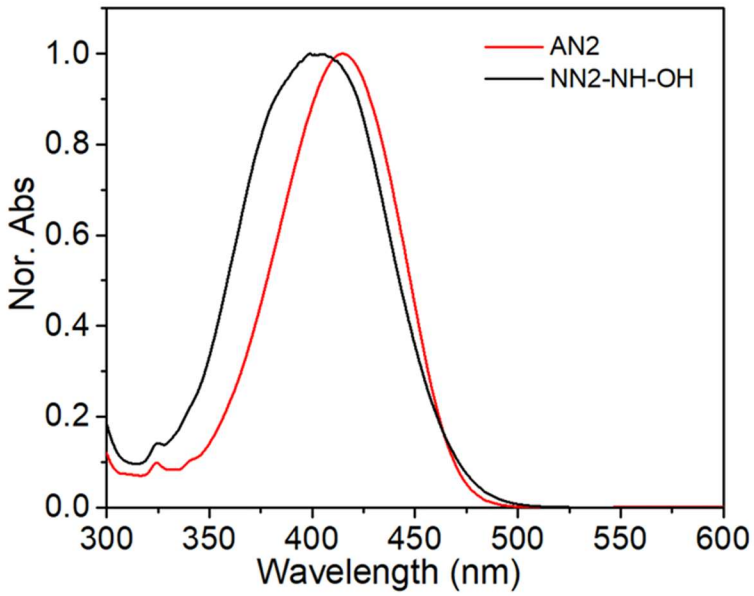

Fig. 5.1.S2: Normalized UV spectra of NN2-NHOH and AN2. The NN2-NH-OH and AN2 isolated products were purified by Preparative HPLC Systems. The UV absorption spectra were recorded by HPLC UV-vis detector, HPLC flow phase 99% CH3CN and 1% water.

NN2 reduction reaction using N_2H_4 as reducing agent

Nitronaphthalimides reduction reaction also tested by using N_2H_4 as reducing agent. 7 mg of Pd@GW and 160 µL of 35% N_2H_4were added to 3 mL of 0.1 mM of NN2 in methanol, the NN2 was fully reduced to AN2 in 15 min, Fig. 5.1.S3 (a). An intermediate with absorption at 550nm was observed in present of N_2H_4. Those intermediates all fully convert to the AN2 at end of the reaction. Two blank experiments were shown in Fig. 5.1.S3(b) and (c). The NN2 reduction reaction without catalyst was shown in Fig. 5.1.S3 (b). We could find that the NN2 solution is stable in the presence of Pd@GW for a long time. The reaction kinetics without Pd@GW were shown in Fig. 5.1.S3 (c). The reaction was not finished after 10 h compared with 15 min in the presence of Pd@GW.

Scheme 5.1.S5: Reduction of the fluorogenic probe NN2 by Pd@GW using N_2H_4.

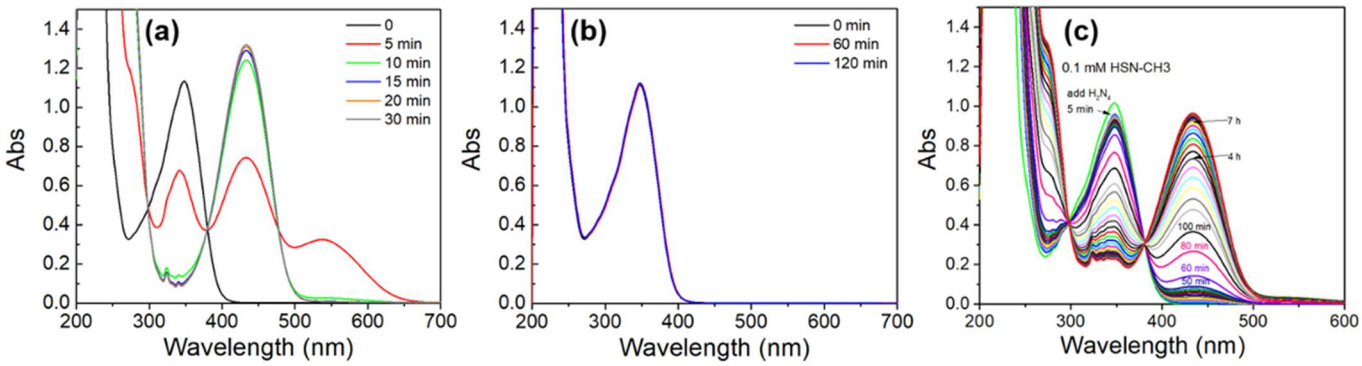

Fig. 5.1.S3: (a) 0.1 mM NN2 reduction reaction using 7 mg of Pd@GW and N_2H_4 (160 µL 35% N_2H_4) as reducing agent; (b) Control experiment: 0.1 mM NN2 solution with 7 mg Pd@GW; (c) 0.1 mM NN2 solution with 160 µL 35% N_2H_4.

From Fig. 5.1.S3 (a), we found the NN2 reduction reaction to have a different intermediate when using H_2 or N_2H_4. While the intermediate will convert to AN2 at end, those intermediates may affect the sensitive microscopy experiment. In order to decrease the influence from the reaction intermediate in single molecule reaction, a series of experiments were designed. The effect of pH was investigated by adding acetic acid or NaOH in NN2 reduction reaction solution. From Fig. 5.1.S4, we could find that acid additive will selectively obtain AN2 product without the formation of a long wavelength intermediate. From the nitro compounds reduction mechanism [40,41], we believe that azo- and azoxy-aromatics products are the intermediates which could be achieved in present of under basic conditions. Similar reactions were applied in 25 µM system (same concentration for most microscopy experiment), as shown in Fig. 5.1.S5.

In conclusion, from Fig. 5.1.S4 and Fig. 5.1.S5, we find the acid additive could avoid both NN2-NH-OH and azo-/azoxy by-products, making it essential to our single molecule experiments.

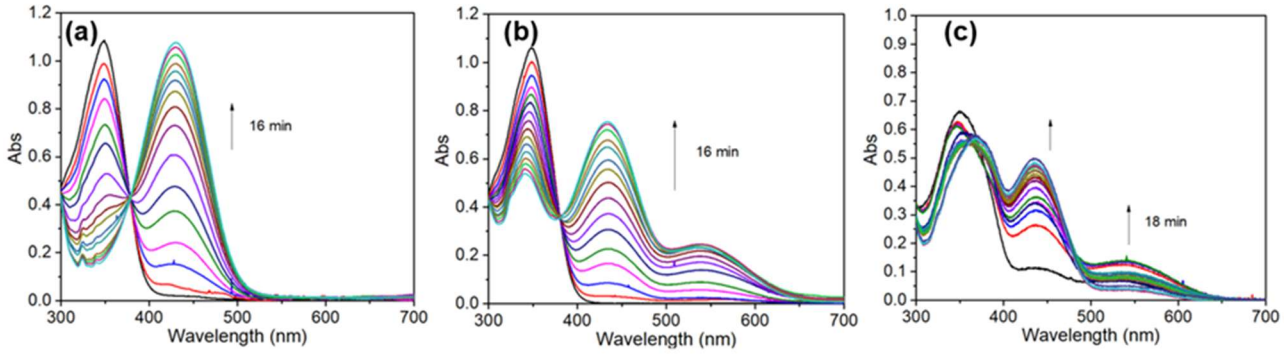

Fig. 5.1.S4: 0.1 mM NN2 reduction reaction using 7 mg of Pd@GW and N_2H_4 (160 µL 35% N_2H_4) as reducing agent in the presence 100 µL 3.3M acetic acid (a), 100 µL MilliQ H_2O (b), and 100 µL 3.3M NaOH (c).

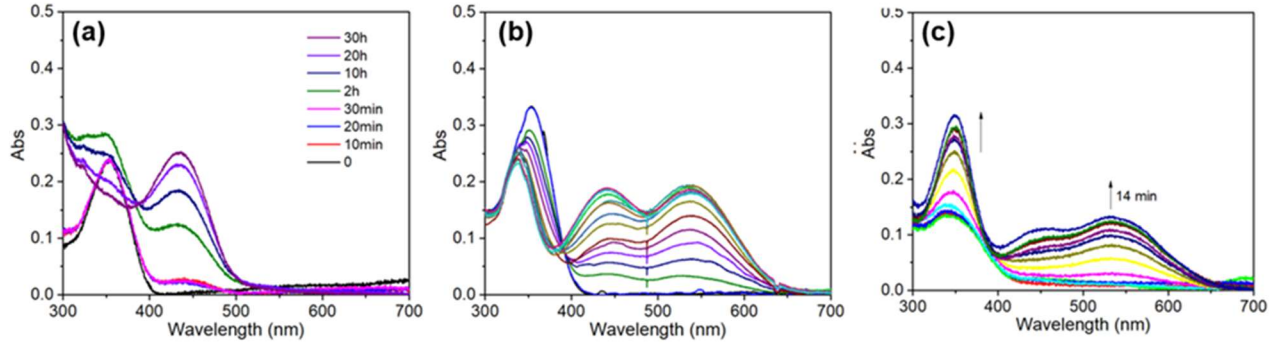

Fig. 5.1.S5: 0.5 mL of 0.01 mM NN2 reduction reaction using 7 mg of Pd@GW and N_2H_4 (160 µL 0.35% N_2H_4) as reducing agent in the presence of 1.5 mL 3.3M acetic acid (a), 1.5 mL MilliQ H_2O (b) and 1.5 mL 3.3M NaOH (c).

NN1 reduction reaction using N_2H_4 as reducing agent

Nitronaphthalimides reduction reaction also tested by using NN1 in aqueous solution using N_2H_4 as reducing agent. 7 mg of Pd@GW, 160 µL of 35% N_2H_4, and 100 µL 3.3 M acetic acid were added to 3 mL of 0.1 mM of NN1 in MilliQ water. The reaction kinetics are shown in Fig. 5.1.S6 (a). Like the NN2 reduction, there is not NH-OH or azo- by-products under acidic conditions. Two blank experiments were shown in Fig. 5.1.S6 (b) and (c). The NN1 is stable in water without N_2H_4. The reduction reaction required almost 2 days to complete in the absence of the catalyst.

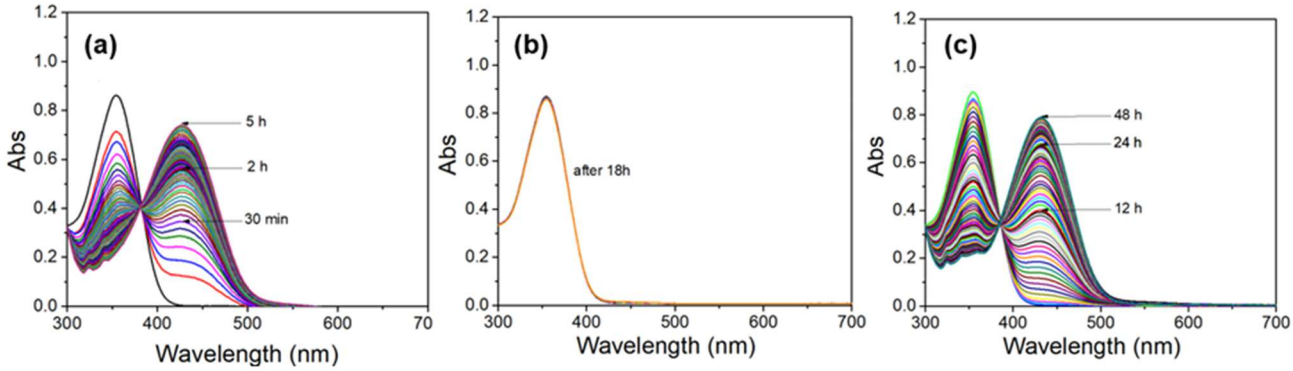

Fig. 5.1.S6: (a) 0.1 mM NN1 reduction reaction using 7 mg of Pd@GW, N_2H_4 (160 µL 35% N_2H_4), and 100 µL 3.3 M acetic acid; (b) 0.1 mM NN1 reduction reaction using 7 mg of Pd@GW and 100 µL 3.3M acetic acid without reduce agent.; (c) 0.1 mM NN1 reduction reaction using N_2H_4 (160 µL 35% N_2H_4) and 100 µL 3.3 M acetic acid without catalyst. Similar reactions were applied in 1 µM NN1 system (same concentration for most microscopy experiment), as shown in Fig. 5.1.S7.

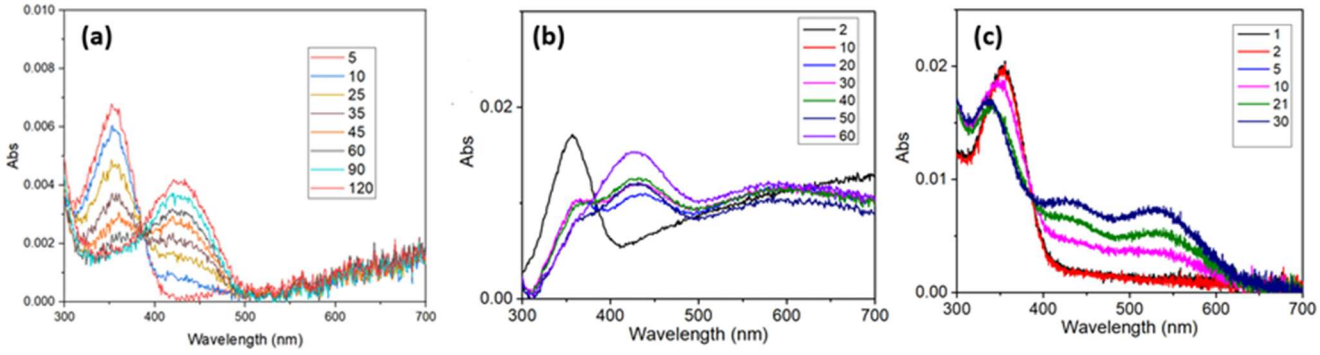

Fig. 5.1.S7: 1 µM NN1 reduction reaction using 7 mg of Pd@GW and N_2H_4 (160 µL 0.35% N_2H_4) as reducing agent in the presence of 100 µL 0.033 M acetic acid (a), 100 µL MilliQ H_2O (b) and 100 µL 0.033 M NaOH (c). The absorption above 500 nm was from the scattering from Pd@GW catalyst.

3 - Catalyst SEM, TEM, and EDS analysis

It is important to understand the size of Pd nanoparticles of Pd@GW. However, the Pd@GW is too thick for TEM characterization, and the particles too small to be observed with SEM. To observe Pd@GW in nano scale, the Pd@GW was ground and disperse in EtOH, the suspension of fragments of Pd@GW was dropped on the TEM grid. The big Pd clusters were still difficult to analysis the size distribution. The size distribution was analysis by the individual Pd particles on the GW surface was shown in Fig. 5.1.5.

SEM images could be gathered by breaking cutting Pd@GW fibres and gently placing them on carbon tape. As glass wool is difficult to image with SEM, the samples were sputter coated with a thin layer of gold for greater clarity (Fig. 5.1.S8 - 5.S11).

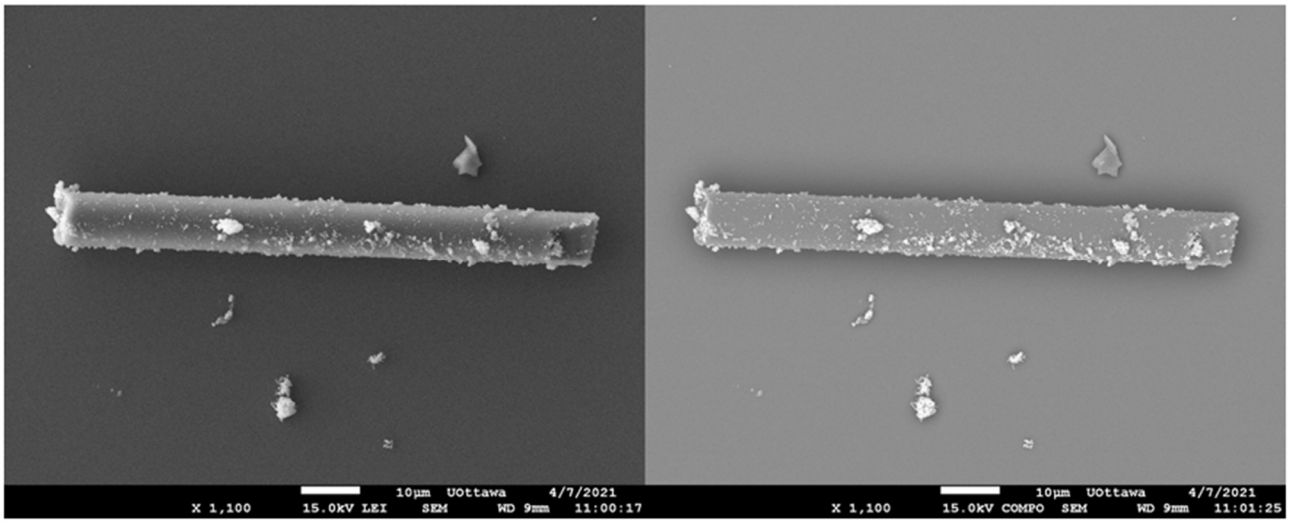

Fig. 5.1.S8: Representative SEM images of representative Pd@GW on a coverslip after the microscope experiment. Left: COMPO image. COMPO is a technique that shows heavier elements as brighter and lighter elements are darker, thus allowing for easy differentiation between metals and support.

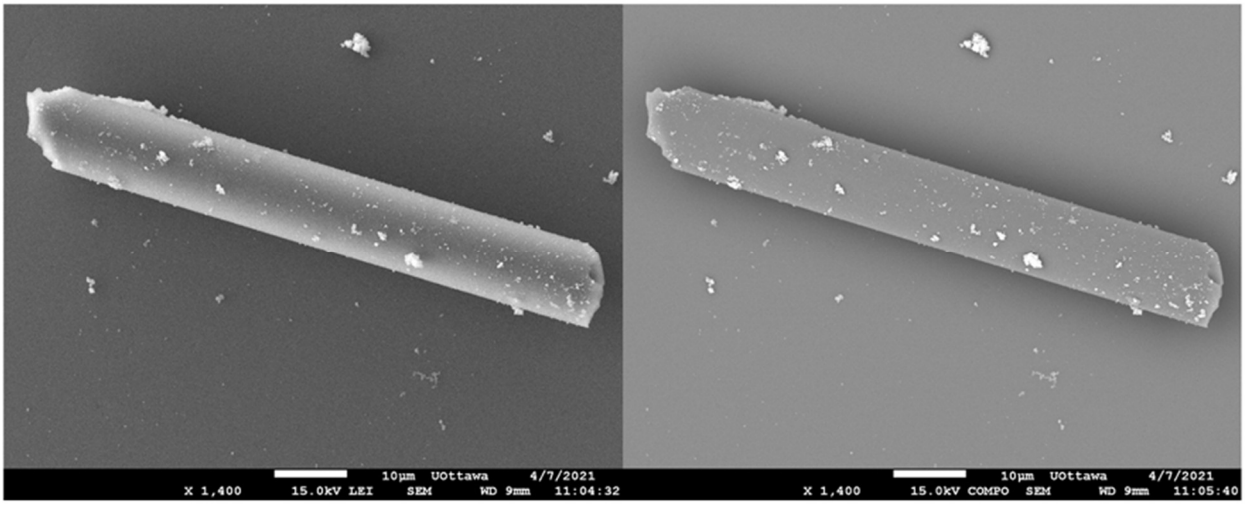

Fig. 5.1.S9: Representative SEM images of representative Pd@GW on coverslip after the microscope experiment. Left: COMPO image.

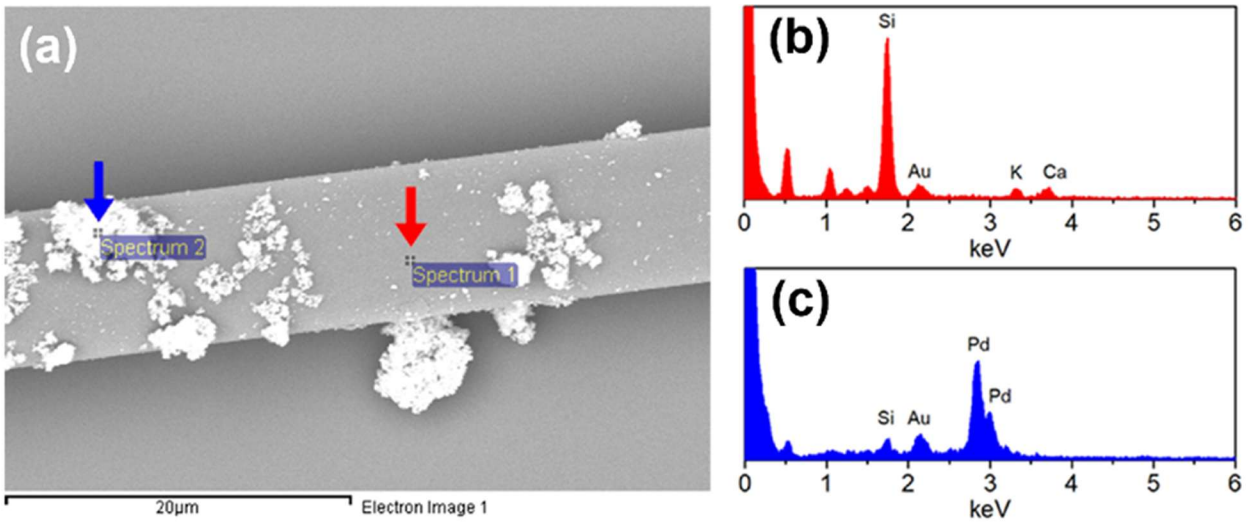

Fig. 5.1.S10: EDS analysis of Pd@GW on coverslip after microscope experiment. (a) SEM of Pd@GW, the lighter structure in the SEM (COMPO) image were Pd particles. (b) Representative EDS spectrum of surface without Pd decoration, the EDS scan area was shown by red arrow. (c) Representative EDS spectrum of surface with Pd decoration, the EDS scan area was shown by blue arrow. The EDS analysis of different areas on the same Pd@GW fiber SEM show the Pd structures were successfully decorated onto the GW surface.

4 – NMR and Mass Spectrometry

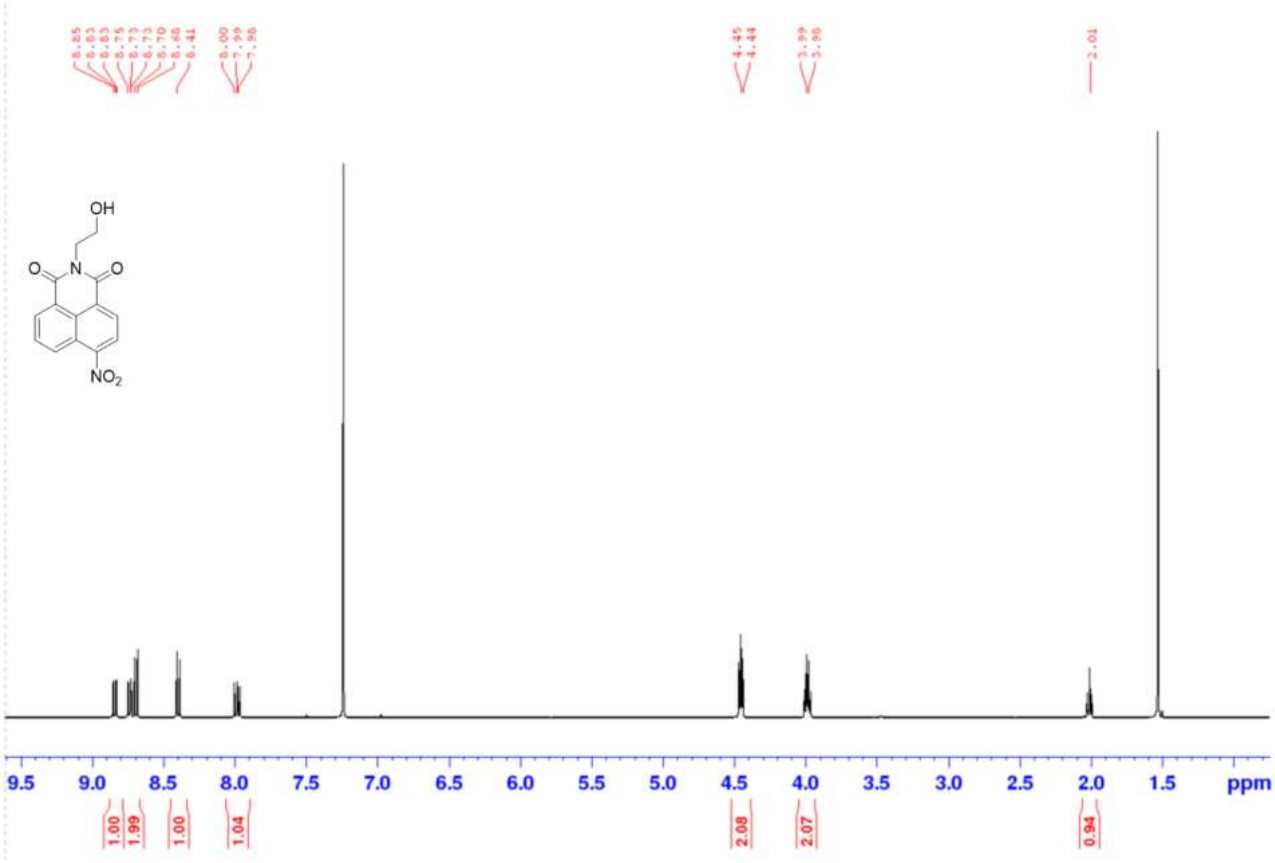

Fig. 5.1.S11: H-NMR of NN1 in $CDCl_3$.

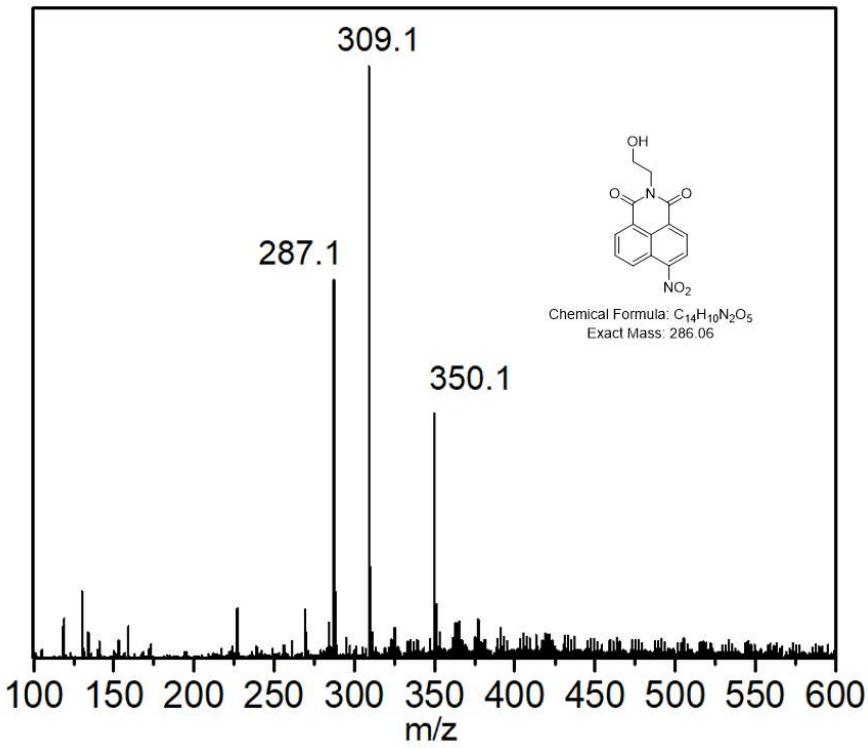

Fig. 5.1.S12: ESI of NN1, positive ESI source. $[NN1 + H]^+$: 287.1; $[NN1 + Na]^+$: 309.1; $[NN1 + CH_3CN + Na]^+$: 350.1.

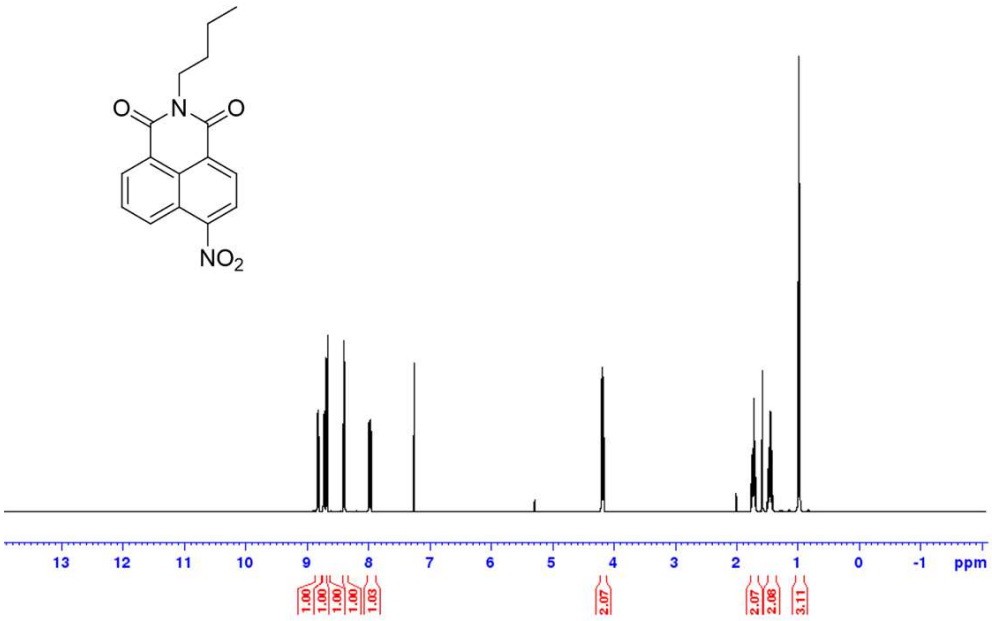

Fig. 5.1.S13: H-NMR of NN2 in $CDCl_3$.

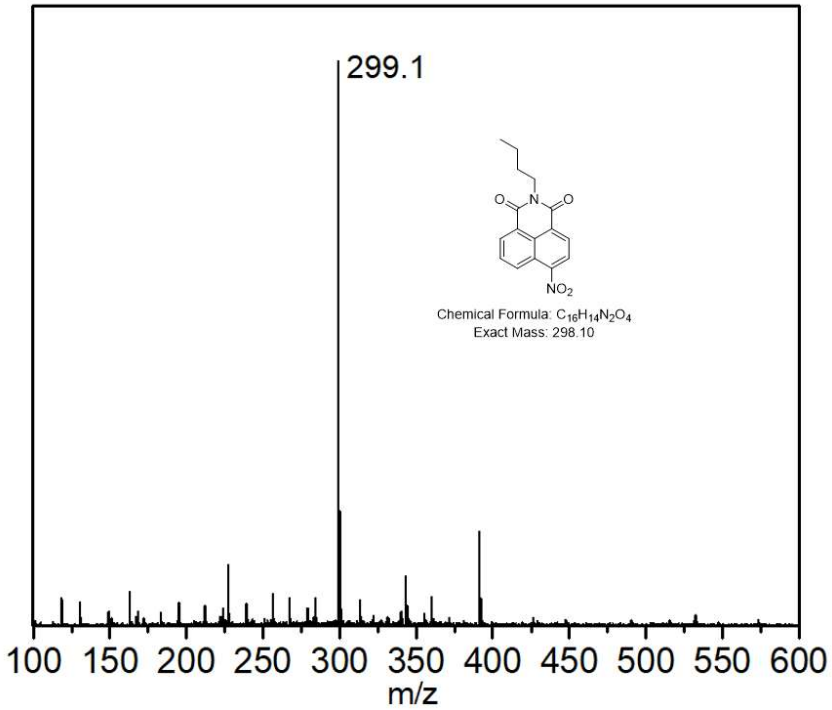

Fig. 5.1.S14: ESI of NN2, positive ESI source $[NN2 + H]^+$: 299.1.

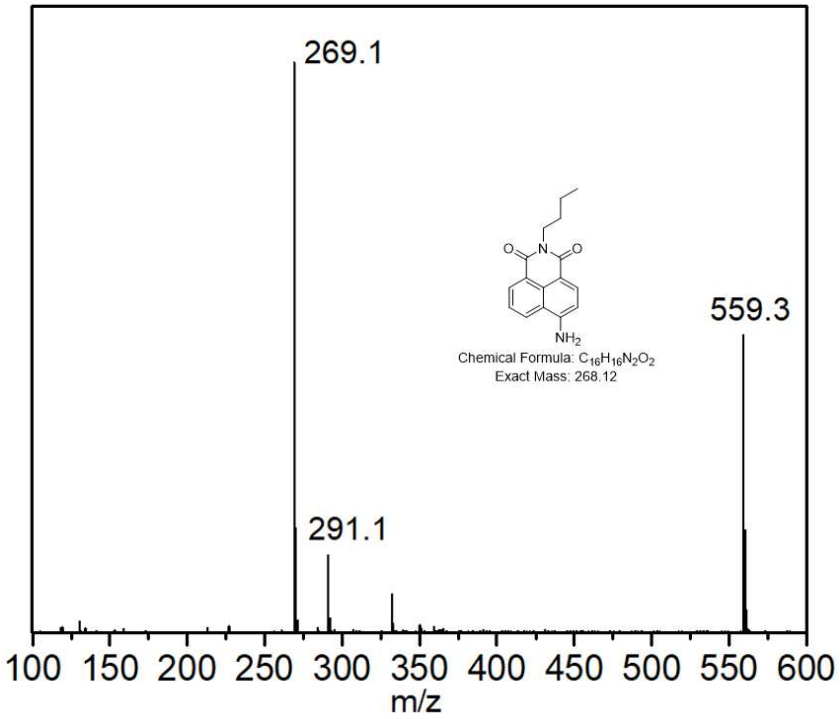

Fig. 5.1.S15: ESI of AN2, positive ESI source. $[AN2 + H]^+$: 269.1; $[AN2 + Na]^+$: 291.1; $[AN2 + AN2 + Na]^+$: 559.2 .

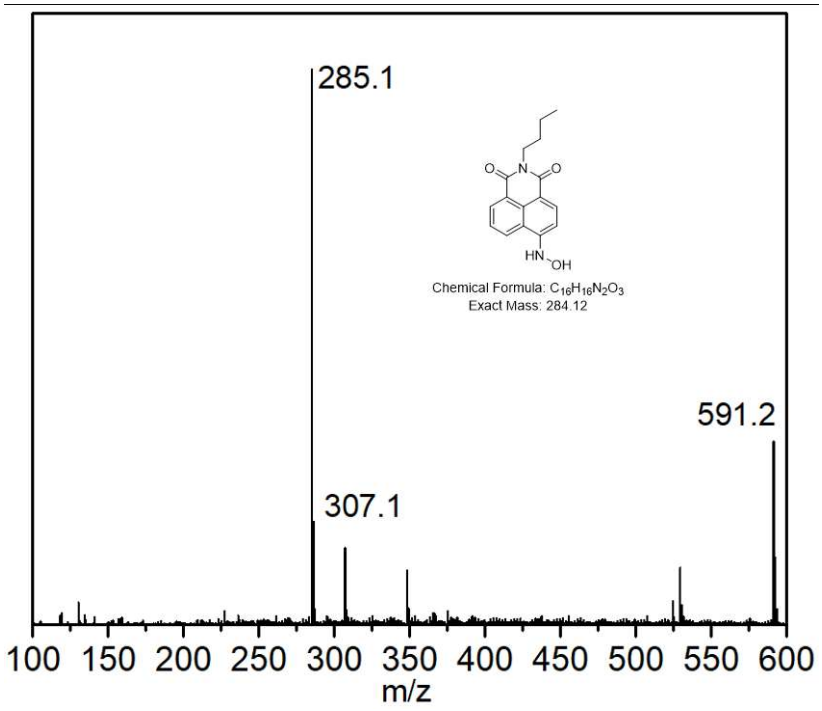

Fig. 5.1.S16: ESI of NN2-NHOH. $[NN2\text{-}NHOH + H]^+$: 285.1; $[NN2\text{-}NHOH + Na]^+$: 307.1; $[NN2\text{-}NHOH + NN2\text{-}NHOH + Na]^+$: 591.2.

5 - Confocal Microscopy

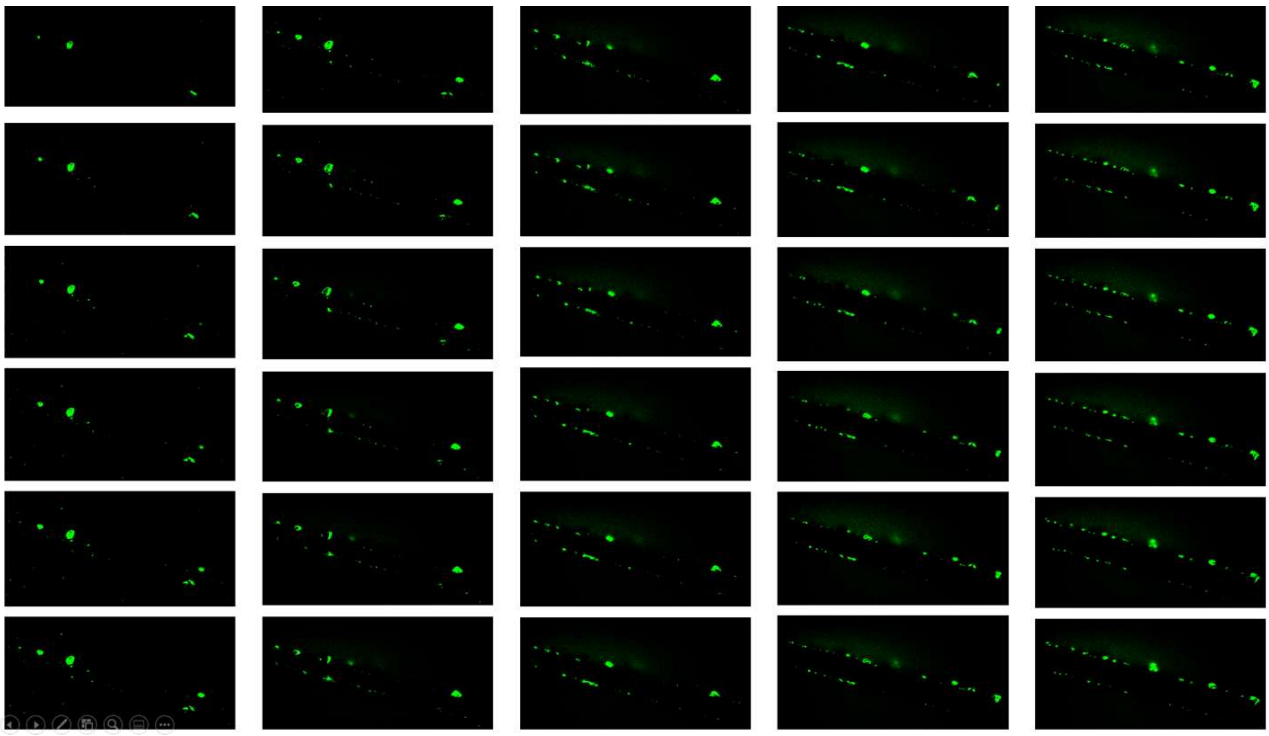

Fig. 5.1.S17: Selected confocal image sequence of Fig. 5.1.3. Each image is a 100 nm step in the z direction (bottom towards top). Sequence order: ↓↗↓↗↓↗↓↗↓.

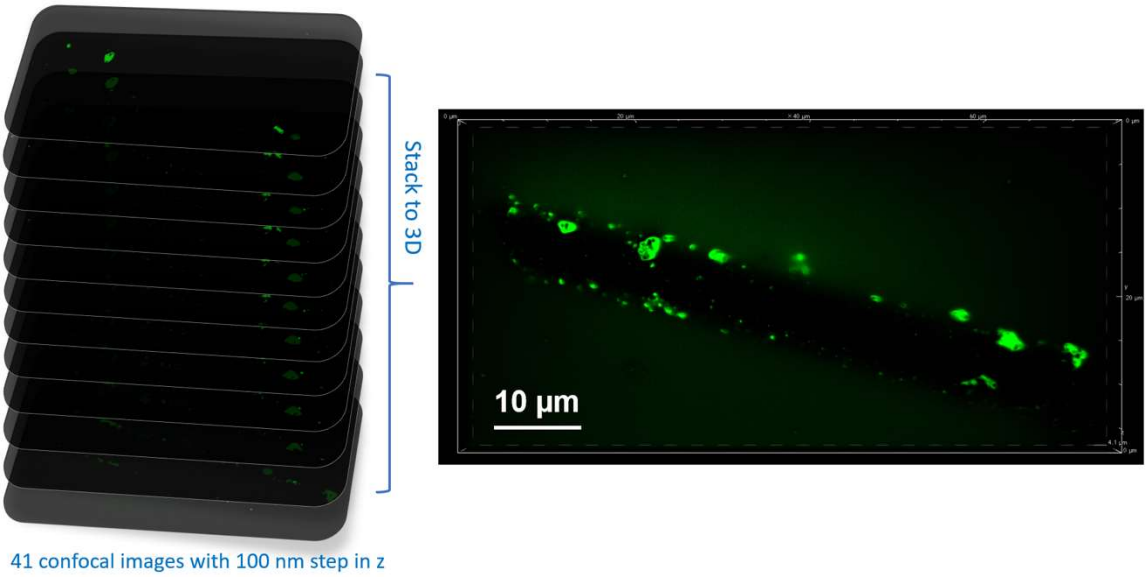

Fig. 5.1.S18: 3D image by 41 2D confocal image stack in z. The z step is 100 nm.

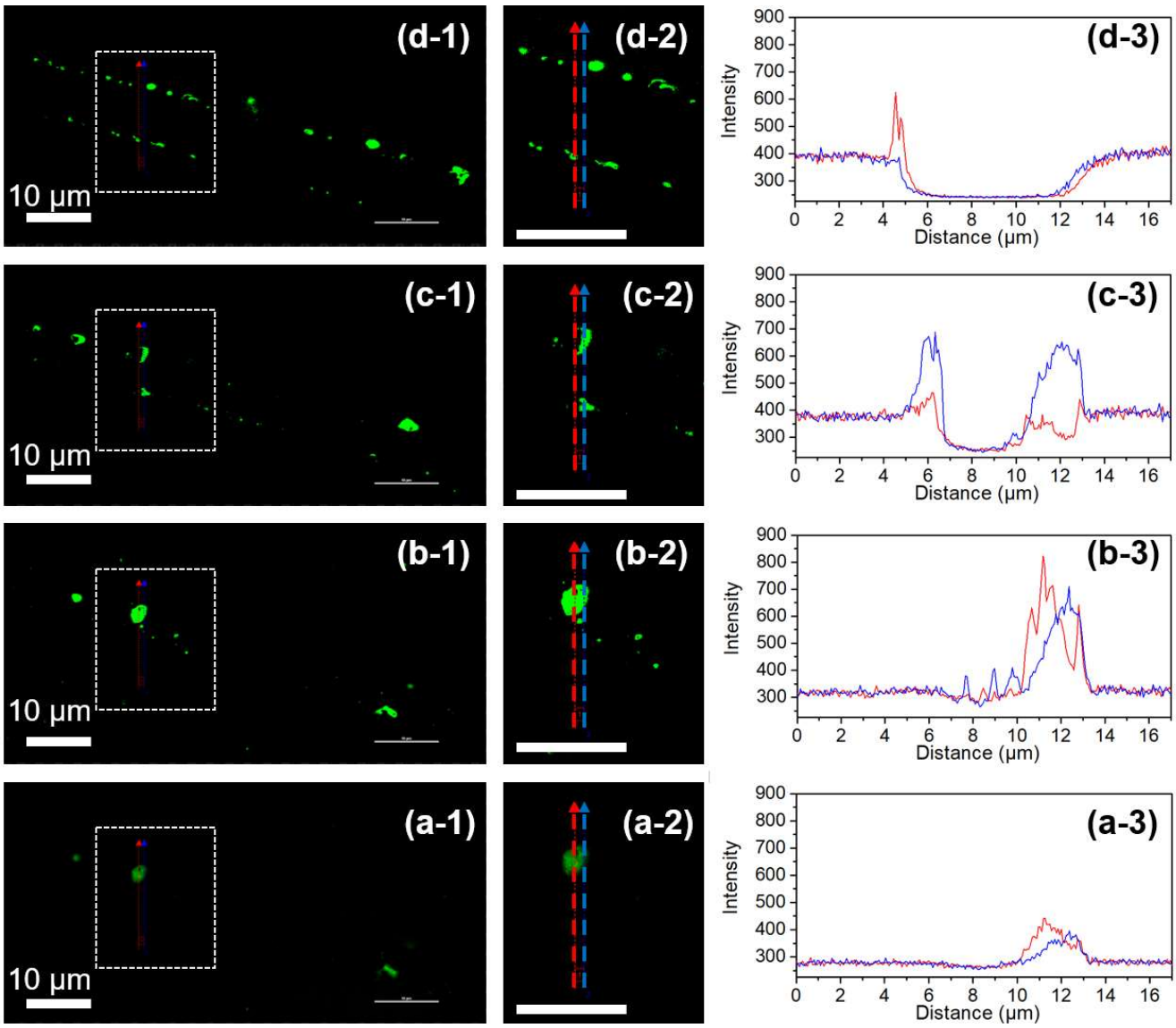

Fig. 5.1.S19: Confocal intensity profile across a Pd@GW catalyst at different z-step. The corresponding confocal images a-d were shown at Fig. 5.1.3 (a-d).

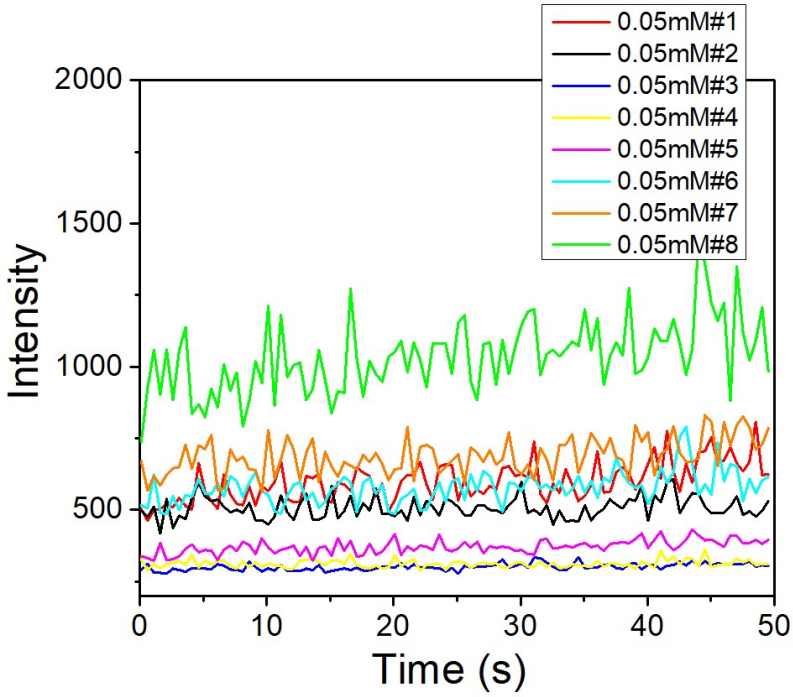

Fig. 5.1.S20: Confocal fluorescence intensity traces of selected areas of 0.05 mM NN1 reaction. The spots number and position are shown in Fig. 5.1.5 of the manuscript.

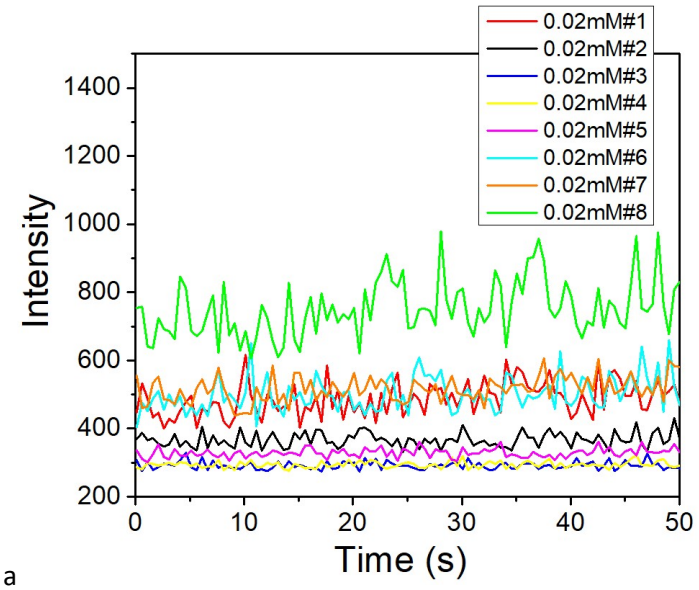

a

Fig. 5.1.S21: Confocal fluorescence intensity traces of selected areas of 0.02 mM NN1 reaction. The spots number and position are shown in Fig. 5.1.5 of the manuscript.

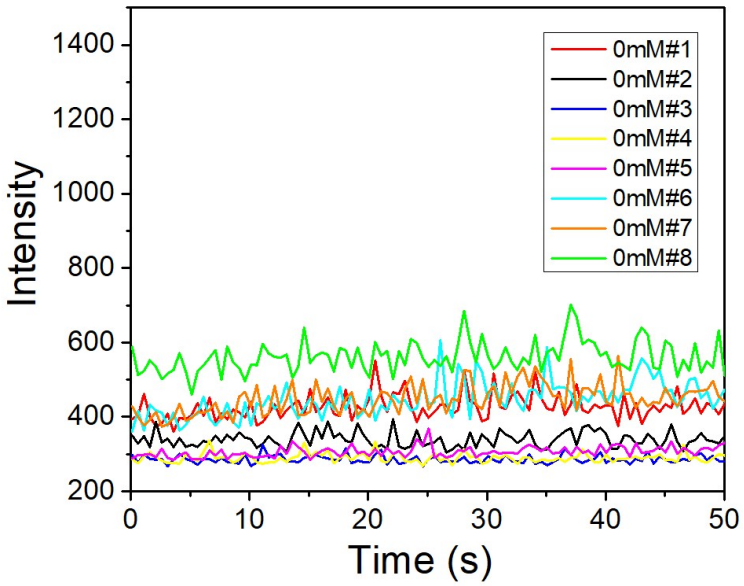

Fig. 5.1.S22: Confocal fluorescence intensity traces of selected areas after H_2O washing (0.3 mL). The spots number and position are shown in Fig. 5.1.5 of the manuscript.

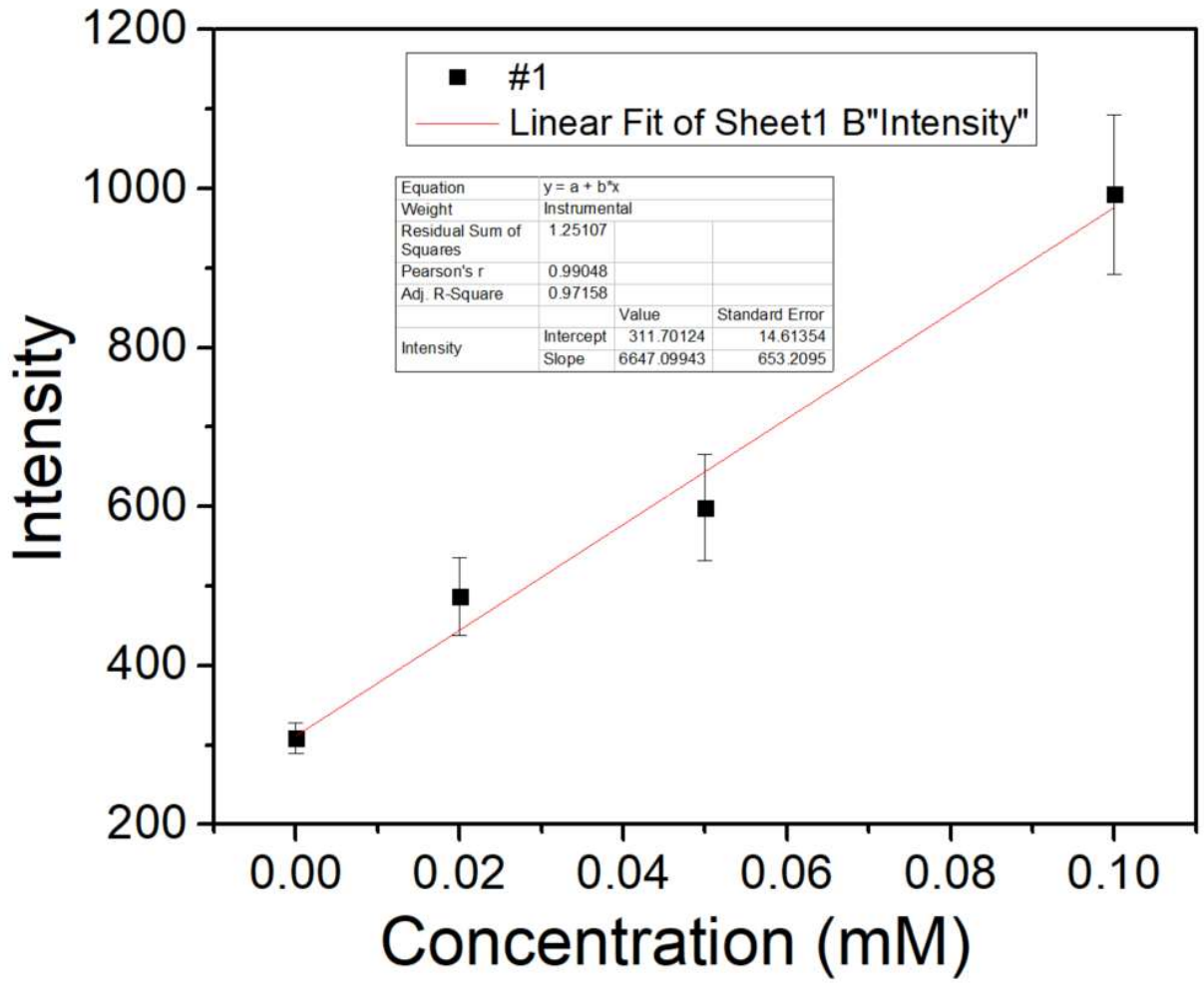

Fig. 5.1.S23: Fluorescence intensity as a function of reaction concentration of position #1. The spots number and position are shown in Fig. 5.1.5 of the manuscript.

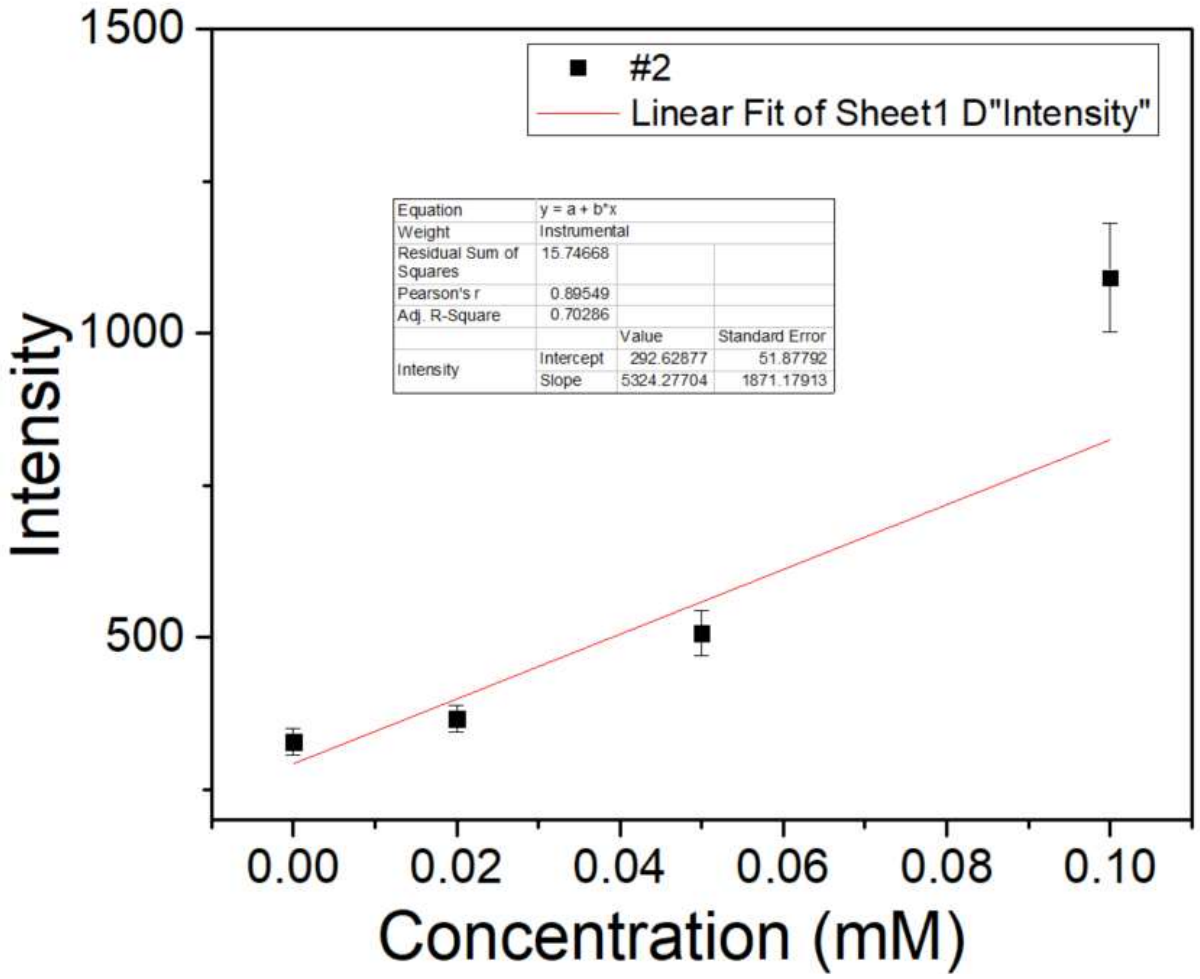

Fig. 5.1.S24: Fluorescence intensity as a function of reaction concentration of position #2. The spots number and position are shown in Fig. 5.1.5 of the manuscript.

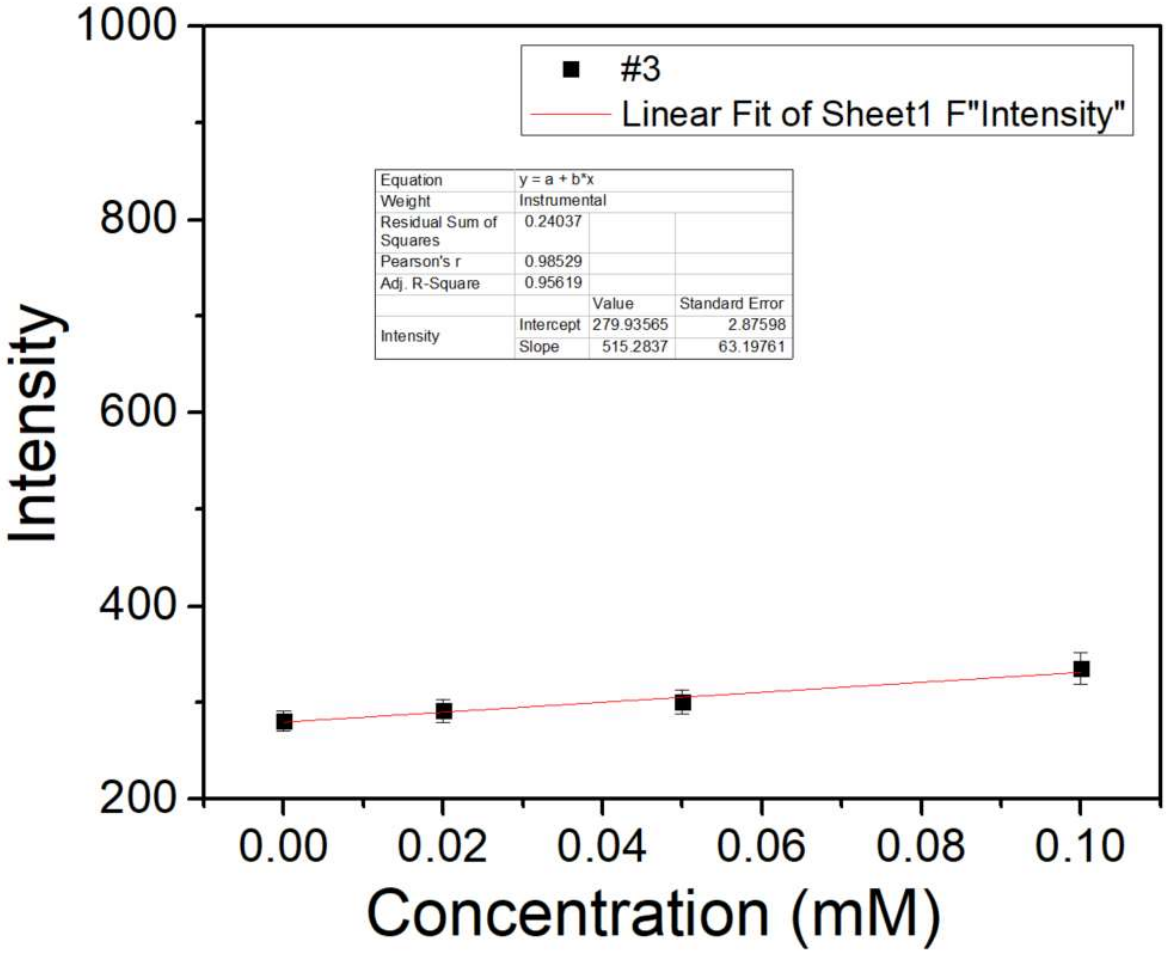

Fig. 5.1.S25: Fluorescence intensity as a function of reaction concentration of position #3. #3 is the inert representative area of Pd@GW without Pd particles. The spots number and position are shown in Fig. 5.1.5 of the manuscript.

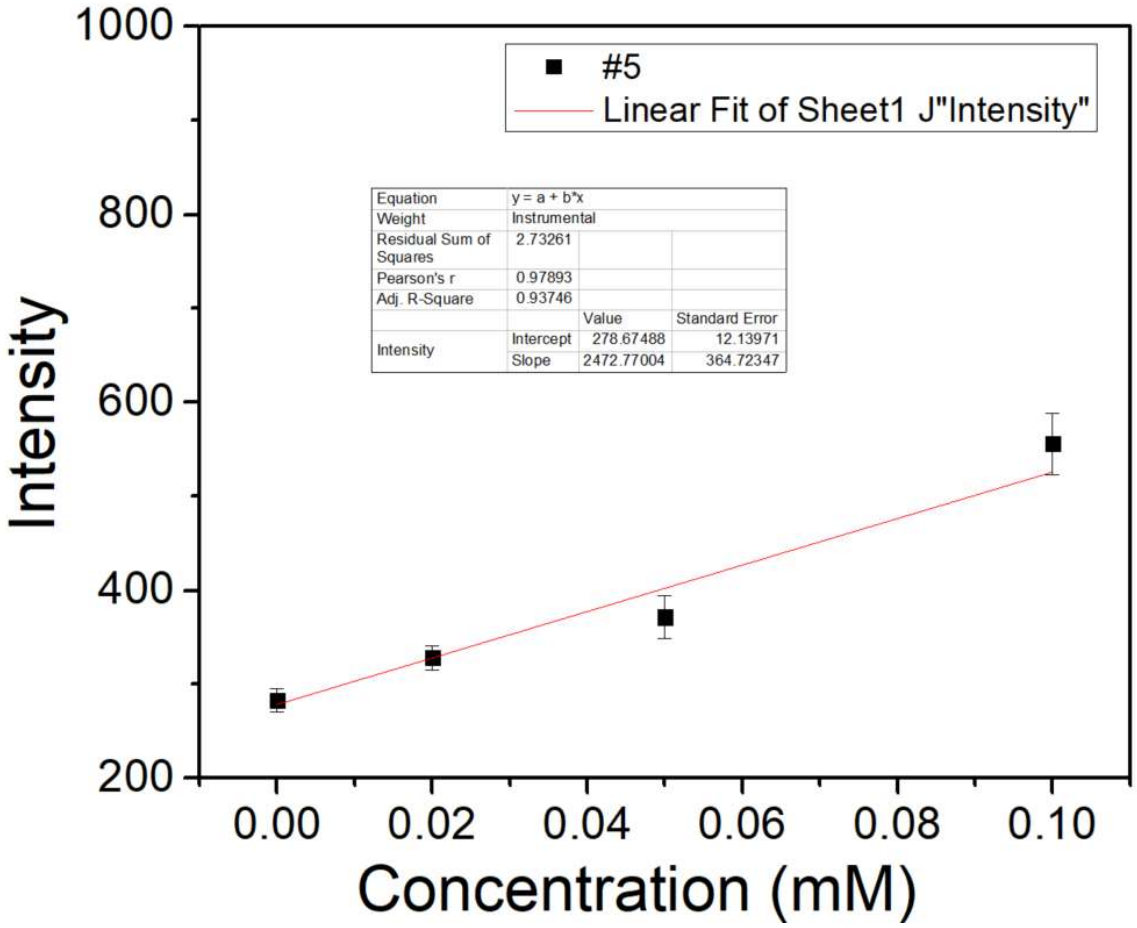

Fig. 5.1.S26: Fluorescence intensity as a function of reaction concentration of position #5 (representative background). The spots number and position are shown in Fig. 5.1.5 of the manuscript.

6 - Single-molecule Microscopy Data (TIRFM)

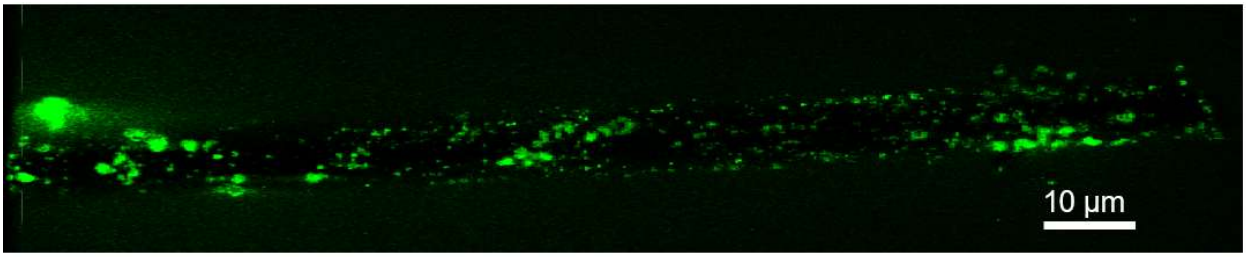

Fig. 5.1.S27: Confocal fluorescence image (2D sum of 9 z-planes) of a ~130 μm long fiber decorated with Pd. Each z-step is 500nm.

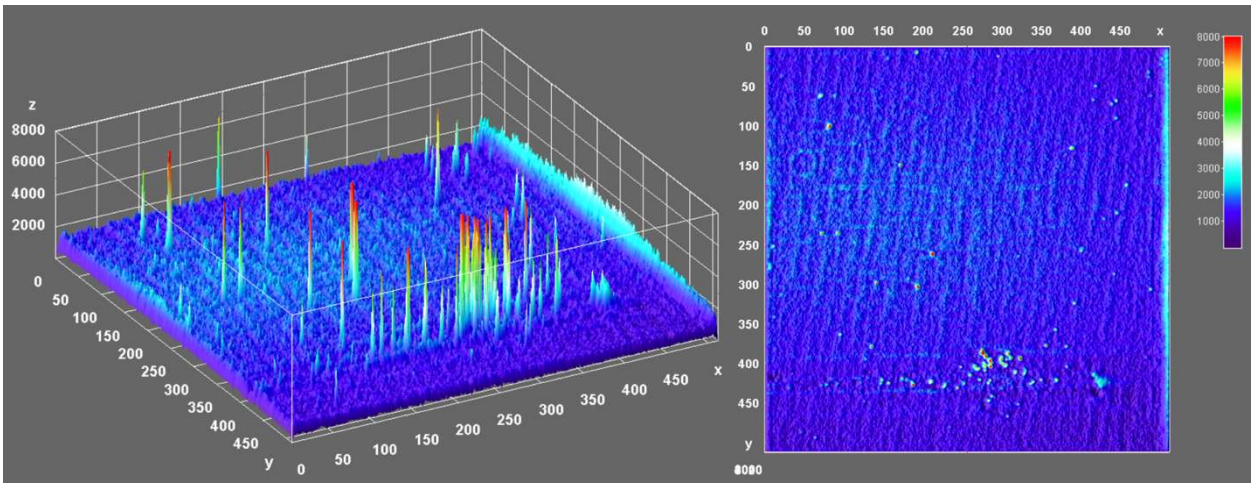

Fig. 5.1.S28: 3D image and intensity stack images of 3000 frames. In the right image the Pd@GW fiber segment used is located approximately at 430 in the y-scale. Each pixel is ~160 nm.

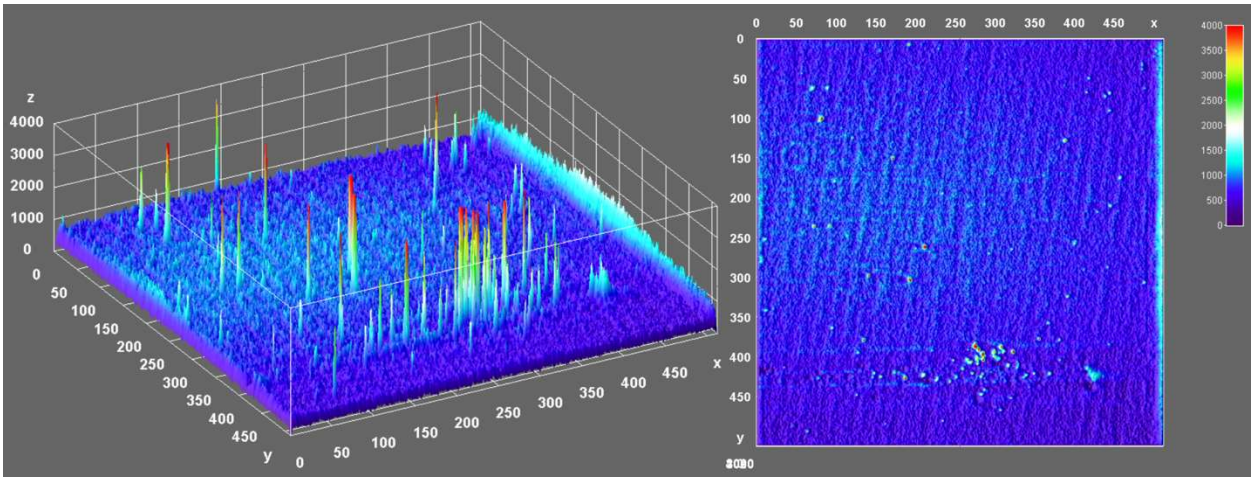

Fig. 5.1.S29: 3D image and intensity stack images of 1-1500 frames (150 seconds).

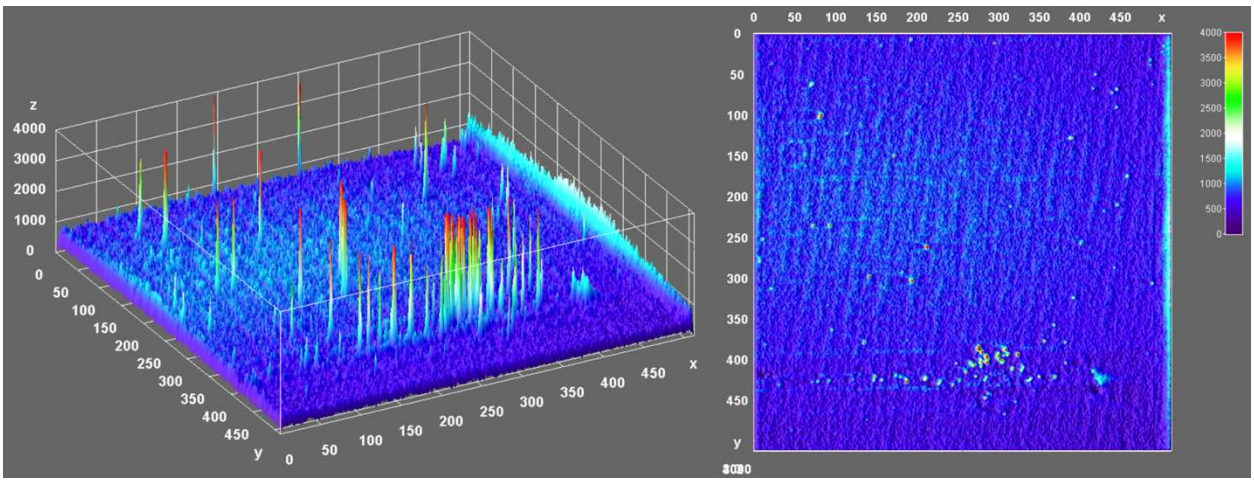

Fig. 5.1.S30: 3D image and intensity stack images of 1501-3000 frames (150 seconds).

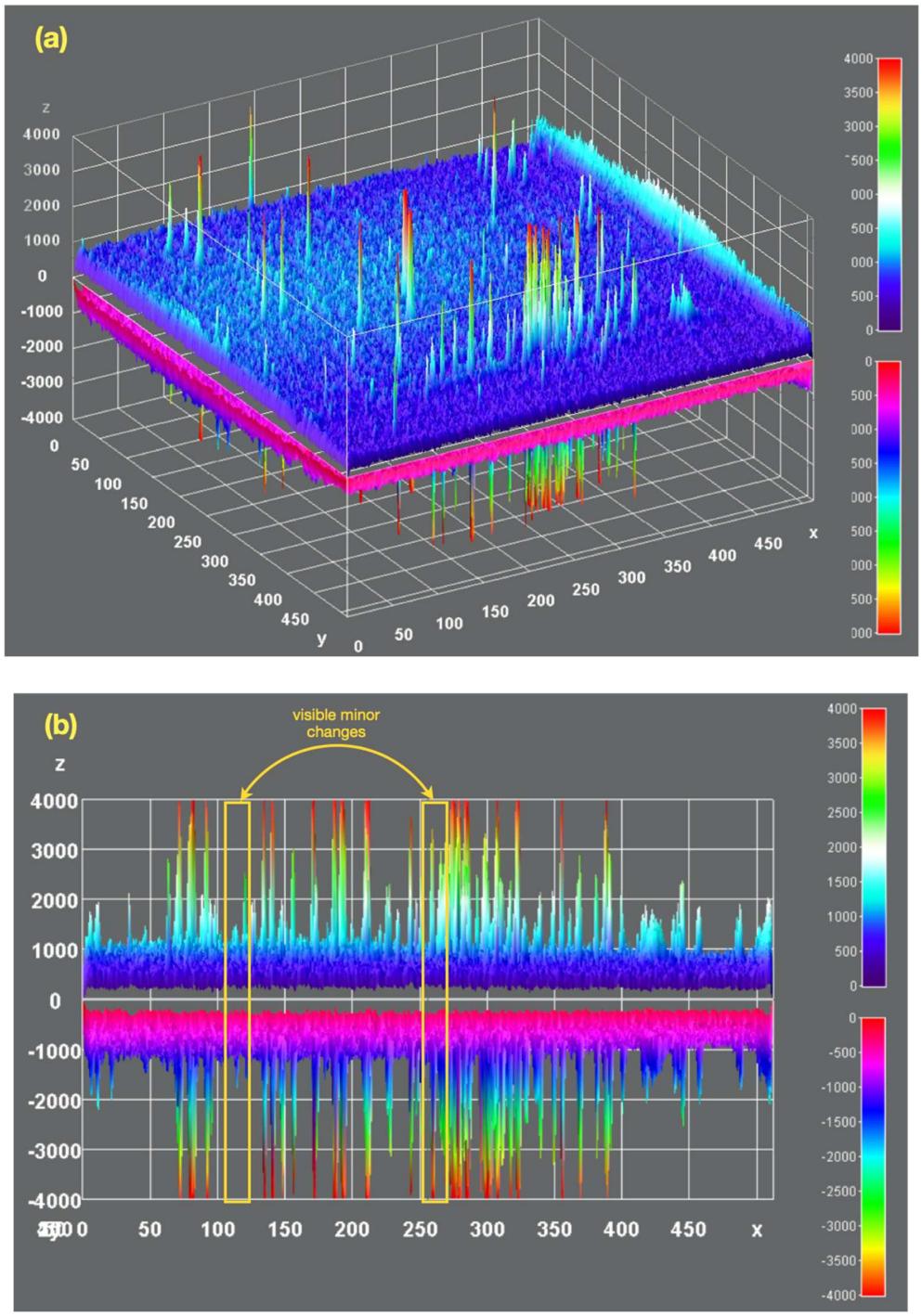

Fig. 5.1.S31: Images of the first 1500 frames (top) and second 1500 frames (inverted, shown at bottom); (a) 3D plot; (b) view from the edge of the x-y plane. Note that the vast majority of the plot features do not change. Detailed observation in the yellow rectangle enclosures do undergo minor changes in site activity when two 150 s acquisitions are compared.

7 - SEM and confocal co-localized analysis

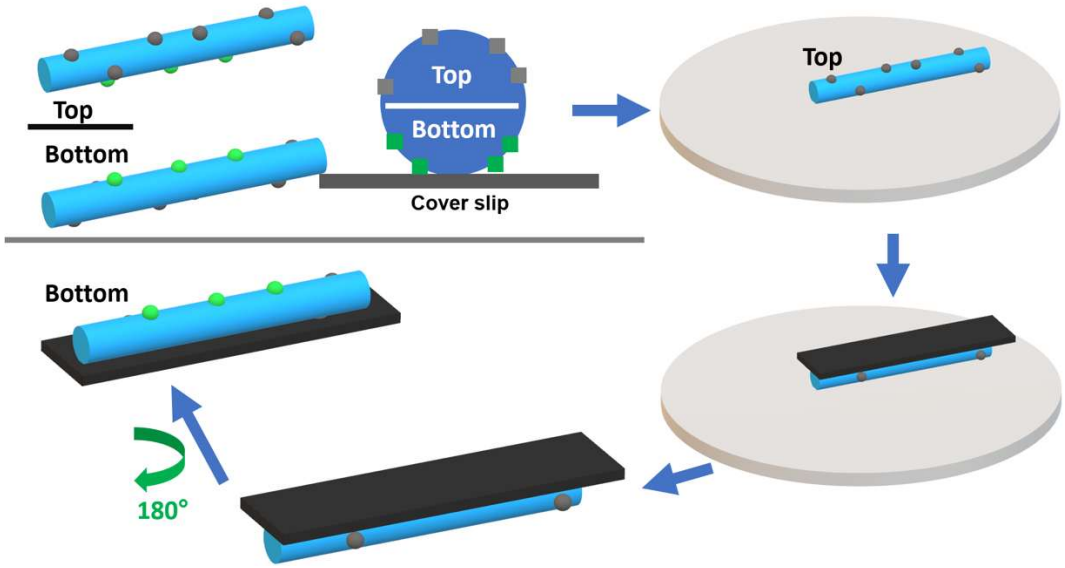

Fig. 5.1.S32: Inversion process of Pd@GW catalyst on cover slip. In this process carbon tape is used to flip the glass fiber, revealing the bottom region of the fiber- the same region which is imaged using confocal microscopy.

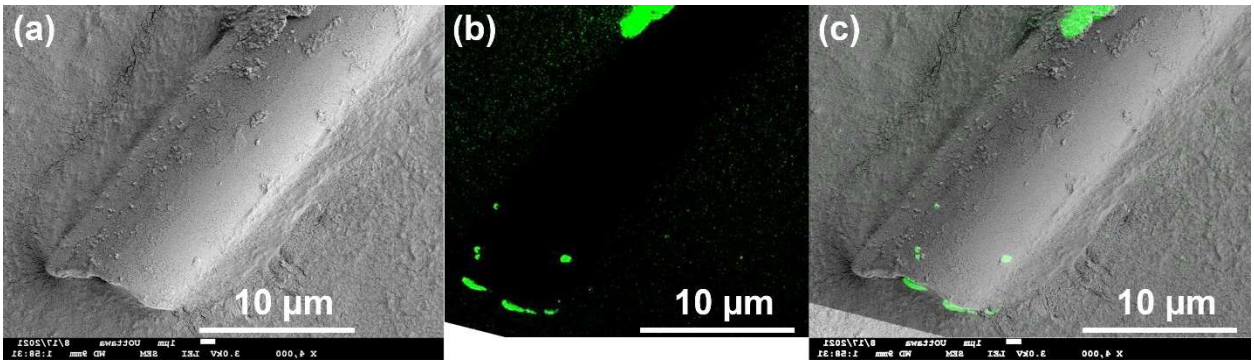

Fig. 5.1.S33: Magnified SEM (a) and confocal (b) images of Pd@GW, and superimposed confocal/SEM combined image (c).

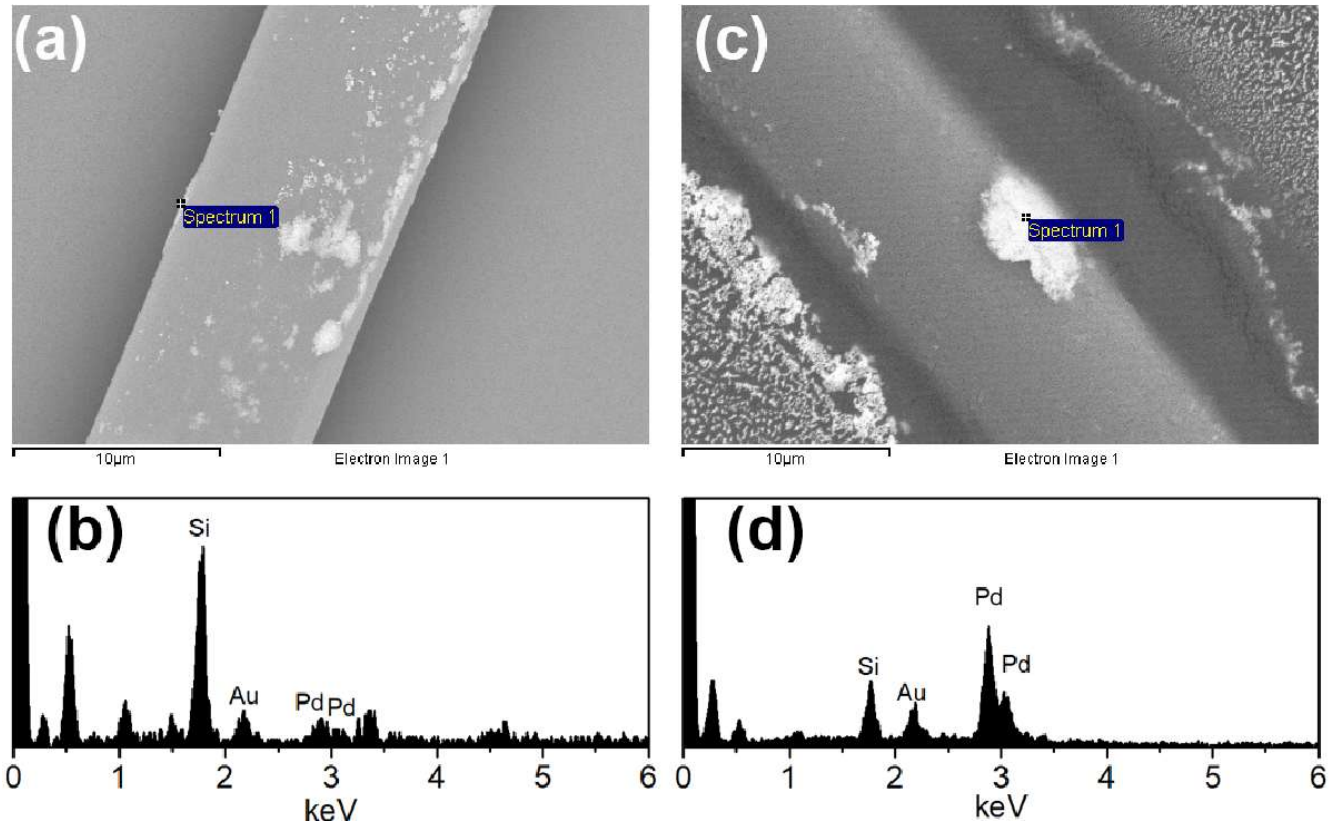

Fig. 5.1.S34: SEM images and corresponding EDS analysis of Pd@GW before (a-b) and after inversion c-d).

8 - FLIM data

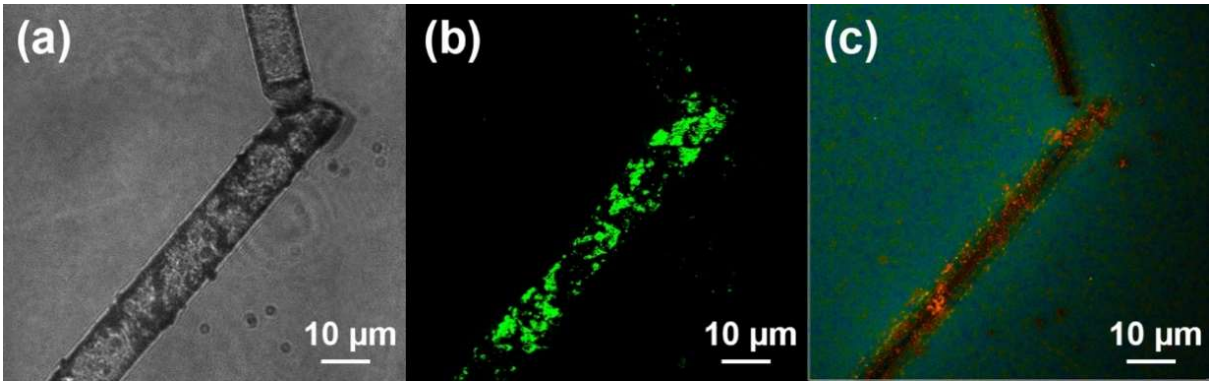

Fig. 5.1.S35: White light transmission (a), confocal 3D stack image (b) and FLIM image (c) of the same fibers.

The FLIM intensity and lifetime profile analysis are shown in Fig. 5.1.S36. The lifetime and intensity traces of surface region of Pd@GW are shown in (a, b). The lifetime dropped to 1.7 ns and the intensity increases to ~60 when the products are close to the Pd particles. Due to the cylinder structure of glass wool, the detectors are not able to receive photons from the inside of the catalyst. The photon intensity is almost zero from 9.5 to 18.0 µm at x-axis and 8.5 to 19.5 µm at y-axis as shown in Fig. 5.1.S36 (f). The lifetime traces of internal structure (~10-18 µm) were not accurate because of the low photon number. It is worth pointing out that the intensity jumps to ~60 when the profile line crosses the Pd structure (see arrows in (f) and (g)), and its lifetime decrease to around 2 ns closed to Pd particles.

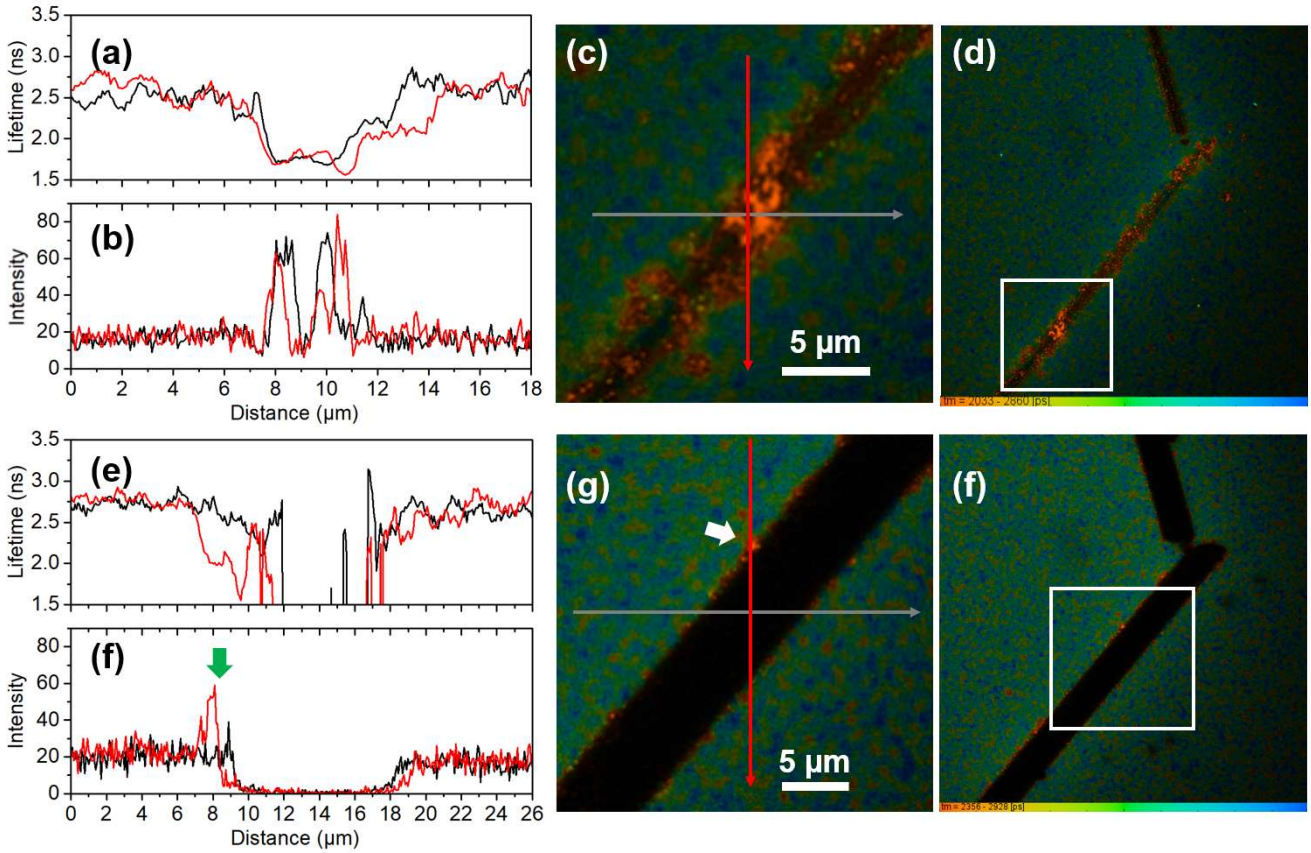

Fig. 5.1.S36: Lifetime profile (a, e) and FLIM intensity profile (b, f) across a Pd@GW catalyst at different z-step (a-d: 0.2 μm; e-f: 1.4 μm). The cross-profile lines were shown in (c) and (g), the original FLIM figures were shown in (d) and (f), the white square was the selected ROI.

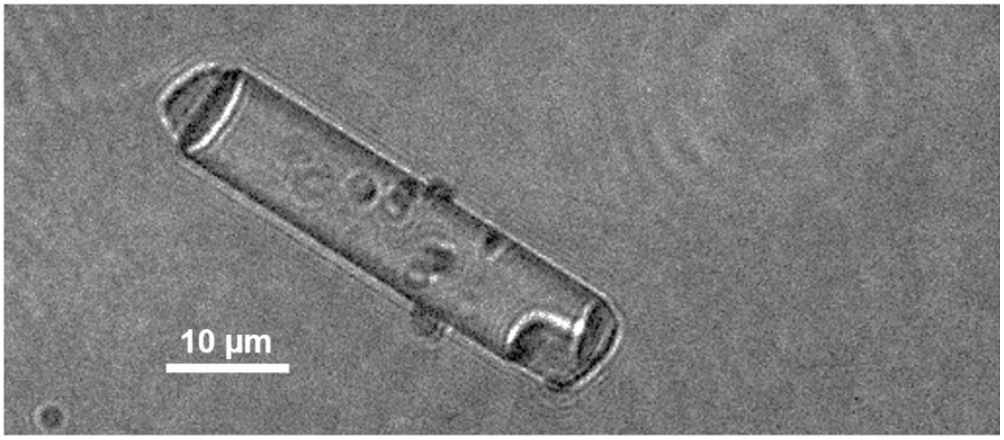

Fig. 5.1.S37: White light image of catalytic fiber in Fig. 5.1.11 (a).

Table 5.1.S1: Confocal z-stack step depth analysis of Fig. 5.1.10.

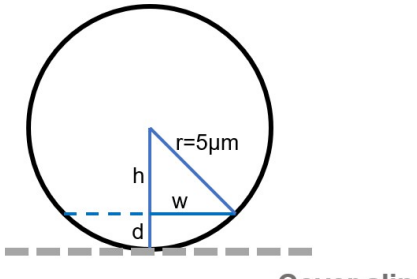

$$d = r - \sqrt{r^2 - w^2}$$

Where:
r: Pd@GW radius ~ 5 µm
w: half width of cross profile from FLIM and confocal images
d: distance of cross profile from coverslip

	Width (µm)	Height (µm)	d (µm)
a, b	8.05	2.97	2.03
c, d	6.9	3.62	1.38
e, f	5.25	4.26	0.74
g, h	2.83	4.80	0.20
I, j	2.05	4.89	0.11

References

1. Y. Zhao , H. Zhou , X. Zhu , Y. Qu , C. Xiong , Z. Xue , Q. Zhang , X. Liu , F. Zhou , X. Mou , W. Wang , M. Chen , Y. Xiong , X. Lin , Y. Lin , W. Chen , H.-J. Wang , Z. Jiang , L. Zheng , T. Yao , J. Dong , S. Wei , W. Huang , L. Gu , J. Luo , Y. Li and Y. Wu , Simultaneous oxidative and reductive reactions in one system by atomic design, *Nat. Catal.*, 2021, 4 , 134
2. G. S. Lee , D. Kim and S. H. Hong , Pd-catalyzed formal Mizoroki–Heck coupling of unactivated alkyl chlorides, *Nat. Commun.*, 2021, 12 , 991
   B. Sun , L. Ning and H. C. Zeng , Confirmation of Suzuki–Miyaura Cross-Coupling Reaction Mechanism through Synthetic Architecture of Nanocatalysts, *J. Am. Chem. Soc.*, 2020, 142 , 13823
   X. Zhang , Z. Sun , B. Wang , Y. Tang , L. Nguyen , Y. Li and F. F. Tao , C–C Coupling on Single-Atom-Based Heterogeneous Catalyst, *J. Am. Chem. Soc.*, 2018, 140 , 954
3. V. Muravev , G. Spezzati , Y.-Q. Su , A. Parastaev , F.-K. Chiang , A. Longo , C. Escudero , N. Kosinov and E. J. M. Hensen , Interface dynamics of Pd–CeO2 single-atom catalysts during CO oxidation, *Nat. Catal.*, 2021, 4 , 469
4. L. Liu and A. Corma , Metal Catalysts for Heterogeneous Catalysis: From Single Atoms to Nanoclusters and Nanoparticles, *Chem. Rev.*, 2018, 118 , 4981
5. L. Djakovitch , M. Wagner , C. G. Hartung , M. Beller and K. Koehler , Pd-catalyzed Heck arylation of cycloalkenes—studies on selectivity comparing homogeneous and heterogeneous catalysts, *J. Mol. Catal. A: Chem.*, 2004, 219 , 121
6. J. A. Widegren and R. G. Finke , A review of the problem of distinguishing true homogeneous catalysis from soluble or other metal-particle heterogeneous catalysis under reducing conditions, *J. Mol. Catal. A: Chem.*, 2003, 198 , 317
   W. Shi , Y. Niu , S. Li , L. Zhang , Y. Zhang , G. A. Botton , Y. Wan and B. Zhang , Revealing the Structure Evolution of Heterogeneous Pd Catalyst in Suzuki Reaction via the Identical Location Transmission Electron Microscopy, *ACS Nano*, 2021, 15 , 8621
   C. Yue , Q. Xing , P. Sun , Z. Zhao , H. Lv and F. Li , Enhancing stability by trapping palladium inside N-heterocyclic carbene-functionalized hypercrosslinked polymers for heterogeneous C-C bond formations, *Nat. Commun.*, 2021, 12 , 1875
   P. P. Mpungose , Z. P. Vundla , G. E. M. Maguire and H. B. Friedrich , The Current Status of Heterogeneous Palladium Catalysed Heck and Suzuki Cross-Coupling Reactions, *Molecules*, 2018, 23 , 1676
7. V. P. Ananikov and I. P. Beletskaya , Toward the Ideal Catalyst: From Atomic Centers to a Cocktail of Catalysts, *Organometallics*, 2012, 31 , 1595
8. C. Gnad , A. Abram , A. Urstöger , F. Weigl , M. Schuster and K. Köhler , Leaching Mechanism of Different Palladium Surface Species in Heck Reactions of Aryl Bromides and Chlorides, *ACS Catal.*, 2020, 10 , 6030
9. M. Pagliaro , V. Pandarus , R. Ciriminna , F. Béland and P. Demma Carà , Heterogeneous versus Homogeneous Palladium Catalysts for Cross-Coupling Reactions, *ChemCatChem*, 2012, 4 , 432
   M. Pagliaro , V. Pandarus , R. Ciriminna , F. Béland and P. Demma Carà , Corrigendum: Heterogeneous versus Homogeneous Palladium Catalysts for Cross-Coupling Reactions, *ChemCatChem*, 2012, 4 , 1030
10. W. Huang , Z. Zuo , P. Han , Z. Li and T. Zhao , XPS and XRD investigation of Co/Pd/TiO2 catalysts by different preparation methods, *J. Electron Spectrosc. Relat. Phenom.*, 2009, 173 , 88

11. B. Dong , N. Mansour , Y. Pei , Z. Wang , T. Huang , S. L. Filbrun , M. Chen , X. Cheng , M. Pruski , W. Huang and N. Fang , Single Molecule Investigation of Nanoconfinement Hydrophobicity in Heterogeneous Catalysis, *J. Am. Chem. Soc.*, 2020, 142 , 13305
B. Wang , A. E. Lanterna and J. C. Scaiano , Mechanistic Insights on the Semihydrogenation of Alkynes over Different Nanostructured Photocatalysts, *ACS Catal.*, 2021, 11 , 4230
X. Mao , C. Liu , M. Hesari , N. Zou and P. Chen , Super-resolution imaging of non-fluorescent reactions via competition, *Nat. Chem.*, 2019, 11 , 687
12. J. C. Scaiano and A. E. Lanterna , Is Single-Molecule Fluorescence Spectroscopy Ready To Join the Organic Chemistry Toolkit? A Test Case Involving Click Chemistry, *J. Org. Chem.*, 2017, 82 , 5011
13. M. Yaghmaei , A. E. Lanterna and J. C. Scaiano , Nitro to amine reductions using aqueous flow catalysis under ambient conditions, *iScience*, 2021, 24 , 103472
14. B. Wang , J. Durantini , M. R. Decan , J. Nie , A. E. Lanterna and J. C. Scaiano , From the molecule to the mole: improving heterogeneous copper catalyzed click chemistry using single molecule spectroscopy, *Chem. Commun.*, 2017, 53 , 328
15. P. Costa , D. Sandrin and J. C. Scaiano , Real-time fluorescence imaging of a heterogeneously catalysed Suzuki–Miyaura reaction, *Nat. Catal.*, 2020, 3 , 427
16. A. Elhage , B. Wang , N. Marina , M. L. Marin , M. Cruz , A. E. Lanterna and J. C. Scaiano , Glass wool: a novel support for heterogeneous catalysis, *Chem. Sci.*, 2018, 9 , 6844
17. R. I. Teixeira , N. C. de Lucas , S. J. Garden , A. E. Lanterna and J. C. Scaiano , Glass wool supported ruthenium complexes: versatile, recyclable heterogeneous photoredox catalysts, *Catal. Sci. Technol.*, 2020, 10 , 1273
18. G. Nechifor , E. E. Totu , A. C. Nechifor , L. Constantin , A. M. Constantin , M. E. Cărăuşu and I. Isildak , Added value recyclability of glass fiber waste as photo-oxidation catalyst for toxic cytostatic micropollutants, *Sci. Rep.*, 2020, 10 , 136
Y. Matatov-Meytal and M. Sheintuch , Catalytic fibers and cloths, *Appl. Catal., A*, 2002, 231 , 1
19. L. Kiwi-Minsker , I. Yuranov , E. Slavinskaia , V. Zaikovskii and A. Renken , Pt and Pd supported on glass fibers as effective combustion catalysts, *Catal. Today*, 2000, 59 , 61
20. S. Xu , J. Du , Q. Zhou , H. Li , C. Wang and J. Tang , Selective and leaching-resistant palladium catalyst on a porous polymer support for phenol hydrogenation, *J. Colloid Interface Sci.*, 2021, 604 , 876
21. M. Gholinejad , F. Zareh and C. Nájera , Nitro group reduction and Suzuki reaction catalysed by palladium supported on magnetic nanoparticles modified with carbon quantum dots generated from glycerol and urea, *Appl. Organomet. Chem.*, 2018, 32 , e3984
22. Y. Monguchi , T. Ichikawa and H. Sajiki , Recent Development of Palladium-Supported Catalysts for Chemoselective Hydrogenation, *Chem. Pharm. Bull.*, 2017, 65 , 2
23. M. Ueno , Y. Morii , K. Uramoto , H. Oyamada , Y. Mori and S. Kobayashi , Catalytic Flow Hydrogenation of Aromatic Nitro Compounds Using Polysilane-Supported Palladium, *J. Flow Chem.*, 2014, 4 , 160
24. J. Tuteja , S. Nishimura and K. Ebitani , Base-free chemoselective transfer hydrogenation of nitroarenes to anilines with formic acid as hydrogen source by a reusable heterogeneous Pd/ZrP catalyst, *RSC Adv.*, 2014, 4 , 38241
25. H. Esaki , T. Hattori , A. Tsubone , S. Mibayashi , T. Sakata , Y. Sawama , Y. Monguchi , H. Yasuda , K. Nosaka and H. Sajiki , Chemoselective Hydrogenation Catalyzed by Pd on Spherical Carbon, *ChemCatChem*, 2013, 5 , 3629

26. D. Bokov , M. Z. Mahmoud , G. Widjaja , W. Suksatan , S. Chupradit , U. Altimari , H. Hussein , Y. Mustafa and M. Kazemnejadi , Transfer hydrogenation of nitroarenes using cellulose filter paper-supported Pd/C by filtration as well as sealed methods, *RSC Adv.*, 2022, 12 , 10933
27. T. J. Colacot Palladium Based FibreCat and SMOPEX® as Supported Homogenous Catalyst Systems for Simple to Challenging Carbon–Carbon Coupling Reactions, *Top. Catal.*, 2008, 48 , 91
28. A. I. Carrillo , K. G. Stamplecoskie , M. L. Marin and J. C. Scaiano , From the mole to the molecule': ruthenium catalyzed nitroarene reduction studied with 'bench', high-throughput and single molecule fluorescence techniques, *Catal. Sci. Technol.*, 2014, 4 , 1989
29. A.Elhage, in Faculty of Science, University of Ottawa, Ottawa, Canada, 2019, p. 194.
30. L. Li , H. Zhao , J. Wang and R. Wang , Facile Fabrication of Ultrafine Palladium Nanoparticles with Size- and Location-Control in Click-Based Porous Organic Polymers, *ACS Nano*, 2014, 8 , 5352
31. A. Chen and C. Ostrom , Palladium-Based Nanomaterials: Synthesis and Electrochemical Applications, *Chem. Rev.*, 2015, 115 , 11999
32. M. L. Marin , K. L. McGilvray and J. C. Scaiano , Photochemical Strategies for the Synthesis of Gold Nanoparticles from Au(III) and Au(I) Using Photoinduced Free Radical Generation, *J. Am. Chem. Soc.*, 2008, 130 , 16572
    K. L. McGilvray , M. R. Decan , D. Wang and J. C. Scaiano , Facile Photochemical Synthesis of Unprotected Aqueous Gold Nanoparticles, *J. Am. Chem. Soc.*, 2006, 128 , 15980
33. B. P. Vinayan , K. Sethupathi and S. Ramaprabhu , Facile synthesis of triangular shaped palladium nanoparticles decorated nitrogen doped graphene and their catalytic study for renewable energy applications, *Int. J. Hydrogen Energy*, 2013, 38 , 2240
34. P. Anger , P. Bharadwaj and L. Novotny , Enhancement and quenching of single-molecule fluorescence, *Phys. Rev. Lett.*, 2006, 96 , 113002
35. Y. Kuwahara , H. Kango and H. Yamashita , Pd Nanoparticles and Aminopolymers Confined in Hollow Silica Spheres as Efficient and Reusable Heterogeneous Catalysts for Semihydrogenation of Alkynes, *ACS Catal.*, 2019, 9 , 1993
    S. S. Islam , S. Riyajuddin , R. A. Molla , N. Yasmin , K. Ghosh and S. M. Islam , POP-Pd(ii) catalyzed easy and safe in situ carbonylation towards the synthesis of α-ketoamides from secondary cyclic amines utilizing CHCl3 as a carbon monoxide surrogate, *New J. Chem.*, 2020, 44 , 1979
    Y. Liu , Q. Xin , D. Yin , S. Liu , L. Li , C. Xie and S. Yu , One-Pot Synthesis of Stable Pd@mSiO2 Core–Shell Nanospheres and Their Application to the Hydrogenation of Levulinic Acid, *Catal. Lett.*, 2020, 150 , 3437
36. Y. Wang , J. Tao , Y. Wang , L. Huang and X. Ding , Remarkable reduction ability towards p-nitrophenol by a synergistic effect against the aggregation and leaching of palladium nanoparticles in dendritic supported catalysts, *Appl. Surf. Sci.*, 2022, 574 , 151702
37. I. L. C. Buurmans and B. M. Weckhuysen , Heterogeneities of individual catalyst particles in space and time as monitored by spectroscopy, *Nat. Chem.*, 2012, 4 , 873
38. N. L. Pacioni, M. González-Bejar , E. Alarcón , K. L. McGilvray and J. C. Scaiano , Surface Plasmons Control the Dynamics of Excited Triplet States in the Presence of Gold Nanoparticles, *J. Am. Chem. Soc.*, 2010, 132 , 6298
39. J. C. Scaiano, K. G. Stamplecoskie, G. L. Hallett-Tapley, Photochemical Norrish type I reaction as a tool for metal nanoparticle synthesis: importance of proton coupled electron transfer, *Chem. Commun.* 2012, *48* (40), 4798-808.

40. A. Corma, P. Concepcion, P. Serna, A different reaction pathway for the reduction of aromatic nitro compounds on gold catalysts, *Angew. Chem.* 2007, *46* (38), 7266-9.
41. Y. Dai, C. Li, Y. Shen, T. Lim, J. Xu, Y. Li, H. Niemantsverdriet, F. Besenbacher, N. Lock, R. Su, Light-tuned selective photosynthesis of azo- and azoxy-aromatics using graphitic C3N4, *Nat. Commun.* 2018, *9* (1), 60.

Chapter 6 – Conclusions

Chapter 2 Summary

This chapter outlined the foundational work that opened the door to later chapters of this thesis. Using both in-flow (Ch. 2.1) and batch (Ch. 2.2) approaches, we show the synthesis is AgNP seeds, decahedra, and triangles. The seeds in particular were produced using a range of photoinitiators in mixed aqueous/alcoholic systems in rapid time-frames, greatly improving the scalability of photoinitated AgNP synthesis. Using flow synthesis with different photoinitiators, we were able to generate particles with a range of sizes between 4.4 to 9.5 nm, with more polar ketyl radical generators giving smaller, narrower size distributions compared to aminoalkyl radical generators yielding particles on the larger end of the scale, with wider size distributions. Observationally, we also found that ketyl radical generators caused less silver deposition within the tubing of our flow reactor, making them more favorable for future projects. The second part of Chapter 2 focused on growing sAgNPs into more complex structures in aqueous batch synthesis. In this approach, sAgNPs are bombarded with high intensity LED irradiation, eventually shifting the shape and absorbance to more useful values. In particular, we were able to control the plasmonic absorbance of tAgNPs across the red/NIR range by adjusting citrate levels between 1 and 15 mM. These tAgNPs had corresponding sizes averaging between 130 to 175 nm, with fairly large size dispersity compared to the much smaller (48-58 nm) decahedral particles.

Future Directions

The flow project has been picked up and further developed by our former undergraduate student Carly Frank, who has joined the lab on a full-time basis as a MSc student. Carly has made incredible progress with the flow synthesis of AgNPs, now extending the capabilities of our method to producing AgNPs of different sizes and shaped including decahedra and triangles, morphologies that we previously only made in lengthy batch synthesis approaches, as outlined in Ch.2.2. The combination of flow and shape control is incredibly useful, and has the potential to substantially accelerate the generation of complex AgNPs, especially triangles. We currently have a manuscript in review on this very topic, and hope that we can continue to improve our control of AgNP synthesis through Carly's investigation.

Chapter 3 Summary

This chapter focused on applying the AgNPs generated in Ch.2.2 in light activated antibacterial applications. We found in this published work that the antimicrobial activity of dAgNPs and tAgNPs could be massive increased by irradiating particles with LED illumination that correspond to the plasmonic absorbance of the particles. Antibacterial experiments showed an increase in antimicrobial activity from <1 log unit of bacterial killing for AgNP solutions with Ag concentrations of 10 ppm under dark conditions to 9 log units of killing when the same solutions were irradiated with light sources matching the wavelength of their plasmonic absorbance for times as short as 10 min. Even solutions with sub-toxic levels of Ag (5 ppm) could be activated to achieve substantial levels of bacterial killing, on the scale of 4 log units of killing within 15 min of complementary irradiation. Similar experiments on human cell lines did not show similar levels of killing, with HT-1080 human fibrosarcoma cells showing no significant loss in viability under similar conditions. Investigation of killing mechanisms suggest that the key contributor to antibacterial activity enhancement is derived from the production of ROS and RNS, as well as the induction of thermal stress from the particles heating their environment, reaching as high as 55°C within 15 min of irradiation in 5 mL batches of 10 ppm tAgNP.

Future Directions

The findings of this work show that when combined with light, AgNPs can have substantially greater antibacterial effects. This effect is underappreciated in many applications of the material, and suggests that the key to unlocking the potential of metal nanoparticles in biological applications may be the use of light. This is still a promising field with ample room for innovation, especially as nanomaterial chemists seek to break through into translational medicine. AgNPs do have drawbacks – namely their sensitivity to their environment (especially Cl^-), which makes their use as phototherapeutic agents a persistent challenge. Thus, future experiments may need to be focused on developing protective layers for the particles which enhance particle stability without compromising efficacy. The findings from this work also inspire more recently our foray into in-flow water disinfection using AgNPs on glasswool, the in-progress topic of Chapter 4. As a biologist originally, I hope to see light activation become a staple of AgNP application in the future.

Chapter 4 Summary

This chapter sought to take advantage of the potent light activated activation of antibacterial AgNPs from Chapter 3, but in a heterogenous setting for the treatment of water. One of the challenges with Chapter 3 was the fact that our AgNPs were colloidal. This is suitable for applications where the particles can be used to disinfect surfaces, but is not ideal for treating large volumes of contaminated media. Therefore, we developed an approach to attach AgNPs to APTES treated glass wool with the goal of creating an in-flow photoreactor for disinfecting contaminated water. Here we described several approaches to making tAgNPs@GW, but ultimately we opted for a light driven approach, as it generated strong absorbance across the visible spectrum as a result of growing and synthesizing new particles of various shapes and sizes on the surface of our fibres. While normally polydispersity is considered to be less favorable, this approach generated fibers with useful absorbance properties that overlap considerably with common white light LEDs, making it a useful tool for accessible water treatment solutions. This reactor used powerful white light irradiation to activate our anchored AgNPs, achieving total in-flow bacterial killing. As a proof of concept, this chapter demonstrates powerful water disinfecting ability for AgNPs, even in a system with room for optimization.

Future Directions

With promising initial results, the future of the project is focused on scaling-up the volume of flow-through, and testing the limits of re-usability that is possible for our tAgNPs@GW. To get the most out of the system some optimizations also need to be considered. For example, in the time frames used for these experiments, the bacterial elimination rate goes from 0% to 100% between the 2 and 10 min timepoints. Clearly, future investigation into shorter residency times is warranted to establish the kinetics of bacterial inactivation for the system and to optimize the flow rates required to have high throughput, while maintaining total disinfection. To achieve ever higher flow, more complex photoreactors may be needed, maximizing the utilization of each photon. To ensure that the Ag and Ag^{+} are not contaminating the water, long term leeching experiments should be performed to confirm that it is safe to use the purified water, and further treatment of the fibres may be necessary to reduce leeching. It should be noted that we have tested for Ag leeching, but to this point have not been able to make a sample concentrated enough to reach the limit of detection for our ICP-OES system.

Given that areas with low water quality often have limited electrical accessibility, it would be valuable to emulate our experiments using a photoreactor driven by the sun to activate the tAgNPs@GW. Solar light powered reactors are naturally highly interesting for the purposes of water treatment and could significantly improve the accessibility of this technology. Finally, an ideal water treatment system can eliminate more than just bacteria from contaminated water. It would be useful to test the catalytic ability of tAgNPs@GW in a variety of photodegradation reactions to see if the system can be multifunctional. Alternatively, combining AgNPs with other photoactive nanoparticles on GW, or different adsorbent materials in general could be a useful path towards whole water treatment.

Chapter 5 Summary

The final chapter of this thesis takes a departure away from AgNPs, instead investigating the mechanisms of heterogenous PdNPs anchored to glass wool in the catalysis of nitro-to-amine reductions. To investigate this reaction, advanced confocal microscopy techniques were used to visualize Pd catalysis using a fluorescent off-on nitro-to-amine probe. Using this technique, we could track the catalytic activity of our Pd@GW fibres under flow conditions over long periods (up to 4 hours), dispelling the notion that heterogenous PdNPs require Pd leeching as a mechanism for catalysis. This work shows that the bulk of heterogenous Pd catalysis occurred on or near the surface of PdNP clusters firmly attached to GW before being washed away under flow. The implications of this challenge theories that heterogenous Pd catalysis is in fact a homogenous or pseudo-homogenous process (as seen on other reactions), but rather is performed in the heterogeneous state, making PdNPs@GW an excellent candidate for flow reactors.

Future Directions

This project has informed future works in our lab, showing that GW is an effective and stable support for PdNPs based heterogenous processes. In fact, it was the results of this work that inspired our attempts to turn AgNPs into heterogenous antibacterial agents, as shown in Chapter 4. Another useful tool from this work is the effectiveness of our NN_x off-on probes. We chose this probe in response to the poor performance of more conventional probes, namely resazurin, which we found to be too sensitive to environmental changes. Using our NN1 probe described in Chapter 5, we have investigated a wide range of catalysts – over 115 in fact, and assessed their performance at performing the nitro-to-amine reduction. This work is summarized in the honors thesis of our former undergraduate student Rama El-Khawaldeh and will hopefully lead to future publications from the group.

Overall Conclusions

The widespread use of LED lighting and the growth of the field of nanomaterials have arrived at the forefront of research at the dawn of the 21st century and, almost as if fated, the interactions between these new age technologies seem to be synergistic beyond my own wildest expectations. We describe this relationship from start to finish in this work, beginning with the formation of sAgNPs using photoinitators to reduce Ag^{+}. From there, we grow the sAgNPs into larger, more robust triangles and decahedra. These particles could be controlled with a high degree of control to manipulate their size, and in the case of tAgNPs, their plasmonic absorbance properties. The powerful absorbance of these materials was utilized effectively for photodisinfection of contaminated bacterial suspensions, with light activation massively amplifying the killing ability of colloidal dAgNPs and tAgNPs against *E. coli* and *S. aureus*. These particles show "silver bullet" potential, showing potent activity towards bacteria, while showing no toxic effects towards the more robust human cell lines. Our investigation of the mechanisms of action showed that this amplification is unlikely to be silver leeching, but rather a combined effort of heat and ROS/RNS generation, leading to the total eradication of bacterial cultures. With great results in colloidal AgNPs, we sought to investigate if the particles could have the same powerful effects when used as heterogenous catalysts for large scale in-flow water treatment. We successfully developed a straightforward approach to attaching AgNPs to a glass wool support, and used this to build a photoreactor that utilizes low cost, high intensity white LED illumination. Our early results show that AgNPs@GW are still excellent antibacterial agents, capable of totally disinfecting water in-flow within time frames of 2 min. Finally, we used advanced microscopy techniques to investigate the mechanisms of action for a popular heterogenous catalyst, PdNPs@GW. The final chapter of this work deeply investigates the mechanisms and mechanical stability of PdNPs@GW using a fluorescent off-on probe, enabling us to characterize our material in incredible detail.

This work highlights how we can make nanomaterials more potent using light. This is a rare example where environmental concerns, human health, and industrial profit margins all stand to gain from taking advantage of the same innovations. If I've learned anything in my time at uOttawa, it's that small things have the potential to make great change, and I hope to see the interface of photochemistry and nanomaterials continue to grow together and address the challenges the future may hold.

Appendix

A.2: AgNP size histograms and TEM images – Chapter 2.1

TEM images of sAgNPs made using different photoinitiators, excluding I-2959 and I-379, which are included in the main text of Chapter 2.1. Table 2.1.2 displays the average diameters and standard deviations of each collection, for a population of 200 nanoparticles per sample. Imaging was performed using an FEI Tecnai G2 spirit Twin TEM microscope.

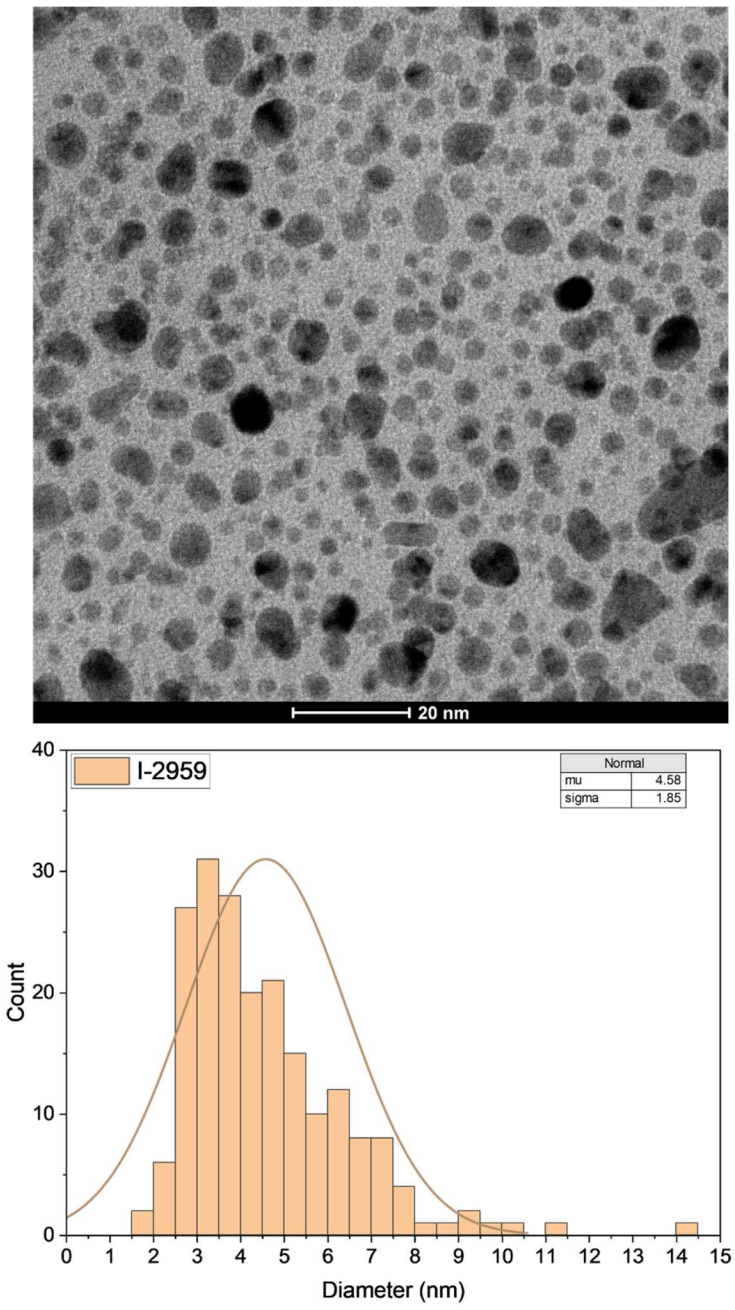

Fig. A.2.1.1 Top: Representative TEM image of AgNPs generated using the optimized flow reaction conditions using I-2959 as a photoinitiator. Bottom: Corresponding histogram for I-2959 generated AgNPs, n = 200 particles. Inset lists average size, mu, and standard deviation, sigma, in nm.

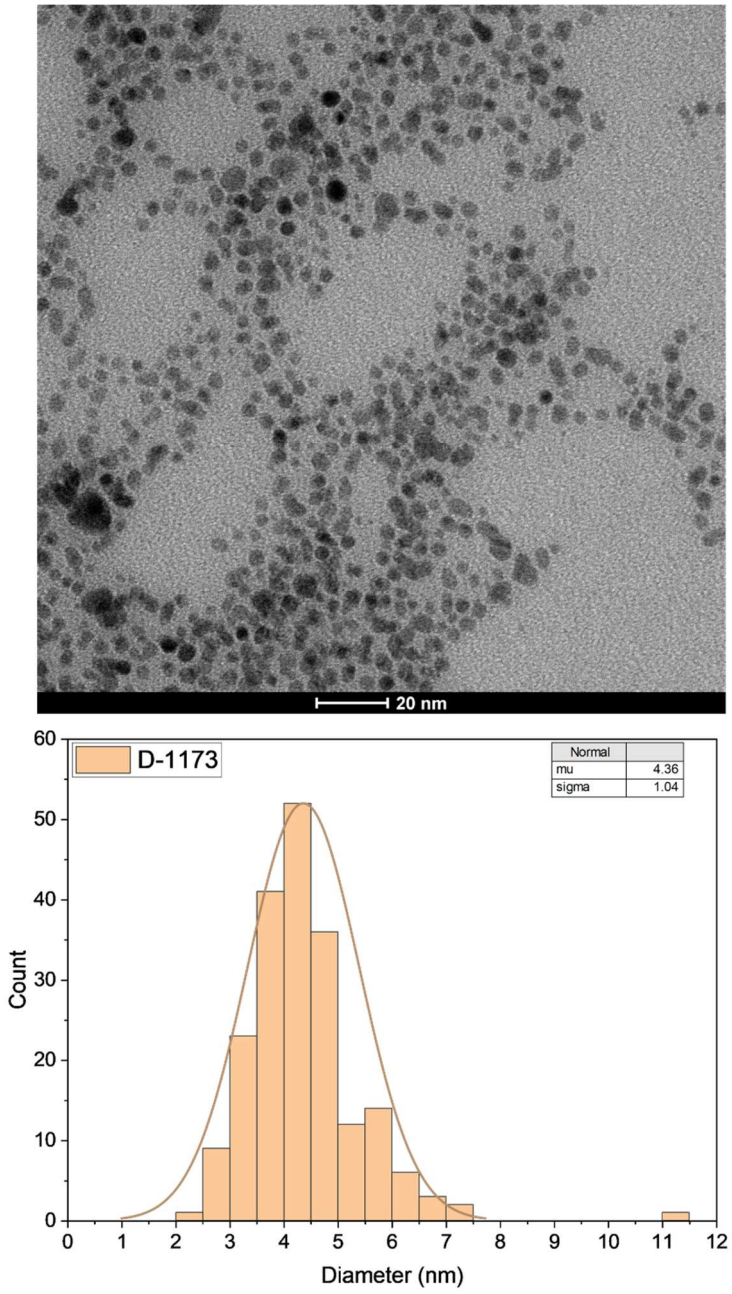

Fig. A.2.1.2 Top: Representative TEM image of AgNPs generated using the optimized flow reaction conditions using D-1173 as a photoinitiator. Bottom: Corresponding histogram for D-1173 generated AgNPs, n = 200 particles. Inset lists average size, mu, and standard deviation, sigma, in nm.

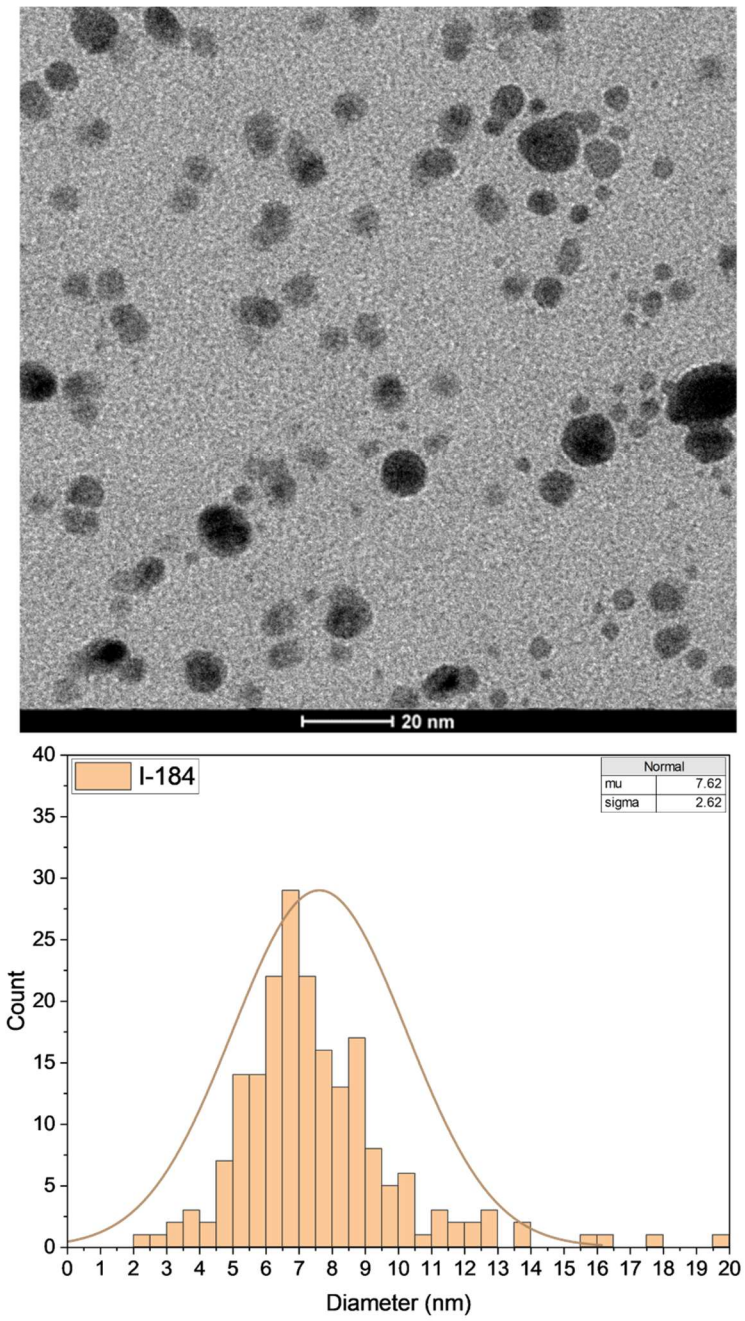

Fig. A.2.1.3 Top: Representative TEM image of AgNPs generated using the optimized flow reaction conditions using I-184 as a photoinitiator. Bottom: Corresponding histogram for I-184 generated AgNPs, n = 200 particles. Inset lists average size, mu, and standard deviation, sigma, in nm.

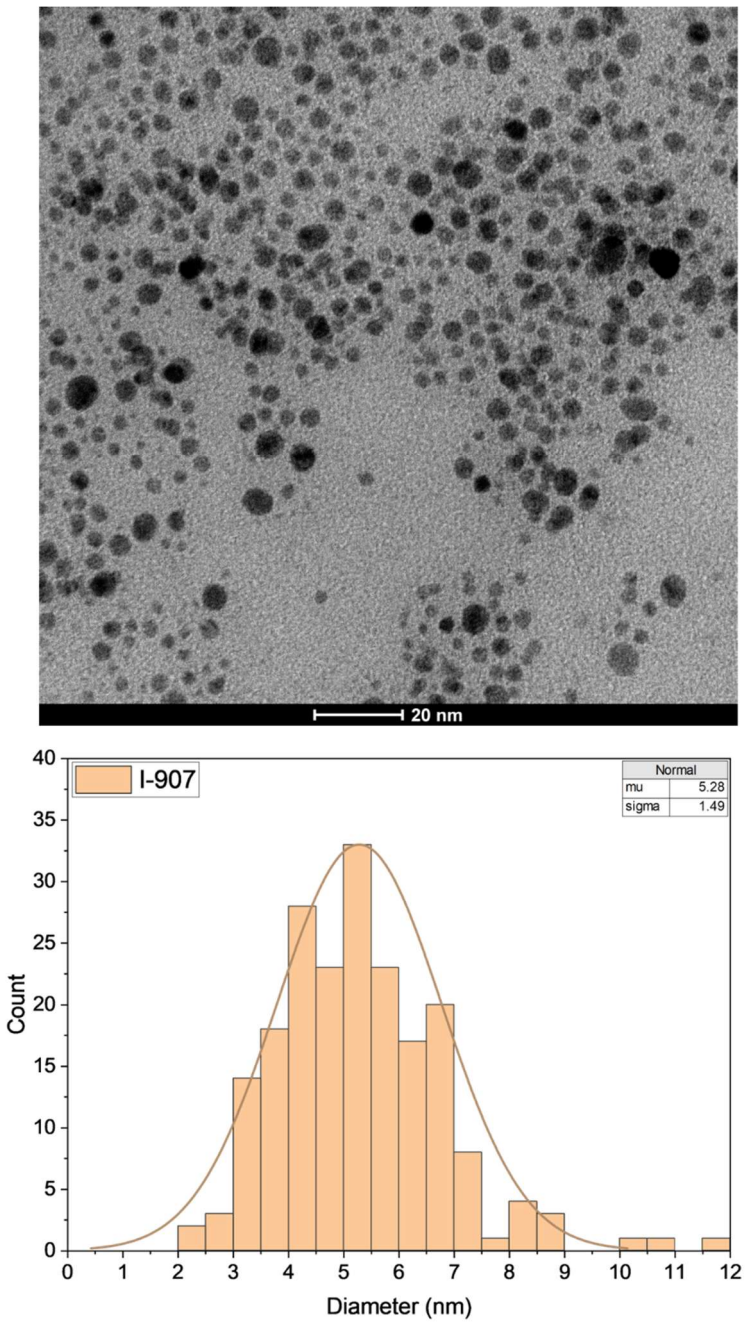

Fig. A.2.1.4 Top: Representative TEM image of AgNPs generated using the optimized flow reaction conditions using I-907 as a photoinitiator. Bottom: Corresponding histogram for I-907 generated AgNPs, n = 200 particles. Inset lists average size, mu, and standard deviation, sigma, in nm.

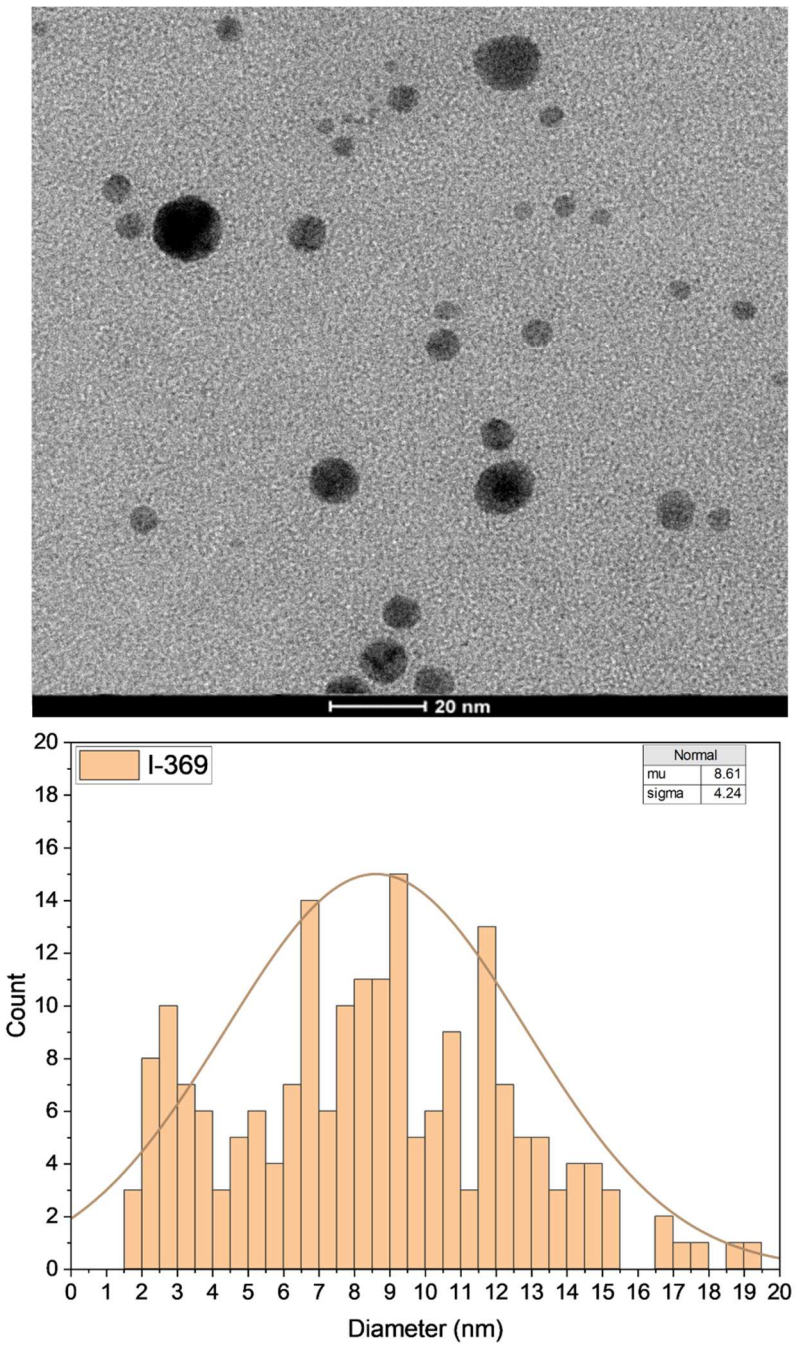

Fig. A.2.1.5 Top: Representative TEM image of AgNPs generated using the optimized flow reaction conditions using I-369 as a photoinitiator. Bottom: Corresponding histogram for I-369 generated AgNPs, n = 200 particles. Inset lists average size, mu, and standard deviation, sigma, in nm.

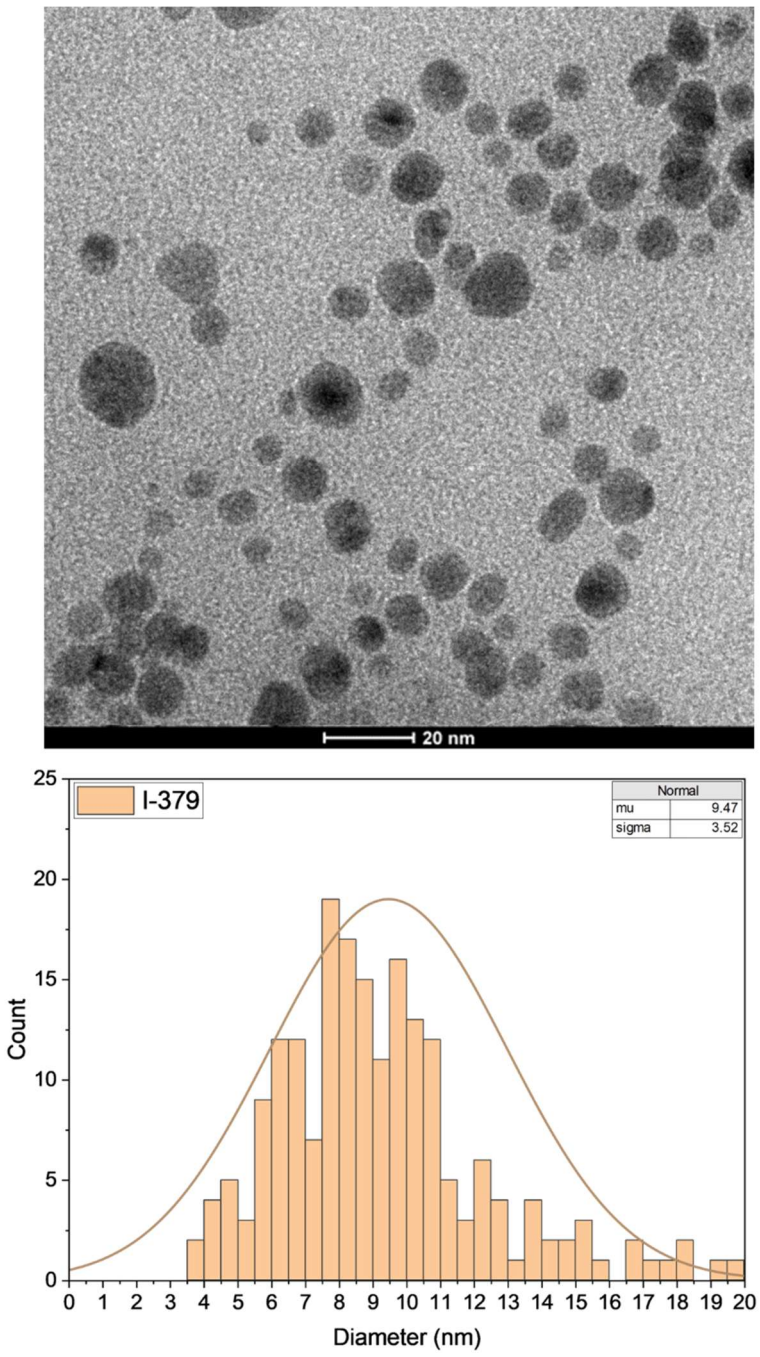

Fig. A.2.1.6 Top: Representative TEM image of AgNPs generated using the optimized flow reaction conditions using I-379 as a photoinitiator. Bottom: Corresponding histogram for I-379 generated AgNPs, n = 200 particles. Inset lists average size, mu, and standard deviation, sigma, in nm.

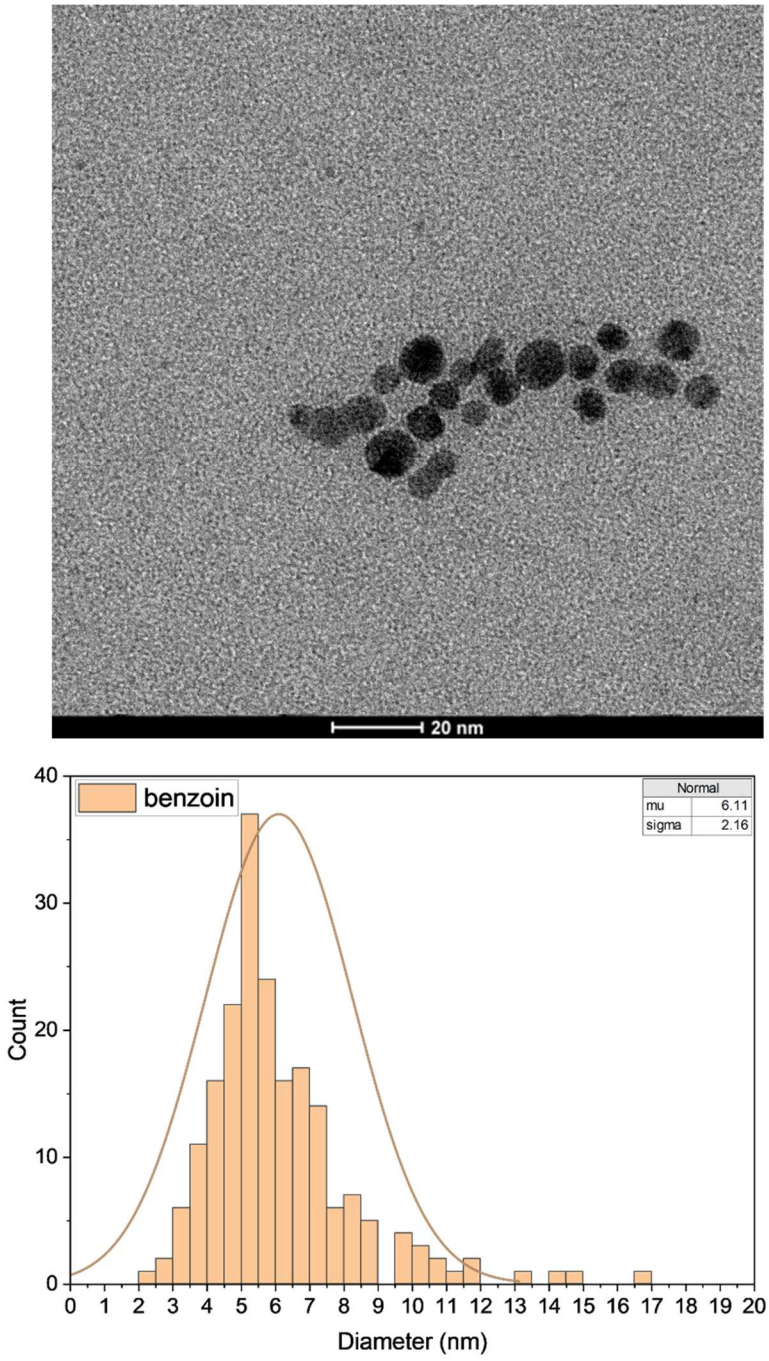

Fig. A.2.1.7 Top: Representative TEM image of AgNPs generated using the optimized flow reaction conditions using benzoin as a photoinitiator. Bottom: Corresponding histogram for benzoin generated AgNPs, n = 200 particles. Inset lists average size, mu, and standard deviation, sigma, in nm.

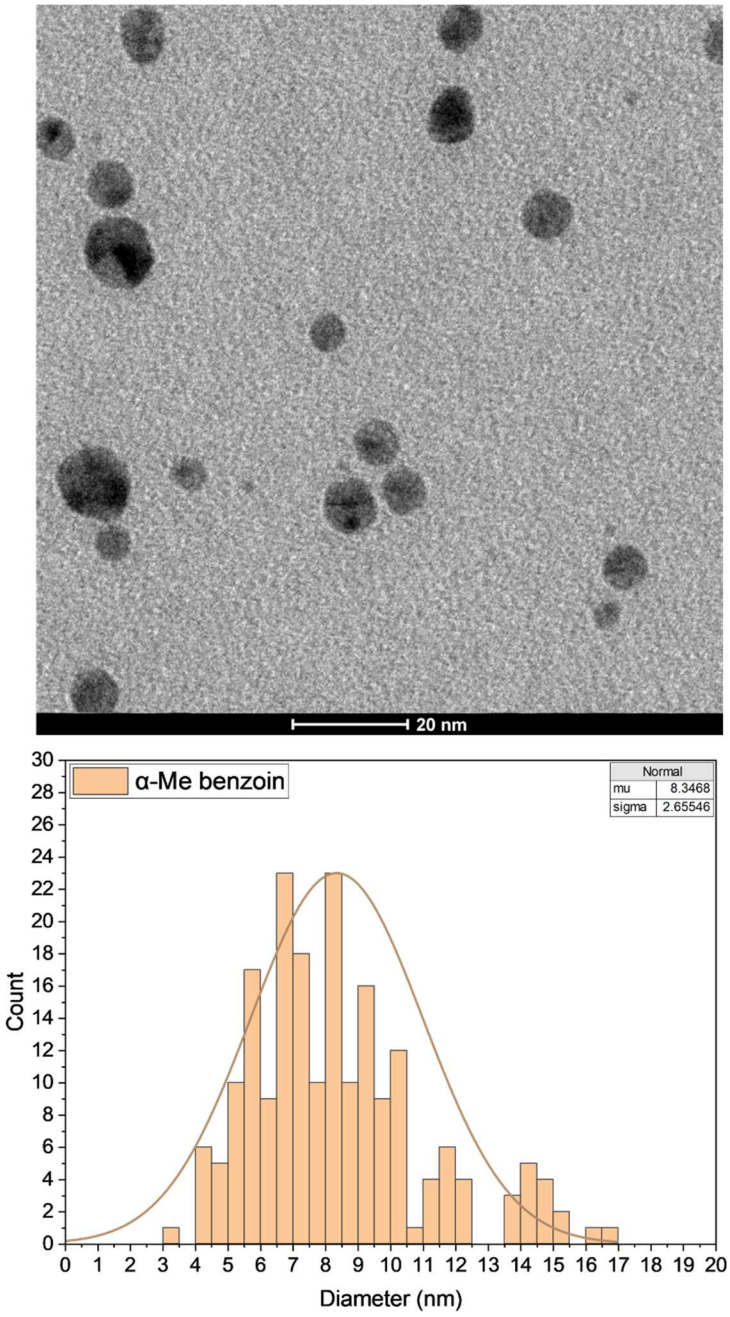

Fig. A.2.1.8 Top: Representative TEM image of AgNPs generated using the optimized flow reaction conditions using α-methylbenzoin as a photoinitiator. Bottom: Corresponding histogram for α-methylbenzoin generated AgNPs, n = 200 particles. Inset lists average size, mu, and standard deviation, sigma, in nm.